UNIVERSITÀ DI PARMA

UNIVERSITA' DEGLI STUDI DI PARMA

DOTTORATO DI RICERCA IN
"FISICA"

CICLO XXXVI

Growth and Raman characterization of selenide and oxide thin-films for photovoltaic and electronic applications

Coordinatore:
Chiar.mo Prof. Stefano Carretta

Tutore:
Chiar.mo Prof. Danilo Bersani

Dottoranda:
Dott.ssa Giulia Spaggiari

Anni Accademici 2020/2021 – 2022/2023

To my mom and to my dad.

"I know, up on top you are seeing
great sights, but down here at the
bottom we, too, should have rights."

Dr. Seuss

Summary

Chapter 1
Introduction

1. 1 - The “semiconductor age”

The history of materials is the history of human civilization. Since the beginning, materials have been playing a key role in the development of society as we know it. It is no coincidence that the first major ages of civilization all are named after a new material, starting from stone, through copper, bronze, iron, and so on. When the ability of making new tools from these materials was passed on from generation to generation, technology widely started to shape, influence, and speed up the development of societies. The more advanced was the knowledge about transforming natural resources into new materials and tools, the higher was the chance of a population to prevail over other.

Over the millennia this ability to create new materials grew exponentially, extending that early knowledge of manipulating matter over many other metal alloys, glasses, ceramics, polymers, and composites. Today we are able to synthetize millions of different materials, with different physical or chemical properties to fulfill different purposes. For many challenges that our society is currently facing, materials in one form or the other are often the heart of the solution.

But what is today’s “age”? Despite R. Buckminster Fuller is often quoted as saying “The Stone Age gave us merely stones, the Bronze Age brought us bronze, and the Iron Age gave us steel. But the Plastic Age has given us almost everything”, his definition is clearly an understatement. Somebody else could claim, indeed, that semiconductors are the heart of today civilization. Gordon Moore, who formulated the well-known empirical relationship

known as “Moore’s law”, used to say that “the semiconductor age is upon us, and it is transforming our world in ways that we can only imagine”.

Current technologies are inextricably dependent on semiconductor-based electronics. Most of our daily work, communications, mobility, energy production, design, health, somehow depend on semiconductors-based technologies. Even the study and the production of new materials often make use of them. And the trend is continuously growing. In 2022 the Semiconductor Industry Association (SIA) estimated an impressive worldwide $574.1 billion revenues for semiconductor market (Figure 1.1).

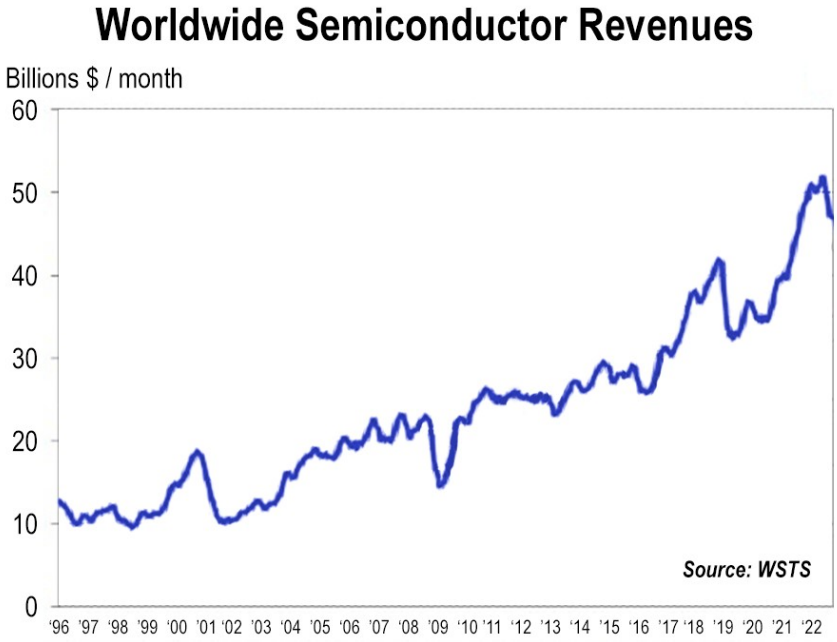

Figure 1.1 - Monthly sales by World Semiconductor Trade Statistic (WSTS) organization. WTST is an independent non profit organization

The most used semiconductors are Silicon, Germanium, and Gallium Arsenide. Germanium was leader in the beginning of this so-called “semiconductor age”, but its high price (1500-3000$ per kg in the last few years) and its geographic availability (60% of total production located in China) paved the way for Silicon. For sure Silicon played a main character role in the past few decades, because its large worldwide availability, together with relatively cheap extraction and purification processes, make it much more cost-effective (1-5$ per kg).

But Silicon cannot be used for any application. Other semiconductors are used to overcome the limits related to its relatively low saturated electron velocity and electron mobility, or its indirect gap and its energy gap value, or its resistivity. Moreover, Silicon

already reached the limit of the previously mentioned "Moore's law" and today, despite lithographic technology reached an impressive 1-2 nm resolution, complex tridimensional transistors, combining Silicon with a multitude of different materials, are required to continuously increase the transistor density of an integrated circuit.

For all these reasons the research of new materials to be used in electronics and energy production is still extremely active.

1.2 - The need of materials in form of thin-films

Today a large number of materials is often needed and hence produced in form of **thin-films**. Layers with a wide range of thickness is ascribed to this definition, generally from less than 1 nanometer (a single monolayer) up to several micrometers. The main advantages of disposing of materials in such a shape are:

- they can be used to create devices that are smaller, lighter, and more efficient than devices made from bulk materials, because of the limited amount of material deposited;
- they can be used to protect (coatings) or modify the properties of other materials, as well as they can be combined to form heterostructures with unique properties;
- if their thickness is low enough to obtain a 2D-material, exotic or quantum-confinement induced properties may arise and some of them can be tuned by controlling the film thickness;
- they can be used to stabilize, through an epitaxial growth on specific substrates, some crystalline phases that otherwise would be meta-stable or impossible to obtain in bulk form, as well as crystal lattices with controlled stress or strain conditions (that in some cases are used to produce quantum-dots 0D-structure);
- some of them can be easily shaped in complex structures, with specific geometries and sizes, by alternating deposition techniques with mechanical or lithographic masks, etching or micro-machining processes;
- a very large number of deposition techniques are available for different materials, producing films with different quality grade at different deposition rates, in inert or reactive environments, at low or high temperatures, enabling the deposition of thin-films on different type of substrate materials.

Thin-films are usually so fragile and/or difficult to handle that in most of the cases they are not obtained in a self-standing form, but they are generally deposited on a thicker and mechanically more robust and handy **substrate material**, that can have both a passive or an active function.

Most of micro-electronic circuits are made by different thin-films, obtained by modifying the surface layers of a material (*e.g.* by doping, implantation, oxidation or nitridation of a semiconductor) or by depositing new materials, arranged in a complex planar and sometimes vertical circuit structure.

Also, a whole class of solar cells is based on thin-films, where alternative materials are used instead of a 160-240 μm thick layer of Silicon. The idea beyond the so-called "second-generation photovoltaics" is to use materials with a higher absorption coefficient and possibly a better absorption range (to better match solar radiation), so that just a very thin layer of about 1 μm can be used to absorb most of the incident light. The use of a much smaller amount of materials is supposed to compensate (and possibly overcome) the higher cost of these materials in comparison with that of cheaper Silicon. Moreover, thin-films are also used to create multi-junction solar cells, complex photovoltaic devices that can overcome the intrinsic limits of each semiconductor in photo-electric conversion efficiency by engineering the light absorption through multiple stacked p-n junctions made of different materials/compositions.

The use of materials in form of thin-films is also in agreement with the more and more pressing need of improving technology sustainability, by using less resources and lowering the power that devices need to operate.

1.3 - Overview of my PhD thesis

This thesis presents the main results achieved during my PhD activity, carried out between the laboratories of the Department of Mathematical, Physical and Computer Sciences and the Department of Chemistry, Life Sciences and Environmental Sustainability at the University of Parma, and those at CNR Institute for Materials for Electronics and Magnetism (IMEM).

As reported in the title, my PhD activity was mainly focused on selenide and oxide thin-films, that are actually under investigation or development in these Institutions for different applications in photovoltaics and electronics devices. Details are here provided on the synthesis of these materials, deposited in form of thin-film with different techniques, as well as their characterization, mainly performed by Raman spectroscopy, but also with other complementary techniques, that were fundamental to determine the thin-films properties and functionality. In most of the cases synthesis and characterization were performed in parallel, since the results of the latter were used from time to time as a feed-back for the progressive optimization of the deposition processes.

After this brief introduction, the used **deposition techniques** and **characterization techniques** are described in brief in **Chapter 2** and **Chapter 3** respectively, so that, if needed, a quick reference is available for the main concept, terms and parameters discussed in the following chapters, where experimental results are reported and discussed.

In **Chapter 4** the deposition of **antimony selenide** (**Sb_2Se_3**) thin-films by Low-Temperature Pulsed Electron Deposition (LT-PED) and Radio Frequency Magnetron Sputtering (RF-MS) is reported and discussed, together with their structural, chemical, morphological and electrical characterization. Both undoped and Cu-doped films were obtained for the fabrication, test, and optimization of photovoltaic solar cells, within which these films are used as alternative absorber material.

In **Chapter 5** the deposition of **gallium oxide** (**Ga_2O_3**) thin-films by MetalOrganic Chemical Vapor Deposition (MOCVD) and LT-PED is reported and discussed, with a specific attention on the correlation between growth parameters and the different characterized phases and properties, that could be exploited for different kind of possible applications (e.g. solar-blind UV detectors or high-power electronics). In particular, Raman characterization proved to be a key-tool to reveal small amounts of secondary phases and the influence of doping with Si and Sn.

Chapter 6 is instead focused on the role that Raman characterization had in the production and isolation of **γ-$BaFe_2O_4$**, both in form of powders (solid state reaction) and thin-films (LT-PED). Samples of this pure compound proved for the first time that this material is a **room-temperature multiferroic compound**.

A general overview of the main result is finally summarized in **Chapter 7**.

Part of these results have been also described in 8 papers, 5 of which are already published and 3 are currently under review:

1) **G. Spaggiari**, F.Pattini, D. Bersani, D. Calestani, A. De Iacovo, E. Gilioli, F. Mezzadri, A. Sala, G. Trevisi, S.Rampino, "Growth and structural characterization of Sb_2Se_3 solar cells with vertical Sb_4Se_6 ribbon alignment by RF magnetron sputtering", ***Journal of Physics D: Applied Physics***, 54 (2021) 385502.
2) **G. Spaggiari**, D. Bersani, D. Calestani, E. Gilioli, E. Gombia, F. Mezzadri, M. Casappa, F. Pattini, G. Trevisi, S. Rampino, "Exploring Cu-Doping for Performance Improvement in Sb_2Se_3 Photovoltaic Solar Cells", ***International Journal of Molecular Sciences***, 23 (2022) 15529.
3) F. Orlandi, D. Delmonte, G. Calestani, E. Cavalli, E. Gilioli, V. V. Shvartsman, P. Graziosi, S. Rampino, **G. Spaggiari**, C. Liu, W. Ren, S. Picozzi, M. Solzi, M. Casappa,

F. Mezzadri, "γ-$BaFe_2O_4$: a fresh playground for room temperature multiferroicity", ***Nature Communications***, 13 (2022) 7968.

4) P. Mazzolini, Z. Fogarassy, A. Parisini, F. Mezzadri, D. Diercks, M. Bosi, L. Seravalli, A. Sacchi, **G. Spaggiari**, D. Bersani, O. Bierwagen, B. M. Janzen, M. N. Marggraf, M. R. Wagner, I. Cora, B. Pécz, A. Tahraoui, A. Bosio, C. Borelli, S. Leone, R. Fornari, "Silane-Mediated Expansion of Domains in Si-Doped κ-Ga_2O_3 Epitaxy and its Impact on the In-Plane Electronic Conduction", ***Advanced Functional Materials***, 33 (2023) 2207821.
5) R. Jakomin, S. Rampino, **G. Spaggiari**, F. Pattini, "Advances on Sb_2Se_3 Solar Cells Fabricated by Physical Vapor Deposition Techniques", ***Solar***, 3 (2023) 566.
6) S. Bienz & **G. Spaggiari**, D. Calestani, G. Trevisi, D. Bersani, N.Kumar, Renato Zenobi, "Nanoscale Chemical Analysis of Sb_2Se_3 Solar Cells Interface using Tip-Enhanced Raman Spectroscopy", ***ACS Applied Materials and Interfaces***, *under review*.
7) R. Jakomin, S. Rampino, **G. Spaggiari**, F. Pattini, F. Mezzadri, G. Trevisi, E. Gombia, E. Gilioli, M. Mazzer, "New Earth-Abundant Thin Film Solar Cells Based on bilayer pulsed electron deposition/sputtering Antimony Selenide", ***Sustainable Materials and Technologies***, *under review*.
8) **G. Spaggiari** , R. Fornari , P. Mazzolini , F. Mezzadri , A. Parisini , M. Bosi , L. Seravalli, F. Pattini , M. Pavesi , S. Rampino , A. Sacchi , D. Bersani, "Raman characterization of Ga2O3 thin-films: a key tool for the study of different phases and crystalline properties", **Applied Spectroscopy**, *under review*.

Three further articles on these topics were published for conference proceedings:

9) G. Spaggiari, S. Rampino, D. Bersani, "Sb_2Se_3: a possible future for thin-film photovoltaics?", *EPJ Web of Conferences*, 268 (2022) 00006.
10) S. Rampino, G. Spaggiari, R. Jakomin, E. Gilioli, F. Mezzadri, M. Meneghini, J.J.N. Barrantes, M. Mazzer, C. De Santi, F. Pattini, "Strategies for Enhancing the Photovoltaic Conversion Efficiency in Sb_2Se_3-based Solar Cells", *Proceedings of the 11th International Conference on Materials for Advanced Technologies (ICMAT 2023)*, (2023).
11) J.J.N. Barrantes, C. De Santi, F. Piva, M. Buffolo, A. Caria, N. Trivellin, S. Rampino, G. Spaggiari, R. Jakomin, F. Pattini, G. Meneghesso, E. Zanoni, M. Meneghini, "Characterization and C-DLTS analysis of antimony selenide solar cells", *Proceedings of Prima conferenza nazionale della Rete Italiana Fotovoltaico per la ricerca e l'innovazione (rete IFV)*, (2023).

Other side-works, that are not reported in this thesis, are instead described in the following papers:

12) M. Bertoncello, M. Barbato, A. Caria, M. Buffolo, C. De Santi, S. Rampino, F. Pattini, **G. Spaggiari**, N. Trivellin, D. Vogrig, E. Zanoni, G. Meneghesso, M. Meneghini, "Comparison between Cu(In,Ga)Se_2 solar cells with different back contacts submitted to current stress", ***Microelectronics Reliability***, 138 (2022) 114612.
13) E. Del Canale, L. Fornari, C. Coppi, **G. Spaggiari**, F. Mezzadri, G. Trevisi, P. Ferro, E. Gilioli, M. Mazzer, D. Delmonte, "High-Pressure Bulk Synthesis of InN by Solid-State Reaction of Binary Oxide in a Multi-Anvil Apparatus", ***Inorganic Chemistry***, 62 (2023) 5016.
14) E. Del Canale, C. Coppi, L. Fornari**, G. Spaggiari**, M. Casappa, F. Mezzadri, G. Trevisi, S. Rampino, F. Pattini, M. Bronzoni, E. Gilioli, M. Mazzer, D. Delmonte, "Ultra-low cost, green and simple RT-mechanosynthesis of Antimony Sulphoiodide, a potential ferro-photovoltaic material", under submission.

Chapter 2
Growth techniques

In this chapter the main growth techniques used to deposit the studied thin-films are briefly described. The purpose is to provide a quick reference for the main concepts, parameters and technical terms, that are then used in the following chapters dedicated to the experimental results and their discussion.

In the next paragraphs three techniques are described:

2.1 Low-Temperature Pulsed Electron Deposition (LT-PED)

2.2 Radio Frequency Magnetron Sputtering (RF-MS)

2.3 MetalOrganic Chemical Vapor Deposition (MOCVD)

I personally used the first two techniques to deposit different types of thin-films, while I provided my direct characterization feed-back to the colleagues at IMEM-CNR for their use of the third technique to obtain Ga_2O_3 thin-films.

2.1 - Low-Temperature Pulsed Electron Deposition (LT-PED)

Pulsed Electron Deposition (**PED**) is a high-energy physical deposition technique. It is a quite unexpensive technique (installation can be lower than 40.000 €) but the efficiency is optimal, and it is also suitable for materials with a complex stoichiometry and/or an incongruent melting point.

In PED technique, pulsed electron beams at very high-power density (up to 10^8 W/cm^2) are used. The frequencies exploited are just a few Hz and the pulses are in the range of 100 ns. With these characteristics, the power density striking the target material is generally two orders of magnitude higher than that required for thermal e-beam evaporation, *i.e.* at about 10^4-10^6 W/cm^2. This electron bombardment produces a brief out-of-equilibrium surface heating, preventing melting of the material and giving rise to the “ablation” phenomenon, which is a rapid emission under non-equilibrium thermodynamic conditions of all the elements contained in the target.

The material emitted from the target is in the form of a plasma, which maintains stoichiometry in the gas phase even when the melting point is thermodynamically incongruent. In addition, since the generated plasma has a very high temperature (thousands of K), the species within it are highly energetic, allowing films of good crystalline quality to be deposited even when the substrate temperature is relatively low. For this reason, in many cases, this technique is also often called "low-temperature" PED (or **LT-PED**).

The stoichiometric ablation of the target ensured by this technique makes PED especially suitable for growing films of alloys, materials with complex state diagrams, or with out-of-equilibrium stoichiometries. In addition, stoichiometric ablation also allows for long-time deposition without the need for intervention on the target material, which will not be depleted of some elements more than others over time.

Among the various materials successfully deposited by this technique, an example suitable for thin-film photovoltaic application is Cu(In,Ga)Se_2 (also referred to as CIGS), whose quaternary composition, incongruent melting point, and high volatility of selenium in the melting phase generally make it much more difficult to be obtained by other single-step techniques (post-growth treatments are generally required to correct the stoichiometry).

A LT-PED deposition (Figure 2.1) takes place in a vacuum chamber in which only the process gas (usually Ar at a pressure close to 10^{-3} mbar) flows. The pulse is generated by a **trigger**, which discharges the accumulated power at the desired frequency (about 10 Hz). The discharge ionizes the process gas, that emits highly energetic electrons with a cascading

effect, from the walls of a special **hollow cathode**. The electrons formed in the hollow cathode are driven to the anode by a voltage of several kV and collimated through a thin alumina **dielectric tube** to the target.

The **electron beam** that reaches the **target** is characterized by electrons of different energy (depending on the number of collisions they have been involved in) and can be divided into three main parts:

- the **first part** consists of a few very fast and energetic electrons
- the **second part** is characterized by a larger but still relatively low current of medium-energy electrons
- the **third and final part** consists of a high current, but such current is made up of slow and low-energy electrons

The ablated material develops a characteristic **"plume" of plasma** in the direction orthogonal to the surface of the target (see inset of Figure 2.1).

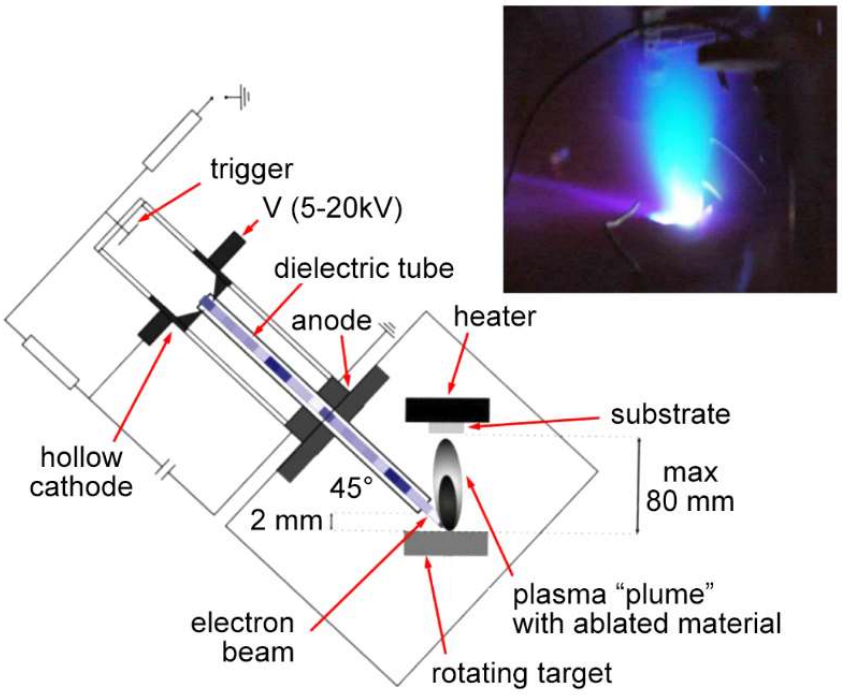

Figure 2.1 – Schematic diagram of a PED deposition chamber. In the upper right inset, an image of the ablation "plume"

The target is usually mounted on a **rotating stage**. In this way it possible to obtain a better homogeneity, less heating and more material available for ablation. The **substrate** is usually placed upside-down above it, in contact with a **heater** that determines its temperature. The upside-down position makes it possible to avoid particulate matter, that

might accidentally come off the target, falling on the film. The graphite heater is large enough to heat the substrate rather homogeneously.

Since electrons are emitted in the hollow cathode by thermo-ionic effect, this distribution can be altered by "overheating" of the source. This means that there is generally an upper limit (Figure 2.2) in the ratio between accelerating voltage and pulse frequency ("**pulse repetition rate**"), within which proper operation is guaranteed to allow the cathode to cool between two successive pulses. This limit may vary depending on the PED deposition system used.

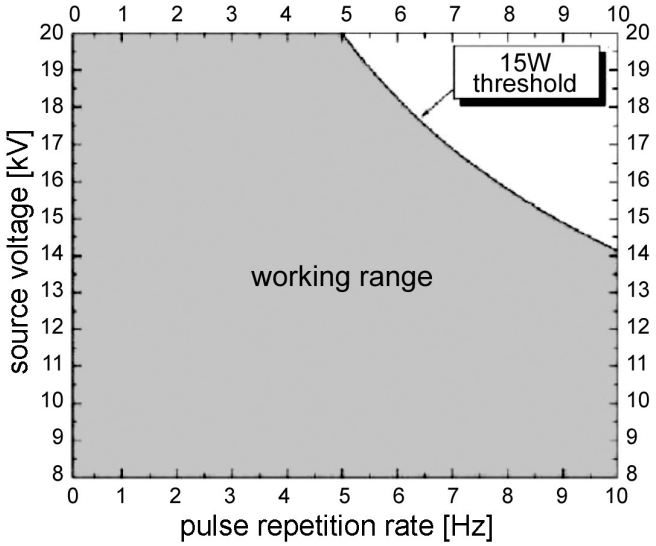

Figure 2.2 - Example of maximum usable voltage as a function of pulse frequency for a PED electron gun operating within a power limit of 15W.

The angular distribution of the plasma plume limits the deposition within a given area on the substrate. In general, the Comsa-David model, which describes this angular distribution by considering both possible evaporative and ablative contributions, uses a function as a function of a double cosine:

$$F(\theta) = a \ \cos[\theta + (1-a)\cos^{p}\theta] \qquad (2.1)$$

where the exponent p is greater than 1, θ is the angle from the deposition axis, and a is the coefficient that weighs the contributions between evaporation at thermal equilibrium and ablation. While in general evaporation has a very broad distribution ($F(\theta)\approx\cos(\theta)$), for very high acceleration voltages such as those used in PED the exponent p increases to values close to 6-7 while $a\approx 0$.

Thus, the emission cone of plasma plume is rather narrow, which means that the deposition area achievable with this technique is generally small (a few square centimeters).

On the other hand, the narrow distribution of the evaporate, which is typical of high-energy techniques, allows for a much higher deposition yield (ratio between the mass deposited on the substrate and the mass evaporated from the target) than in the thermal evaporation technique, where most of the evaporated material goes on the walls of the chamber, rather than on the substrate.

Systems have been designed over the years at the IMEM-CNR Institute to partially overcome the problem of a narrow deposition cone. The first is a multi-cannon PED system, capable of having four or more electron guns operating in parallel on as many targets and positioned so that the plumes deposit material on the substrate in an array with minimal overlap, sufficient to form a homogeneous film over a larger area (up to 256 cm^2). The second is a roll-to-roll PED deposition system on sliding substrates or ribbons of flexible substrates.

2.2 - Radio Frequency Magnetron Sputtering (RF-MS)

The term "**sputtering**" is used to define the process of erosion of a surface by charged particles accelerated towards it. The charged particles mainly exploited to achieve sputtering are ions in a plasma, typically of inert gas (Ar^+, Kr^+, ...) or small molecules (N_2^+, O_2^+). The term "sputtering deposition," on the other hand, is the process of accumulating on a nearby substrate the atoms undermined by the surface subject to sputtering.

Sputtering deposition is a widely used technique for the production of thin-films. In particular, due to its high efficiency and easy scalability over large areas, it is one of the leading techniques in industry.

To fully understand how this technique works, and therefore its pros and cons, it is essential to go into a little more detail. First, it is useful to define the **"yield" Y** of the sputtering process, defined as the ratio:

$$Y = \frac{\text{emitted particles}}{\text{incident particles}} \qquad (2.2)$$

The yield of this erosion process is mainly a function of the energy of the particles (ions) used to hit and undermine atoms from the surface of the target material. In fact, five regimes can be defined as a function of energy:

- **<20 eV: subthreshold** - in this energy range the sputtering process is largely inefficient ($Y < 10^{-4}$)
- **30-50 eV: low energy** - in this range only extremely thin films can be obtained, which, because of the low energy, tend to deposit almost everywhere inside the deposition chamber instead of being directed toward the substrate ($Y \approx 10^{-2}$-10^{-1})
- **50-1000 eV: "knock-on" energy** - this is the ideal range to use in order to obtain good deposition from the sputtering process; in this range, effective displacement of multiple atoms as well as ejection of surface atoms can be achieved by impact, as depicted in Figure 2.3a ($Y \approx$1-10)
- **1-50 keV: cascade collisions** - at this range of energies all chemical bonds within a spherical region close to the impact point are broken; unfortunately, plasma generation at these energies is difficult to achieve technologically, both in terms of the instrumentation and the associated costs. For these reasons it is not usually exploited for film deposition (Y <1-100)
- **>50 keV: high energy** - in this range of energies the sputtering process is less efficient because the ions have sufficient energy to be implanted deeply and therefore make atoms ejection from the surface less likely.

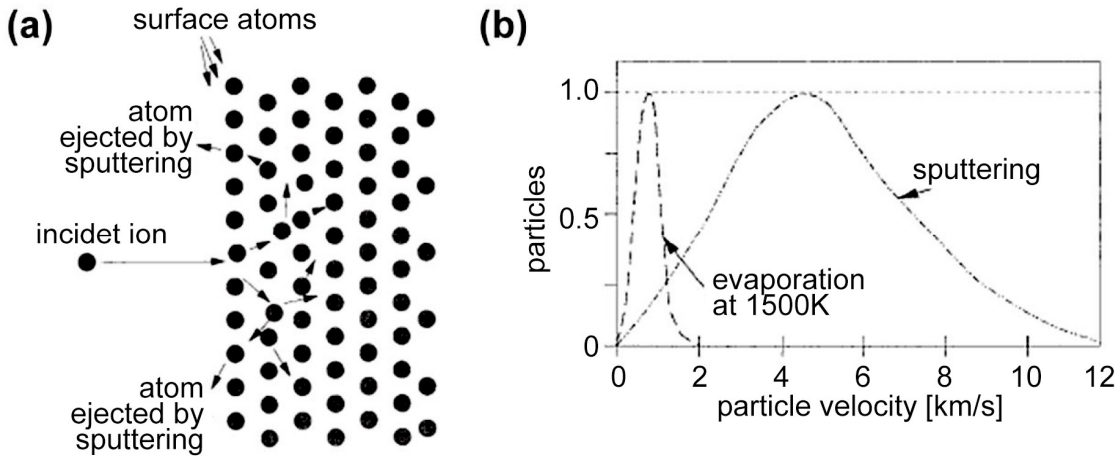

Figure 2.3 - (a) schematic representation of the atoms ejection process from the surface during the sputtering phenomenon; (b) comparison of the typical velocity distribution of evaporated particles and particles ejected by sputtering

In the "**knock-on**" regime generally used for sputtering deposition, the velocity (hence the kinetic energy) with which atoms are ejected from the surface is not as high as in the case of PED deposition but, nevertheless, much higher than that with which atoms simply evaporate (Figure 2.3b).

In this optimal regime, the sputtering yield increases roughly linearly with the energy of the incident ions and, therefore, with the applied accelerating voltage (Figure 2.4a).

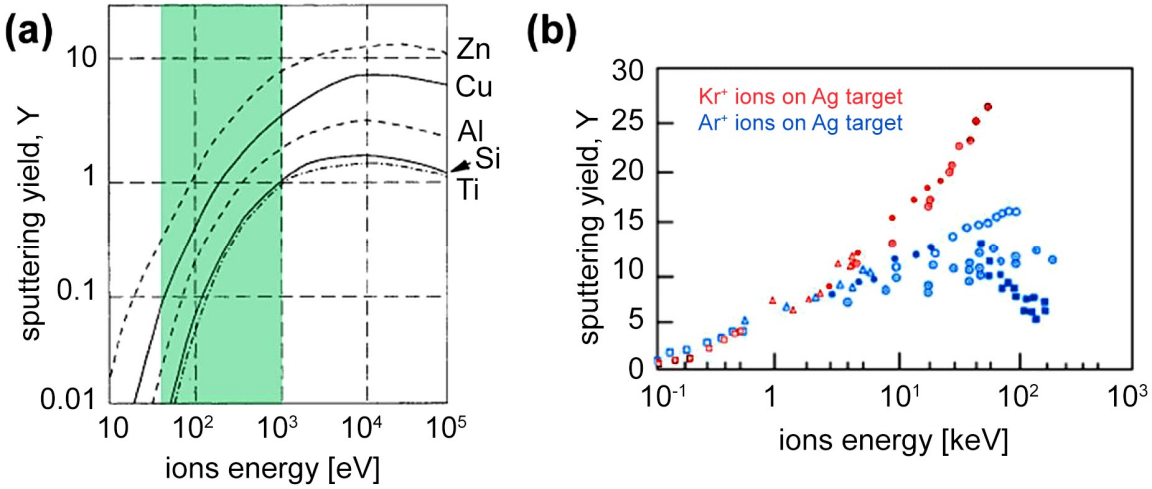

Figure 2.4 – (a) sputtering yield as a function of target material using the same ions (Ar+); (b) sputtering yield as a function of ions used with the same target material (Ag)

Moreover, within certain limits, an increase in ion flux (ion current) results in an almost proportional increase in the number of atoms ejected from the target by sputtering. This

means that, in many cases, the deposition rate (or "deposition rate") scales approximately the same as the power.

It can be seen that Y also depends on:

- the **kind of ions used**: on the same target Kr^+ ions produce a higher yield than Ar^+ ions due to their higher mass;
- the **target atoms**: the trend with atomic number in this case is not at all easily described because, in addition to the mass of the atoms, it also depends on the crystal structure and the strength of the chemical bonds;
- the **angle of incidence**: the yield, which is typically proportional to the cosine of the angle with the normal to the surface, can for some energies and some target materials have a maximum for a non-zero angle.

From these last points we can easily understand that in the case of sputtering compounds of different atoms, the atoms ejected from the target will generally not have the same stoichiometry among them as they had in the target. This implies that the deposition by sputtering of these materials, over time, could generate compositional drifts or oscillations. For this reason, in some cases, it is necessary to use the so-called co-sputtering technique: a simultaneous sputtering process from targets of different elements, each of which has appropriately optimized conditions/parameters to achieve the correct final stoichiometry.

Several sputtering systems are commercially available, differing both in the voltage applied between the cathode and anode of the plasma generation chamber and in whether magnetic fields are used or not.

The simplest of these is so-called "**DC sputtering**", so named because of the use of a DC voltage between cathode and anode. DC sputtering takes advantage of the plasma formed by glow discharge ("glow discharge") when an appropriate voltage is applied between a cathode and an anode in a volume in which a relatively low-pressure gas is present. In the appropriate pressure range, plasma initiation can be achieved with voltages that are not too high (Paschen's law - Figure 2.5).

In Figure 2.6, instead, the different regions that are established in this system are shown.

Starting from the cathode, from which electrons are initially emitted, the first region encountered is a thin gap known as the **Aston dark space**. In this space the secondary electrons released from the cathode are accelerated toward the anode to then reach sufficient energy to ionize the atoms of the working gas and generate the light emission of the cathode glow.

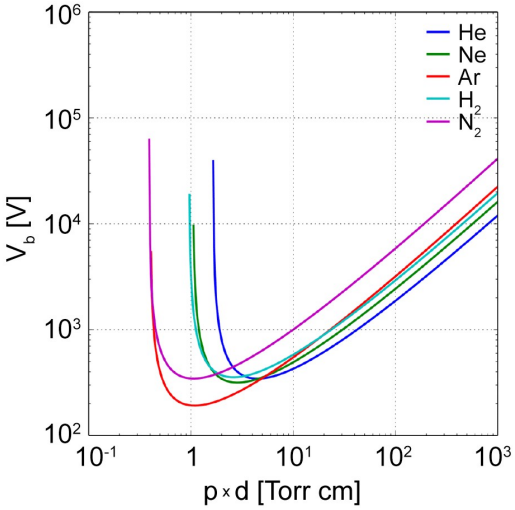

Figure 2.5 - Ignition discharges voltage for different gases as a function of pressure

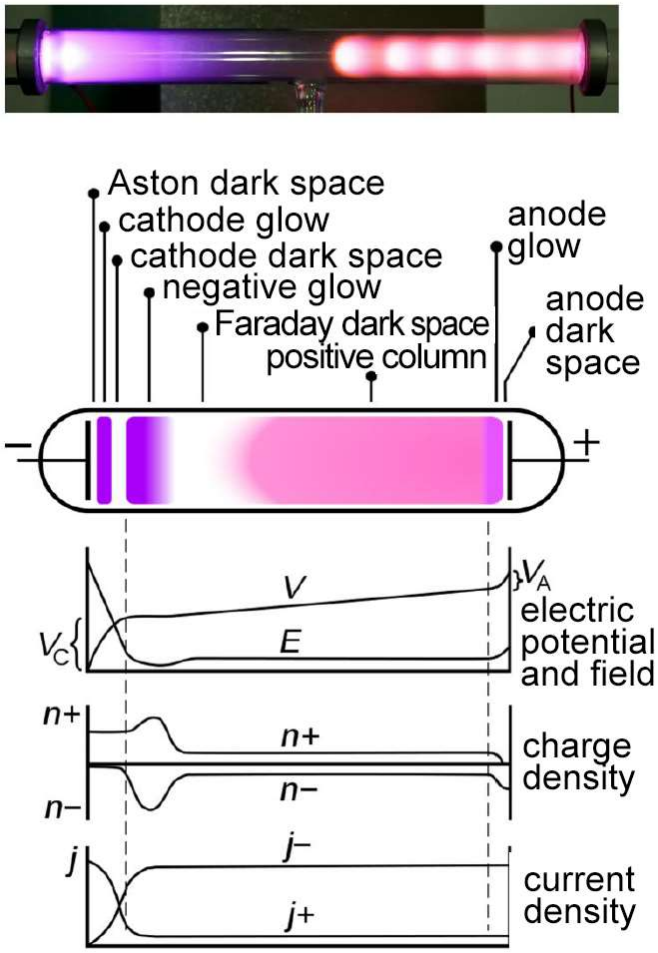

Figure 2.6 - Image and diagram of the different regions established during a glow discharge in a continuous electric field; the trends along the axis of potential and electric field, charge density and current density are shown below.

The **cathode glow** is the zone where avalanche ionizations take place, and it is the zone where electrons have high energy (evidenced by the higher luminosity). In the next dark zone of the cathode ("**cathode dark space**"), also called the Crookes/Hittorf dark space, the density of ions gradually increases as the electrons multiplied by the ionizations in the cathode glow zone are accelerated and swept away by the electric field in the direction of the anode.

Continuing to the anode, the next zone is known as the "**Faraday dark space**", where electrons lose most of their energy and in general excitation and ionization can no longer occur. Finally, within the positive column region there is a quasi-neutral plasma (nearly equivalent ionic and electron current). The last glow occurs near the anode ("**anode glow**").

The positive ions generated, however, will instead be accelerated toward the cathode where, if they have sufficient energy, they will give rise to sputtering. In the sputtering phenomenon, other secondary electrons will also be re-emitted, which, if in sufficient numbers, will allow the generated plasma to be self-sustaining over time.

In a DC sputtering deposition chamber, the target material forms the cathode while the substrate is placed a short distance away at the anode position (Figure 2.7a). The main advantages of this variant are the cost (since the related deposition apparatus is the least complex) and the possibility to work at relatively high pressures (the ionization cross section for secondary electron collision is generally low for most gases, especially at high voltages).

The disadvantages with respect to the other variants (that we will see later), however, are that the deposition rate is not particularly high and that it can be used only with conductive materials (therefore also the inability to use oxygen as a working gas because it could form insulating oxides on the cathode surface). On insulating materials, in fact, plasma ions have difficulty discharging and their accumulation leads to the formation of a positive field on the surface, which slows down subsequent ions and thus the entire sputtering process.

To prevent the latter drawback, radio frequency sputtering ("**RF sputtering**") is generally used. In fact, the use of alternating currents that reverse the polarization between anode and cathode for only a short time (Figure 2.7b) allows ions that have accumulated on the surface of insulating materials to be discharged, making it possible to obtain sputtering depositions even from these materials or metal targets in a reactive environment.

The deposition rate is also higher, for this configuration, due to the additional movement of the secondary electrons induced by the field oscillations, which increases both the plasma density and the ion current to the cathode. On the other hand, the deposition apparatus, which in this case also includes the radio frequency generation and control system, is more

expensive than the "DC" variant. In addition, this system is less efficient at high pressures because the high density of ions leads to collisions between ions even within the dark zone, slowing them down precisely where they are generally accelerated.

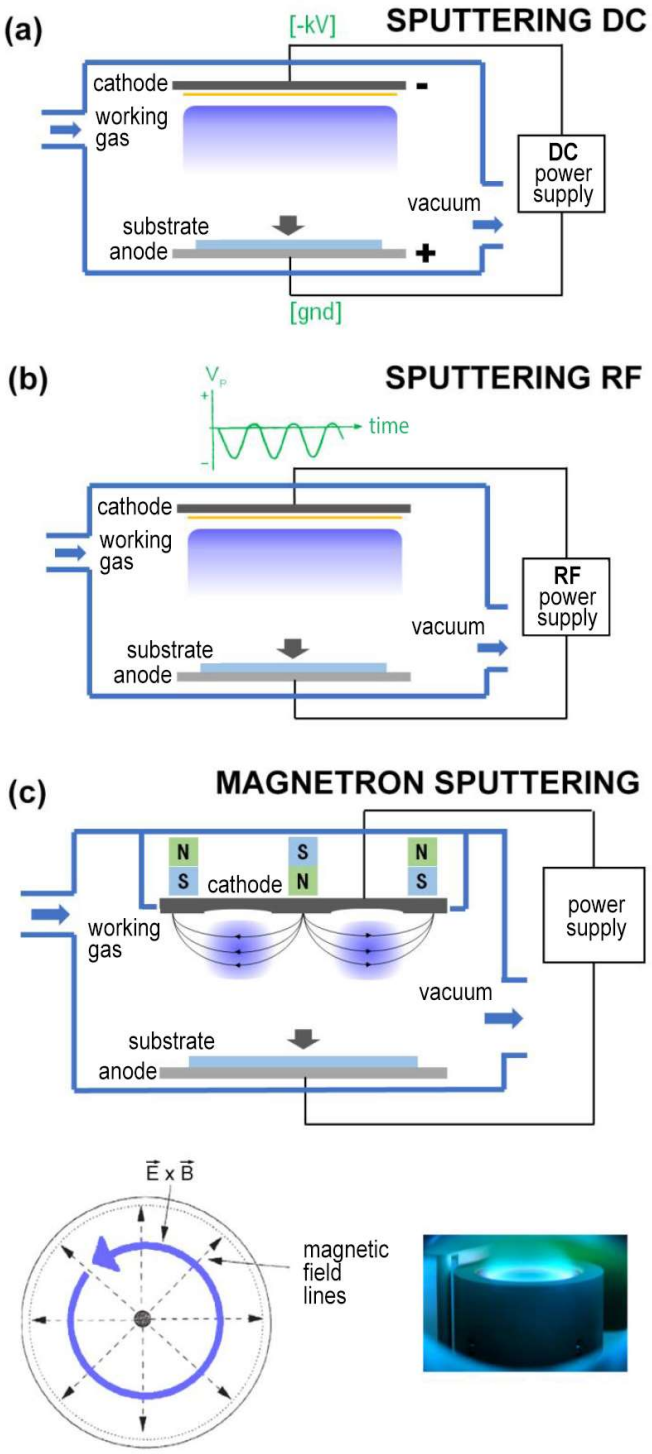

Figure 2.7 - Different configurations of sputtering deposition technique: (a) direct voltage sputtering (DC sputtering); (b) radio frequency sputtering (RF sputtering); (c) magnetron sputtering (MS)

Finally, it is important to mention the "**magnetron sputtering**" (MS) configuration. This involves the use of a magnetic field placed near the cathode. By generating a radial magnetic field, ions and electrons are "trapped" along a circular trajectory (also called a "racetrack") on the surface of the target (Figure 2.7c) due to the Lorentz force. The plasma in this annular region has a high density, so a high sputtering current can be obtained even at low voltages (although under these conditions I is proportional to $V[\mathrm{kV}]^n$, with n between 5 and 10, applies). Because of its higher yield and higher deposition rate, the MS variant is by far the most widely used in the field of coatings. The MS system is applicable to both DC and RF sputtering and, with appropriate design of the generated magnetic field, is also available in more complex configurations/geometries of anode and cathode. In contrast, this variant also carries with it an obvious additional cost for the deposition apparatus, the target is consumed unevenly (annular groove), and the efficiency drops at higher pressures due to excessive ion density.

In general, it can be said that the sputtering deposition technique is characterized by:

- a radial distribution greater than that of high-energy techniques (the Comsa-David model predicts a trend proportional to $\cos^2\theta$) and a deposition area that depends almost exclusively on the size of the target;
- a good deposition rate (especially in the MS configuration);
- a good energy of the atoms ejected from the target: typically 3-5 eV, lower than that of high-energy deposition techniques such as PED (>10 eV), but still vastly higher than that of evaporated atoms (0.1-1 eV);
- a not always good preservation of target stoichiometry in compounds consisting of multiple elements and a slight variation in the concentration of ejected atomic species over time;
- the possibility of trapping impurities from the plasma working gas in the film or damaging/defecting the already grown film when high voltages are used, and very energetic particles may hit its surface.

2.3 - MetalOrganic Chemical Vapor Deposition (MOCVD)

MetalOrganic Chemical Vapor Deposition (MOCVD) is one of the multiple variants of chemical vapor deposition (CVD) technique. In MOCVD starting precursors are volatile metalorganic compounds, which are vaporized in separate chambers, where their temperature is controlled to provide a fixed saturated vapor pressure (Figure 2.8).

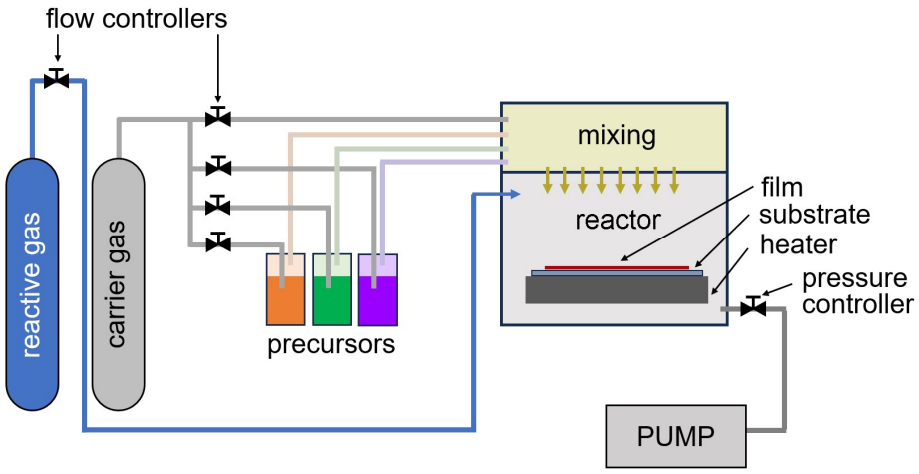

Figure 2.8 – Scheme of a possible MOCVD system configuration

These vapors are singularly combined with the proper amount of a carrier gas (in which they are stable enough) that transports them towards the reaction chamber in the desired concentrations and ratios. After their mixing and eventual further dilution with carrier gas, precursors enter the reaction chamber, where the substrate is placed at a temperature that is high enough to promote the decomposition and reaction of metalorganic reagents (Figure 2.9).

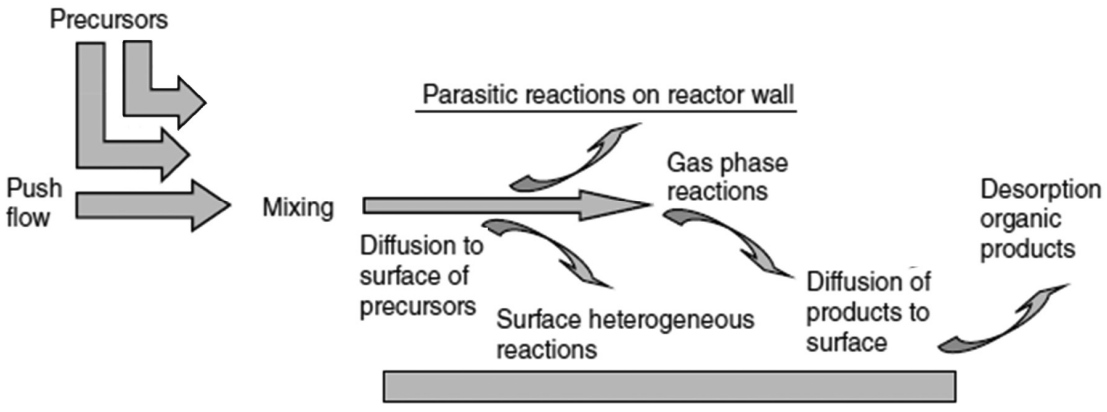

Figure 2.9 – Scheme of the deposition process steps occurring in a MOCVD reactor

Unlike the previously described techniques, in this case we have a chemical deposition instead of a physical one. With this technique it is possible to deposit polycrystalline or monocrystalline films, depending on the growth rate, the process parameters, the purity of the precursors and the match with the substrate. In the best case, indeed, it is possible to obtain an effective epitaxial growth and for this reason sometimes this technique is sometimes also called MetalOrganic Vapour-Phase Epitaxy (MOVPE) or OrganoMetallic Vapour-Phase Epitaxy (OMVPE). "MOCVD" is however a more common and all-inclusive name for this process, more clearly involving also the deposition of not-epitaxial growth of polycrystalline films.

MOCVD has been initially introduced for the deposition of semiconductors thin-films, especially III-V compounds. In that case usually alkyls were used as organometallic precursor of the Group III element and hydrides for the Group V element, in a flow of hydrogen (H_2) as carrier gas. As an example, in Figure 2.10a it is possible to see the scheme of the reactions occurring for trimethylgallium ($Ga(CH_3)_2$) and arsine (AsH_3) to deposit GaAs.

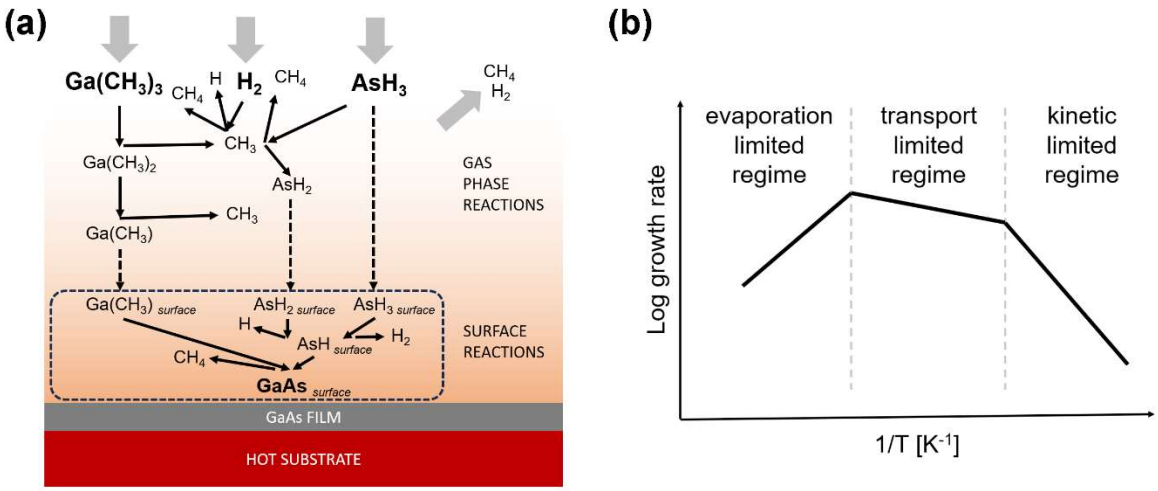

Figure 2.10 – (a) detail of the multiple reactions taking place in a MOCVD deposition of GaAs thin-films starting from $Ga(CH_3)_2$ and AsH_3 precursors, in a flow of H_2 as carrier gas; (b) schematic plot of the growth rate regimes vs. temperature for a MOCVD process.

However, MOCVD is a versatile process that can be used to grow a wide variety of materials, including semiconductors, insulators, and metals. The choice of precursors is not limited to simple alkyls and hydrides but can be extended to almost any volatile organometallic and/or gas, as carriers for the elemental components of a film. Most of the time organometallic precursors are in liquid form. The important properties of liquid precursors, and their selection, are:

- their saturated vapor pressure should ideally be in the range of 1–10 mbar in the temperature range of 0–20 °C; outside of this range precautions have to be taken into account, like hot bubblers or heated lines;
- they should be stable for long periods at room temperature;
- they have to react efficiently at the desired growth temperature (the combination of precursors may need to be considered here);
- their reaction must produce stable leaving groups and low carbon incorporation;
- they should not be subject to unwanted side reactions (*e.g.* polymerization).

The reaction kinetics change with substrate temperature (Figure 2.10b) but, in general, the increase of substrate temperature can reach a regime in which the deposition rate is no longer determined by the overall reaction rate, but it is rather determined by the supply rate of precursors. This effect produces a depletion of the precursor concentration in the region immediately above the surface and a gradient in precursor concentration toward the incoming stream. In this case the rate of diffusion through the depleted boundary layer determines the rate at which the film grows. This is called "transport-limited growth" regime and it is characterized by high growth rates and only a weak dependence of growth rate on substrate temperature. On the contrary, in a higher temperature regime, the growth rate decreases again because the equilibrium vapor pressure of the elements in the film increases so much that desorption rates become comparable with the deposition rate. In this regime also other mechanisms can induce a decrease in growth rate, such as free radical etching or undesired precursor desorption before the final reaction occurs.

Inhomogeneities in the film growth may arise in simple horizontal reactors, which usually are used only for small substrates or research purposes. In this linear system assemblies, the precursors concentrations may decrease, indeed, along the furnace (and flow) axis, as more and more of these compounds react and is deposited in form of film on the substrate. Hence, thickness and/or compositional gradient may be found in the deposited thin film. To overcome this problem several approaches have been studied. Some of the most effective are vertical assemblies with "showers" that distribute the vapors and gases homogeneously on a wide surface (like in the scheme in Figure 2.8) and rotating substrates.

MOCVD is particularly used in the industry of semiconductors for optoelectronic devices, such as lasers and LEDs. This technique has some undeniable advantages such as the high quality and good uniformity of the deposited films, it is a relatively low-cost technique, and it works quite well with a wide range of materials. Although it is indeed a complex process, unfortunately many times there is the need of toxic chemicals and some of the equipment can be expensive.

Chapter 3
Characterization techniques

In this chapter the main characterization techniques, used to study the different thin-films properties, are briefly described. As for the previous chapter, its purpose is only to provide a quick reference for the main concepts, parameters and technical terms, that are used to describe and discuss the experimental results in the following chapters.
The technique here described are:

3.1 Raman Spectroscopy

3.2 X-Ray Diffraction (XRD)

3.3 Scanning Electron Microscopy (SEM) and Energy Dispersive X-ray Spectroscopy (EDS)

3.4 Electrical Characterizations

I personally dealt with the measurements and the data analysis related to Raman spectroscopy; I made only a part of the XRD measurements, but I personally analyzed most of the XRD data presented in this thesis; I was assisted by colleagues for SEM and EDS characterization and electrical characterization, but I personally elaborated most of the presented data.

3.1 - Raman Spectroscopy

Raman spectroscopy is a chemical-structural characterization technique that relies on the phenomenon of **inelastic scattering** of photons from a monochromatic light source when they interact with a material. The technique derives its name from the Indian physicist Sir Chandrasekhara Venkata Raman, who in 1928 first observed the phenomenon: light scattered by some substances illuminated with monochromatic light carried a weak electromagnetic radiation of frequency ν', different from the incident ν by an amount $\pm\Delta\nu$. The changes in frequency $\Delta\nu$ generally do not depend on the frequency of excitation, but instead are characteristic material studied. The study of the spectrum emitted under these conditions therefore becomes a powerful analytical tool.

Inelastic scattering of near-visible light, from near-infrared to near-ultraviolet, is in fact related to interaction with the vibrational modes of atoms and molecules in the material. More precisely, Raman scattering is related to the "switching on" or "switching off" of **phonons**. In the former case we speak of "**Stokes**-type" Raman scattering, in the latter of "**anti-Stokes**-type" Raman scattering (Figure 3.1). However, the intensity of these Raman peaks in the collected spectrum is much lower (3 to 10 orders of magnitude) than that of elastic scattering (Rayleigh) at the same frequency as incident radiation. For this very reason, the study of what is now called the "Raman effect" really developed only after the advent of lasers, which made available very intense monochromatic light sources.

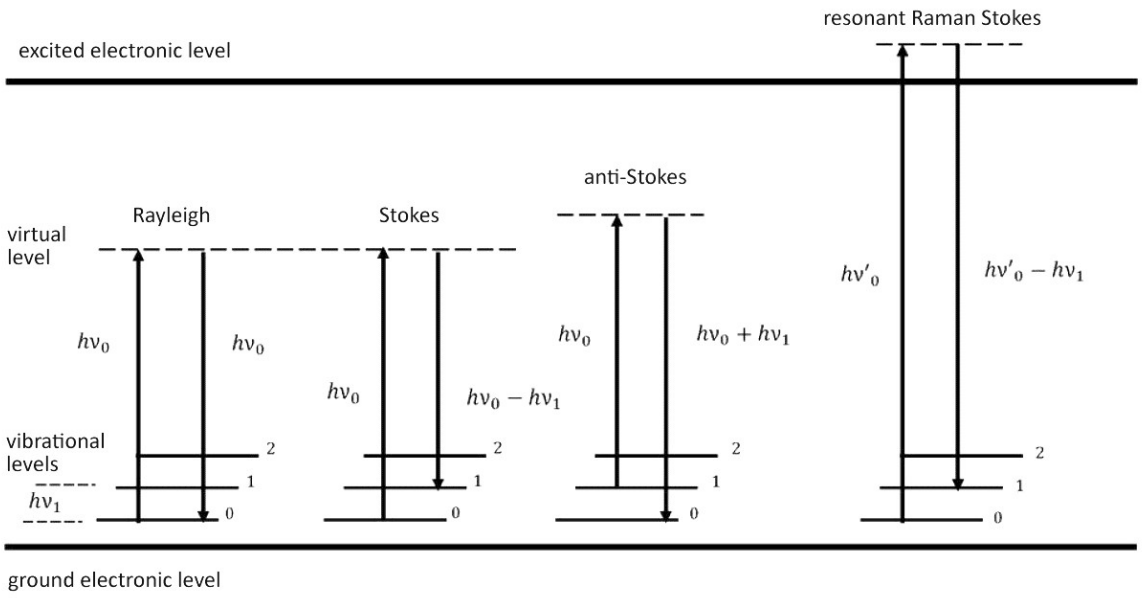

Figure 3.1 - Diagram of transitions between different energy levels involved in Raman scattering processes

A Raman spectrum is represented as a function of the "**shift**" with respect to Rayleigh scattering, which represents zero on the x-axis. The part of the spectrum closest to zero, which is dominated by Rayleigh scattering, is often not taken into account. Stokes lines are in the positive part of the axis and anti-Stokes lines are in the negative part. The row patterns are the same in both cases. The intensity of the Stokes lines, however, is greater than that of the anti-Stokes lines. This is because of the different vibrational levels' population (anti-Stokes transitions must necessarily start at a higher energy level), which follows the Boltzmann statistic and therefore also depends on temperature. For all these reasons, generally only Stokes lines are reported by convention in a Raman spectrum.

Anti-Stokes lines do have, however, a big role in Raman Spectroscopy, because the temperature of a material can be ascertained by evaluating the intensity ratio between Stokes and anti-Stokes Raman bands signals. If the signal intensities of a specific Raman band are measured at both Stokes and anti-Stokes positions, the temperature can be calculated by considering the Boltzmann distribution of the populations in the ground and first excited states. The relationship often used to describe this phenomenon is:

$$\frac{I_{AS}}{I_S} = \frac{(\nu_l + \nu_v)^4}{(\nu_l - \nu_v)^4} e^{\left(\frac{-h\,\nu_v}{kT}\right)} \qquad (3.1)$$

where T is the temperature, k is Boltzmann's constant, h is Planck's constant, ν_l is the incident laser frequency, ν_v is the frequency of the vibrational mode (position of the Raman band), while I_{AS} and I_S respectively denote anti-Stokes and Stokes Raman scattering intensities, respectively, which are determined experimentally.

Raman shift is reported in spectra as a function of **wavenumber**, which is the inverse of wavelength ($1/\lambda$), in units of cm^{-1}. To convert the spectral wavelength and Raman shift wavenumbers, the following relationship exists:

$$\Delta\omega\ [\mathrm{cm}^{-1}] = \left(\frac{1}{\lambda_0[\mathrm{nm}]} - \frac{1}{\lambda_1[\mathrm{nm}]}\right) \cdot \frac{10^7[\mathrm{nm}]}{[\mathrm{cm}]} \qquad (3.2)$$

where $\Delta\omega$ is the Raman shift, λ_0 is the excitation wavelength and λ_1 is the wavelength in the Raman spectrum.

When the incident energy is sufficient to reach a real excited electronic state (instead of a virtual state), this is referred to as "resonant" Raman (Figure 3.1), and the phenomenon is associated with an increase in intensities of even several orders of magnitude. On the other hand, if the system reaches a real excited electronic state, this can also dissipate some of the energy through non-radiative transitions between vibrational levels, prior to the re-emission of a photon. This phenomenon, known as fluorescence, can mask the Raman spectrum under some circumstances and pose a significant problem.

Incident radiation excitation can involve electronic states, vibrational states and rotational states. However, the levels associated with these different types of excitations involve very different energies:

- transitions between **rotational levels** alone give rise to spectra in the far-infrared or microwave;
- transitions that also involve changes in **vibrational levels**, on the other hand, give rise to spectra in the infrared (IR);
- spectra that also involve changes in **electronic energy levels** may instead reach the visible or ultraviolet.

Raman spectra essentially reveal transitions between vibrational states. However, there is a **selection rule**: *only transitions between states involving a change in electrical polarizability are active in Raman spectroscopy*. In fact, the electric field E of the incident wave induces a dipole moment in the molecule/solid equal to:

$$\mu_{\text{ind}} = \alpha E = \alpha E_0 \cos(2\pi \nu_{exc} t) \qquad (3.3)$$

where α is the polarizability and ν_{exc} is the frequency of the incident wave. If α is constant, the dipole will oscillate at the same frequency as the incident wave and thus only Rayleigh scattering will occur. If, on the other hand, α changes as a function of the distance between the nuclei, the transition is Raman active. In fact, in the simplest case it can be written that:

$$\alpha = \alpha_0 + (r - r_{eq})\left(\frac{\partial \alpha}{\partial r}\right) = \alpha_0 + r_m \cos(2\pi \nu_{\text{v}} t)\left(\frac{\partial \alpha}{\partial r}\right) \qquad (3.4)$$

where r is the internuclear distance, r_{eq} the equilibrium internuclear distance, r_m the maximum internuclear distance with respect to the equilibrium distance, and ν_v the vibration frequency. Therefore, it is possible to rewrite:

$$\mu_{\text{ind}} = \alpha_0 E_0 \cos(2\pi \nu_{exc} t) + E_0 \left(\frac{\partial \alpha}{\partial r}\right) \cos(2\pi \nu_{\text{v}} t) \cos(2\pi \nu_{\text{exc}} t) \qquad (3.5)$$

which, by trigonometric property, becomes:

$$\mu_{\text{ind}} = \alpha_0 E_0 \cos(2\pi \nu_{exc} t) + \frac{E_0}{2}\left(\frac{\partial \alpha}{\partial r}\right) \cos[2\pi (\nu_{\text{exc}} - \nu_{\text{v}})t] +$$

$$+ \frac{E_0}{2}\left(\frac{\partial \alpha}{\partial r}\right) \cos[2\pi (\nu_{\text{exc}} + \nu_{\text{v}})t] \qquad (3.6)$$

The first term in this equation is the Rayleigh scattering term, the second the Raman Stokes term, and the third the Raman anti-Stokes term. The last two terms, namely the Raman terms, exist only if the derivative of polarizability is nonzero.

In the three-dimensional case, however, having three components for both the incident electric field and the dipole moment, the polarizability will be a tensor. Each vibration will then be associated with a "Raman tensor", equal to the derivative of the polarizability tensor with respect to the vibration coordinates. This means that the intensity of Raman peaks also depends on the relative orientation of the molecule or solid with respect to the polarization of the incident radiation (laser). Since Raman modes that are totally symmetric are characterized only by diagonal elements, they keep polarization of incident light unaltered, while all the modes of phonons with out-of-diagonal elements induce polarization changes.

In material sciences, the possibility of measuring in different polarizations configurations it's an important additional tool. Polarized light, restricted to a specific direction, provides entry only to certain Raman-active modes. However, by altering the polarization orientation, different modes become accessible (Figure 3.2).

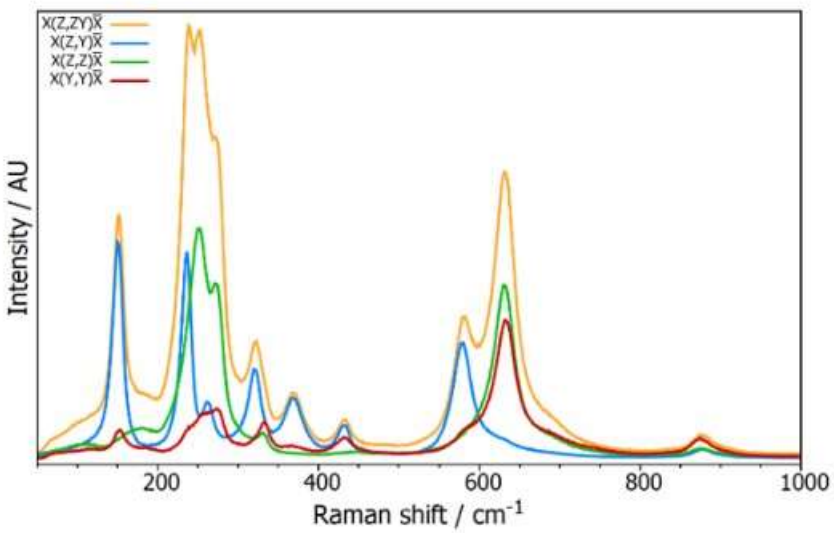

Figure 3.2 – Example of polarization dependent Raman measurement: Lithium niobate polarised Raman spectra (532 nm, 1800 gr/mm) [Source: Edimburgh Instrument - www.edinst.com]

Raman technique thus provides partial information with respect to all possible variations in vibrational states. For this reason, it is often considered complementary to **infrared (IR) spectroscopy**. The latter is a technique that is based on the absorption of infrared photons by molecules and solids. This absorption is associated with a direct transition to an excited vibrational state. IR spectra report the transmittance T as a function of the incident radiation wave number.

In IR spectroscopy, there is a different selection rule: an infrared radiation gives rise to a transition between vibrational levels only if it causes a change in the molecular/crystalline

electric dipole as a result of the change in atoms positions. Thus, for example, all molecules composed of equal atoms, such as O_2 or N_2 are not active in the IR, while molecules such as H_2O or CO_2 can resonate with incident radiation when asymmetric vibrations (producing an instantaneous dipole) occur.

Figure 3.3 shows, just for example purpose, the Raman spectrum and the IR spectrum of the same molecule (benzene), which is active, for different transitions, in both spectroscopic techniques. As for any centrosymmetric molecule or crystalline lattice, the mutual exclusion principle states that even-modes are only Raman-active, while odd-modes are only IR-active.

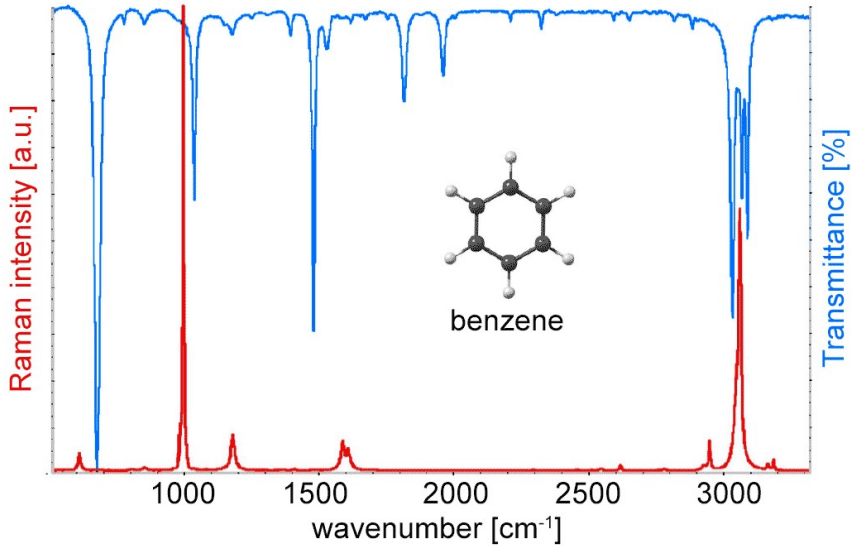

Figure 3.3 - Raman spectrum (red) and IR spectrum (blue) for the benzene molecule

The set of all spectral lines of detectable intensity constitute a kind of **fingerprint** for many molecules and some solids. Libraries of Raman peaks exist for the most common substances or for specific areas of materials of application interest, such as minerals or pigments.

Although a modern Raman acquisition system can also be quite complex, a simple diagram of the basic components, more or less common to all systems, is shown in Figure 3.4.

The light radiation source is generally a **laser**, which best meets the required conditions of monochromaticity, high intensity, and polarization. **Scattered light** is then filtered by a **filter** whose task is to eliminate most of the radiation with the same frequency as the incident laser (*i.e.* the Rayleigh component). The radiation passing the filter is finally collected by a lens system and analyzed through a **spectrometer**, where the radiation is

first scattered by a **grating** that spreads the different wavelengths and then measured quantitatively as a function of energy, usually by means of a **CCD**-type sensor array.

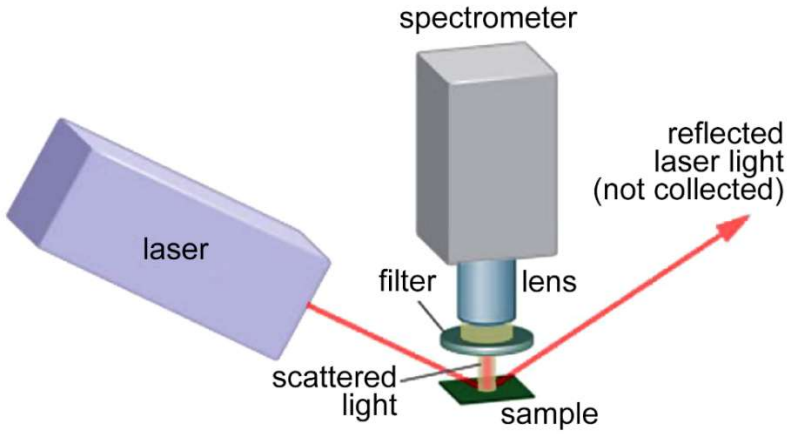

Figure 3.4 - Schematic diagram of a Raman measurement system basic components

3.1.1 - Micro Raman Spectroscopy

The coupling of an **optical microscope** with a Raman spectrometer gives rise to the so-called **micro-Raman technique**, which extends the potential of the traditional technique by allowing areas as small as a few μm^2 to be illuminated and thus analyzed. Spectral analysis in this case can be focused on local areas on the sample surface at the micrometer scale. When this analysis is accompanied by scanning systems, high-resolution analytical Raman mappings can be obtained.

Two different instruments were used for the results reported in this thesis work.

The first one is a LABRAM Horiba Jobin-Yvon micro-Raman spectrometer, equipped with an Olympus BH-4 confocal microscope. The microscope used has x4, x10, x50, x100 objectives. A scheme of the system is shown in Figure 3.5.

The second and most used one is a Horiba LabRam HR Evolution micro-Raman spectrometer, equipped with a confocal Olympus microscope and 10x, 50x, ULWD50x, 100x objectives (spatial resolutions of approximately 1 μm). The Micro-Raman apparatus is completed by a He-Ne laser emitting at 632.8 nm, a Nd:YAG laser at 532 nm, a laser diode at 785 nm and a Nd:YAG laser at 1064 nm. The system is also equipped with BraggRate Notch Filters (low cut-off <10 cm^{-1}), Silicon CCD + InGaAs Diode Array detectors, gratings 300-600-1800 lines/mm, and density filters.

The "stage" (support) is motorized along the planar *x* and *y* axes with sub-micron pitch. The movement of the support along the *z* focal axis, on the other hand, is manual in the case

of LABRAM Horiba Jobin-Yvon, adjustable by means of graduated knobs while is fully automatized in the case of the Horiba LabRam HR Evolution.

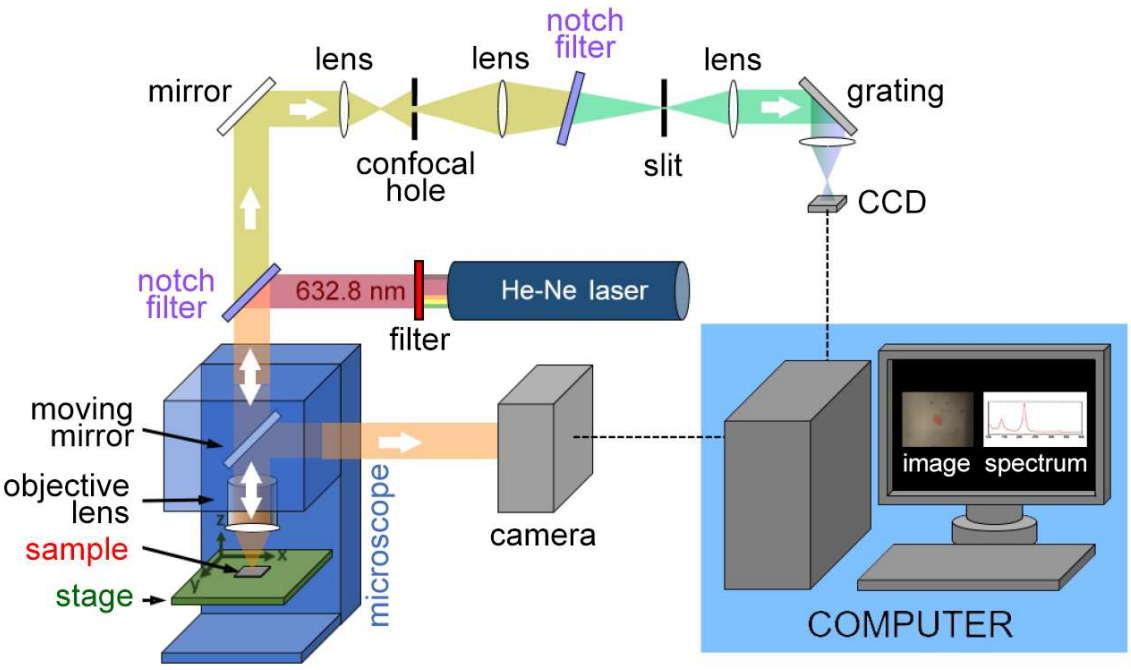

Figure 3.5 - Schematic diagram of the micro-Raman experimental apparatus

The image collected by the objective, along with scattered radiation from the sample, returns into the microscope where, depending on the position of a moving mirror, it is transmitted either to a color camera, to get a traditional optical image of the sample, or to the spectrometer components. For convenience, while viewing the sample optical image, the stage can also be illuminated with white light, both from top and/or bottom.

In order for only the scattered radiation to be transmitted from the point where the excitation beam is in focus, the collected radiation passes through a spatial filter, *i.e.* a confocality aperture (Figure 3.6). The use of a **confocal microscope configuration** offers numerous benefits both for optical and Raman microscopy. This design enables a precise management of the depth-of-field, facilitating optimal axial and lateral spatial resolution. Moreover, confocal microscopes aid in the reduction of background noise and undesired signal. It hence proves valuable for quantifying Raman signals across coverslips or transparent media, minimizing interference from these substances. In confocal configuration the optimal condition is obtained when the aperture size of the diaphragm is equivalent to the image size of the excited zone: the smaller the aperture size, the better the spatial and spectral resolution, but at the expense of brightness.

A second notch filter and a suitable slit allow even more selective exclusion of the part of the radiation close to the laser wavelength (Rayleigh-type elastic component). The radiation passing through the filter is then spatially scattered as a function of wavenumber by an appropriate grating (different for different laser lines) and focused on the detectors. The signal collected by the CCD or the InGaN Diode Array is then processed by computer for spectrum recording and analysis. System control and data collection is performed via computer using **LabSpec** software in both cases.

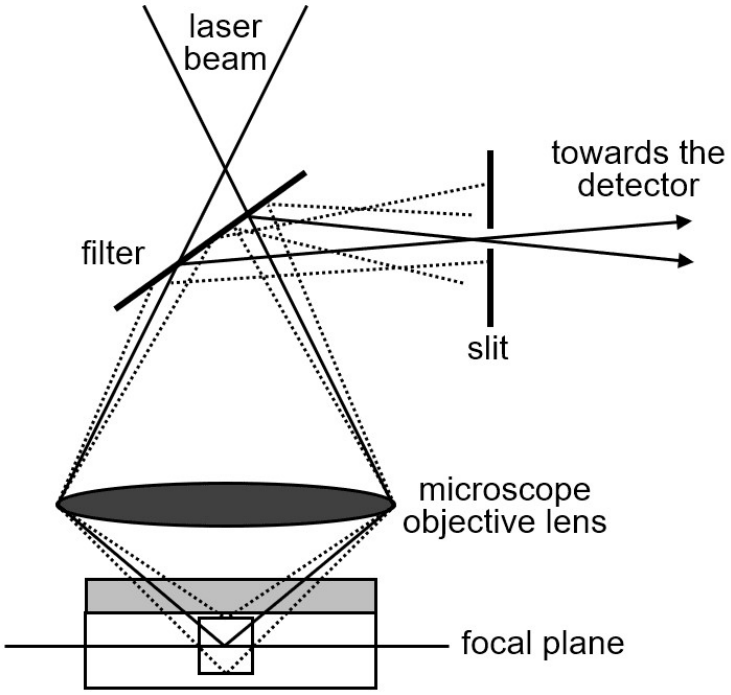

Figure 3.6 - Confocality principle: signals from out-of-focus areas cannot reach the detector bhind the slit.

3.1.2 - Tip-Enhanced Raman Spectroscopy (TERS)

Tip Enhanced Raman Spectroscopy (**TERS**) upsets intrinsic limits of Raman spectroscopy by enabling **nanoscale resolution measurements**. Functioning as a super-resolution chemical technique with scanning capability, TERS offers the unique advantage of label-free imaging at the nanoscale.

The TERS imaging process takes place within system that couples Scanning Probe Microscopy (SPM, operational in atomic force, scanning tunneling, or normal/shear force modes) and a confocal Raman spectrometer via an opto-mechanical link (Figure 3.7a).

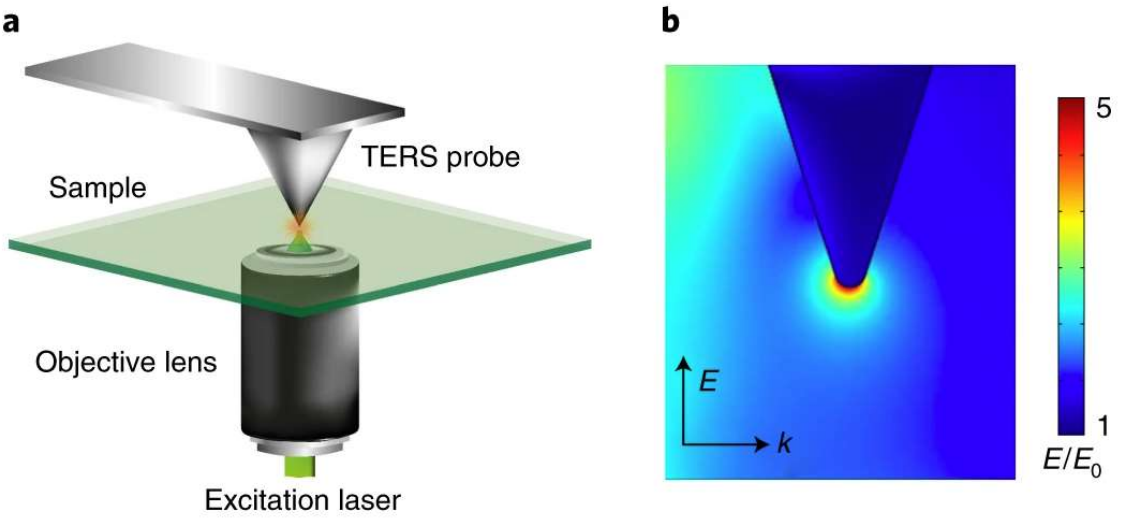

Figure 3.7 - (a) schematic diagram illustrating the principle of TERS; (b) simulated electric field amplitude map of an Ag TERS probe apex irradiated with a 532-nm laser with an electric field parallel to the probe axis. [reproduced from "Nanoscale chemical imaging using tip-enhanced Raman spectroscopy" by N. Kumar et al., *Nature Protocols* volume 14, pages 1169–1193 (2019), licence number 5618260317696]

The scanning probe microscope facilitates nanoscale imaging, the optical coupling directs the excitation laser to the functionalized "**tip**" (or **probe**), and the spectrometer analyzes the resulting Raman (or other scattered) light. This analysis yields a hyperspectral image featuring chemical contrast at the nanometer scale.

The foundation of a TERS system relies on a metallic tip, typically composed of gold or silver, which serves the purpose of concentrating the incident light field at its apex. Functioning as both a nano-source of light and a local field enhancer, this tip significantly amplifies Raman sensitivity (by factors ranging from 10^3 to 10^7) while minimizing the probed volume to the nanoscale region located directly beneath the tip.

The electromagnetic enhancement at the tip apex, is a consequence of the interaction of localized surface plasmon (LSP) resonance and the antenna effect. These factors collectively generate a concentrated and intensified electric field within the immediate vicinity (Figure 3.7b). A further enhancement of localized electric field occurs at the tip apex when the LSP resonance wavelength of the tip corresponds with the excitation laser's wavelength.

LSP wavelength of the TERS can be modified by changing the material, radius, or roughness of the tip apex. This adjustment enables better alignment with the wavelength of the excitation laser.

The optical arrangements of a TERS setup can be categorized into three main types: bottom (transmission mode), side, and top illumination (Figure 3.8).

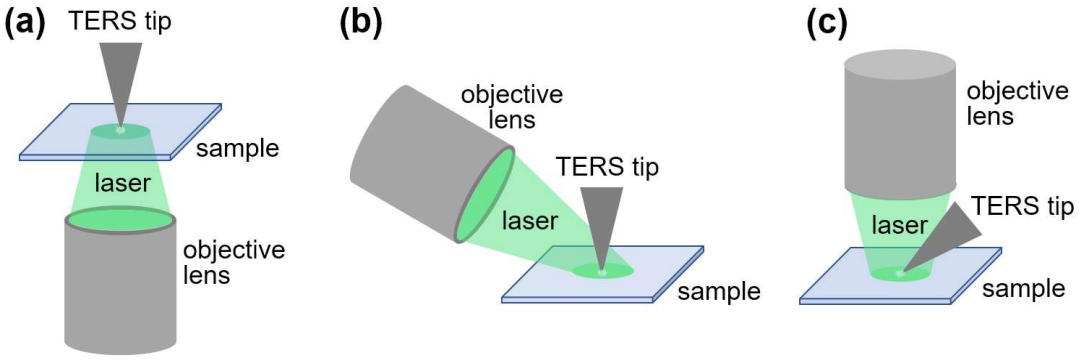

Figure 3.8 - schematic diagrams of the most frequently employed TERS configurations: (a) bottom illumination set-up, (b) side illumination set-up, (c) top illumination set-up

In the case of the **transmission illumination setup** (Figure 3.8a), a laser beam is focused onto the sample through a transparent substrate using a high numerical aperture (NA) objective lens. Unfortunately this configuration is constrained by the fundamental requirement of employing a transparent substrate.

In the **side illumination setup** (Figure 3.8b), a linearly polarized beam is directed onto the tip apex from the lateral side of the tip, through a long working distance objective lens. Due to the alignment of polarization with the tip direction, substantial electromagnetic enhancement can be achieved at the tip apex, even when using a low NA objective lens. This arrangement proves particularly advantageous for TERS characterization of nanoelectronic devices, where the substrates are generally non-transparent.

In the **top illumination setup** (Figure 3.8c), the laser is focused from the top onto either the end of a tilted STM tip or a nose-type AFM tip. This geometry offers the benefit of being immune to chromatic aberration, boasting a high NA (approximately 1), and achieving a tightly focused laser beam.

The side and top illumination setups are also commonly referred to as "**reflection modes**".

3.2 - X-Ray Diffraction (XRD)

The **X-ray diffraction** (**XRD**) technique is fundamental for the characterization of **crystalline materials**. It is based on coherent elastic scattering (Thompson) of incident radiation that gives rise to interference phenomena when a lattice of diffusing centers is hit. Since radiation wavelength must be close to the value of lattice spacing, for a periodic crystalline structure with spacing generally below 1μm, a X-ray source of few keV is needed.

The diffraction condition, described qualitatively by Bragg, rests on a simple formula that considers diffraction as reflection of the incident ray by a family of lattice planes, spaced by a distance d. For constructive interference, the formula is as follows:

$$n\lambda = 2d \sin\theta \qquad (3.7)$$

where n is an integer and is called “diffraction order”, λ is the radiation wavelength, d is the “grating constant”, while θ is the angle for which the condition is verified and, for this reason, it is called the "**Bragg angle**" (Figure 3.9).

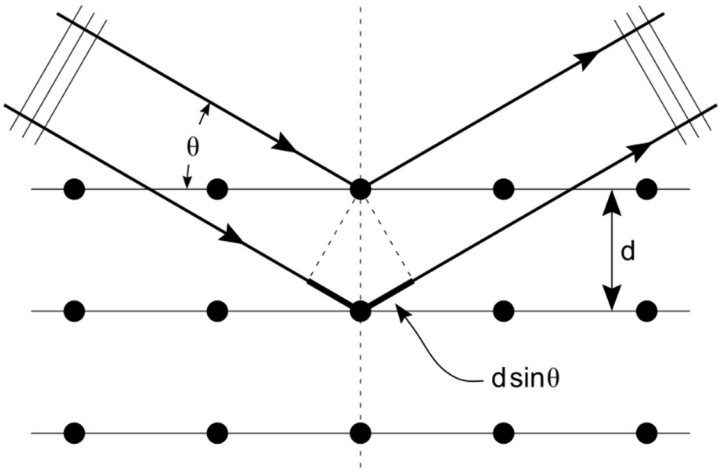

Figure 3.9 – Scheme of Bragg diffraction principle: two beams with the same wavelength and phase reach a lattice and are scattered off two different atoms of the periodic lattice; the lower beam runs through an extra $2d\sin\theta$ length so constructive interference occurs only when this quantity is equal to an integer multiple of the radiation wavelength.

XRD analysis can be made both on single crystals or on powder/thin-film samples. The most common experimental set-up for powders/thin-films XRD measurements is the Bragg-Brentano **theta-theta** configuration (Figure 3.10): in this geometry, the angle formed between source and sample and the angle between sample and detector are kept the same. For this to happen, the three elements must always lie on what is called a "focusing circle", while source and detector move synchronously along a second, variable circle

("diffractometer circle" or "goniometer circle") at the center of which the sample is placed. X-rays from the source impinge on the sample and are subsequently refocused on the detector.

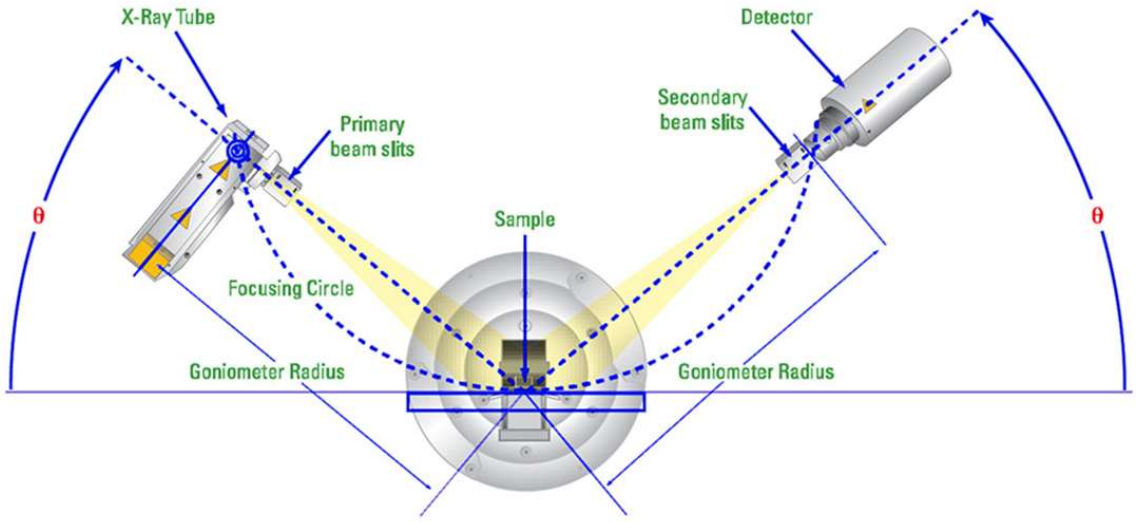

Figure 3.10 - Diffractometer in Bragg-Brentano theta-theta configuration

The main advantage of theta-theta configuration over the theta-2theta configuration, where the x-ray tube is kept steady, the sample is tilted of a θ angle and the detector 2θ to obtain the same relative condition, is that in the first one the sample, which may be also made of powders, is never titled. Theta-theta configuration has become more and more common as X-ray tubes became lighter and more compact over the years.

A powder XRD measurement results in a **pattern**, given by the plot of detected intensities of diffracted X-rays as a function of 2θ angle (Figure 3.11). The position of peaks in the pattern is clearly typical of each crystalline material/compound, depending mainly on the crystallographic cell size and geometry. Each peak corresponds to a specific *h*, *k*, and *l* set of values, that form the so called "**Miller index**". Each *hkl* index identifies a family of (parallel) lattice planes of a given **Bravais lattice** (like the one of the studied crystalline structures) and, by definition, these planes are orthogonal to the vector:

$$\boldsymbol{g}_{hkl} = h\boldsymbol{b}_1 + k\boldsymbol{b}_2 + l\boldsymbol{b}_3 \qquad (3.8)$$

where $\boldsymbol{b}_i$ are the basis vectors of the **reciprocal lattice** for the given Bravais lattice. So, in short, each peak in the pattern correspond to the *hkl* families of planes in the crystalline material that generated it (Figure 3.11b) and this pattern, as in the case of Raman spectra, can be considered like a fingerprint for the recognition of crystalline materials.

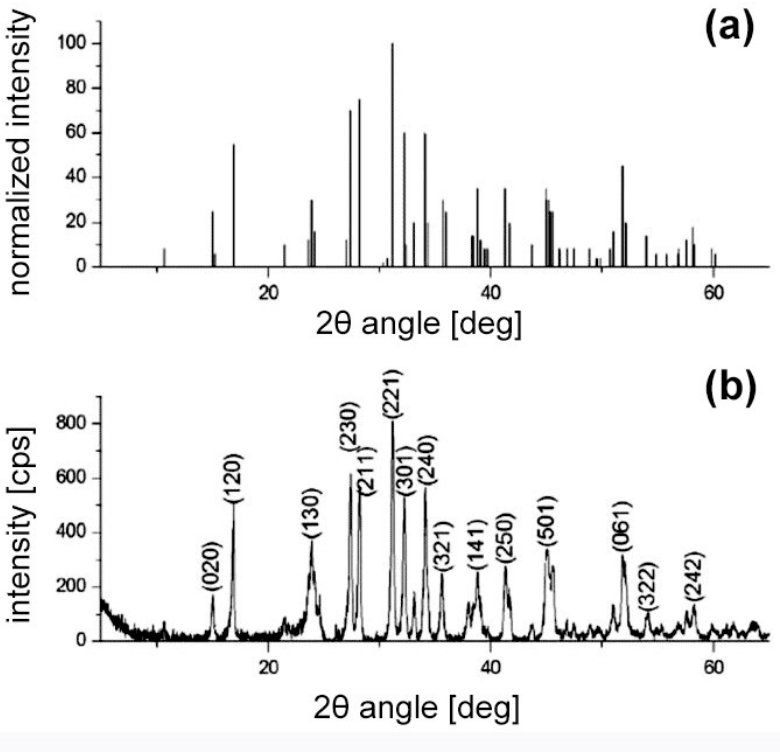

Figure 3.11 – Examples of XRD patterns for Sb_2Se_3: (a) theoretically calculated pattern; (b) experimentally measured pattern, where main peaks have been addressed to the corresponding *hkl* Miller indexes.

The peak intensity, on the other hand, is mainly affected by the positions of atoms inside the cell (Figure 3.11a). But, at the same time, it can be also strongly influenced by the presence of preferential orientations. Indeed, while in a polycrystalline sample of completely random oriented grains each Bragg condition is satisfied by a conical distribution of directions, a preferential orientation can enhance the diffraction probability in some directions and decrease (or even suppress) the probability in other directions. So, an intensities distribution that is different from the expected one is generally a symptom of the presence of grain with preferential growth directions on the substrate or powders with a crystalline habit (like needle- or platelet-shaped crystals) that naturally arrange themselves in preferential ways on the holder.

Finally, the peak with is inversely proportional to crystallite size, accordingly with the Scherrer equation:

$$\tau = \frac{K\lambda}{\beta \cos\theta} \qquad (3.9)$$

where τ is the mean size of the ordered (crystalline) domains, K is a dimensionless shape factor (with a value close to unity), λ is the radiation wavelength, θ is Bragg angle and β is the peak broadening at half the maximum intensity (FWHM). This broadening is usually

evident at the nanoscale, while above 100 nm this law is generally not applied since for these sizes the width peak is essentially determined only by the instrumental broadening/resolution.

Another important diffractometer configuration for the characterization of thin-films is **Grazing Incidence X-Ray Diffraction** (**GIXRD**). In this method, a steady parallel X-ray beam is directed towards the sample with a very low angle of incidence (almost parallel to the sample surface), while only the detector is tilted along the goniometer circle. X-rays penetrate several microns in the sample during a standard XRD measurement, so on a thin-film most of the signal generally comes from the substrate. In GIXRD, on the contrary, the radiation beam crosses the film along a much longer path, almost parallel to the film plane. Hence, this grazing angle setup allows for enhanced sensitivity in the near-surface region of thin-films and helps minimize the contribution of substrate scattering. GIXRD is commonly employed in materials science, surface science, and the study of thin-film devices. It provides more detailed insights into thin film growth mechanisms, crystal orientation, and phase transitions that can be crucial for optimizing the performance of electronic, photonic, and optoelectronic devices.

The last XRD-based tool, used in the characterization of the deposited thin-films, were the so called "**Pole Figures**". Pole figures in X-ray diffraction (XRD) are graphical representations that provide valuable information about the possible presence of preferential crystallographic orientations (texture) within a polycrystalline material. These "figures" are used to visualize the distribution of several XRD data collected from different crystallographic planes and orientations, by transforming them into graphical representations, where each point on the figure corresponds to a specific crystallographic plane orientation (Figure 3.12). The density of points in different regions of the figure indicates the abundance of specific crystallographic orientations.

Conventional pole figure assessments involve registering the intensity of a specific Bragg reflection while altering the sample's orientation through rotation and tilting. In the case of an in-plane pole figure, adjustments are made to the incident beam, sample rotation, and detector angle, obviating the need to tilt the sample. Moreover, the in-plane pole figure facilitates the capture of a broader spectrum of texture variations since it encompasses the texture present within the plane of the sample's surface.

By analyzing pole figures, researchers can gain insights into the preferential orientation of grains, crystal symmetry, and the underlying microstructural characteristics of a material.

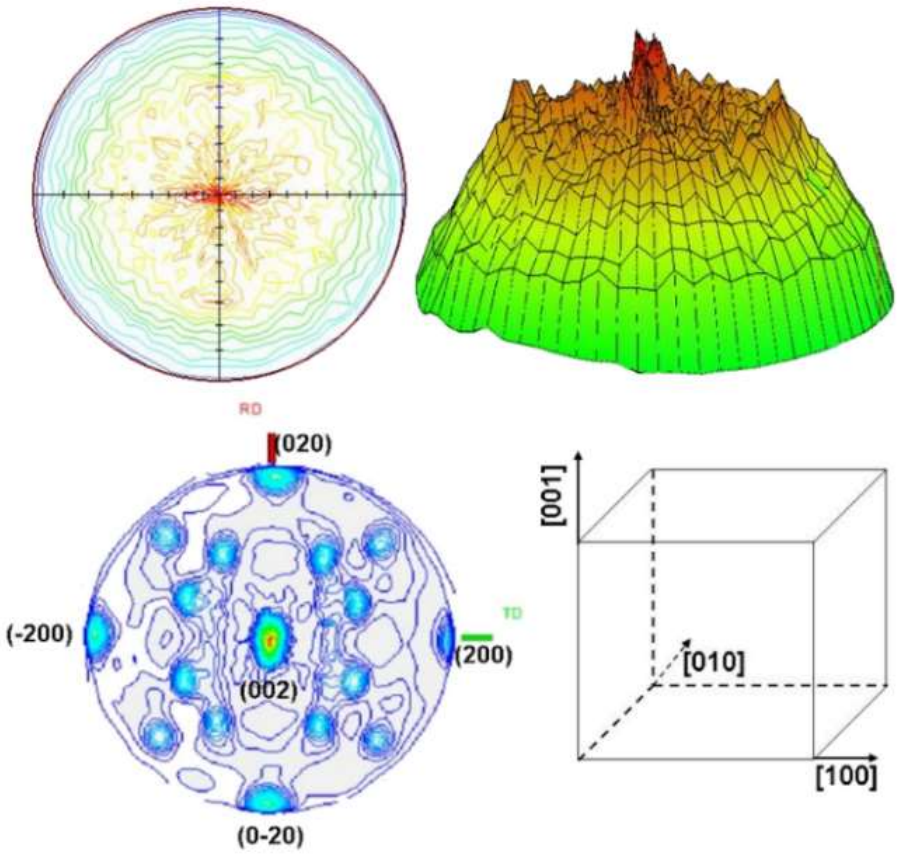

Figure 3.12 – Example of in-plane pole figure of the reflection for a rolled steel sheet sample [source: Rigaku Corporation - www.rigaku.com]

The XRD instruments that was used for this thesis work are a Siemens D500 system with a Cu K_α X-ray source, in Bragg–Brentano geometry, and a a Rigaku Smartlab XE diffractometer, also configured in Bragg-Brentano geometry and making use of Cu K_α wavelength (λ=1.5406 Å), with a Ni filter to suppress the K_β contribution. The latter was also used for pole figures, thanks to an Euler cradle, making use of Cu K_α radiation parallelized by a parabolic mirror mounted on the Cross Beam Optics unit. The incident beam was shaped through the use of incident slits and length limiting slits to 1 × 1 mm^2, well above the area of the sample. In addition, Schultz slit was employed in order to further limit the defocusing effects at high χ. Pole figures were collected by 360° ϕ scans (5° step) at fixed χ values, ranging from 0° to the experimental limit of 75°. For each measurement, the background signal was measured and subtracted. Data plotting and analysis were carried out by using proper homemade Matlab code.

3.3 - Scanning Electron Microscopy (SEM) and Energy Dispersive X-ray Spectroscopy (EDS)

The **Scanning Electron Microscope** (generally referred to by the acronym **SEM**) is an advanced microscopy instrument that, through the interaction between highly accelerated electrons and matter, can provide various information about the sample being analyzed.

A SEM does not exploit light as a radiation source, but uses a beam of (primary) electrons generated by an electron source (filament or field emission). The electrons emitted from the source are accelerated, focused by a series of electromagnetic lenses, and finally deflected by an objective lens onto the surface of the sample to scan a specific area. (Figure 3.13).

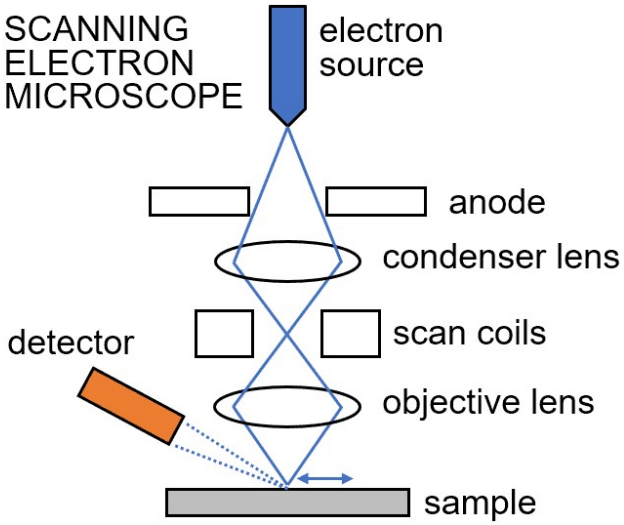

Figure 3.13 – Scanning Electron Microscope scheme

Electrons and photons that re-emerge from the surface after interaction with the sample are captured by detectors and transformed into a corresponding electrical signal (Figure 3.14).

When the beam is made to **scan** over a given region of the sample, amplifying, modulating, and recording the collected signal makes it possible to obtain a corresponding **monochromatic image** (each pixel is associated with a point on the sample) with brightness directly proportional to the signal intensity.

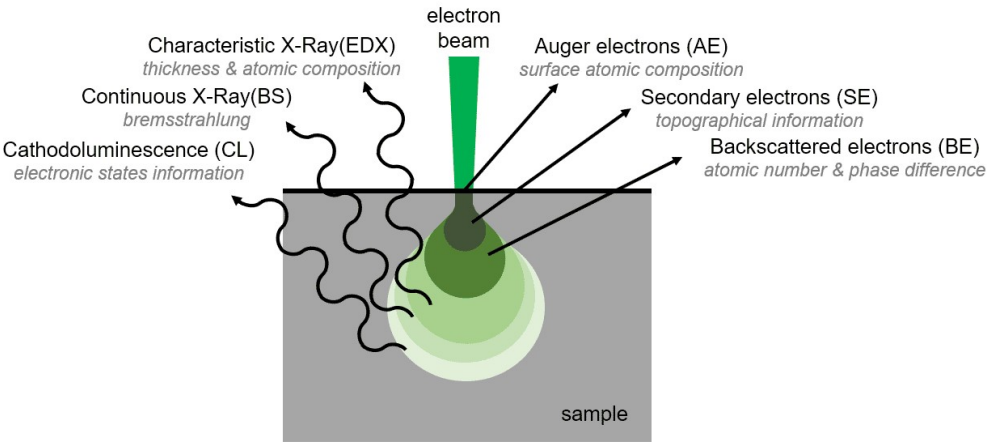

Figure 3.14 – Scheme of the different kind of signals (electrons or photons) that can be collected after the interaction between highly accelerated electrons and the sample to get different type of information

The most frequently used signal generally comes from low-energy "**secondary electrons**" (SE). The image obtained with the secondary electron detector (SED) signal succeeds in providing, primarily, information about the morphology of the scanned area. The ratio of image size to scanned sample portion size provides the magnification. The resulting image is in grey-scale (the only quantity represented is the signal intensity), but it generally possesses a good depth of field even at high magnifications. Moreover, electrons allow SEM resolution to go beyond the limits of visible light, reaching generally up to 1 nm value for SE morphological imaging.

More energetic electrons (called "**backscattered**") carry, instead, compositional information. The image obtained with the backscattered electron detector (BED or BSD) signal is characterized by a contrast related to the differences in sample composition. In fact, the signal is related to the backscattering probability, which is, in turn, proportional to the atomic number Z of the atom hit by the electron. Hence, in BSD imaging, the light areas are related to compositions with higher average Z, while the dark areas to lower average Z. The interaction generating occurs within a certain volume below the surface (not just on the sample surface) because electron size is significantly smaller than that of atoms in the sample. The geometry and size of the interaction volume will therefore depend on the atomic species involved and especially on their atomic number Z.

The two main limitations for the analysis of a sample by SEM are:

- it must **withstand vacuum**, since the electronic beam can be generated and controlled without any spark discharge only in this condition;
- it should be rather **electrically conductive**, in order to avoid that electrons from the beam accumulate on the material, shielding more and more the incoming beam;

if not, it must be coated with a very thin conductive layer (typically Au, graphite, Ag, …).

Only specially designed SEM, called “environmental” or “low-vacuum”, can work with insulating samples by exploiting the ionization of a low pressure gas injected near the sample surface.

SEM can be also equipped to detect photons emitted by the material upon the interaction with the electron beam. For example nrear-infrared to near-ultraviolet photons can be collected by a **CathodoLuminescence** (**CL**) detector to study the electronic properties of the samples. The interaction of the accelerated electron beam with a field of several kV and the sample also produces X-rays. Some SEMs, such as the one used (Figure 3.15), can be also equipped with a detector that can measure the number and energy of photons emitted at a given solid angle.

Figure 3.15 – FESEM-FIB with EDS tool at IMEM-CNR

Energy Dispersive X-ray Spectroscopy analysis (**EDS** or **EDX**) is a technique that allows elemental analysis of the sample by exploiting the emission of generated X-rays. In fact, the energy of the X-photons emitted as a result of electronic relaxation is characteristic of each element. This type of elemental measurement can be done at a single point, resulting in a spectrum that can be analyzed and quantifyied, or by exploiting the scanning capabilities of the SEM, along lines or areas to obtain compositional profiles or maps respectively.

For this thesis work an AURIGA Compact Field-Effect SEM (FESEM) has been mainly used. This microscope operates up to 30kV and is also equipped with:

- an OXFORD Aztec EDS system with a Xplore30 Silicon Drift-Detector (SDD)

- a Focused Ion Beam (FIB) column that can both operate in “milling” mode using gallium ions or in “deposition mode” using a platinum precursor.

3.4 - Electrical Characterization

Part of the thin-films studied during this PhD work were employed as absorber layer in solar cells. For this reason, electrical characterization played a key role in the study of the material itself (defects for example), but also in the study of devices performance.

In order to understand the physical phenomena beyond these measurements, at first a few fundamental concepts are here recalled.

3.4.1 - p-n junction

A "**p-n junction**" is defined as the coupling of two semiconductors characterized by different types of conductivity, namely, one (called the "**p-type**") in which the majority carriers are holes and one (called the "**n-type**") in which they are electrons. The different type of conductivity in semiconductors may be due to the natural presence within the material of impurities or defects, or introduced artificially through appropriate "doping", that is, the replacement of small percentages of atoms in the semiconductor with atoms of different type (and valence).

When these two materials are put into contact, as a result of the different charge near the interface, part of the **electrons** diffuse from the n-type semiconductor to the p-type semiconductor, and conversely part of the **holes** diffuse from the p-type semiconductor to the n-type semiconductor (Figure 3.16a).

This diffusion of carriers generates a negative charge in the p-type semiconductor and a positive charge in the n-type semiconductor, breaking the condition of electrical neutrality. In fact, the unshielded charge gives rise to an electric field and a potential difference ΔV that, under equilibrium conditions, opposes further diffusion of carriers. The portion of the material affected by this phenomenon is called the "**space charge region**" or "**depletion layer**", and no free carriers are present within it.

Dimensionally, the depletion layer W will be inversely proportional to the N_A and N_D densities of carriers in the p-type semiconductor and n-type semiconductor, respectively, according to the relationship:

$$W = \sqrt{\frac{2\varepsilon}{q}\Delta V\left(\frac{1}{N_D}+\frac{1}{N_A}\right)} \qquad (3.10)$$

where ε is the material dielectric constant and q is the elemental charge.

Because the Fermi level must remain constant throughout the junction, when a p-n junction is formed the valence and conduction bands are subject to the so-called bending shown in Figure 3.13b.

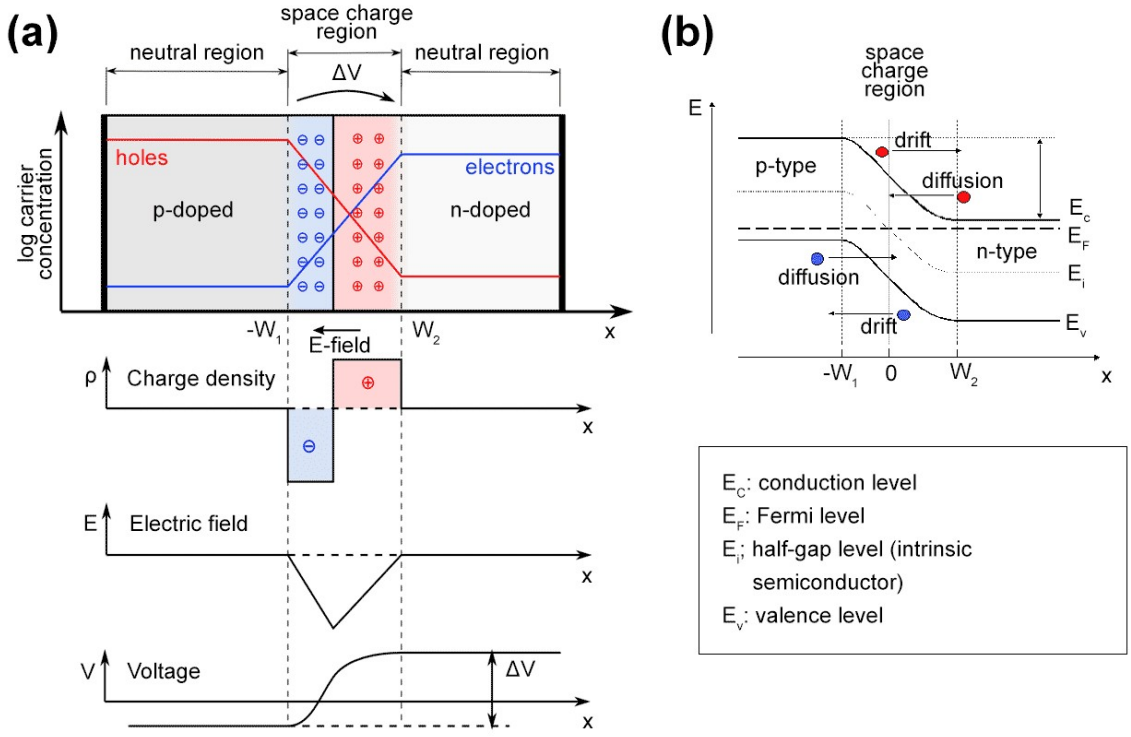

Figure 3.16 - (a) schematic of a p-n junction, with qualitative indication of the electric charge, electric field, and electric potential established in the space charge region; (b) band bending due to the effect of the junction

If, on the other hand, the p-n junction is inserted into an electrical circuit, it will exhibit different behavior depending on the polarization. When the junction is subjected to "**direct**" ("**forward**") polarization, the p-side of the junction is connected to the positive terminal and the n-side to the negative terminal: in this case, the electrons injected into the n-type semiconductor are directed toward the junction, where they progressively neutralize the depletion layer, thus decreasing its width.

For higher applied voltages, above a so-called "**threshold voltage**" (V_S), the empty region becomes so small that most of the carriers pass through it, giving rise to a current. The density of this current (called precisely "direct" or "forward" as the bias that generates it) is defined by the **Shockley equation**:

$$J = J_0 \left(e^{\frac{qV}{Ak_BT}} - 1 \right) \qquad (3.11)$$

where J_0 is the inverse saturation current density, V is the voltage applied to the junction, A is the so-called "ideality factor" (which takes into account the difference between the real

junction and an ideal, perfect junction), k_B is the Boltzman constant, and T is the temperature.

On the other hand, when the junction is subjected to "**reverse**" polarization, the connection to the terminals is opposite: in this condition, the depletion layer increases and only a small current due to the diffusion of minority carriers, called "leakage current", flows through the junction. When a sufficiently high value of applied negative voltage (V_b) is reached, there is the so-called "breaking" ("**break down**") phenomenon of the junction and the passage of large currents. However, this "break down", due to chain ionization phenomena or tunneling effects, is generally reversible.

The described behavior is summarized in Figure 3.17.

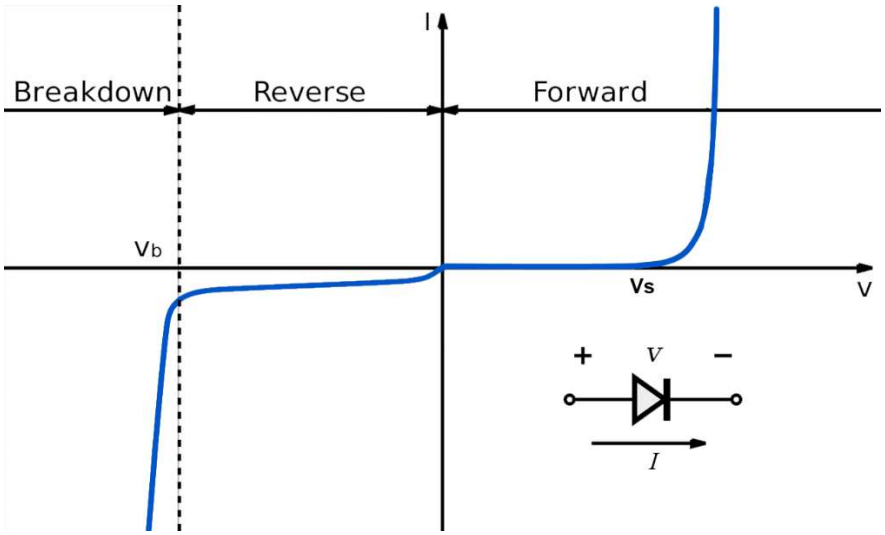

Figure 3.17 - I-V characteristic of a diode based on the p-n junction

The p-n junction is the basis of several modern electronic devices. In addition to the diode, these include LEDs, transistors, and, particularly for our purposes, photovoltaic cells.

3.4.2 - Electrical characteristics of a photovoltaic cell

A "**photovoltaic cell**" is a device that is based on the p-n junction, capable of converting electromagnetic radiation into electric current through the photovoltaic effect. When we refer to devices optimized to convert radiation from the sun, we also generally refer to "solar cells".

In general, when a photon of energy $h\nu = hc/\lambda$ (where h is Planck's constant, c the speed of light, ν and λ the frequency and wavelength, respectively) has an energy equal to or greater than that of the band gap of the semiconductor, it is "absorbed" creating an electron-hole pair. The energy in excess is thermally dissipated.

This absorption and the related carriers generations occurs at a given depth within the material, which depends substantially on the absorption coefficient. The generated electron-hole pair has an average lifetime τ, beyond which generally the carriers recombine (especially the minority carriers that are in an opposite sign charge surround).

If the electron-hole pair is generated near the depletion layer of a p-n junction, it is subject to the electric field, that will lead to the separation of the two carriers of opposite sign, helping to prevent their immediate recombination (τ increases). "Diffusion length" is defined as the distance L that the carriers can travel before recombining and is defined by the relation:

$$L = \sqrt{D\tau} \qquad (3.12)$$

where D is the diffusivity.

It is therefore intuitive to understand that in order to achieve efficient collection of the charge generated by the photon, it is important that the pair is formed near the region of depletion.

Due to the illumination of the junction and the generated carriers, the current density J, previously seen for an unilluminated junction, is changed by this additional contribution (Figure 3.18).

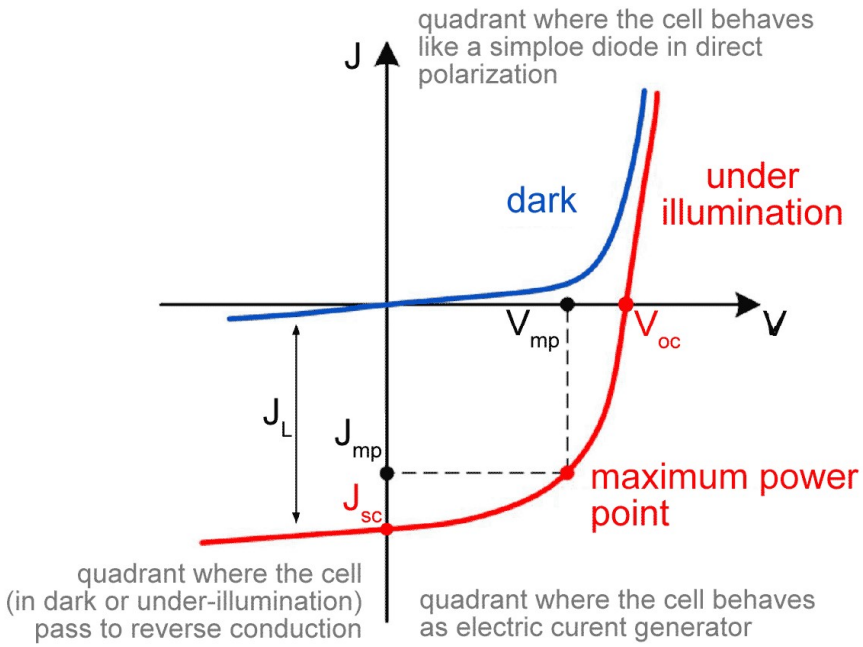

Figure 3.18 - J-V curve of a photovoltaic cell in the dark and under illumination

Looking at the graph, it is possible to define some particular values of this new J-V curve that will come in handy in the following discussion:

- $\boldsymbol{J_L}$ is the current density generated due to the effect of illumination

- $\boldsymbol{J_{mp}}$ is the current density corresponding to the maximum power point of the cell

- $\boldsymbol{V_{mp}}$ is the voltage corresponding to the maximum power point of the cell

- $\boldsymbol{J_{sc}}$ is the **short circuit current density**, which is the current generated when no voltage is applied to the cell

- $\boldsymbol{V_{oc}}$ is the **open circuit voltage**, which is the voltage measured at the ends of the cell when no current is flowing.

These quantities in real thin-film cells usually depends on how the cell was constructed (materials chosen, interfaces, defects, etc.). In particular, $\boldsymbol{J_{sc}}$ depends on the value of the bandgap, as does $\boldsymbol{V_{oc}}$, which, however, also depends on the band alignment of the various layers of the cell and recombination, especially at the heterojunction interface.

Depending on these values, it is also possible to define two very useful quantities when it comes to photovoltaic cells: the "**Fill Factor**" (**FF**) and the **cell efficiency** (**η**):

$$FF = \frac{V_{mp}\, J_{mp}}{V_{oc}\, J_{sc}} \qquad (3.13)$$

$$\eta = \frac{V_{mp}\, J_{mp}}{P} = \frac{V_{oc}\, J_{sc}\, FF}{P} \qquad (3.14)$$

where P is the total power incident on the cell, which is the product between the power of the incident radiation per unit area and the area of the cell.

Efficiency $\boldsymbol{\eta}$ expresses the ratio (usually in percentage) between the electrical power generated and the power that radiates the cell, regardless of the area considered. On the other hand, the concept of **Fill Factor *FF*** is easier to understand when represented graphically, as the maximum theoretical power $I_{sc}V_{oc}$ and the rectangular area subtended by the maximum power that can be extracted from the $I_{mp}V_{mp}$ device. The same *FF* value can be calculated if current density J is used instead of current I (Figure 3.19).

A real cell differs from an ideal cell due to several contributions related to both the structure of the cell and the materials used, their defects and the defects that can be formed at the interfaces. However, the effect of all these contributions can be summarized by two quantities, which have the form of electrical resistances, and which can be placed within the so-called equivalent circuit of a photovoltaic cell as in Figure 3.19b. These are:

- $\mathbf{R_s}$: **series resistance** is defined as the derivative of the curve $V(J)$ at the V_{oc} point and is represented in the equivalent circuit as a series resistance with respect to the cell. It is mainly attributable to parasitic resistances due to the finite mobility of the carriers

through the material and the resistances established between the various components of the cell. In the case of thin-films also parameters such as possible crystalline anisotropy, thickness, width of the neutral region, and electrical compensation typical of very defective polycrystals, have an influence on this quantity.

- **R_{sh}: "shunt" resistance** is defined as the derivative of the $V(J)$ curve at the J_{sc} point and is represented in the equivalent circuit as a resistance in parallel with respect to the cell. It is related to all the lower resistance paths present in the cell and generally due to defects in the semiconductor, which locally bring the contacts at the sides of the junction to a reduced or even zero distance (short circuit) or create preferential percolative paths for the current. For example, in thin-film cells this quantity is affected by "pinholes" in the films, preferentially conducting grain edges, charge reversal on the defects, and some cell insulation techniques, such as scribing or laser patterning, not compatible with brittleness of polycrystalline materials.

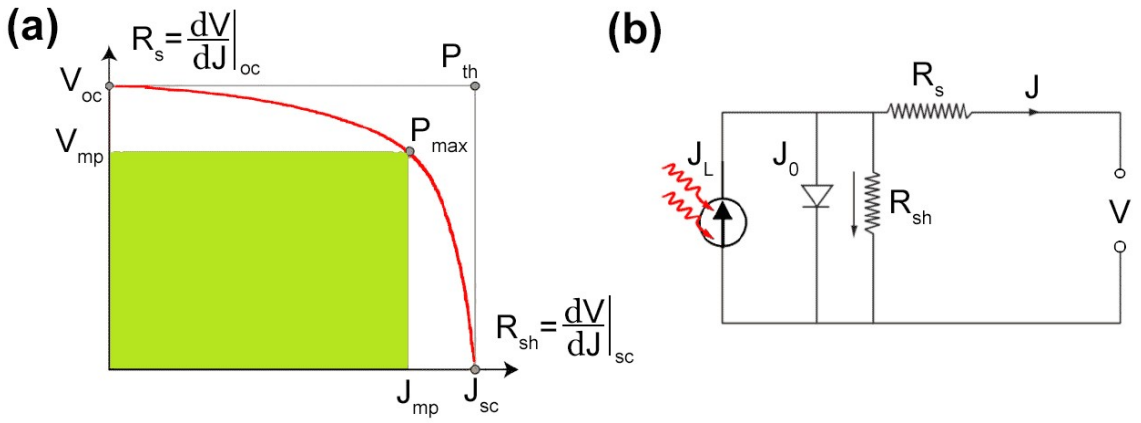

Figure 3.19 - Graphic representation of the real and ideal (theoretical) values of the J-V curve; (b) equivalent circuit of a photovoltaic cell

R_s and R_{sh} are usually expressed as **resistances per unit area** (Ω cm^2) to neglect the effect of device area. It is clear from their definition that the more R_s and R_{sh} deviate from the values R_s=0 Ω cm^2 and R_{sh}=∞ Ω cm^2, the more the power generated by the cell deviates from the maximum theoretical value $J_{sc}V_{oc}$, while FF is reduced.

Shockley's equation can be modified for real photovoltaic cells to account for all these factors as follows:

$$J = J_0\left(e^{\frac{q(V-J\,R_S)}{Ak_BT}} - 1\right) - \left(\frac{V-J\,R_S}{R_{sh}}\right) - J_L \qquad (3.15)$$

where R_s and R_{sh} are the quantities just defined, J_0 is the inverse saturation current density, J_L is the illumination current density, V is the applied voltage, A is the "ideality factor," k_B is the Boltzman constant, and T is the temperature. Explicitly, therefore, it follows that for the contribution $((V - J R_s) / R_{sh})$ to be minimal, R_s must ideally have the lowest possible value (typically less than 1 Ω cm^2), while R_{sh} must be very high (typically greater than 1 kΩ cm^2).

When dealing with thin-film photovoltaic cells, it may also be useful to define one last quantity: the "**sheet resistance**" $\boldsymbol{R}_{\square}$, which is the resistance that a square sample of uniform thickness d would have, regardless of its actual area.

$$R_{\square} = \rho / d \qquad (3.16)$$

3.4.3 - Deep levels

In semiconductors an important role is played by **defects**. The presence of an impurity usually creates a distortion in the lattice periodicity leading to the creation of additional energy levels inside the energy gap.

Defects can be classified as **shallow** or **deep**. Shallow defects are usually due to very soluble impurities and are widely used to modify the conductivity. Deep defects on the other hand are very common. They are caused by vacancies, interstitial defects, antisites, etc. These kinds of defects often lead to a high local distortion, which means strong local wave functions. In other words, they tend to create traps or recombination sites which have a strong correlation with the carrier lifetime.

This is clearly a problem for all the devices that require long carrier lifetime (e.g., solar cells) and high radiative recombination efficiencies (e.g., laser or LED).

Deep levels are influenced by many factors, but most of them are generally related with the deposition/growth techniques (growth parameters and/or by the system "cleaness").

An important distinction has to be made between "traps" and "recombination centers" and for this is necessary to remember the definition of "capture velocity" for electrons ($\boldsymbol{c^*_n}$) and holes ($\boldsymbol{c^*_p}$):

$$c^*_n = \sigma_n \langle v \rangle_n n = c_n n \qquad c^*_p = \sigma_p \langle v \rangle_p p = c_p p \qquad (3.17)$$

where n and p are free electrons and holes densities respectively, $\langle v \rangle$ are the mean thermal velocities and σ the capture cross sections, c the capture constants.

An electron trap is a defect for which the velocity of electron capture c^*_n is much higher of the hole one c^*_p ($c^*_n >> c^*_p$). A recombination center, instead, is a defect for which the capture velocity for electrons is comparable to the hole one ($c^*_n \approx c^*_p$). This means that a site,

with specific values for σ (cross section) can act as a trap or as a recombination center depending by the free carrier density (Figure 3.20a).

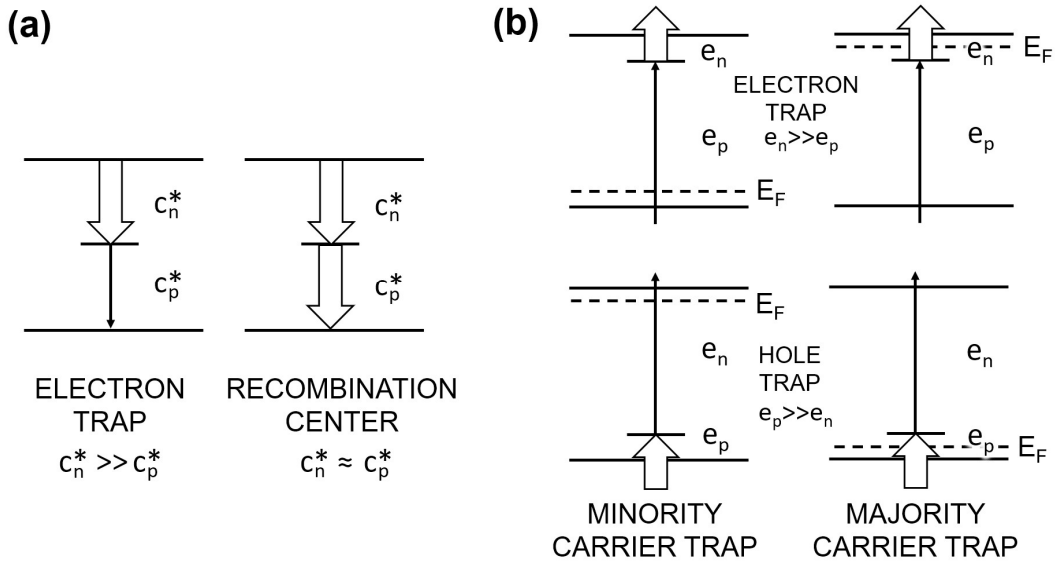

Figure 3.20 – Scheme of the definition of defects (a) in a semiconductor and (b) inside the depletion layer, on the basis of capture or emission coefficients

Inside the depletion layer, it is more appropriate to talk in terms of "majority carriers" (the carrier type that is more prevalent within the material) and "minority carriers" (the less abundant carrier type). In this case it is also inappropriate to define the defect properties using capture velocities, because they are zero. A "**majority carrier trap**" is hence defined as a specific type of defect for which the thermal emission velocity associated with the majority carrier is significantly greater than the corresponding emission velocity for the minority carriers ($e_{maj}>>e_{min}$) (Figure 3.20b). On the other hand, in this context a "**recombination center**" refers to a defect for which the emission velocity of majority carriers and minority carriers are relatively similar, or at least comparable in magnitude ($e_n \approx e_p$). Emission, in this case, is $e_n=c_n n^*$ for electrons and $e_p=c_p p^*$ for holes, where n^* and p^* are electrons and holes concentrations at the point where Fermi level and the energy of the deep level *E'* overlap (Figure 3.21).

The presence of a recombination center deep level *E'* inside the depletion layer (Figure 3.21) implies that it participates in the process of carrier recombination, wherein carriers (electrons and holes) combine and neutralize each other. This recombination process is crucial in determining the overall lifetime of carriers within the material. The deeper understanding of how *E'* operates as a recombination center provides insights into the material's behavior, especially in terms of its electrical and optoelectronic properties.

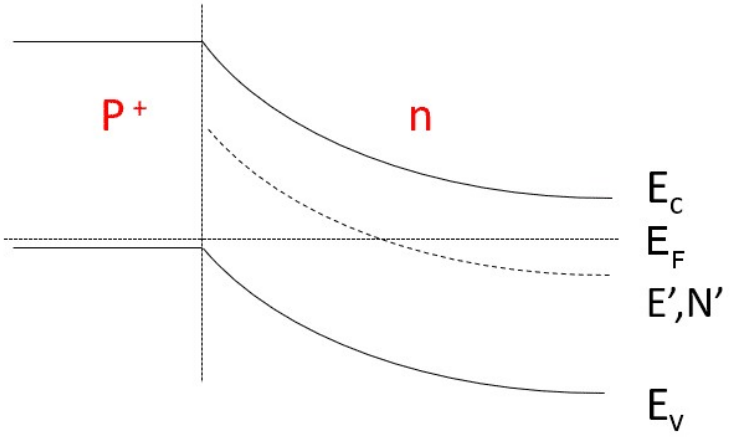

Figure 3.21 – Example of a deep level *E'* inside the depletion level with *N'* concentration

A generic deep level E_t, that acts as a recombination center inside the depletion level, with N_t concentration, determines the carrier's lifetime:

$$\tau = \left(\frac{N_c}{\langle v\rangle_p \sigma_p n_0 N_t}\right) e^{\frac{-E_c - E_t}{kT}} \qquad (3.18)$$

where N_c is the effective density of states in the conduction band, $\langle v\rangle_p$ is again the mean thermal velocity of holes, σ_p is the capture cross section for holes, n_0 is free electron concentration at the equilibrium, E_c is the conduction energy level. If the levels are two (E_{t2} and E_{t2}) or more, the carrier lifetime is dominated by the deepest energy level, unless the shallow one concentration is much higher, because:

$$\tau_1/\tau_2 = \left(\frac{\sigma_{p2} N_{t2}}{\sigma_{p1} N_{t1}}\right) e^{\frac{E_{t1} - E_{t2}}{kT}} \qquad (3.19)$$

The calculation of deep level energy becomes straightforward through the analysis of e_n and e_p with respect to temperature (T). Considering the dependency, where velocity exhibits a square root of temperature ($T^{1/2}$) relationship, and the concentration (N) follows a cubic root of temperature ($T^{3/2}$) relationship, the pre-exponential factor $\langle v\rangle_{n,p} N_{c,v}$ takes on a quadratic (T^2) dependence.

$$e_n = c_n N_C e^{\frac{E_C - E'}{kT}} = \sigma_n \langle v\rangle_n e^{\frac{E_C - E'}{kT}} \qquad (3.20)$$

$$e_p = c_p N_V e^{\frac{E' - E_V}{kT}} = \sigma_p \langle v\rangle_p e^{\frac{E' - E_V}{kT}} \qquad (3.21)$$

Hence, from the Arrhenius plot of e_n and e_p over T^2, it is possible to deduce the values of (E_C-E') or (E'-E_V) (Figure 3.22). It is important to keep in mind that with the variation of T

we have a variation in the energy gap. Consequently, we have a change in the separation between the deep level energy and the bandwidths.

For semiconductors there are three main techniques for investigating deep level:

- Thermally Stimulated Capacitance (TSCAP)
- Admittance Spectroscopy (AS)
- Deep Level Transient Spectroscopy (DLTS)

The first two techniques have been used during this thesis work.

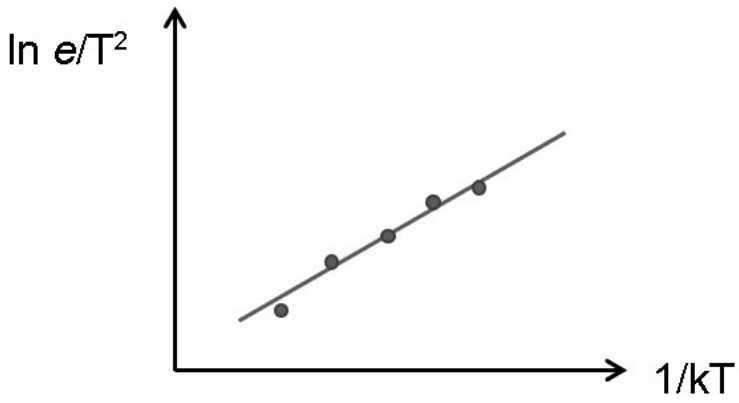

Figure 3.22 - Arrhenius plot of e_n and e_p over T^2

3.4.4 - Capacitance measurements

Investigations based on **capacitance** measurements involve the study of alterations in capacitance resulting from electric or optical stimulation within a Schottky barrier or a p-n junction. Indeed, the introduction of a deep level (donor) leads to an increase of the capacitance within the depletion layer (Figure 3.23).

The way used for measuring this is by applying a small alternated signal $\Delta V = V_0 e^{i\omega t}$ to a continuous bias V, where ω is directly correlated to the signal frequency. This signal causes charge variations in proximity of the depletion layer edge and in a small area around the intersection point between the Fermi level and the deep level. It is possible to demonstrate that:

$$C(\omega) = C\infty + \frac{C_0 - C\infty}{1+(\omega/\omega*)} \qquad (3.22)$$

where C_0 is the junction capacitance for ω=0 so a capacitance that considers the deep level presence, while ω at high frequency is the capacitance without the presence of deep levels; ω* is the characteristic frequency of the analyzed deep level and it is related to the thermal

emission velocity by the relation $\omega^* \approx 2e_n$. The presence of a deep level makes the measured capacitance dependent on the frequency of the test signal.

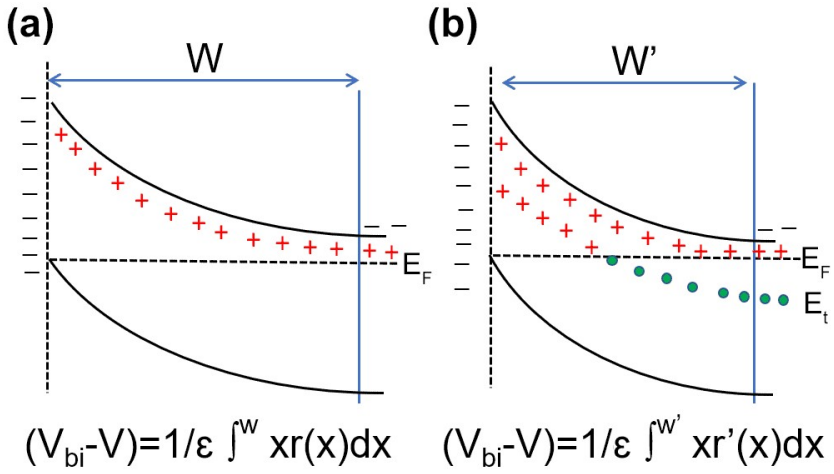

Figure 3.23 – Depletion layer (here between a metal and a n-type semiconductor for simplification) where (a) only shallow impurity levels are present and (b) also a deep donor level is present

If there aren't deep levels and the semiconductor is homogeneous, the *C-V* profile can be expressed as:

$$C = \sqrt{\frac{q\varepsilon N_d}{2(V_{bi}-V)}} \qquad (3.23)$$

where q is the electric charge, ε is the dielectric constant, N_d is the concentration of not-compensated ionized donors. So if $1/C^2$ vs V is plotted, a linear trend is find out: the slope gives us a value for N_d, while the intercepts a value for the built-in potential V_{bi} (Figure 3.24).

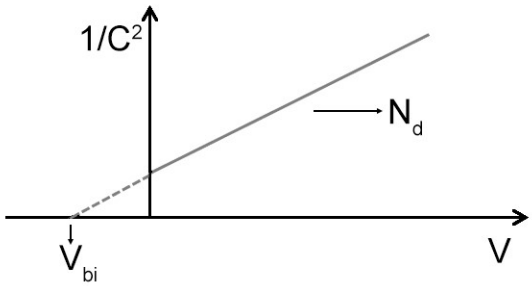

Figure 3.24 – Plot of $1/C^2$ vs V in a semiconductor without deep levels.

In presence of deep levels the *C-V* profiles change. Starting with the hypothesis that $N_d(x)$ and $N'(x)$ are constant, for a test signal with high frequencies and for slow increase of the applied voltage ΔV_r, compared to the emission velocity of the deep level ($e_n >> \omega(\Delta V_r)$),

the characteristic $1/C^2$ is no longer linear. It can be demonstrated that the profile of free carriers $N(x)$ obtained by the $1/C^2$ derivative is:

$$N(x) = -\frac{2\,\Delta C^2}{q\varepsilon\Delta V_r} \qquad (3.24)$$

with $x=\varepsilon/C$ is given by:

$$N^d(x) = N_t\left(\frac{1-\lambda}{x}\right) + N_d \quad \text{and} \quad N^a(x) = N_d - N_t\left(\frac{\lambda}{x}\right) \qquad (3.25)$$

for donor or acceptor traps, where λ is the portion of x for which the deep level is lower than the Fermi level. If $\omega(\Delta V_r) >> e_n$, (i.e. low T), the measured profiles will be:

$$N^d(x) = N_d \quad \text{and} \quad N^a(x) = N_d - N_t \qquad (3.26)$$

In short, confronting ***C* vs. *V* plots** for $e_n >> \omega(\Delta V_r)$ and for $\omega(\Delta V_r) >> e_n$, it is possible to calculate $\mathbf{N_t}$.

3.4.5 - Admittance Spectroscopy

Admittance spectroscopy is a powerful technique employed to investigate the electrical properties of semiconductor materials and devices. This method focuses on the measurement of the admittance (Y), which is the reciprocal of impedance (Z), of a semiconductor structure as a function of frequency or bias voltage. Admittance spectroscopy provides valuable insights into the density of electronic states, energy levels, and charge carrier dynamics within the material.

Admittance in a junction is defined as the ratio between the increase in current δi and the increase δv in alternate tension signal of frequency ω, so:

$$Y = \frac{1}{Z} = \frac{\delta i}{\delta v} = G + \mathrm{i}S = G + i\omega C(\omega) \qquad (3.27)$$

where G is the conductance, S the susceptance and C the capacitance.

In the case of Admittance Spectroscopy the application of a sinusoidal signal $\delta v=\delta v_0 e^{i\omega t}$ produces space charge perturbations $\delta Q(x^*)$ near $x=x^*$ and $\delta Q(w)$ near $x=w$ (Figure 3.25).

The signal amplitude must be small enough (a few mV), so that during the positive and negative half-period, only the traps close to $x=x^*$ change their occupation state. Near this point is also possible demonstrate that capture time τ_c and emission time τ_c are equal:

$$\tau_e = \tau_c = \frac{1}{c_n(n(x)+n*)} = \frac{1}{2e_n} \qquad (3.28)$$

where c_n is capture cross section for electrons, n(x) is free electron density function along x, n* is free electron density at x=x* and e_n is emission velocity for electrons. So, if $\omega \leq e_n$ electrons captured by traps during the positive semi-period are then emitted during the negative semi-period, while if f $\omega >> e_n$ emission and capture processes around x=x* cannot follow the variations of δv.

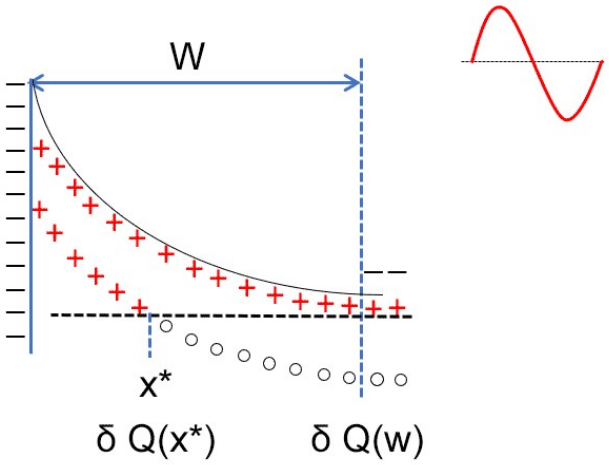

Figure 3.25 – Effect on the depletion layer of the application of sinusoidal signal

Because of the sinusoidal signal, admittance becomes:

$$Y = \frac{\delta i}{\delta v} = \frac{\frac{d\delta\ (x*)}{dt} + \frac{d\delta\ (w)}{dt}}{\delta v} \qquad (3.29)$$

and by applying Gauss theorem we can then obtain:

$$C = \frac{\delta Q}{\delta v} = \varepsilon \frac{\delta Q(x*) + \delta Q(w)}{x* \delta Q(x*) + w \delta Q(w)} \qquad (3.30)$$

Hence the capacitance C depends on x^* value and, hence, on the energy level position, while it becomes the well-known expression $C = \varepsilon/w$ when $\delta Q(x^*)=0$.

In practice, it is possible to measure both $\boldsymbol{\Delta E}$ and $\boldsymbol{N_t}$ by using this technique.

To measure ΔE*:*

1) $G(T)$ is measured at a given frequency and its maximum is found at $T=T_m$. At this temperature $\omega = \omega^* = 2e_n$. Hence, knowing ω, it is possible to determine e_n at $T=T_m$.
2) $G(T)$ is measured at different frequencies in order to obtain ω^* (and so e_n) dependance on T (i.e. $e_n(T)$).
3) From $e_n(T)$, under the hypothesis that σ_n is independent from T, we can obtain the activation energy, from the slope of $\ln e_n/T^2$ vs $1/kT$.

To measure N_t, it is possible to demonstrate that:

$$\frac{C_0 - C\infty}{C\infty} = \left(\frac{N_t}{N_d(1 - x*/w)}\right) / \left(1 + \frac{x*N_t}{wN_d}\right) \qquad (3.31)$$

In this case, once C_0 and $C\infty$ are measured in ***C* vs *ω* plots***, the **traps concentration** $\boldsymbol{N_t}$ can be easily determined from equation 3.31.

Chapter 4
Sb_2Se_3

In this chapter all the growth and characterization activities regarding Sb_2Se_3 thin-films are reported. After a brief introduction on the applications and properties of this material, a quick resume of the results previously achieved during my Master's Degree thesis work is provided as a reference, since this part of my PhD activity started just after that and it is the natural continuation of that research. Then all the experimental results are described and discussed in the following paragraphs. More in detail:

4.1 - Material properties and applications

4.1.1 - Sb_2Se_3 and the thin-film photovoltaic application

The thin-film photovoltaic industry today is dominated by three main leading materials (Figure 4.1): amorphous silicon (**a-Si**), cadmium telluride (**CdTe**), and copper indium gallium diselenide (**$Cu(In,Ga)Se_2$** or simply "**CIGS**"). Cells based on a-Si have the great advantage of a low cost, but since a few years the photovoltaic conversion efficiency value achieved in worldwide laboratories is not exceeding 14% (<10% for modules). On the other hand, the use of CdTe-based cells, despite the excellent results achieved (record cell efficiency to date of 22.3% and 19.5% for modules), has been severely slowed down due to the hazardous nature of the cadmium they contain. CIGS-based cells have reached a record efficiency of 23.6% (20.3% for modules) and, although they do not suffer from the same problems of the previous two types, to date they still occupy a minimal percentage of the market. CIGS, indeed, contains indium and gallium, which are rather expensive elements today and more difficult to find (sufficient abundance, but concentrated in few countries).

On the other hand, modules based on **monocrystalline silicon** have in several cases exceeded all these efficiency values, while their higher material consumption is largely compensated by the very low production costs.

So thin-film photovoltaic research today is investigating alternative solutions, especially for specific applications (e.g. flexible and/or lightweight panels, building integration, bifacial panels, tandem solar cells, etc.), in order to achieve high efficiencies with **more abundant** and **cheaper** materials also in these fields.

Among the various materials tested, two are the main studied families: on one hand **perovskite** materials, with their very high efficiencies, but still suffering of long-term stability issues (especially for hybrid perovskites) and/or often containing elements that are toxic or expensive; on the other hand alternative **selenides** and **sulfides**, mainly belonging to the families of semiconductor compounds with chalcopyrite or stibnitic type structure, that are more stable but today still far from the 24% efficiency of silicon.

Among the latters, increasing interest has been recently directed toward **antimony selenide** (**Sb_2Se_3**, also referred to as "**ASe**"), a binary semiconductor based on relatively low cost elements (Figure 4.2), with a direct gap of about 1.2 eV (1.03 eV indirect), absorption coefficient greater than 10^5 cm^{-1} and, according to the Shockley-Queisser (S-Q) model, it could achieve a theoretical predicted efficiency up to 32.2%.

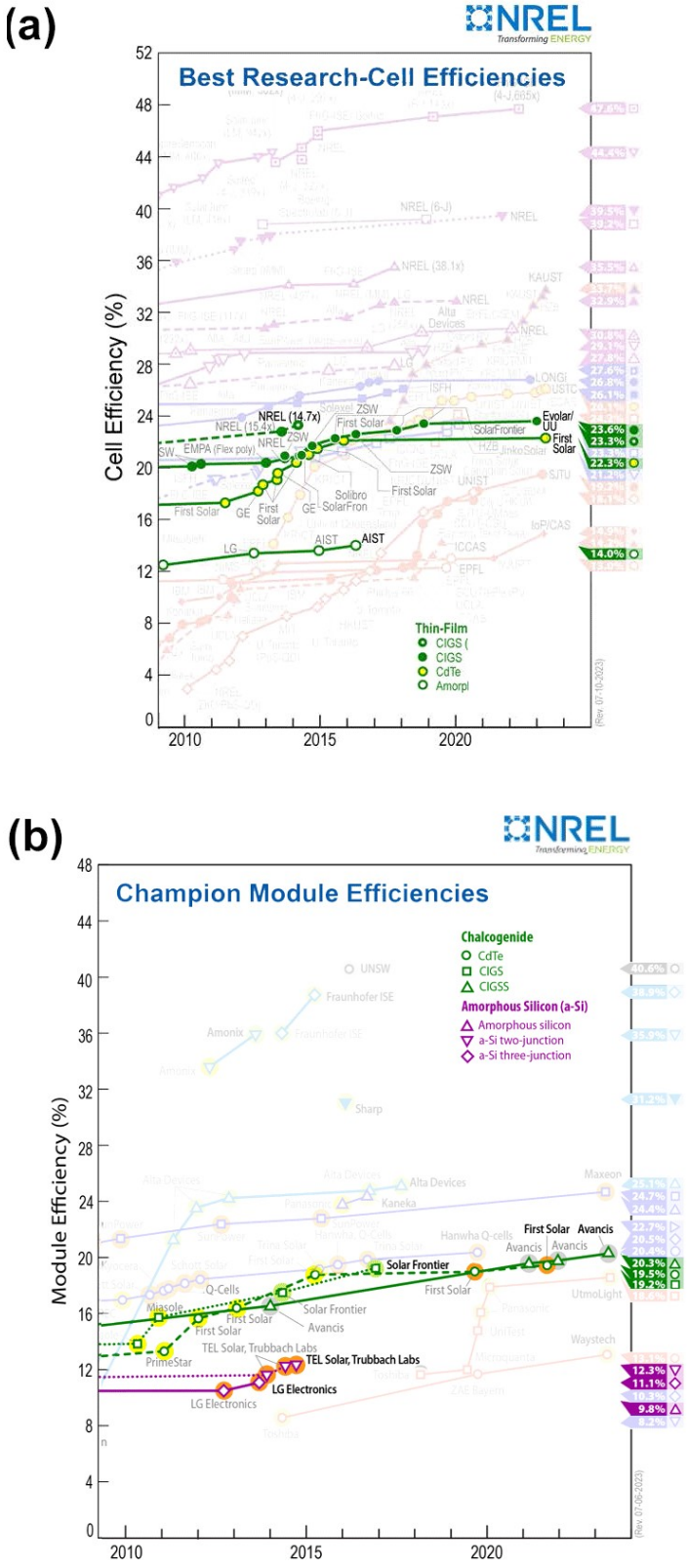

Figure 4.1 - Record photoelectric conversion efficiencies values for thin-film photovoltaics: (a) cells on laboratory scale, (b) commercial modules [source: NREL]

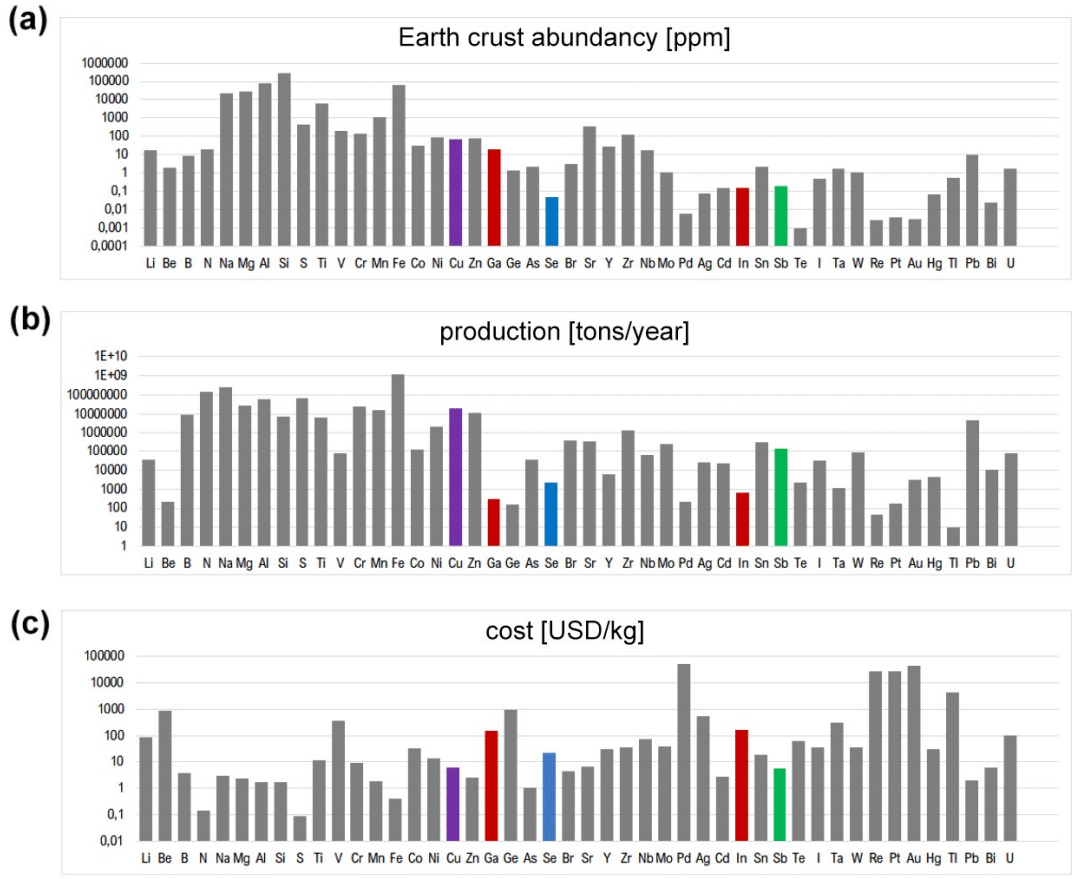

Figure 4.2 - Approximate indication of abundance in the Earth's crust (a), annual production (b) and cost (c) for some of the most common elements used in materials production.

4.1.2 - Crystalline structure

The structure of antimony selenide is of the stibnitic type, with **orthorhombic primitive cell**. In literature we can find this cell alternately described with two equivalent space groups, *Pnma* and *Pbnm*, which differ only by a permutation of the axes. In the first case the cell parameters are a=11.77 Å, b=3.962 Å, c=11.62 Å, so that the b axis is identified as the short axis of the cell. In the second case, instead, c is the short axis (a=11.62 Å, b=11.77 Å, c=3.962 Å). Since even in the literature this ambivalence has often created confusion and sometimes some errors, it is here better to unambiguously state that the ***Pbnm*** space group is always used in this thesis (Figure 4.3a).

Sb_2Se_3 crystal structure is characterized by Se-Sb-Se chains that develop into **columns** (often also called "**ribbons**") aligned along the ***c*-axis**. More in detail, these columns/ribbons are formed by Sb_4Se_6 units stacked together to form one-dimensional structures, with strong chemical bonds only within them and weak Van der Waals-type Se-Se bonds between adjacent columns (Figure 4.3b).

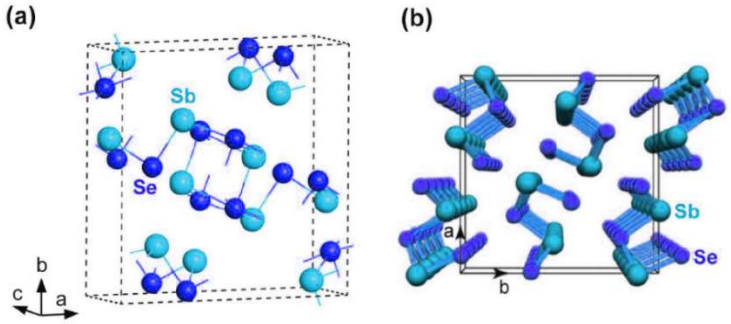

Figure 4.3 - (a) orthorhombic crystallographic cell (*Pbnm*) of antimony selenide; (b) stacking of some cells along the *c*-axis showing the columnar structures generally called "ribbons"

This columnar structure underlies the strong **anisotropy** that characterizes many properties of this material, including charge transport.

Once again, using the *Pbnm* space group as a reference, it is possible to see that these ribbons are oriented along the crystallographic direction [001]. Thus, in general, generic planes (00*l*) will be perpendicular to this [001] direction and to the ribbons, while [001] direction will lay on planes characterized by (*hk*0) index.

In the case of a thin film:

- if the main surface of the film is formed by a plane **(00*l*)**, the ribbons will be aligned perpendicular to it and to the substrate surface (Figure 4.4a);
- if the main surface of the film is formed by a plane **(*hk*0)**, the ribbons will be aligned parallel to it, thus lying parallel to the substrate surface (Figure 4.4h);
- if the main surface of the film is formed by a plane with generic **(*hkl*)** index, not falling in any of the previous two cases, the ribbons will be inclined with respect to the substrate surface at a variable angle (Figure 4.4b-g).

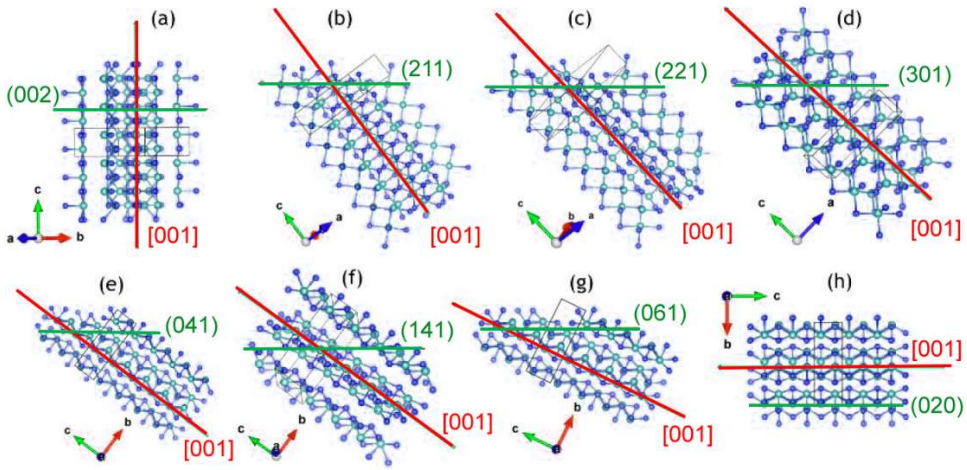

Figure 4.4 - Illustration of the relative orientation of column-like "ribbons" structures (directed along [001]) with respect to different planes of the Sb_2Se_3 crystal structure

It is easy to see that charge transport will occur preferentially along chains, since hopping mechanisms must instead be exploited to move from one ribbon to another. Thus, in a thin-film photovoltaic cell, in which charges must move perpendicular to the substrate, all film grains that expose a (00*l*) face on the surface will participate much more efficiently in transport than grains that expose a (*hk*0) face. For grains that exposing intermediate (*hkl*) faces, instead, transport will essentially depend on the degree of ribbons inclination.

To provide a more immediate representation of the "degree of orientation," several parameters have been introduced in literature. In our results, the following "texture coefficient" (TC) is generally reported:

$$\mathrm{TC}(hkl) = \frac{\frac{I(hkl)}{I_0(hkl)}}{\sum_n \frac{I(h'k'l')}{I_0(h'k'l')}} \times 100\% \qquad (4.1)$$

where "*hkl*" represents Miller's set of indices for a specific reflection, *I(hkl)* is the normalized intensity of the corresponding peak in the diffraction pattern, $I_0(hkl)$ stands for the relative intensity as documented in the literature for a standard Sb_2Se_3 pattern (JCPDS 15-0681). The denominator summation is computed on the base of the ratio of these same values for the *n* major *h'k'l'* reflections.

The set of 10 reflections reported in Table 4.1 has been used for the evaluation of the results here reported. According to the TC definition, a preferential orientation of Sb_2Se_3 film grains along one of these directions is present when its TC exceeds 10.0%.

Table 4.1 - Set of principal reflections for the range 10°<2θ<60°, selected for analysis of the degree of film texture and orientation. For each, the angle between the columns and the normal to the surface (*hkl*) and the EVC value are reported.

crystallographic orientation (hkl)	***angle between [001] ribbons direction and (hkl) surface normal [deg]***	***Effective Vertical Component (EVC)***
(002)	0	1
(211)	37.3	0.79
(221)	43.8	0.72
(301)	45.7	0.70
(041)	53.4	0.60
(141)	54.2	0.58
(061)	63.6	0.44
(020)	90	0
(120)	90	0
(130)	90	0

Table 4.1 also reports the Effective Vertical Component (EVC), which corresponds to the cosine of the angle between the ribbons of Sb_2Se_3 structure and the (*hkl*) surface normal. The EVC achieves its maximum value (1) for those orientations promoting a vertical ribbons orientation on the substrate, and its minimum value (0) for orientations promoting ribbons lying parallel to the substrate. The EVC value is directly linked to how specific orientations, if "preferential", can enhance charge transport within the film for photovoltaic applications.

Finally, the product of TC and EVC, called "Ribbon Carrier Transport" (RCT=TCxEV), can be calculated for each reflection in an XRD spectrum, offering a quantitative assessment of the overall degree of "beneficial" alignment for charge transport in a given Sb_2Se_3 film, when employed in cell fabrication.

Density Functional Theory (DFT) theoretical calculations have indeed shown that the electron density is concentrated within the ribbons. In addition, surfaces orthogonal to the (001) plane, such as (100), (010), (110) or (120), appear to be prevalent for grain boundaries. In fact, since the sides of the columns lack in "dangling bonds", the formation of these edges is energetically favored. While the average surface potential for antimony selenide has been calculated to be about 9.1 mV, for other materials widely used in photovoltaics, such as CIGS and CZTS, it turns out to be much higher (>100 mV). This means that the naturally dominant faces are "benign" for photovoltaic application, because they are lacking in those "dangling bonds" that are generally source of charge carrier recombination and hence require passivation processes or doping to overcome/reduce the problem.

Therefore, while the use of Sb_2Se_3 makes proper alignment of the film grains an imperative condition to achieve efficient charge transport, grain boundaries might be in this case just considered a second order problem.

4.1.3 - Electronic structure

Sb_2Se_3 is characterized by a direct bandgap (E_g) of 1.17 eV and an indirect bandgap of 1.03 eV, measured experimentally at room temperature. These values are slightly higher than those calculated through DFT, which instead settle around 1.07 eV for the indirect bandgap and 0.99 eV for the direct bandgap (the discrepancy is reasonably given by the fact that these models are usually calculated at a temperature of 0 K).

These values place Sb_2Se_3 in the most favorable area of the diagram connected to the Shockley-Queisser model for photovoltaic efficiency (Figure 4.5). In fact, Sb_2Se_3 has a bandgap very close to that of crystalline silicon, GaAs or CdTe.

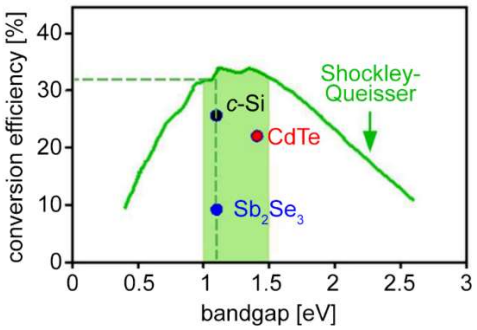

Figure 4.5 - Theoretical maximum efficiency curve according to the Shockley-Queisser model as a function of the bandgap value of the absorber material

This very model makes it possible to estimate for this material the achievement of a **theoretical maximum conversion efficiency** of **32.2%**. Although this value only indicates the "potential" of this material, it is high enough to make it very attractive.

In addition to this the **density of states** (**DOS**) is also particularly favorable, since it is particularly high near the top of the valence band and at the bottom of the conduction band (Figure 4.6).

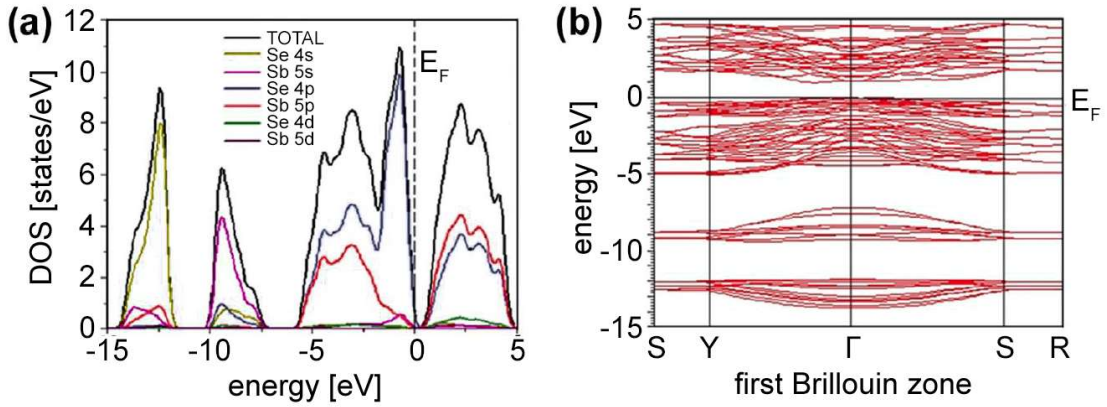

Figure 4.6 - Total and partial density states (a) and band structure (b) calculated for antimony selenide [source: Koc et al., 2012]

Such a high DOS is generally related to a high value of the **absorption coefficient**, which, in the case of Sb_2Se_3, is indeed higher than 10^5 cm^{-1} for most of the solar spectrum. This is equivalent to saying that sunlight can be completely absorbed by a film much less than 1 μm thick.

In particular, a very high absorption coefficient is also important when dealing with a material that does not possess exceptional transport properties. For Sb_2Se_3, in fact, the mobility of electrons (μ_e) is about 15 cm^2 V^{-1} s^{-1}, while that of holes (μ_h) is around 42 cm^2 V^{-}

[1] s^{-1}. A value of about 1.7 μm is reported in literature for the diffusion length (L_e). These values, although measured along the "favorable" [001] direction, are rather low when compared with those of other materials used in solar cells, but for films as thin as those needed for Sb_2Se_3, they should not be a particular problem.

4.1.4 - Electrical properties

The columnar structure of Sb_2Se_3 leads to significant **charge transport anisotropy**. Sb_2Se_3 is typically a **p-type** semiconductor, although there are instances of n-type conductivity (achieved through Te or Bi doping or substantial stoichiometric deviations in Sb) reported in literature. The **charge density** due to free carriers is relatively low, approximately 10^{13} cm^{-3}. This value is notably lower than those typically required for photovoltaic applications (around 10^{16} cm^{-3}). Under dark conditions, the electrical conductivity is only 10^{-8} S/m.

Numerous studies conducted on this material have reported high activation energies. These high activation energy values, ranging from 0.54 to 0.66 eV, are generally consistent with the hypothesis that the Fermi energy is pinned within the bandgap. Such elevated activation energies likely indicate the presence of deep traps, which can diminish *Voc* values and consequently affect cell performance.

These findings underscore the critical importance of conducting future systematic investigations into defects and potential doping strategies for Sb_2Se_3. In literature, three main types of electrically active defects have been identified. These defects have been studied using Admittance Spectroscopy technique and theoretical Density Functional Theory (DFT) calculations. They are positioned at energy levels approximately 0.3-0.4 eV (D1), 0.2-0.6 eV (D2), and 0.5-0.6 eV (D3) above the valence band maximum. D1 and D2 are considered bulk defects, while D3 is categorized as an interface defect and its specific impact on PV cell efficiency is not yet fully understood.

In Sb_2Se_3 films (as depicted in Figure 4.7), prevalent defects are $\mathbf{V_{Sb}}$ antimony vacancies, $\mathbf{Se_{Sb}}$ substitutional selenium, and $\mathbf{Sb_{Se}}$ substitutional antimony. The first two act as hole traps, while the third acts as an electron trap. V_{Sb} and Se_{Sb} are the primary acceptor-type defects and are generally responsible for intrinsic p-type doping in Sb_2Se_3 films.

On the other hand, $\mathbf{V_{Se}}$ selenium vacancies are highly undesirable due to their behavior as n-type donors, which counteracts/reduces p-type conductivity. Furthermore, they act as recombination centers, negatively impacting cell performance. Experimental evidence supports these considerations, as the best-performing Sb_2Se_3-based cells typically use films

that are slightly deviated in stoichiometry toward an **excess of selenium**, to discourage the formation of this type of defect (see Figure 4.7c).

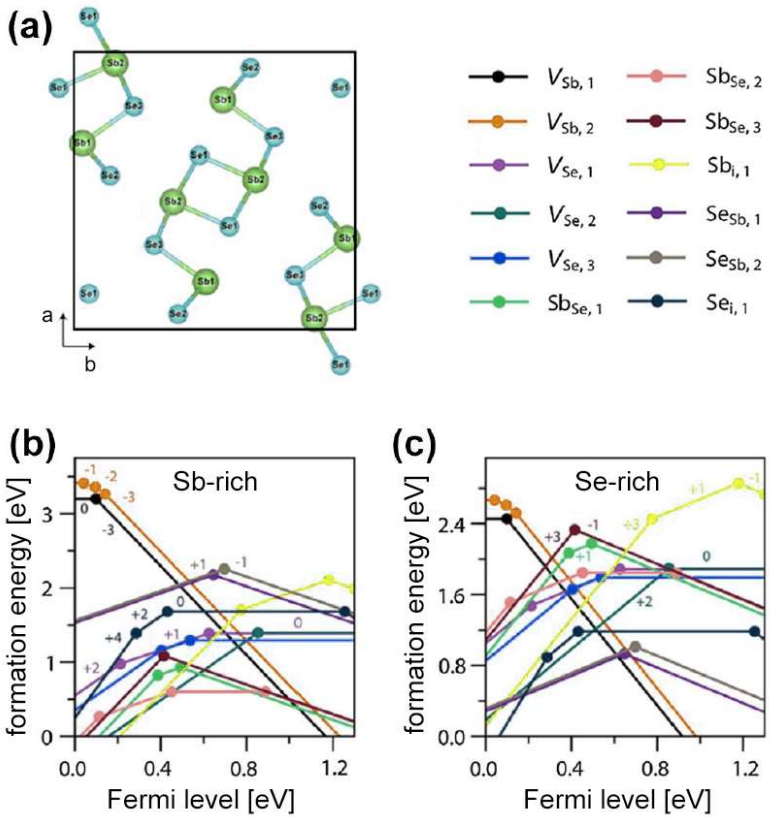

Figure 4.7 - Crystal structure of Sb_2Se_3 showing the positions of the atoms in the nonequivalent single site(a). Calculated formation energy for intrinsic defects as a function of Fermi energy above the conduction band maximumfor a stoichiometric composition rich in Sb (b) and rich in Se (c). The legend in the top right corner indicates the colors used for diverse defects. Transition levels are highlighted by dots, and charge state is indicated near the lines [source: Savory et al., 2019].

Doping this material holds promise in addressing the issue of low charge density through the introduction of acceptor dopants without adding intrinsic defects that may also act as traps. Additionally, doping can help to mitigate the impact of "harmful" active defects on cell performance by binding and inhibiting those defects or impurities that act as traps or recombination centers and are difficult to eliminate.

The available data, unfortunately, is yet largely incomplete and not universally applicable. This is primarily due to variations caused by different growth and doping techniques employed, which can produce diverse results, especially for dopants with multiple possible valence states that may occupy distinct positions within the crystal structure. Consequently, it is evident that more extensive and systematic studies are imperative to establish conclusive findings in this regard.

4.1.5 - Solar cell architecture

A solar cell is made of **multiple layers**, each with a specific function. Typically, the semiconductor materials forming the p-n junction sits between two metallic contacts. The layers above the junction, facing the light source, must be highly **transparent** to maximize photon penetration.

The structure of a thin-film solar cell generally is made of the following components (bottom to top):

- **Substrate** - This provides structural strength to the cell, compensating for its intrinsic thinness and brittleness. Typically composed of cost-effective materials such as **glass**, it can also be metallic, plastic, or ceramic. In the case of thin-film cells, a flexible substrate can be used to make flexible solar panels. The substrate material needs to be compatible with the cell manufacturing processes, including resistance to high vacuum, chemical inertness, high temperature tolerance, and a thermal expansion coefficient matching the film. A smooth, defect-free surface is essential to ensure uniform subsequent layer deposition and minimize the occurrence of "shunts."
- **Back-contact** - Its role is to collect the charges generated within the junction from underneath. Typically metallic, it may consist of a stable element/alloy that withstands high temperatures and doesn't react adversely with upper cell layers. In "bifacial" cells, opaque metals are substituted by a transparent conductive layer to facilitate light absorption also from the back side.
- **Absorber layer** - This is where the majority of photon pairs are generated within the junction. Often, in solar-cells like those studied here, the **p-type** “absorber” semiconductor has a lower doping level, compared to the heavily doped n-type semiconductor: this imbalance results in a highly shifted depletion region within the p-type part of the junction. Since it absorbs most of the photons, its band gap needs to be tailored to maximize absorption across the solar spectrum.
- **Emitter** + **Buffer layer** ("Buffer") - This is the counterpart of the junction. As previously mentioned, it's often composed of a heavily doped **n-type** semiconductor and it is typically thinner than the absorber. Its band gap is typically chosen to be transparent or, at most, complementary to the one of the absorber. For this reason, this part of the cell, together with the upper layers, is sometimes called "**window layer**”. Due to potential lattice mismatch issues that can be present in heterojunctions of different materials and can introduce defects adversely affecting cell performance (e.g., traps, recombination centers), a "**buffer**" layer is often introduced between the absorber and the emitter. The buffer layer's role is to mitigate most of these defects.

Typically, it has very low doping, it is very thin, and it is chosen so that its band structure prevents significant potential barriers within the junction.

- **Upper contact** ("**Front-contact**") – It is generally made of a **transparent electrode** ("**TE**") and, eventually, a **metal grid contact**. This contact is employed to complete the electrical circuit within the junction. It's typically made of a **transparent conductive oxide** (known as "**TCO**") to allow solar radiation to penetrate and reach the underlying junction. The thickness and carrier concentration in this material are determined by the balance between keeping the layer thin enough to minimize radiation absorption (transparency in these materials isn't absolute) and ensuring adequate electrical conductivity so that series resistance is not too high. To mitigate the impact on series resistance, a portion of the transparent surface is often allocated for the deposition of a **metallic grid-like contact**, which enhances charge collection. Additionally, an **anti-reflective** layer may be also applied to reduce the proportion of reflected (and hence non-utilizable) light on the cell surface.

In order to reduce the recombination between the two sides of the junction and their respective contacts, sometimes extra layers are added between them. These layers are generally characterized by a strong asymmetry in the transport of charge carriers, so that they favor the transport of electrons only or holes only. The most commonly used are the so called "**hole-transport layers**" ("**HTL**"), usually fitted between the p-type absorber and the back contact.

To pile-up the multiple layers constituting a thin-film photovoltaic cell over the substrate, two opposite deposition approaches exist. More in detail, the layers can be applied in a sequence known as the "**superstrate**" configuration (Figure 4.8a), with the window layer deposited just above the substrate, or conversely in the reverse sequence, called "**substrate**" configuration (Figure 4.8b), where the first layer to be deposited is the back-contact.

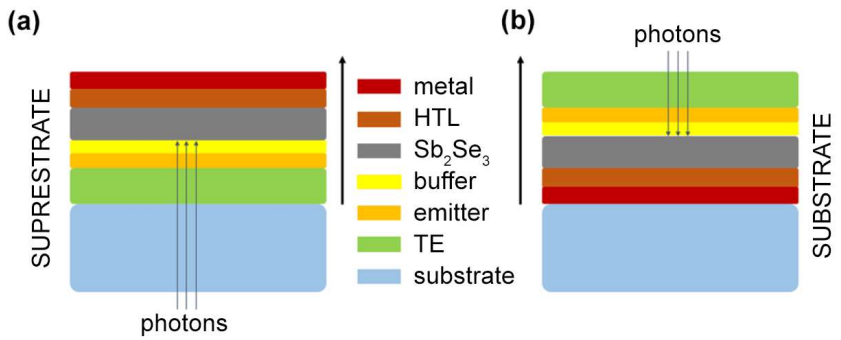

Figure 4.8 - Deposition sequence of cell layers on the substrate (bottom to top): (a) in "superstrate" configuration and (b) in "substrate" configuration. (HTL="hole transport layer"; TE="transparent electrode")

In superstrate configuration, light first crosses the substrate before reaching the absorber layer, so a transparent substrate is mandatory. In contrast, this issue is not present for cells in the substrate configuration. However, several considerations apply to both configurations and may contribute, depending on the specific circumstances, to the choice between the two:

- The layers deposited earlier act as substrates for subsequent layers. This aspect is particularly noteworthy when discussing Sb_2Se_3 because the underlying film can influence and promote a specific orientation of columnar structures.
- The layers that have been previously deposited must also be able to endure the growth conditions of the subsequent layers, including factors like temperature annealings and possible reactions between the layers.
- The use of high-energy deposition methods, such as sputtering and LT-PED, especially when very high acceleration voltages are applied, may potentially cause damage or alter the properties of the underlying layers (etching, implantation, heating, diffusion, etc.).

4.2 - Previous results (as a reference)

4.2.1 – Sb_2Se_3 thin-films deposited by LT-PED

Before the beginning of this PhD Thesis, I worked on the deposition of **Sb_2Se_3 thin-films** using **LT-PED** for my Master Degree Thesis.

Sb_2Se_3 films were deposited in the LT-PED high-vacuum chamber, employing a commercial PEBS-20 Nocera source and a starting vacuum level of approximately $2.0x10^{-4}$ Pa. The pulsed electron beam initiation occurred at a discharge voltage of 16 kV, a value determined as the optimal compromise between growth rate and final film morphology, through a systematic series of exploratory depositions. The pulsed repetition rate was set at 9Hz. To initiate and maintain electron beam propagation, ultra-pure Argon (5.0) was continuously introduced into the chamber during the deposition process, maintaining a pressure of roughly $3.0x10^{-1}$ Pa.

The Sb_2Se_3 deposition target, synthesized at IMEM-CNR from the single elements (Sb and Se, 99.999% purity), was a cylinder approximately 10 mm thick and 1 inch in diameter. The target was intentionally selenium-rich, so that a similar stoichiometry can be transferred to the resulting films. The distance between the target and the substrate within the chamber was set at 8 cm.

The chosen substrates for the deposition were made of a $2.5\times2.5cm^2$-wide soda-lime glass coated with:

- molybdenum (**Mo**)
- fluorine tin oxide (**FTO**)
- cadmium sulfide on FTO (**CdS/FTO**)
- undoped zinc oxide on FTO (**ZnO/FTO**)

so that different options for the realization of substrate or superstrate cells were then available.

Initially, the substrates were placed within a load-lock chamber for pre-vacuum and then they were moved into the primary chamber. Within the primary chamber, they were positioned above a graphite susceptor that was heated using halogen lamps. To monitor substrate temperature, which ranged from 200 °C to 400 °C in different experiments, both a type-K thermocouple and a 2.4 μm IR pyrometer (Fluke Endurance 3 M) were employed. The IR pyrometer was positioned behind a ZnSe-bandpass viewport at a 45° angle to the sample surface.

Sb_2Se_3 film depositions were preliminary tested on bare soda-lime glass so that the optimal LT-PED process parameters and film crystallization could be determined on an amorphous substrate. Before the deposition, the glass substrates underwent a preliminary cleaning procedure with a sequence of ethyl acetone, ethanol and isopropyl alcohol. This cleaning was necessary to eliminate any surface impurities that might have interfered with the film's nucleation process.

The structural characteristics of the obtained films were initially examined via **XRD** utilizing Bragg-Brentano geometry with incident CuKα radiation. In this way it was possible to evaluate their crystalline quality and the potential preferential orientation of grains.

Figure 4.9 resumes the main results for depositions on a bare glass substrate, while Figure 4.10 resumes the main results obtained for the depositions under identical conditions on Mo coated glass.

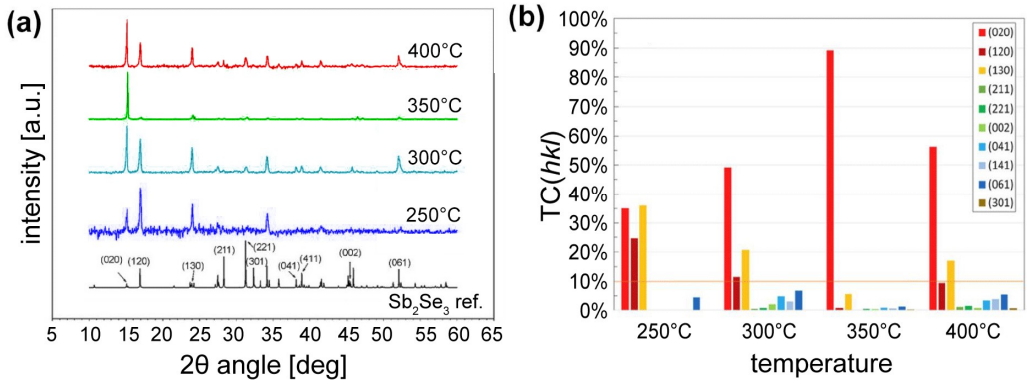

Figure 4.9 - (a) XRD patterns of Sb2Se3 thin-films deposited by LT-PED on glass substrates at increasing temperature; a reference pattern for Sb2Se3 is shown at bottom. (b) TC values for the chosen top ten peaks; the orange line at 10% indicates the threshold of partial preferential orientation.

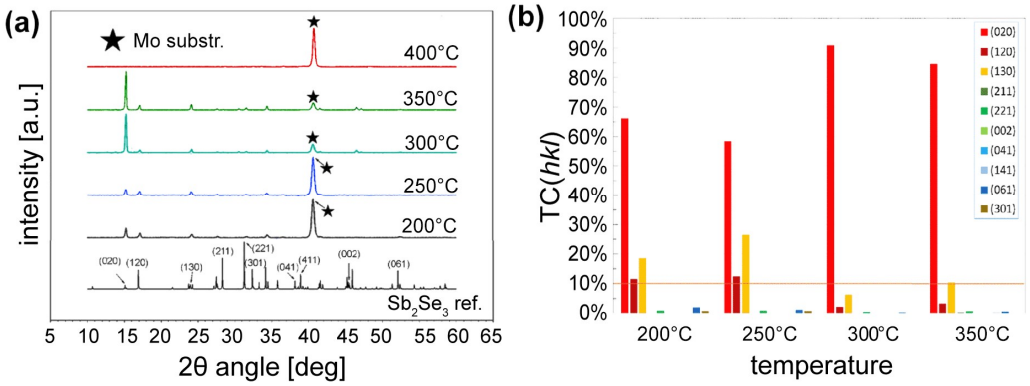

Figure 4.10 - (a) XRD patterns of Sb_2Se_3 thin-films deposited by LT-PED on Mo coated glass substrates at increasing temperature; a reference pattern for Sb_2Se_3 is shown at bottom. (b) TC values for the chosen top ten peaks; the orange line at 10% indicates the threshold of partial preferential orientation; values at 400°C are not shown because there are no Sb_2Se_3 peaks in the spectrum at this temperature

Figure 4.9a illustrates that the crystalline properties of the film are strongly dependent on the deposition temperature. Films deposited below 250°C exhibit minimal to no crystallinity, whereas raising the temperature leads to improved crystallization. Notably, these temperatures are relatively low, thanks to the high energy of the plasma, and, above all, they are compatible with the glass substrate (*i.e.* lower than glass softening temperature). Figure 4.9b confirms a significant increase in some preferential orientation with rising temperature. However, it is worth noting that TCs (texture coefficients) are notably high for orientations associated with the development of columnar structures within the substrate plane.

In the case of Sb_2Se_3 films on a Mo substrate, a discernible crystal structure becomes evident as early as 200°C, as depicted in Figure 4.10a. This early crystalline formation provides an initial and significant clue regarding the substrate's role in the film growth process. However, at 400°C, no Sb_2Se_3 peak is observable in the spectrum, suggesting that at this temperature, the energy input may be excessive, hindering compound formation. Unfortunately, even in this second case, the rising preferential orientation correlated with increasing temperature, is associated with indices (020), as illustrated in Figure 4.10b.

Based on the obtained results obtained, a temperature of **300°C was set as standard** for growing Sb_2Se_3 films on other substrates as well.

Certain materials exhibit a lattice spacing that is somehow comparable to that of antimony selenide, whereas in the literature, it is mentioned that some materials have the capability to induce perpendicular column growth with respect to the substrate. FTO, CdS, and ZnO were selected for the following tests, as illustrated in Figure 4.11.

Figure 4.11a illustrates the successful formation of Sb_2Se_3 films on all substrates. It's worth noting that the patterns for CdS and ZnO exhibit substantial peaks attributed to FTO, as these substrates feature a double layer on glass (CdS/FTO/glass and ZnO/FTO/glass). This double layer was required to eventually build complete photovoltaic cells out of these samples. Figure 4.11b reveals that while reflections (020), (120), and (130), which correspond to in-plane column orientations, are notably predominant on glass and Mo substrates, different preferred orientations *(hkl)* with $l \neq 0$ (indicating tilted or vertical ribbons) appear with high texture coefficient (TC) values for ZnO, CdS, and FTO. A particularly favorable case is observed for **FTO substrate**, which promoted the deposition of a Sb_2Se_3 film at 300°C featuring some “beneficial” ribbons orientations.

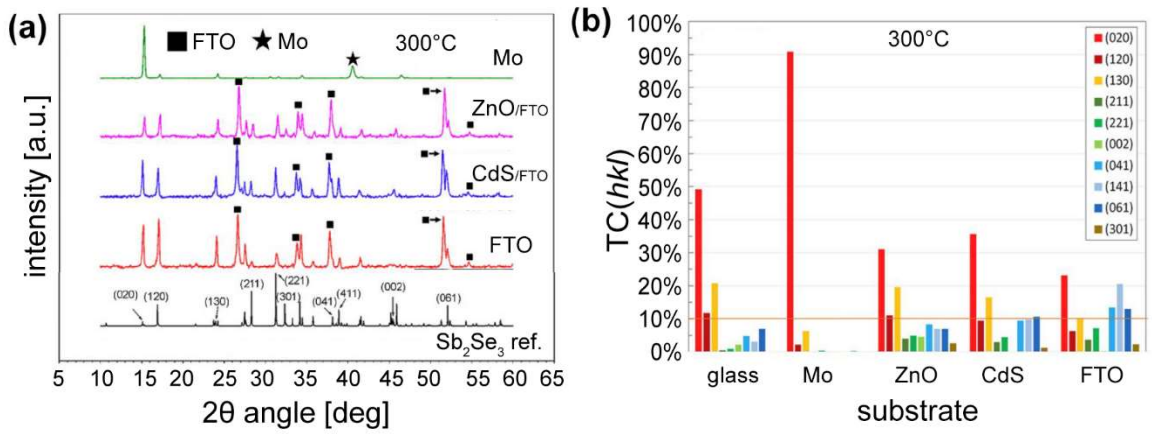

Figure 4.11 - (a) XRD patterns of Sb_2Se_3 thin-films deposited by LT-PED on different substrates (glass, Mo/glass, FTO/glass, CdS/FTO/glass, ZnO/FTO/glass) at 300°C; a reference pattern for Sb_2Se_3 is shown at bottom. (b) TC values for the chosen top ten peaks; the orange line at 10% indicates the threshold of partial preferential orientation.

These measurements showed two important insights. Firstly, they highlight how grain preferential orientation with ribbons parallel to the substrate plane often dominate over orientations more favorable for charge transport. This observation sheds light on a significant factor that has limited the efficiency of cells utilizing this material for decades. Secondly, they demonstrate that even with the high energy low-temperature pulsed electron deposition (LT-PED) technique, **the substrate plays a substantial role in determining the preferential orientation of the grains**.

An overview of TC and RCT values for Sb_2Se_3 films grown at 300°C on different substrates, is reported in Table 4.2 for the ten chosen reflections, as well as the summations ΣTC for the "good" orientations (*hkl* with $l \neq 0$) and the "bad" orientations (*hkl* with $l=0$).

Table 4.2 - Summary of TC and RCT values for ten chosen reflections, calculated from the patterns of Sb2Se3 films deposited at 300°C on different substrates; the right columns also show the sum of TCs of reflections with index (hkl) with l=0, the sum of TCs of reflections with with index (hkl) with l≠0, and the sum of all RCTs.

substrate		*020*	*120*	*130*	*211*	*221*	*022*	*041*	*141*	*061*	*301*	$\Sigma TC_{(l=0)}$	$\Sigma TC_{(l\neq0)}$	*ΣRCT*
FTO	TC	**23.2**	6.3	**10.3**	3.6	7.2	0.2	**13.4**	**20.5**	**13.0**	2.3	39.8	60.2	
	RCT	0	0	0	2.9	5.2	0.2	8.0	11.9	5.7	1.6			**35.5**
ZnO	TC	**31.0**	**11.1**	**19.6**	4.0	4.9	4.6	8.3	6.9	7.0	2.6	61.7	38.3	
	RCT	0	0	0	3.2	3.5	4.6	5.0	4.0	3.1	1.8			**25.1**
CdS	TC	**35.6**	9.5	**16.5**	2.9	4.4	0	9.5	9.8	**10.6**	1.2	61.6	38.4	
	RCT	0	0	0	2.3	3.1	0	5.7	5.7	4.7	0.8			**22.3**
glass	TC	**49.2**	**11.7**	**20.7**	0.5	0.9	2.2	4.8	3.1	6.9	0	81.6	18.4	
	RCT	0	0	0	0.4	0.6	2.2	2.9	1.8	3.0	0			**10.9**
Mo	TC	**90.8**	2.2	6.3	0.1	0.3	0	0	0	0.2	0	99.4	0.6	
	RCT	0	0	0	1.5	1.2	0	0.8	0	0.6	0			**4.1**

The orientation of the ribbons in a solar cell has a significant impact on the transport characteristics of the Sb_2Se_3 absorber and, hence, on the electrical performance of the device. To understand the scale of this phenomenon and the effect of carrier transport on the J-V (current-voltage) performance of the solar device, electrical simulations were conducted.

These simulations employed the wxAMPS-1D tool and replicated the architecture employed in CIGS-based cells (AZO/ZnO/CdS/CIGS/Mo), replacing the absorber layer with Sb_2Se_3. The physical parameters and carrier concentrations for all layers were obtained from existing literature sources.

A 4 nm thick defect layer was introduced at the interface between the Sb_2Se_3 absorber and the Mo back contact to represent device interface properties. Details of all material parameters are provided in Table 4.3. The hole mobility of Sb_2Se_3 films was varied, ranging from 45 $cm^2\ V^{-1}s^{-1}$ (the highest reported mobility value in literature) to 0.69 $cm^2\ V^{-1}s^{-1}$ (the mobility value measured along the (020) direction). The simulations were performed for a temperature of 300 K and an AM 1.5G solar spectrum illumination, with an incident power density of 100 mW/cm^2.

Table 4.3 - Input parameters of solar cell layers for the numerical simulation. The surface recombination speed of electrons and holes is fixed at 1×10^7 cm/s for both front and back contact. The reflection coefficient on front and back surfaces is 0 and 0.9, respectively (Source: A.C. Busacca et al, 2014; Y. Cao et al, 2019)

Parameters and units	***ZnO:Al***	***ZnO***	***CdS***	***Sb_2Se_3***	***Sb_2Se_3 interface***
Relative permittivity	9	9	10	18	18
Band gap (eV)	3.3	3.3	2.4	1.19	1.19
Electron affinity (eV)	4.4	4.4	4.2	4.04	4.04
Thickness (nm)	800	100	70	1500	4
Effective density of states of conduction band (cm^{-3})	$2.2x10^{18}$	$5x10^{19}$	$2.2x10^{18}$	$2.2x10^{18}$	$2.2x10^{18}$
Effective density of states of valence band (cm^{-3})	$1.8x10^{19}$	$1x10^{20}$	$1.8x10^{19}$	$1.8x10^{19}$	$1.8x10^{19}$
Mobility of electrons ($cm^2V^{-1}s^{-1}$)	10	130	100	15	15
Mobility of holes ($cm^2V^{-1}s^{-1}$)	2.5	30	25	0.69-45	0.69-45
Acceptor concentration (cm^{-3})	0	0	0	$1x10^{13}$	$1x10^{13}$
Donor concentration (cm^{-3})	$1x10^{18}$	$1x10^{7}$	$1x10^{18}$	0	0
Gaussian Defects Donor and Acceptor State Density (cm^{-3})	0 $1x10^{17}$	0 $5x10^{14}$	$1x10^{18}$ $1x10^{18}$	$1x10^{16}$ $1x10^{16}$	$1x10^{19}$ $1x10^{19}$
Capture Cross Section of Donor-like Gaussian State for Electron and Holes (cm^2)	0 0	0 0	$1x10^{-12}$ $1x10^{-16}$	$1x10^{-18}$ $1x10^{-17}$	$1x10^{-18}$ $1x10^{-17}$
Capture Cross Section of Acceptor-like Gaussian State for Electron and Holes (cm^2)	$1x10^{-12}$ $1x10^{-12}$	$2x10^{-10}$ $2x10^{-10}$	$1x10^{-16}$ $1x10^{-12}$	$1x10^{-17}$ $1x10^{-18}$	$1x10^{-17}$ $1x10^{-18}$

The results of this simulation, as depicted in Figure 4.12a, reveal that reducing the hole mobility of Sb_2Se_3 primarily impacts the short-circuit current density, J_{sc}, causing it to decrease from 20.5 to 0.5 mA/cm^2. However, Voc is also affected, dropping from 489 mV to 250 mV in the case where transport is mainly governed by the hopping phenomenon.

Despite a different cell structure was simulated also by R.A. Lomas-Zapata et al. (Figure 4.12b-e), similar trends in the results were obtained.

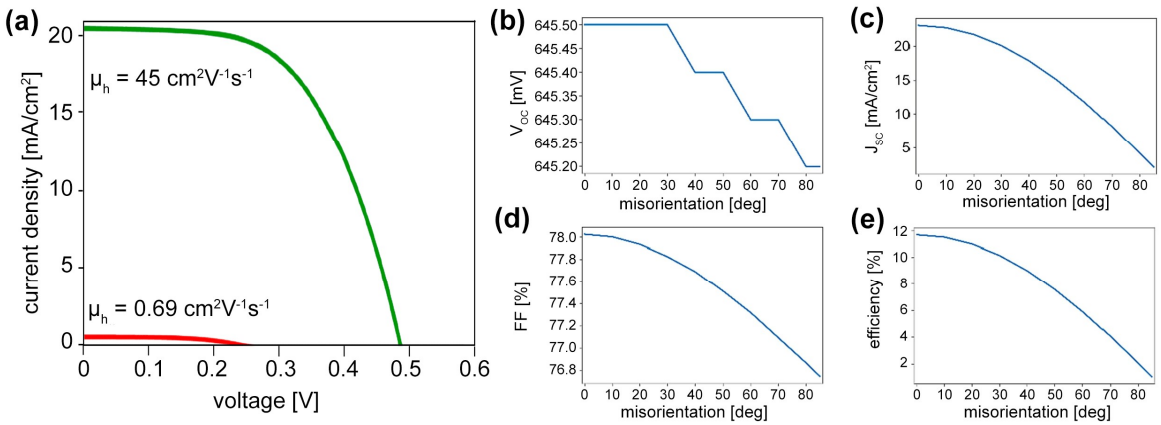

Figure 4.12 – (a) Simulated J-V curve of AZO/ZnO/CdS/Sb_2Se_3/Mo solar cells, assuming a hole mobility of 45 cm^2 V^{-1}s^{-1} (perpendicular ribbons orientation - green line) and of 0.69 cm^2 V^{-1}s^{-1} (parallel ribbons orientation - red line). (b-e) V_{OC}, J_{SC}, FF and efficiency values simulated by R.A. Lomas-Zapata et al. as a function of the degree of misorientation respect to substrate normal.

The simulated structure was then reproduced in laboratory by depositing 60 nm of CdS as a buffer layer on an Sb_2Se_3/Mo sample. CdS was chemically deposited via a chemical bath deposition (CBD) technique, which is widely used for CIGS-based cells. The bi-layer window layer was created with 120 nm of ZnO and 500 nm of AZO, deposited by RF-Sputtering. Through mechanical scribing, 16 cells were obtained, each with an area of 0.15 cm^2. The contacts were made of Ag paste, both on the front-contact and back-contact.

The characteristic J-V curve for these cells is shown in Figure 4.13. All AZO/ZnO/CdS/Sb_2Se_3/Mo/glass cells measured showed similar behavior to that simulated for low mobility values, with an extremely low J_{sc} of only 0.3 mA/cm^2. This result is in agreement with the fact that the Sb_2Se_3/Mo sample had a preferential crystallographic orientation with ribbons parallel to the substrate.

To further confirm the correlation between orientation of ribbons and performance of the photovoltaic cell, a second photovoltaic cell was made with Sb_2Se_3 films deposited on FTO, characterized by the highest RCT value (Table 4.2). In this case, for the best values measured were 20.28 mA/cm^2 for J_{sc}, 256 mV for V_{oc} and an FF of 39.2% (Figure 4.13). These values correspond to a conversion efficiency of 2.1%. The obtained J_{sc} is very similar

to the one calculated in the simulation for high mobility conditions (green line in Figure 4.12). The fact that XRD measurements of Sb_2Se_3/FTO samples showed a significant grain orientation with ribbons aligned out of the substrate plane, confirms the previously seen correlation between **RCT values and cell performance increase**.

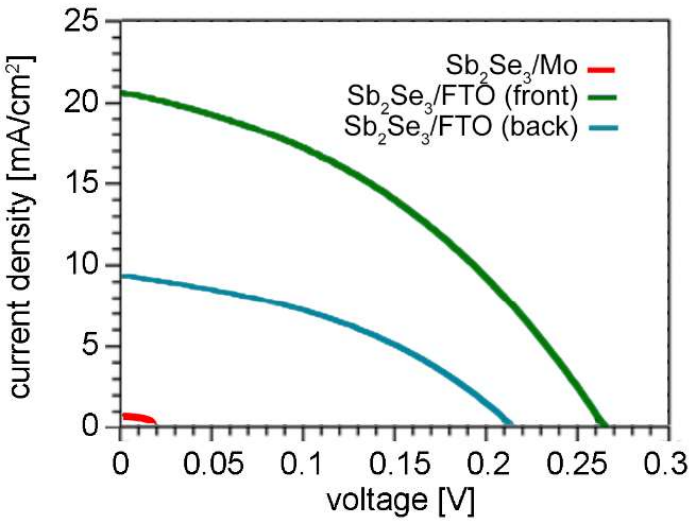

Figure 4.13- J-V characteristics of a AZO/ZnO/CdS/Sb_2Se_3/Mo/glass solar cell and of a AZO/ZnO/CdS/Sb_2Se_3/FTO/glass solar cell; the latter was measured both from front side and from back side, being a bifacial solar cell.

Unfortunately, the measured efficiency of the AZO/ZnO/CdS/Sb_2Se_3/FTO/glass cell is rather low and far from the maximum theoretical value. Efficiency is indeed here strongly affected by particularly low FF and V_{oc} values, probably due to the contact between Sb_2Se_3 and FTO, which is far from being perfectly ohmic.

4.2.2 – Preliminary results on Sb_2Se_3 thin-films deposition by RF-MS

During my Master Degree research, also a very preliminary study on the deposition of Sb_2Se_3 thin-film by **RF- Magnetron Sputtering** (RF-**MS**) technique was done. More in detail, the initial calibration of process parameters was set for this material.

As for the samples deposited by LT-PED, at this stage of the experimental activity the deposition process and the adjustment of growth parameters were exclusively carried out on bare soda-lime glass substrates. This approach was once again adopted to eliminate the additional variables that a potentially "templating" crystalline substrate may have.

Sb_2Se_3 films were deposited using a 3'' RF-MS cathode (Kenosistec) powered at 30 W, starting from a binary Sb_2Se_3 target (99.99% purity, supplied by Testbourne Ltd). The films

were deposited directly onto 2.5 × 2.5 cm^2 wide bare soda-lime glass, previously cleaned with the same procedure described for LT-PED.

A commercial target with a purity of 5N (99.999%) was utilized for the deposition process. The vacuum chamber was evacuated with a turbomolecular pump. The operational pressure was maintained by introducing Argon (Ar) into the chamber in a range between 10^{-3} and 10^{-1} mbar. This range is the ideal one for initiating plasma, since a lower pressure leads to failed plasma ignition, while a higher pressure results in an inadequate plasma control, often causing secondary plasma ignition.

A special sample holder was employed for the substrate sample, that thanks to the connection with a translational feedthrough, can be moved from the load-lock chamber, where a pre-vacuum of 10^{-4} mbar was made, to the main chamber, where high vacuum was kept before the deposition process begins. When the interconnection valve between the chambers was open, the pressure differential was equalized in a few seconds due to the substantial volume difference between them. The end position of the sample was set just 1 mm away from the graphite heater and 8 cm away from the RF-MS cathode. The deposition temperature was varied between room temperature (RT) and 330°C, and it was monitored using a thermocouple positioned on the surface of the graphite heater. Under standard conditions, approximately 20 minutes were necessary to ensure the complete and homogeneous heating of the substrate, as well as surface desorption of gaseous species, before the deposition process. Since it was not possible to place the thermocouple directly in contact with the substrate, a more precise temperature monitoring was made with a thermal imaging camera, which measures the temperature through a ZnSe window that is transparent in the far-infrared spectrum.

Once the desired substrate temperature was reached, the power and the pressure were progressively increased and decreased for the plasma ignition and stabilization up to the final operating values, through a series of preliminary steps. Finally 30W and $5x10^{-3}$ mbar were maintained for 5 minutes and then the shutter in front of the target plasma was open, initiating the deposition process.

The duration of Sb_2Se_3 film deposition varied depending on the desired thickness: about 25 minutes for 350-500 nm thin films, 100 minutes for thicker 1.5-2 μm films. At the end of the deposition process, the shutter was closed, and the sample was left on the heater at the same temperature of deposition for 25 minutes.

The crystallinity of the film was also in this case studied by **XRD** measurements in Bragg-Brentano configuration, following the same procedure used for the samples grown by LT-PED. The main focus was the correlation between the growth conditions and the properties of the deposited Sb_2Se_3 film, to study which were the optimal ones to obtain a

crystalline film, possibly oriented in the right direction. Figure 4.14 and Figure 4.15 show respectively the XRD patterns and TCs values as a function of the different temperatures used for the glass substrate.

From these XRD data, it was evident to see that at a low 50 °C temperature the sample lacked the necessary energy for crystallization, while in a temperature ranges between 90°C and 190°C the XRD patterns reveal a preferential orientation mainly associated those reflections for which ribbons lay parallel to the substrate plane: (020), (120), (130), and (240), all with an *hkl* index where *l*=0.

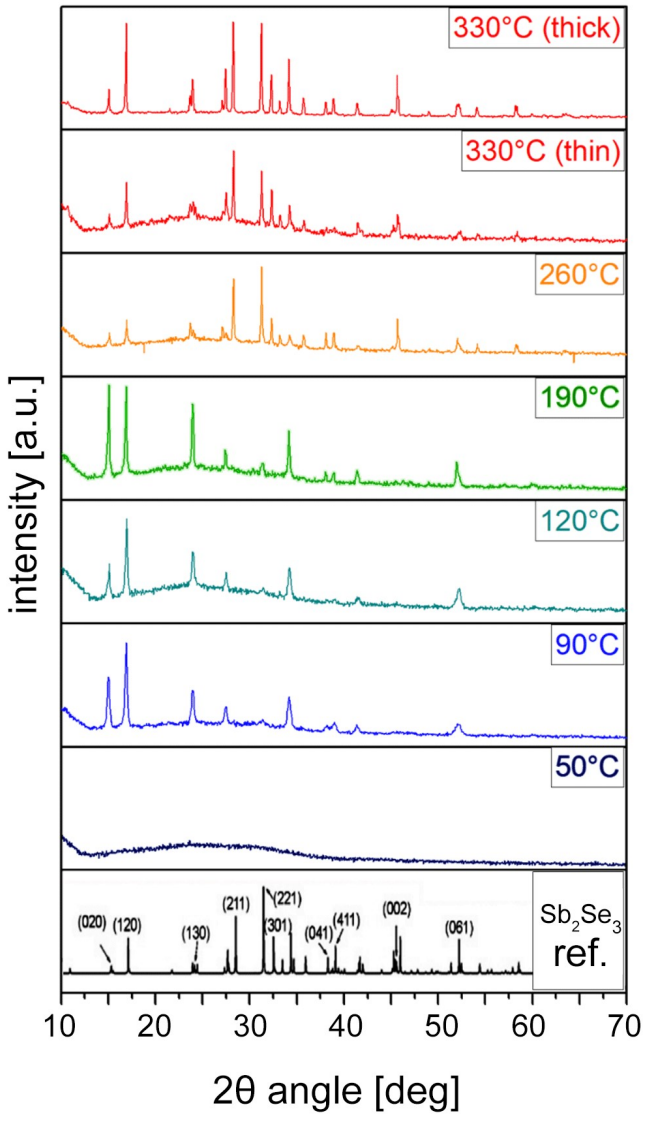

Figure 4.14 - XRD patterns of Sb_2Se_3 films deposited on glass by RF-MS, as a function of substrate temperature. Two different films are shown for deposition at 330°C: one thinner ("thin"-300 nm) and one thicker ("thick" 1 μm). A reference spectrum for Sb_2Se_3 is shown at bottom.

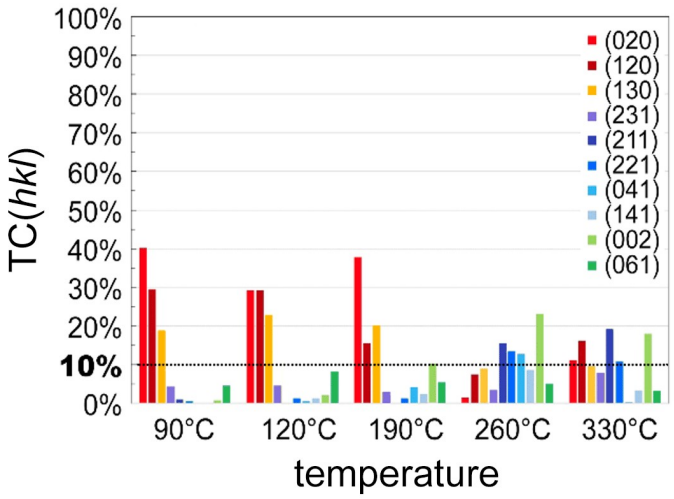

Figure 4.15 - TC values for the chosen set of ten hkl reflections of Sb_2Se_3 films deposited on glass by RF-MS, as a function of substrate temperature.

Above 260°C, however, the intensities of reflections with $l \neq 0$ start to rise, surpassing the critical TC value of 10%. Above all, the samples deposited at 330°C exhibit the most favorable orientation for photovoltaic applications.

For depositions carried out at 330°C, we considered two distinct Sb_2Se_3 films, with different deposition times: one designated as "thin", with a thickness of 300 nm, and another one designated as "thick", with a thickness of about 1µm. The thicker sample displayed **significantly higher intensity for the (002) reflection**, which corresponds to crystal grains with "good" vertical ribbons on the substrate. This intensity notably surpassed that of (120) and (020) reflections.

Figure 4.16 provides a comparative analysis of the spectra between a Sb_2Se_3 film deposited on glass by LT-PED technique and a film deposited by RF-MS at the same temperature (330°C). This comparison clearly shows that the film deposited via LT-PED exhibits a distinct preferential (020) orientation, while the film deposited by RF-MS shows a significant increase for the intensities of most of the peaks with $l \neq 0$ and, in particular, of the (002) peak.

This means that **RF-MS provided better conditions for the crystallization of films with "good orientation"** even on an amorphous glass substrate, that clearly cannot provide any boost of this result by lattice matching. This positive result is hence only related to the deposition technique.

An additional observation is presented in Figure 4.17. This plot show a comparison between the XRD pattern of the sample deposited at room temperature (RT), recorded immediately after the growth process, and the one recorded after a 25-minute thermal

annealing process at 200°C in vacuum. It is evident that thermal annealing, in this case, does facilitate the induction of crystallization in the initially amorphous film. However, it is regrettable that once again, this process promotes the formation of grains with "bad" ribbons orientations.

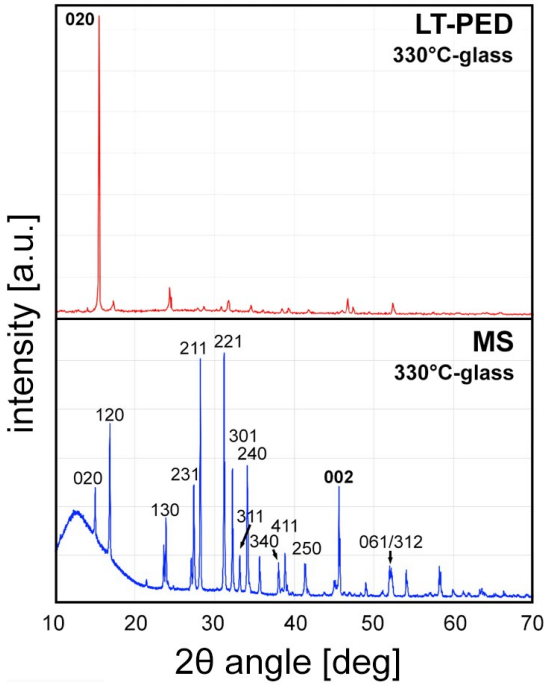

Figure 4.16 - XRD patterns of Sb_2Se_3 films deposited on glass substrates by LT-PED (top) and RF-MS (bottom) at the same temperature (330°C).

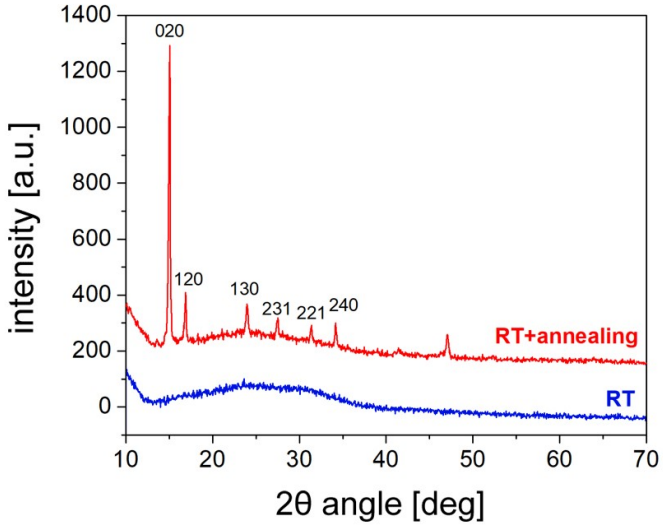

Figure 4.17 - XRD patterns of Sb_2Se_3 films deposited on glass substrate by MS at room temperature, immediately after the deposition process (RT) and following a 25-min thermal annealing at 200°C (RT+annealing).

All samples were also characterized by **micro-Raman** spectroscopy. In all samples, the primary phase of Sb_2Se_3 was consistently identified through the main peak at approximately **190 cm^{-1}**, with no significant variations noted.

The focus of the Raman characterization, instead, soon shifted towards examining a noteworthy secondary aspect: the presence and origin of the **250 cm^{-1}** peak, which was present only in some of the deposited samples and with different intensities, despite no difference could be observed in the corresponding XRD patterns. The origin of this specific peak unfortunately received discording interpretations in the literature, ranging from an unidentified Sb_2Se_3 feature to the potential presence of amorphous Se or even Sb_2O_3.

An initial hypothesis emerged when it was observed that Sb_2Se_3 film samples, left exposed to air for extended periods, exhibited higher intensity in the 250 cm^{-1} peak (as illustrated in Figure 4.18).

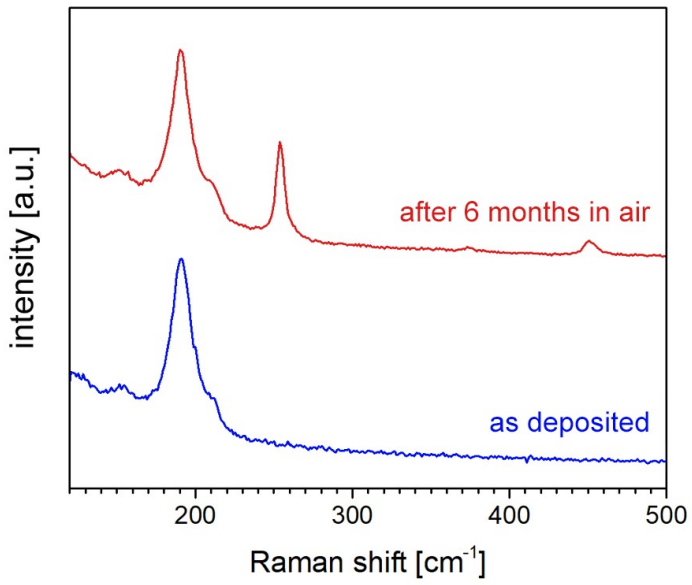

Figure 4.18 - Raman spectra of a freshly deposited Sb_2Se_3 sample (blue) and a sample exposed to air for 6 months (red).

This initial conjecture suggested a potential association with oxidation. To test this hypothesis, certain samples displaying this 250 cm^{-1} peak were subjected to chemical etching using a 3 mM ammonium sulfate solution in water. This etching method was chosen due to its reported effectiveness in removing Sb_2O_3 while being relatively gentle on Sb_2Se_3. As depicted in Figure 4.19, following the etching process, the sample no longer exhibited the 250 cm^{-1} peak. This result provided a strong initial indication that the peak could indeed be attributed to the presence of oxide.

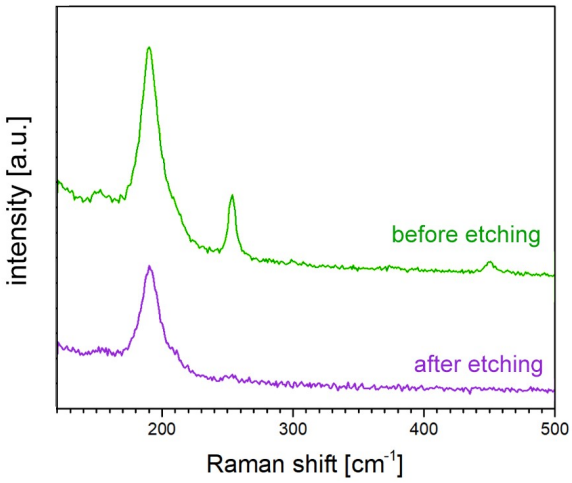

Figure 4.19 - Raman spectra of the same sample with Sb_2Se_3 film characterized by the presence of the peak at 250 cm^{-1}, before (green) and after (violet) the chemical etching process.

This outcome prompted an exploration of whether the Raman spectroscopy laser itself could potentially induce oxidation through heating. To investigate this possibility, various filters were employed to diminish the incident beam's power, and consecutive measurements were conducted on the identical location to assess the spectrum's changes over time and increasing laser power. The results of one of these experiments are reported in Figure 4.20, where three spectra, acquired on the same sample location with increasing laser intensity, just after an etching treatment to ensure the removal of any surface oxide traces, are compared.

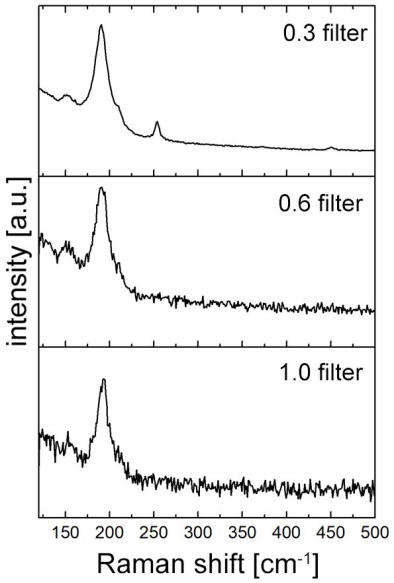

Figure 4.20 - Raman spectra measured at the same spot on a Sb_2Se_3 film, after etching treatment to remove the oxide, with progressively higher laser powers (filters with progressively lower optical density: 1.0, 0.6, 0.3).

When the two filters with the higher optical density (1 and 0.6) were used, no peak was observed at 250 cm^{-1}, although the spectra exhibited a higher noise-to-signal ratio due to reduced incident power. Repeated measurements with the same filter produced consistent results. However, when the filter with 0.3 optical density was used, the recorded spectrum featured a distinct peak at 250 cm^{-1}, accompanied by a lower-intensity peak at 450 cm^{-1}. Both peaks are documented in the literature as significant indicators of **Sb_2O_3**. In particular, the consistent appearance of the 450 cm^{-1} peak discards the alternative hypothesis of amorphous Se formation. Consecutive measurements at the same power and location revealed that the 250 cm^{-1} peak tends rapidly increase up to saturation. Further intensity increase in this peak could be observed only when the filter was completely removed, allowing the laser source to exert its full power on the surface. Hence also a maximum oxide layer thickness seems to be related to the incident laser power.

These measurements underscore the critical importance of caution and of limiting laser power when analyzing Sb_2Se_3 films.

One last additional observation emerged while examining different points on the same sample: while 1.0 and 0.6 filters never induced the presence of the 250 cm^{-1} peak and the absence of a filter always induced it, when the intermediate 0.3 filter was used, the appearance of this peak was not always replicable, and intensities varied significantly from point to point (see Figure 4.21). This observation implies that the laser's energy output with the 0.3 filter closely approaches a threshold value, inducing oxide formation only under specific concurrent conditions.

In the context of polycrystalline samples, where individual grains may possess different orientations, this variation from point to point may be associated with the different crystalline faces exposed to the air. Given the highly anisotropic nature of Sb_2Se_3 structure, grains with distinct orientations are expected to exhibit differing properties:

- Heat conduction occurs more efficiently along the [001] direction of the columnar ribbon structures, potentially leading to different heating responses to the laser, *i.e.* grains with ribbons parallel to the substrate surface may experience preferential heat dissipation.
- Surfaces inclined with respect to ribbon structures feature a gradually increasing density of dangling bonds, reaching a maximum on the (00*l*) faces: this density is directly proportional to surface energy, potentially lowering the energy threshold required for oxygen bond formation.

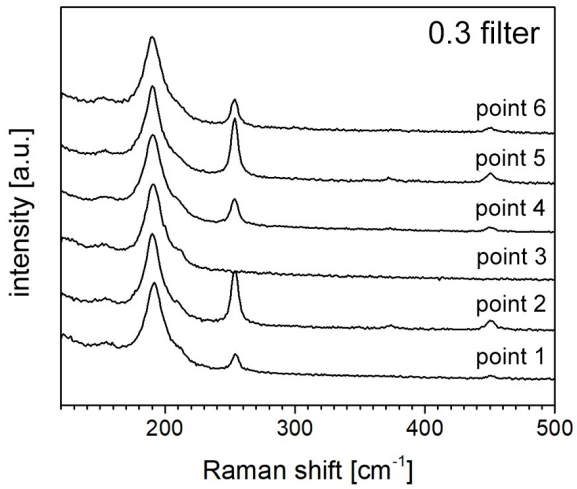

Figure 4.21 - Raman spectra measured at different points of a Sb_2Se_3 film after etching treatment to remove the oxide, using the 0.3 filter.

One or both of these conditions may explain why the 0.3-filtered laser appears to unluckily induce oxidation more prominently in grains with a more favorable orientation for photovoltaic applications. Furthermore, this hypothesis is in agreement with the observation that 250 cm^{-1} Raman peak was more frequently observed in samples with the highest solar cell performance.

4.3 - Sb_2Se_3 thin-films deposited by RF-MS

The first activity during my PhD research focused on the study of the nucleation and seeding effects that various substrates might exert on the orientation of the Sb_2Se_3 films deposited by RF-MS. These chosen substrates, like in the previous case of films deposited by LT-PED, are commonly used in the layered structure of thin-film solar cells and include:

- molybdenum (**Mo**)
- fluorine doped SnO_2 (**FTO**)
- cadmium sulfide on FTO (**CdS/FTO**)
- undoped zinc oxide (**ZnO**)

Despite Sb_2Se_3 films depositions were obtained at different temperatures on each of these substrates, **XRD** analysis determined that those carried out at 300°C consistently yielded superior crystallinity and optimal orientation across all substrates (Figure 4.22).

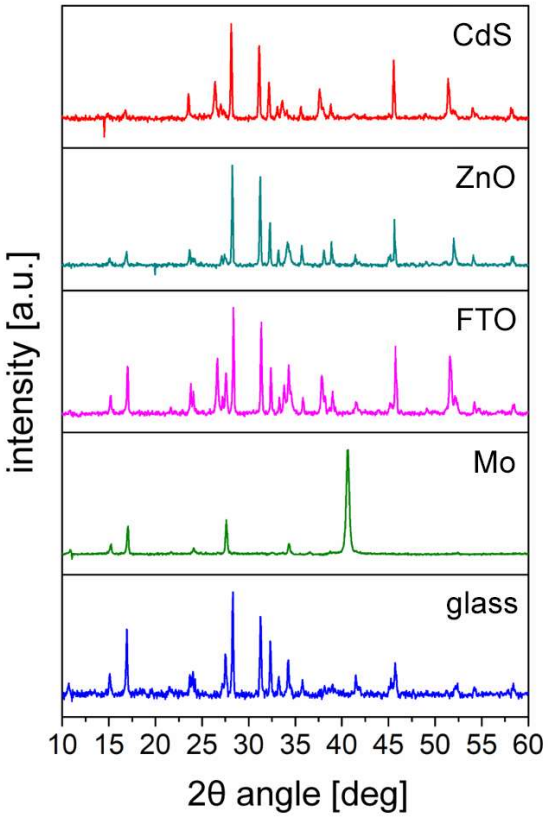

Figure 4.22 - XRD patterns of Sb_2Se_3 films deposited on different substrate at 300°C

In summary, Figure 4.23a presents ΣTC(l≠0) and RCT values for Sb_2Se_3 film deposition conducted at 300°C on various substrates. A sample was also deposited on plain soda-lime

glass at the same temperature, although it is not directly suitable for solar cell construction, serving as a reference for comparison with the other results.

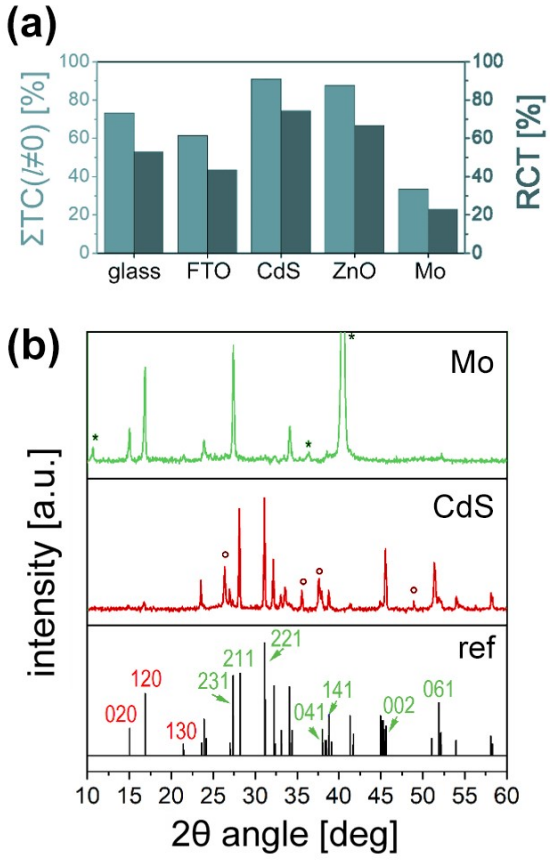

Figure 4.23 - (a) ΣTC(l≠0) and RCT values for the Sb_2Se_3 films deposited at 300°C on different substrates; (b) XRD patterns of Sb_2Se_3 films deposited on Mo and CdS/FTO substrates (JPCDS 15-0681 reference for Sb_2Se_3 is reported at the bottom).

The most favorable outcomes were achieved on **CdS/FTO** substrates (Figure 4.23b), where ΣTC(l≠0) reached 91%, and RCT stood at 74.4%. Even on ZnO substrates, the Sb_2Se_3 ribbon alignment displayed a significant vertical component (ΣTC(l≠0)>80%), surpassing the surprisingly high alignment observed on glass substrates. Conversely, in films deposited on Mo, the ribbon orientation predominantly exhibited a horizontal alignment (ΣTC(l≠0)<35%), as previously observed also in films deposited by LT-PED. This observation reinforces the assumption that the "bad" orientation on Mo substrates is strongly influenced by Mo itself.

The notably high RCT values on CdS (74%) and ZnO (67%) strongly suggests that optimal carrier transport may be achieved by constructing Sb_2Se_3 solar cells in a "superstrate" configuration, where Sb_2Se_3 is directly grown on the window layer.

An overall comparison with the LT-PED technique, where the highest achieved ΣTC(l≠0) value on an FTO substrate was just slightly above 60%, MS proved to be a more effective method for achieving the desired ribbon orientation. This outcome might be attributed to the lower deposition rate of adatoms in RF sputtering (approximately 2.5 $Å s^{-1}$) that promotes the formation of thermodynamically favorable cohesive covalent bonds, predominantly aligning over the (002) surfaces.

Pole figures were also constructed for specific reflections, namely the (200), (020), and (002), to go more in-depth with the study of preferential orientation (Figure 4.24). Data were collected in the 0°–75° χ range. All pole figures exhibited cylindrical symmetry, indicating orientation perpendicular to the substrate but a random distribution of crystallites within the plane. This aligns with the expected behavior for growth processes involving polycrystalline substrates.

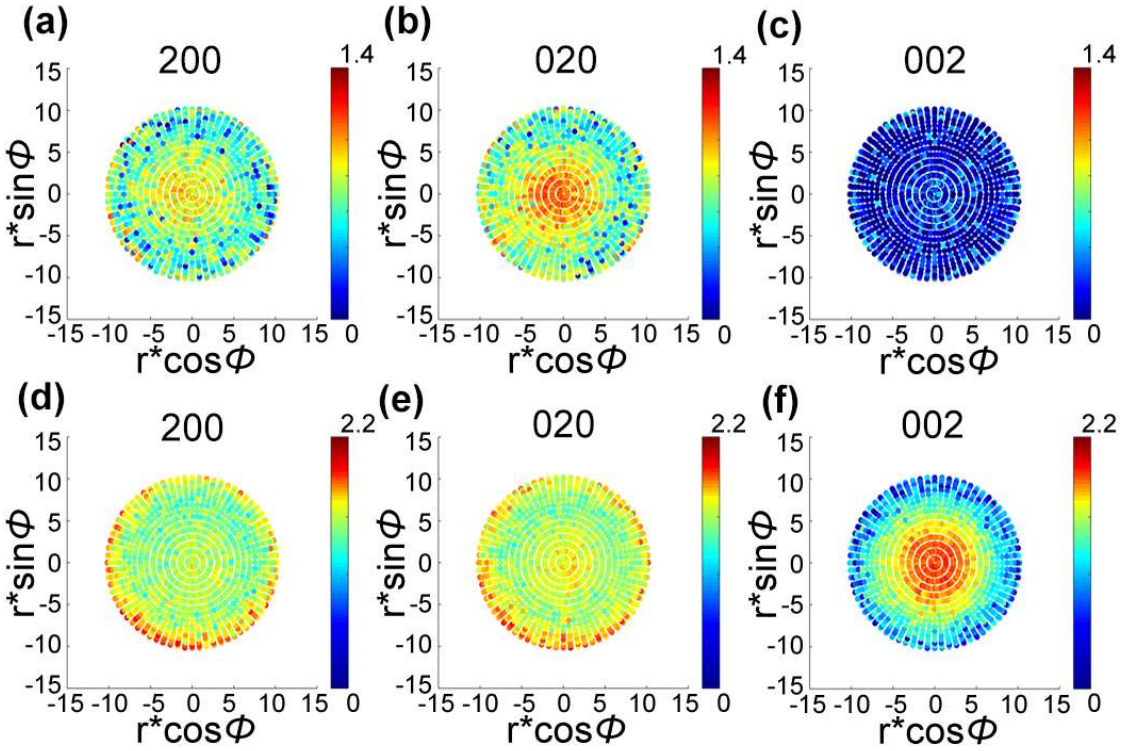

Figure 4.24 - Pole figures of the (200), (020) and (002) reflection of Sb_2Se_3/Mo (top—(a)–(c)) and Sb_2Se_3/CdS/FTO films (bottom—(d)–(f)). Intensities are on a logarithmic scale.

The data analysis corroborates the findings previously suggested by the texture coefficient. Notably, when comparing the Sb_2Se_3/Mo and Sb_2Se_3/CdS samples, significant differences emerge. The former exhibits a slight preferential orientation along the [100] and

[010] directions, which seem to align more frequently with the substrate normal. Consequently, the [001] direction is anticipated to be at χ=90°, but due to the low intensity of this reflection, it registers little to no signal. Conversely, a close examination of Figure 4.24c clearly reveals that the number of crystals with the [001] direction normal to the substrate is very limited, particularly when compared with the Sb_2Se_3/CdS sample. This observation is reinforced by a prominent pole in the (002) polar map shown in Figure 4.24f, affirming the significant influence of the choice of substrate on the growth process.

EDS microanalysis revealed **excellent composition uniformity** in the samples. All the analyzed films exhibited a consistent 2:3 stoichiometry for the Sb:Se ratio, with a slight average excess of Se: 39.6% Sb and 60.4% Se. Notably, this Se excess was observed even without employing a selenization treatment or a Se-rich target. These measurements indicate that the low substrate temperatures (<350°C) and low sputtering power effectively prevented Se losses or significant deviations in stoichiometry across all samples, regardless of the substrate type. Moreover, as often reported for MS depositions, a transport from the target that is slightly deviated towards the more volatile element is observed and here "desirable" for the p-type conductivity.

SEM characterization was conducted to gain insights into the film morphology. SEM images of the obtained Sb_2Se_3 film surfaces deposited at different temperatures (on glass) are reported in Figure 4.25. The surface morphology undergoes significant changes, transitioning from a smooth surface at lower temperatures, typical of nearly amorphous films, to rougher surfaces at higher temperatures, with more distinct grain shapes.

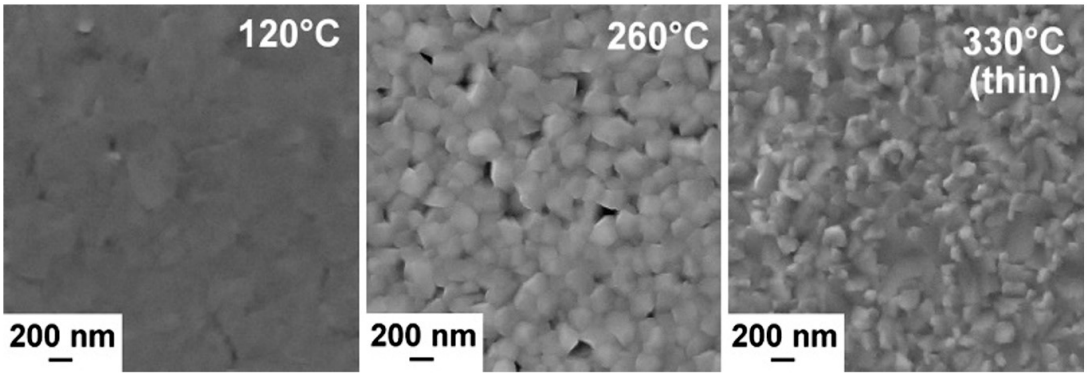

Figure 4.25 - SEM images of the surface of Sb_2Se_3 films deposited at different temperatures on glass substrate

The comparison between two samples grown at the same temperature (330°C) but with different thicknesses (500 nm and 1000 nm) is also interesting. While the surface of the thinner sample is depicted in the last (right) image of Figure 4.25, the thicker sample

exhibits an unexpected morphology (Figure 4.26a), where evident elongated "rod-like" crystals began to grow off the surface.

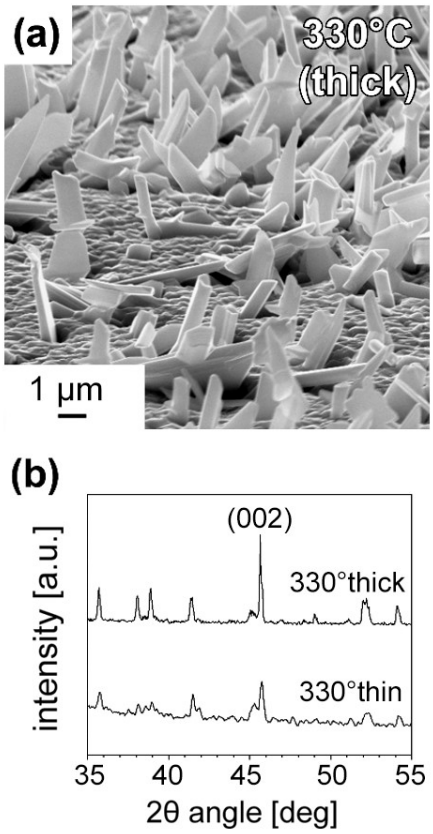

Figure 4.26 - (a) SEM image of the surface of Sb_2Se_3 "thick" film deposited at 330°C on glass substrate (tilted view); (b) focused comparison of XRD patterns for "thin" and "thick" films deposited at 330°C on glass substrate, in the 35°<2θ<55° range.

This observation, supported by the high TC(002) value and lower TC(120) and TC(020) values evident in its XRD pattern (Figure 4.26b), suggests a distinct growth mechanism for RF-sputtered Sb_2Se_3. During the initial layer nucleation, adatoms preferentially attach to the substrate using a layer-by-layer mechanism, forming (*hk*0) crystal surfaces with the lowest free energy (horizontal ribbons), as it happens in LT-PED depositions. But in films deposited by RF-MS, thanks to a lower deposition rate, a transition from layer-by-layer to island growth (isolated crystals) is possible when a certain thickness is reached, *i.e.* when covalent cohesive forces become stronger than surface adhesion forces, resulting in the 3D growth of vertical columnar crystals.

Furthermore, different nucleation behaviors were observed based on the substrate type. Figure 4.27 illustrates that on the CdS/FTO substrate, adatom–adatom interactions appear to be stronger than adatom-substrate interactions, causing 3D growth to start at an earlier

stage, leading to the emergence of small columnar Sb_2Se_3 crystals in thinner films. On the contrary, in thicker films, grain coalescence results in a more homogeneous and continuous film, making it suitable for Sb_2Se_3-based solar cells within the 0.6–1 μm range, offering higher uniformity and reduced shunt probability.

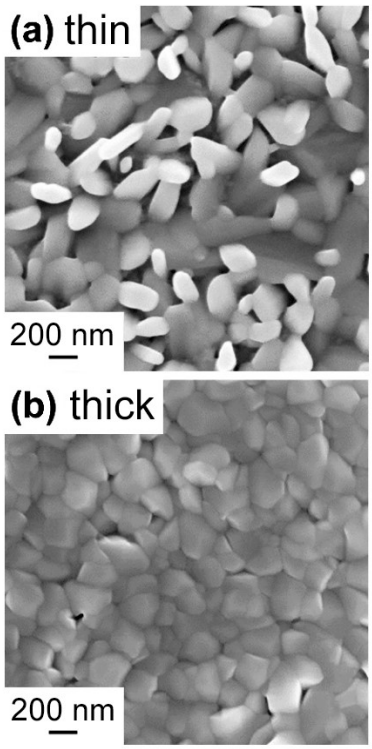

Figure 4.27 - SEM images of the surface of thin (500 nm) and thick (1000 nm) Sb_2Se_3 films deposited at 300°C on CdS/FTO substrate.

The variation in nucleation likely originates from the distinct substrate nature and morphologies. On flat glass, initial layers favor adhesion with the *c*-axis parallel to the surface, so that only weak Van Der Waals bonds face towards the a-periodic substrate lattice. This leads to a layer-by-layer morphology and columnar crystals appear only when cohesive forces outweigh surface adhesive forces. Conversely, on rough and more chemically active substrates, like in the case of the CdS/FTO, covalent 3D island formation initiates directly on the substrate surface, becoming more homogeneous and continuous only with increasing thickness.

The **optical characteristics** of the films were assessed as a function of growth temperature and substrate type. The columnar growth of the film results in a rough surface, leading to significant light scattering from the surface. Consequently, **diffuse reflectance spectra** were gathered to evaluate the optical bandgap of the samples.

Kumar et al. established a proportional relationship between the Sb_2Se_3 absorption coefficient and the term $\ln[(R_{max} - R_{min})/(R - R_{min})]^2$, where R, R_{max}, and R_{min} denote the diffuse reflectance at a specific frequency *v*, along with the maximum and minimum values observed in the spectra, respectively. The direct **optical bandgap** value can be determined as the point where the tangent to the straight part of the $\ln[h\nu(R_{max} - R_{min})/(R - R_{min})]^2$ vs. hν curve intersects y=0. Figure 4.28 illustrates the extrapolated bandgap values of Sb_2Se_3 films grown on glass, highlighting a strong dependence on growth temperature.

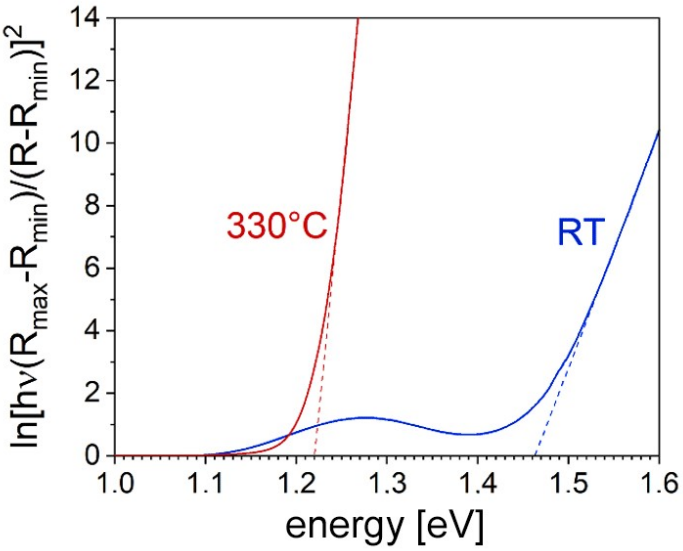

Figure 4.28 - Diffuse reflectance spectra of Sb_2Se_3 film deposited on glass at RT (black line) and at 330°C (red line).

Specifically, the bandgap value consistently decreases with increasing temperature, from 1.46 eV at room temperature (RT) to **1.22 eV** at 330°C, which is in agreement with the theoretical direct bandgap value of Sb_2Se_3 (Table 4.4).

Table 4.4 - Extrapolated values of the direct bandgap in the films grown at different temperatures.

Growth Temperature [°C]	***Direct Bandgap [eV]***
RT	1.46
90	1.36
120	1.33
190	1.31
260	1.26
330	1.22

A similar temperature-related trend and the same extreme bandgap values were observed in Sb_2Se_3 films grown on both CdS and Mo substrates, indicating that the variation in bandgap is not contingent upon the preferential orientation of the grains. As previously observed in other studies, this trend can be reasonably attributed to the quality of Sb_2Se_3 crystals. Films grown at low temperatures by various techniques generally exhibits bandgap values significantly higher than the theoretical prediction. The common thread among these studies and the present one is that as the temperature rises, the bandgap quickly decreases toward the theoretical value of 1.22 eV. This trend is associated with improvements in Sb_2Se_3 crystal quality, including improved crystallinity, larger grain size, and a reduction in defect states. More in detail, the limited crystallization resulting from low growth temperatures appears to lead to a non-uniform spatial distribution of optical properties, causing broadening of the measured bandgap. In contrast, the high crystal quality achieved at elevated temperatures fosters more consistent optical properties throughout the films, resulting in a narrower optical transition and a bandgap value that converges toward the theoretical prediction.

To assess the impact of ribbon orientation on the performance of these Sb_2Se_3 films as a solar cell absorber, different devices were prepared with the following configurations (Figure 4.29):

- ZnO:Al/ZnO/CdS/(**Sb_2Se_3/Mo**)/Glass (**#1**) (substrate-configuration)
- ZnO:Al/ZnO/CdS/(**Sb_2Se_3/FTO**)/Glass (**#2**) (substrate-configuration)
- Au/(**Sb_2Se_3/CdS**)/FTO)/Glass (#3) (superstrate-configuration)

In all these devices, 70 nm-thick CdS layers were deposited using Chemical Bath Deposition (CBD), while 500 nm of ZnO:Al and 120 nm of ZnO were grown via RF Sputtering, utilizing the same parameters previously used for solar cells from LT-PED thin-films.

Capacitance–Voltage measurements were the conducted to determine the net carrier concentration (NA) in Sb_2Se_3, employing the formula:

$$\frac{1}{C^2} = \frac{2(Vb-V)}{qA^2\varepsilon\, NA} \qquad (4.2)$$

where ε=18 represents is relative dielectric constant of Sb_2Se_3, A is the cell area, and Vb is the built-in potential of the junction. Independently on the cell structure under investigation, NA consistently falls within the range of $\mathbf{10^{13}\ cm^{-3}}$, confirming a very low density of acceptors in unintentionally doped Sb_2Se_3.

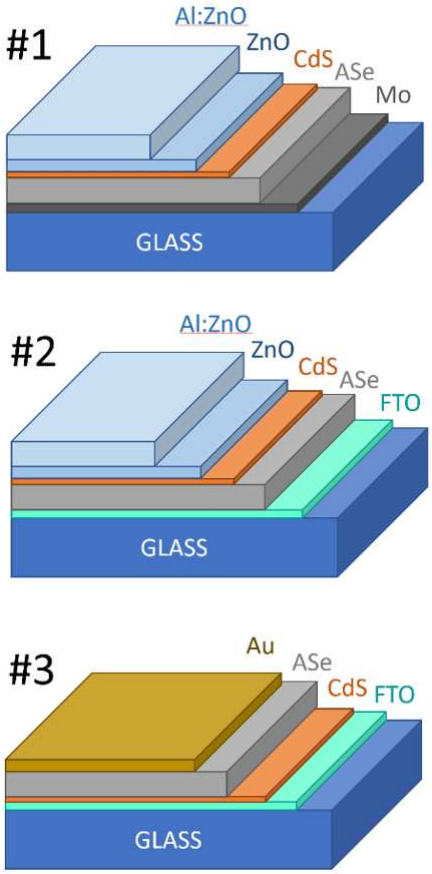

Figure 4.29 - Schemes of the three different layered cell structure used for the PV performance tests

Despite the consistent low levels of acceptors, the Current-Voltage characteristics displayed in Figure 4.30 reveal distinct electrical behaviors, tied to the structural characteristics of the Sb_2Se_3 films.

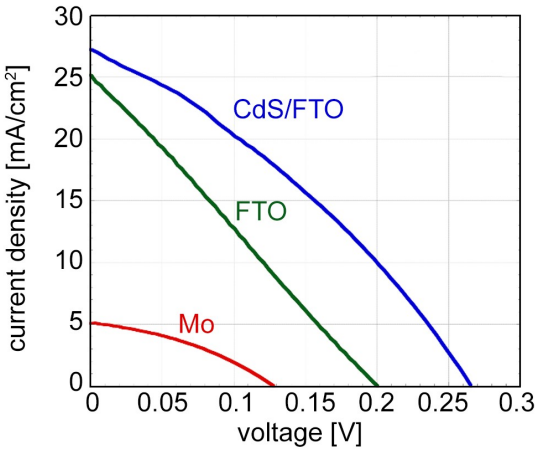

Figure 4.30 - J-V characteristics of solar cells from Sb_2Se_3 thin-films deposited on different substrates and architectures.

A summary of the average performance across all types of solar cells is presented in Table 4.5.

In device #1, where Sb_2Se_3 grown on Mo predominantly exhibits horizontal ribbon orientation and the associated RCT value is 22.6%, the cell performance is significantly affected by the short-circuit current density J_{sc} at 5 mA/cm².

In device #2, where the RCT value is doubled compared to Sb_2Se_3/Mo films, J_{sc} indeed experiences a big boost, reaching 24.8 mA/cm². However, the poor fill factor (FF), likely linked to the Schottky barrier at the Sb_2Se_3/FTO contact, limits the power conversion efficiency (PCE) of the cell.

Table 4.5 - Electrical performances of solar cells from Sb_2Se_3 thin-films deposited on different substrates and architectures. Series (R_S) and shunt resistance (R_{SH}) were measured under dark conditions.

Cell Type	*Voc [mV]*	*Jsc [mA/cm²]*	*FF [%]*	*Rsh [Ωcm²]*	*Rs [Ωcm²]*	*PCE [%]*
#1	128	5.11	36.5	10	3.5	0.24
#2	200	24.83	25.7	15	2.8	1.28
#3	266	27.06	32.7	70	1.0	2.36

For superstrate devices #3, where the RCT value of the Sb_2Se_3 absorber reaches 75%, J_{sc} surpasses 27 mA/cm², confirming the importance of maximizing vertical ribbon alignment for achieving high J_{sc} values. Also the lower series resistance (R_s) values measured in device #3 may be attributed to the vertical ribbon alignment, enhancing charge mobility in the absorber layer. Nonetheless, the FF and V_{oc} values of #3 fall short of the promising J_{sc}.

As noted by other researchers, low V_{oc} values can be primarily attributed to the extremely low charge-carrier density, significantly limiting cell voltage, and the suboptimal cell architecture design, where interface defects can act as strong recombination centers. Also the presence of Sb_2O_3 may affect defect passivation. Conversely, the low V_{oc} observed in cells #1 and #2 can only be partially explained by the low Sb_2Se_3 acceptor level.

SEM measurements revealed that the mechanical scribing, used to create sub-cells and define their area, failed to separate them completely at the cells' edges. Indeed, due to Sb_2Se_3 malleability, the cutter's edge flattens and crushes the film, leaving debris and small particles along the edges, inevitably creating undesired cross-contacts between adjacent cells or between the top and back contact (Figure 4.31).

This directly impacts the reverse saturation current (R_{SH}) values, consequently lowering both FF and Voc. To address this issue, a non-mechanical approach based on laser scribing has been explored as a solution.

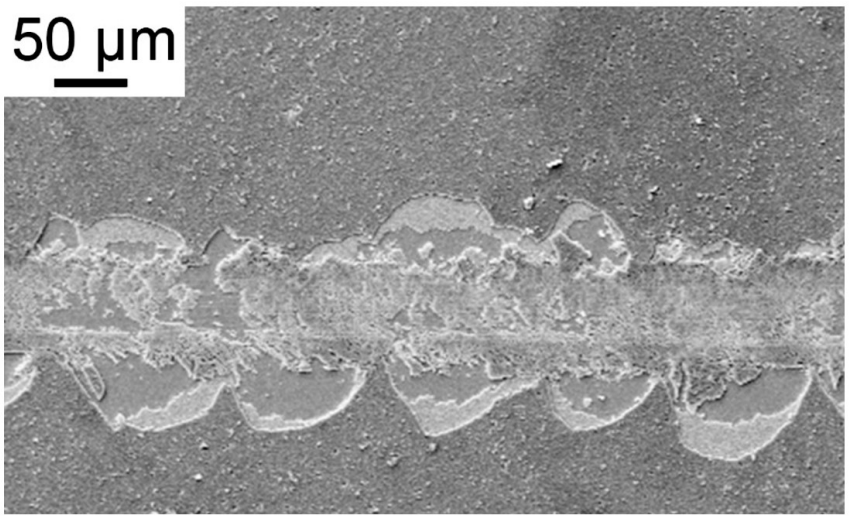

Figure 4.31 - SEM image of the effect of the mechanical scribe on some regions of a #1 type cell.

4.4 – Laser scribing and photolithography process

In order to overcome and side-issue in the measurement of the cells performance, alternative techniques were tested to replace the mechanical scribing procedure for sub-cells separation. Two different techniques were applied and compared:

- **laser scribing** (carried out at the Engineer Department of University of Parma)
- **photolithography** (carried out at IMEM)

The first technique makes use of a pulsed laser (Innolight Helios IR with λ= 1064 nm and pulse duration of 530 ps, with tunable repetition rate up to 70kHz is used) to remove material from the 2.5x2.5cm^2 cell following lines of a chosen grid (Figure 4.32 left).

Figure 4.32 – Two halves of the same Sb_2Se_3-based solar cell, processed in different ways for sub-cells separation: laser-scribing (on the left) and photolithography (on the right)

IR radiation generally helps to prevent a well-known problem of melting at the edge of the scribing. The process was calibrated in terms of laser power (the laser source is used in combination with a rotary waveplate to control the output power and a beam expander) and scan rate (adjustable from a few mm/s to some m/s) so that the removal went just so deep that only the upper layers are removed but not the last contact on the substrate. The only undesired effect of laser scribing is the presence on the cell of some fragments of the removed layers (Figure 4.33), that in some cases are not so easy to remove ant that may interfere with the electrical characterization.

Photolithography have been instead used to deposit a photo-resist mask on the cell before a chemical etching is used to remove material from the regions that are not covered

by the mask. The chemical etching was carried out using a HCl solution (HCl 37% = 12M). Within 40-60 s the sample was subject to an evident change in color, that indicated that the top layers were completely removed. The etching process wan then interrupted by placing the sample into water.

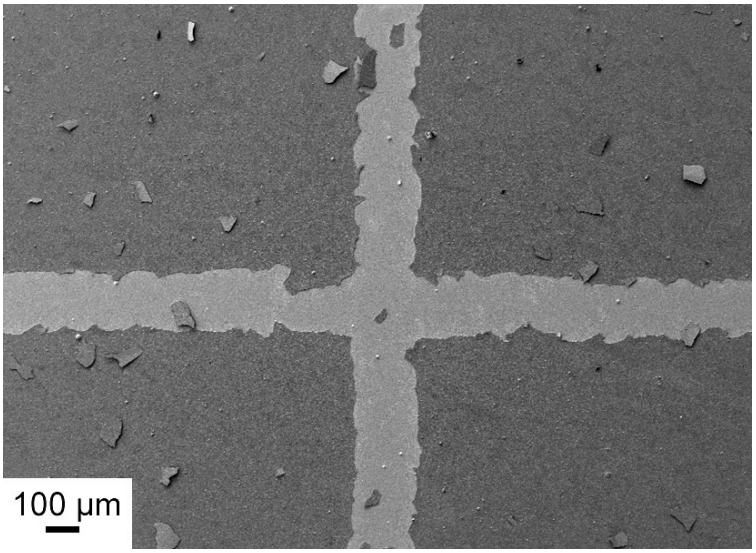

Figure 4.33 – SEM image of a Sb_2Se_3-based solar cell immediately after the laser scribing procedure. In the brighter linear areas the back-contact is exposed.

A comparison of the effectiveness of both procedures has been made by applying them on two halves of the same cell. The cell performance tests revealed that the cell processed by photolithography had superior performance (Table 4.6), probably because the fragments/residuals left by laser scribing between adjacent cells can negatively impact on the charge collection. The variation in Jsc can be associated with the uncertainty on the value of cell area and shading area of the top metal contact.

Table 4.6 – Compared values for the same kind of Sb_2Se_3 cell, when processed with laser scribing and with photolithography

Laser scribing		***Photolitography***
17	J_{sc} [mA/cm^2]	11
156	V_{oc} [mV]	191
29	FF [%]	33
0.8	η [%]	0.7
2	R_s [Ωcm^2]	3
12	R_{sh} [Ωcm^2]	21

4.5 - Cu-doped Sb_2Se_3 thin-films deposited by LT-PED

Even in the highest-performing Sb_2Se_3-based cells, the observed V_{OC} and FF values were typically quite low. This limitation can be attributed not only to deep defects resulting in a short carrier lifetime but also, as shown before, to the extremely low hole density (approximately 10^{13} cm^{-3}) in undoped Sb_2Se_3.

To address this issue, several studies in literature have explored the doping of Sb_2Se_3 with various elements, both theoretically and experimentally. Enhancements in p-type conductivity have been observed or predicted through doping with elements like Pb, Sn, Mg, N, and a minor concentration of Bi. Yet, since Bi and Sb are from the same group, Bi's primary effect is on the Sb/Se ratio and the number of intrinsic defects. In fact, a heightened Bi concentration leads to n-type conductivity. Similarly, Te, being valence-matched with Se, impacts the Se/Sb ratio. Conversely, elements such as Fe, I, and other halides have been found to exclusively induce n-type conductivity.

While Cu doping has shown potential for boosting p-type conductivity, its effective implementation has been challenging. Achievements so far include high trap densities that unfortunately reduce V_{OC} to less than 300 mV, or post-growth surface treatments using $CuCl_2$ that cause an n-type switch at grain boundaries. On the contrary, most of the research reporting the ad of Cu to Sb and Se were instead aimed to produce the $CuSbSe_2$ compound. To the best of current knowledge, there haven't been any studies documenting the use of PED or LT-PED technique for the production of **Cu-doped Sb_2Se_3 films** prior to the work here reported.

Cu, primarily exhibiting +1 and +2 oxidation states, was selected to enhance the p-type conductivity of Sb_2Se_3, which has an oxidation state of +3. Stable compounds for Cu and Se include Cu_2Se and CuSe, while a $CuSbSe_2$ phase also exists. However, since their crystal structures strongly differ from the one of Sb_2Se_3, an excessive Cu substitution could lead to phase segregation.

Polycrystalline targets with different Cu contents were prepared and used for the deposition of Cu-doped Sb_2Se_3 films using LT-PED. Micro-Raman spectroscopy showed that films with up to 5% Cu (atomic percentage on the whole stoichiometry,

corresponding to $Sb_{1.75}Cu_{0.25}Se_3$) retained only the Sb_2Se_3 phase characteristics. On the contrary, films with higher content of Cu displayed some evidence of $CuSbSe_2$ phase segregation, as visible in Figure 4.34: the defining Sb_2Se_3 spectrum usually displays a prominent peak near 190 cm^{-1}, but a peak around 212 cm^{-1} clearly also indicates the

presence of $CuSbSe_2$. For this reason, the **5% Cu target** was chosen for subsequent experiments.

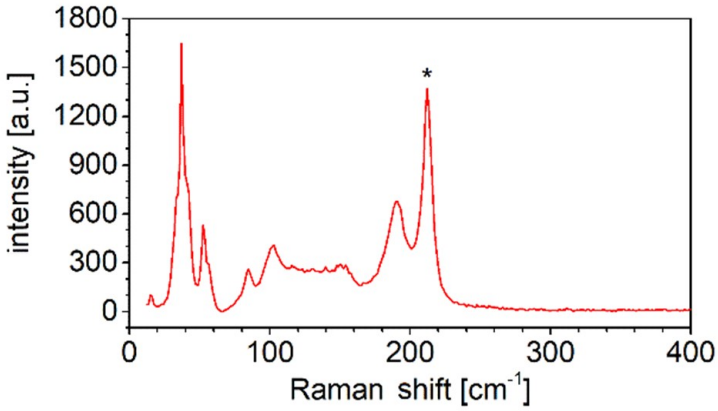

Figure 4.34 - Raman spectrum collected on a local spot of a thin-film deposited by LT-PED with a $Sb_{1.5}Cu_{0.5}Se_3$ target, where $CuSbSe_2$ phase was also present, as revealed by the peak at ~210 cm^{-1} (highlighted with * symbol). All the other main peaks in the spectrum are typical of a Sb_2Se_3-like phase.

A preliminary investigation was conducted varying LT-PED acceleration voltage, that already proved to significantly influence factors like film composition and crystallization. Cu-doped Sb_2Se_3 thin films were initially deposited on Mo substrates at voltages of 12 kV, 14 kV, 16 kV, and 18 kV. All the other parameters, except for the deposition time. were kept fixed. Deposition time was changed accordingly to the need of obtaining films with similar thickness, even if the growth rate was quite different for different acceleration voltages. The structural properties of these films, analyzed by **XRD** and **Raman** spectroscopy, are presented in Figure 4.35.

The film deposited at 12 kV was amorphous, with only substrate-related peaks visible in the XRD pattern. On the contrary, the 14 kV film displayed improved crystallization, with distinguishable peaks resembling those of pure Sb_2Se_3. However, the relative peak intensities suggest a primary growth direction of the 1D ribbons parallel to the substrate, with predominant *hk*0 indexes (*l*=0). Films from 16 kV and 18 kV showed even more pronounced *hk*0 peaks, especially with a high peak for the 020 reflection, consistent with previous results for undoped Sb_2Se_3 films deposited by LT-PED on Mo substrates. Some peaks, notably at 29.0° and 46.3°, couldn't be matched with the Sb_2Se_3 structure and might indicate Cu-rich phases, particularly at increased accelerating voltages.

Figure 4.35b adds supplementary information. The Raman spectrum for the 12 kV film was very similar to that of an almost amorphous material, with weak and broad peaks hinting at characteristics of $CuSbSe_2$. On the other hand, the 14 kV film's Raman spectrum

had a strong similarity to that of pure Sb_2Se_3. Films deposited at 16 kV and 18 kV yielded similar Raman spectra, suggesting that the prevailing structure is Sb_2Se_3-like. The lower peak around 210 cm^{-1} can be more likely attributed to the Sb–Se vibrational mode in Sb_2Se_3, rather than $CuSbSe_2$, because in Sb_2Se_3 this peak is always expected to have a much lower intensity than that at 190 cm^{-1}, independently of laser polarization.

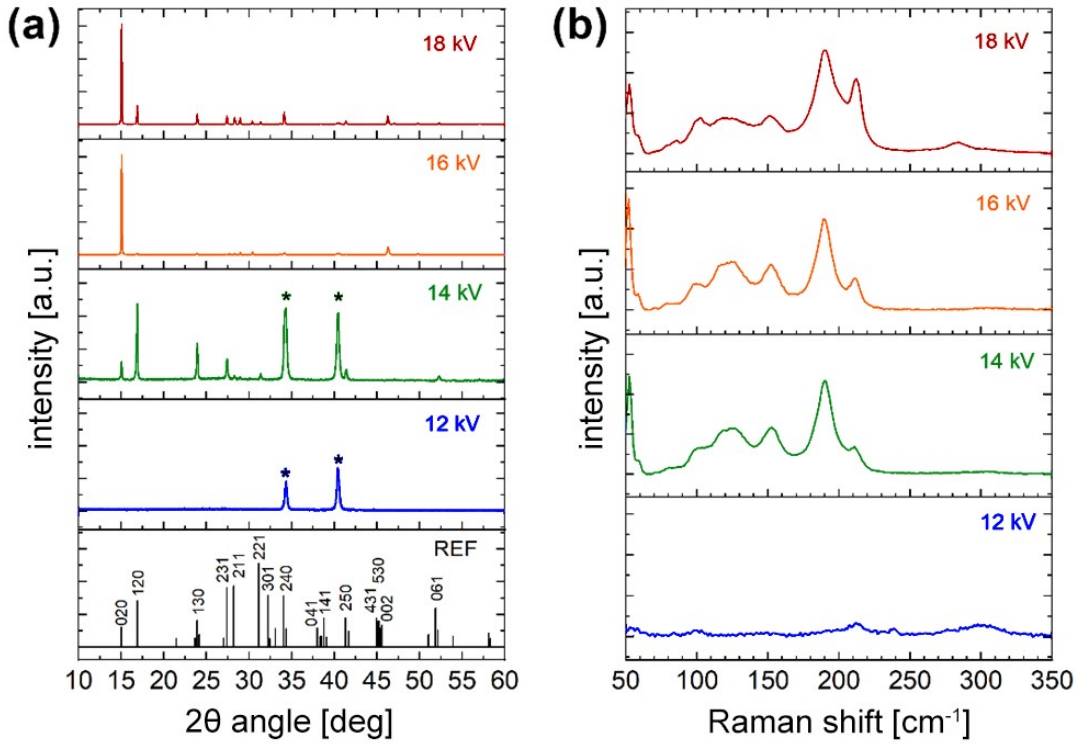

Figure 4.35 - Structural characterization of Cu-doped Sb_2Se_3 thin-films deposited by LT-PED on Mo substrate with different accelerating voltages: (a) XRD patterns, with indexed reference (JCPDS 15–0681) for undoped Sb_2Se_3 at the bottom (* indicates Mo substrate); (b) Raman spectra.

The same samples were further examined using **SEM** and **EDS** to study their morphology and composition. SEM images, presented in Figure 4.36, show a growth in grain size relative to the increased LT-PED accelerating voltage. Specifically, the 18 kV sample was characterized by clusters of “needle-like” or “rod-like” elongated crystals protruding from the surface (as shown in Figure 4.36b).

EDS analysis indicated that the Cu concentration in the films deposited at 12 kV and 14 kV was a mere 1-2%. However, this rises to approximately 5% (matching the target) in films from the 16 kV and 18 kV depositions. This difference can be probably attributed to an insufficient electron beam energy to achieve a full ablation of the target's surface in the first two cases, resulting in Cu, which has the highest melting point, not being transferred in a stoichiometric ratio.

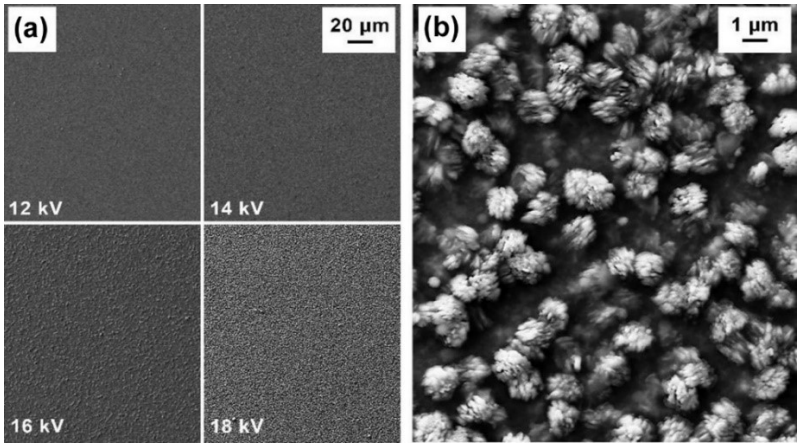

Figure 4.36 - SEM images of Cu-doped Sb_2Se_3 thin-films deposited by LT-PED on Mo substrate: (a) a surface morphology comparison for samples deposited with different accelerating voltages; (b) a higher magnification of the sample deposited at 18 kV.

The 16 kV deposition appears to strike the best balance. Although it exhibits non-optimal *hk*0 orientations, it yields films with the highest Cu concentration and shows no significant signs of secondary phases. Moreover, the deposition rate at this acceleration voltage was way more reasonable that the one obtained at 14 kV. Therefore, **16 kV** acceleration voltage was selected for the following experiments.

Also in the case of Cu-doped thin-films, substrates played an important role to obtain different preferential ribbons orientations.

Like for undoped Sb_2Se_3 films deposited by LT-PED, it was found that the Mo substrate led to an unfavorable orientation for photovoltaic application, predominantly displaying grains with a preferred *hk*0 orientation. For Cu-doped Sb_2Se_3 films deposited on Mo substrate at 16 kV, the combined $\Sigma TC(l\neq0)$ value was as low as 1.2%. On the contrary, Cu-doped Sb_2Se_3 films deposited on FTO substrate at the same voltage were characterized by a more beneficial ribbon orientation, and its $\Sigma TC(l\neq0)$ was definitely higher (41.3%). This difference is quite evident in Figure 4.37, where their XRD patterns are reported for comparison.

Solar cells were then fabricated using these Cu-doped Sb_2Se_3 thin films, using the same procedure previously outlined. The complete structure for the two cell types was:

- AZO/ZnO/CdS/(**Cu:Sb_2Se_3/Mo**)/Glass
- AZO/ZnO/CdS/(**Cu:Sb_2Se_3/FTO**)/Glass

The main goal of this experiment wasn't about the optimization of the cell layers. Thus, even though these layer configurations might not represent the most efficient choice, they were chosen in order to make a direct comparison with results previously obtained for the undoped Sb_2Se_3 absorber.

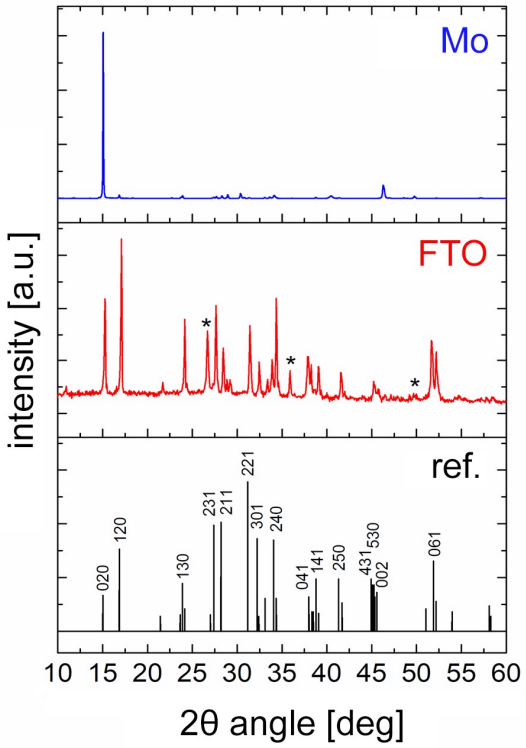

Figure 4.37 - XRD patterns of Cu-doped Sb_2Se_3 thin-films deposited by LT-PED at 16 kV on Mo and FTO substrates; indexed reference (JCPDS 15–0681) for undoped Sb_2Se_3 is reported at the bottom; * indicates peaks from the FTO substrate.

Figure 4.38 depicts the free-carrier profiles derived from $d(1/C^2)/dV$ at 120 K for two solar cells, one with an undoped Sb_2Se_3 layer and the other with a 5% Cu-doped Sb_2Se_3 layer.

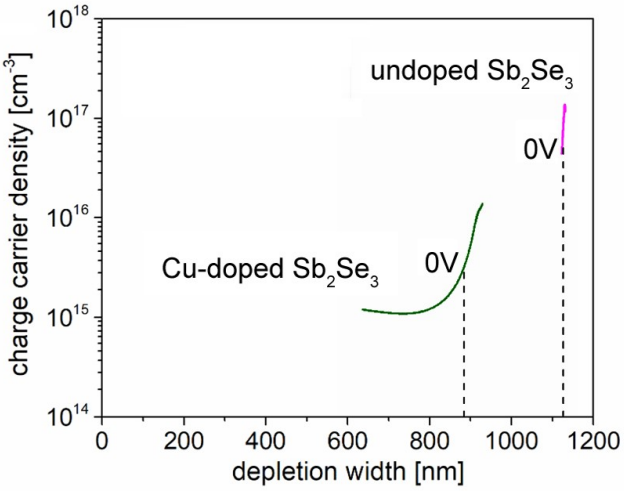

Figure 4.38 - Free carrier profiles obtained from the d(1/C2)/dV at 120 K on undoped and Cu-doped Sb_2Se_3 solar cells. Test signal frequency is 1MHz and amplitude is 35 mV.

While the 1100 nm thick undoped Sb_2Se_3 layer appears to be fully depleted, the free-carrier concentration of the Cu-doped Sb_2Se_3 can be roughly estimated, from the lowest point of the characteristic u-shaped curve, to be around 10^{15} cm^{-3}, with the depletion layer at V=0 V being less than 900 nm. Given that Sb_2Se_3 is inherently almost an intrinsic semiconductor with an exceptionally low free carrier density (10^{13} cm^{-3}), this suggests that Cu doping successfully increased the free-carrier concentration by approximately two orders of magnitude.

Thermal Admittance Spectroscopy (TAS) measurements were instead used to determine the activation energy (E_A) responsible for the primary capacitance shift observed in the *C* versus ω plots is found to be E_A=0.505±0.015 eV for both cells, as illustrated in Figure 4.39a and 4.39b.

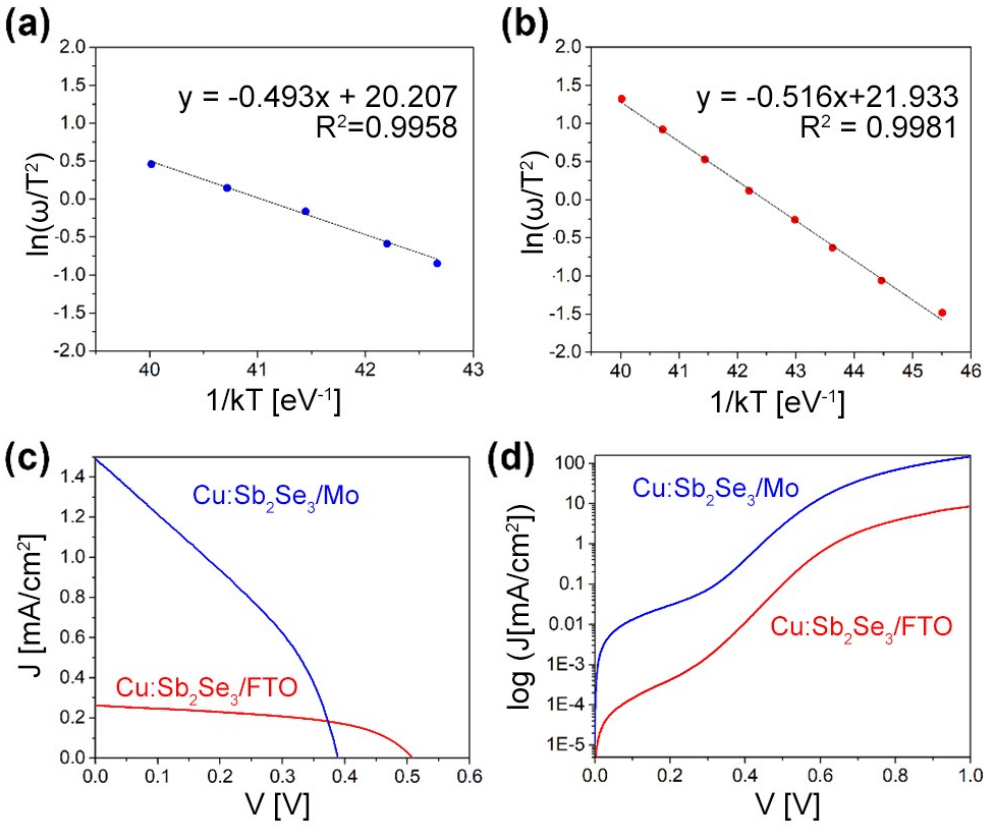

Figure 4.39 - Electrical characterization of the two cells with Cu-doped Sb_2Se_3 on Mo (Glass/Mo/ Cu: Sb_2Se_3 /CdS/ZnO/AZO) and on FTO (Glass/FTO/Cu: Sb_2Se_3 /CdS/ZnO/AZO) with the highest recorded Voc values: Arrhenius plots of ln (ω/T^2) vs 1/KT calculated from the C vs ω plots in the 250K-300K temperature range, for the cell on Mo (a) and on FTO (b). J-V plot for the two cells under illumination (c) and in dark (d).

These measurements were carried out at different temperatures, where $\omega=2\pi f$ and f is the frequency of the test signal. The E_A value was nearly the same for cells with different

back-contacts. Such a value aligns also well with findings from other TAS studies on Sb_2Se_3 solar cells, which ascribe this mid-gap energy level to an unspecified defect at or near the Sb_2Se_3/CdS interface.

The J-V characteristics for both type of cells, here reported for those exhibiting the highest recorded V_{OC} values, are presented in Figure 4.39 c-d (illuminated and dark measurements respectively, for both the cell types).

If compared with the results obtained for undoped Sb_2Se_3 films, here it is possible to see that the V_{OC} raised from 315 mV to 388 mV for the cell on Mo substrate, and from 256 mV to an impressive 509 mV for the cell on FTO substrate. This latter value ranks among the top three V_{OC} values ever documented for Sb_2Se_3-based solar cells. The J_{SC} also exhibited a marginal rise for the cell on Mo substrate, going from a modest 0.3 mA/cm^2 to 1.5 mA/cm^2. Conversely, the J_{SC} abruptly decreases for the cell on FTO substrate, shifting from 25.6 mA/cm^2 down to 0.3 mA/cm^2. This reduction undermine the fill factor (FF) boost, which climbed from 39.2% to 51.9%. Calculations from the dark I-V plots for both solar cell types at ambient temperature typically hovered around ideality factors of 1.8–1.9. This suggests that the saturation current predominantly stems from SRH recombination within the space charge zone (as shown in Figure 4.39d).

The electrical parameters for both cell types are listed in Table 4.7. The notably high R_{sh} values in both cell types highlight the quality of the device fabrication.

Table 4.7 - Electrical parameters of Cu-doped Sb_2Se_3 solar cells on Mo and FTO substrates calculated from IV characteristics under dark conditions at 300K

Substrate type	***Ideality factor***	***R_s (Ωcm^2)***	***R_{sh} (Ωcm^2)***
Mo	1.87	0.48	$2.5x10^5$
FTO	1.81	4.64	$2.5x10^7$

For the cell on FTO, a significant series resistance nearing 5 Ω cm^2 was measured. This resistance might be caused by a non-ohmic interface between the n-type FTO conductor and the doped p-type Sb_2Se_3, which could also be the reason for the substantial decrease in current. Analyzing the V_{oc} vs. T plot of these cells with Cu-doped Sb_2Se_3 thin-films on MO and FTO substrates (Figure 4.40), the T=0 K intercept implies a recombination energy barrier of roughly 1.02 eV.

Given that this value closely aligns with the bandgap-energy of the Sb_2Se_3 absorber, it indicates that the primary recombination mechanism likely takes place within the absorber's bulk.

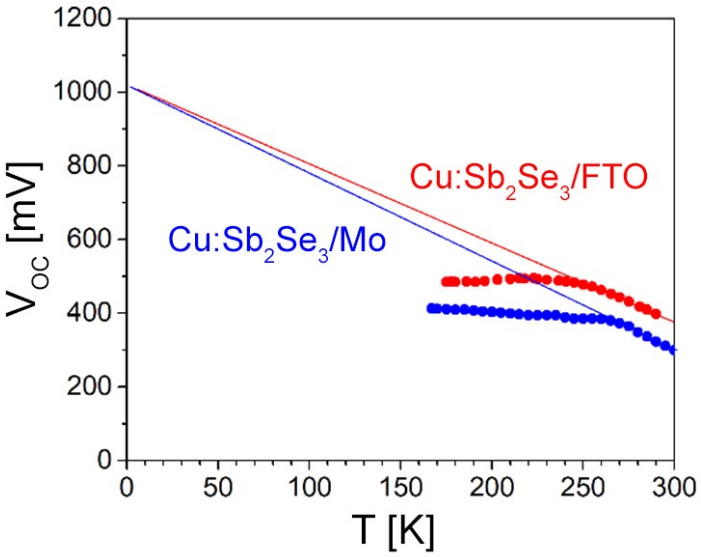

Figure 4.40 - Temperature dependence of V_{OC} for Cu-doped Sb_2Se_3 tested cells. The extrapolated value of V_{OC} as T→0 is indicated by the dashed line (≈1.02 V).

4.6 - TiO_2 thin-films as potential buffer- or seed-layers

Starting from the results just shown in chapter 4.5, a collaboration with the University of Genova (carried out by the group of Prof Diego Colombara) to try a different approach to overcome the problems raised while using pure FTO as a back contact for solar cells based on Cu doped Sb_2Se_3 and to replace the toxic CdS component.

TiO_2 samples on FTO substrate, with nominal different concentrations of oxygen vacancies, were produced at University of Genova by *Dr. Christian Rossi* through the following procedure. V_O are the main source of intrinsic n-type conductivity in TiO_2, so their concentration can directly control the layer conductivity and can be used to improve different interfaces.

Titanium dioxide (TiO_2) thin films were deposited on 1-inch square fluorine-doped SnO_2 (FTO) substrates using a **sol-gel** spin coating method. Initially, the FTO substrates were cleaned by sonication in deionized (DI) water, ethanol, and acetone for 10 minutes each, in that sequence and at room temperature. The sol-gel precursor solution was prepared by combining 325 µl of titanium ethoxide, 5 ml of ethanol, and 125 µl of DI water, resulting in a white precipitate. To clear the solution, several drops of 35% HCl were added until no precipitate remained. This precursor solution was then magnetically stirred for an hour and refrigerated until needed. The spin coater was pre-set to operate at 3000 rpm for 25 seconds. A cleaned FTO substrate was placed on it, and after 5 seconds of spinning, 200 µL of the prepared sol-gel solution was dynamically pipetted onto the rotating substrate. To add extra layers, an equal volume of the solution was statically poured onto the surface of the sample before being spun again at 3000 rpm for 20 seconds. Once all layers were deposited, the samples underwent annealing in a muffle furnace in air, initially at 115 °C and subsequently at 450 °C, each for 30 minutes (with a heating ramp of 20-25 °C/min).

To achieve a certain concentration of oxygen vacancies within the TiO_2 thin films, the samples were subjected to three distinct acidic treatments. In three separate crystallization dishes, deionized (DI) water and 35% HCl were combined to produce solutions with concentrations of 2M, 4M, and 6M. The TiO_2 films were then horizontally immersed in each of these acidic solutions for 12.5 hours. Throughout this process, the dishes were sealed with parafilm to prevent contamination. Subsequently the samples were washed multiple times with DI water and then annealed in a muffle furnace at 500°C for 1 hour. After annealing, they were allowed to cool at room temperature and were then stored in an argon-filled container.

A resume of the different characteristics of the 18 available TiO_2 films is reported in Table 4.8a-b.

Table 4.8 – List of available TiO_2 film samples (identified by #number) and their preparation parameters.

(a)	***TiO_2 film sample numbers (standard procedure*)***			
		increasing nominal film thickness →		
increasing nominal film thickness		**1 coating**	**2 coatings**	**3 coatings**
	No HCl	#63	#60	#65
	HCl 2M	#40	#56	#48
	HCl 4M	#52	#51	#61
	HCl 6M	#4	#54	#43

(b)	***TiO_2 film sample numbers (additional samples)***
#23	std. procedure* + 1h stirring of precursor solution
#35	std. procedure* + 24h stirring of precursor solution
#38	std. procedure* + 48h stirring of precursor solution
#15	std. procedure*
#16	std. procedure* + 4000rpm 20s
#18	std. procedure* + 6000rpm 20s

** standard procedure: 3000 rpm, spin casting after 5s at max speed*

XRD and **micro-Raman** measurements were performed to evaluate the TiO_2 quality before the deposition of Sb_2Se_3. As shown in Figure 4.41, however, XRD were not able to detect signal from the TiO_2 in either Rutile or Anatase phase, coating, showing only the peaks of the FTO substrate (probably because of the layer thinness).

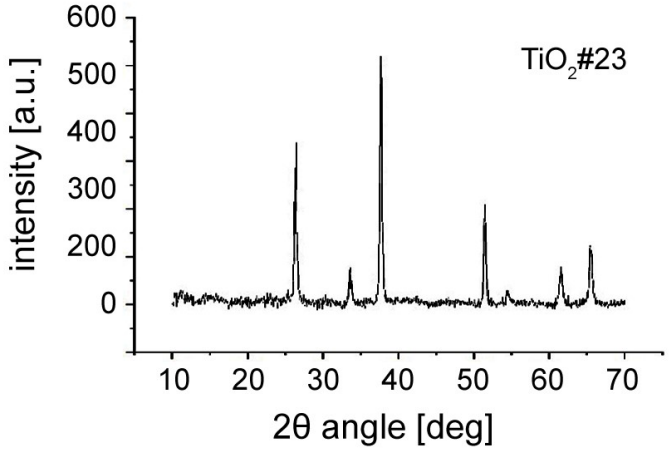

Figure 4.41 – XRD pattern of sample TiO_2#23 as reference.

Raman measurements, on the other hand, were effective in detecting peaks from the Anatase TiO_2 phase in all the samples analyzed, independently by the different treatments (Figure 4.42)

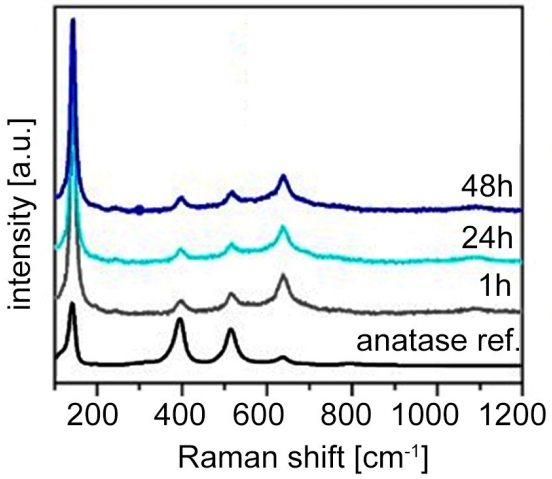

Figure 4.42 - Raman spectra of different TiO_2 samples obtained with different precursors stirring times.

An analysis of the possible impact of thermal treatment, mirroring the conditions of the Sb_2Se_3 deposition, was also conducted on one of the thicker samples. This assessment was crucial to ensure that the substrate would remain unaffected during the deposition process. As depicted in Figure 4.43, optical evidence of some contamination was observed.

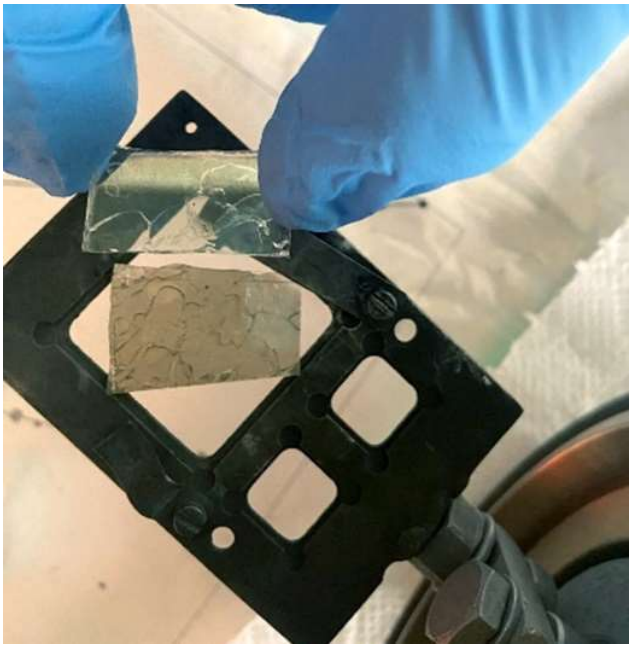

Figure 4.43 – Optical difference between the sample annealed (bottom) and the original sample (top).

Raman analyses, however, revealed no notable discrepancies, validating the efficacy of the TiO_2 deposition procedure. So, the optical variation previously observed was attributed to a Sb_2Se_3 contamination from the deposition chamber degassing where the treatment was performed.

SEM characterization was also carried out to gain deeper insights into the morphology of the different substrates. All Samples, irrespective of their thicknesses, were showing cracks on the surface, as shown in Figure 4.44.

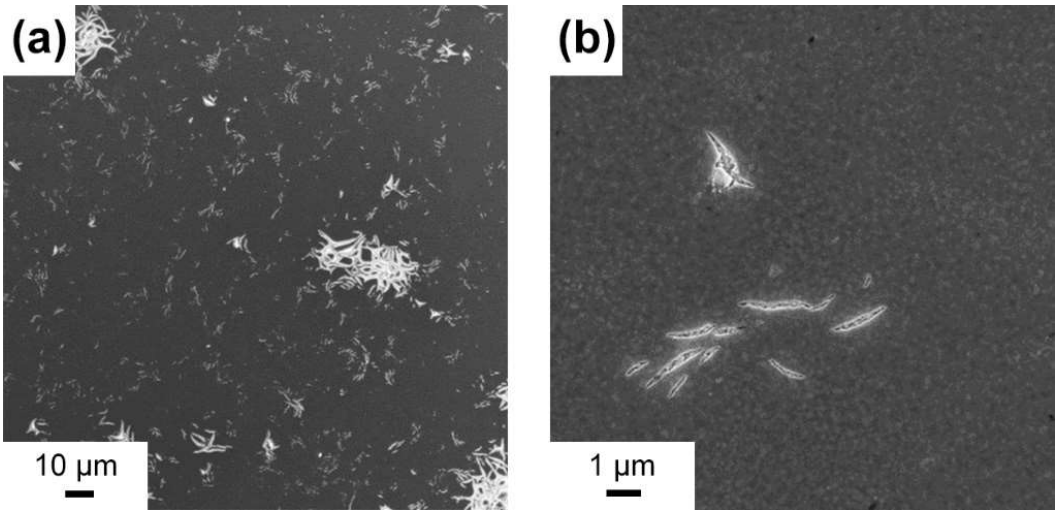

Figure 4.44 – SEM images of cracks in the TiO_2 layer

These cracks in the TiO_2 surfaces were used to estimate the thicknesses of the coating, as shown in Figure 4.45. The thicknesses were estimated to be about 50 nm for the thinner samples and almost 200 nm for the thicker ones.

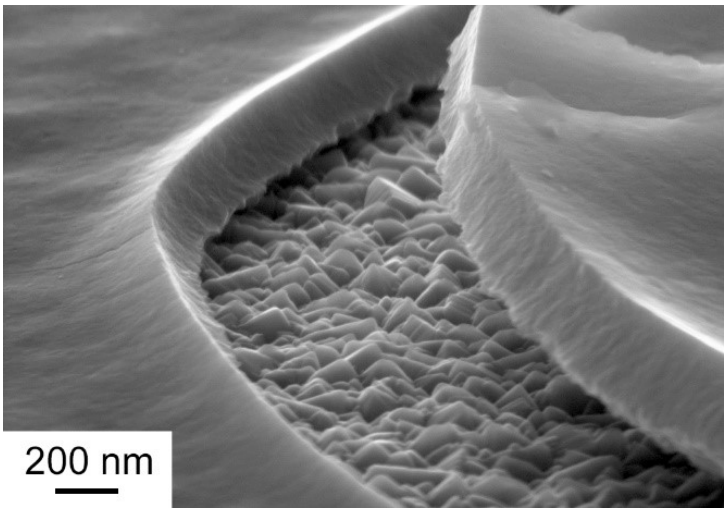

Figure 4.45 – SEM image of a crack on a tilted TiO_2 sample. Bottom rougher surface is that of the FTO substrate

Cu-doped Sb_2Se_3 depositions were then made by LT-PED on preliminary samples using the standard conditions mentioned before at 16 kV. Three of the four samples were characterized by a ΣTC(l≠0) around 20%. Only one sample, labeled as #23, had a ΣTC(l≠0)=32.1%. This improved orientation was further corroborated by Raman analyses, which indicated signs of oxidation processes triggered by the laser, as seen in Figure 4.46. Nonetheless, the correct Sb_2Se_3 phase was identified in all four samples.

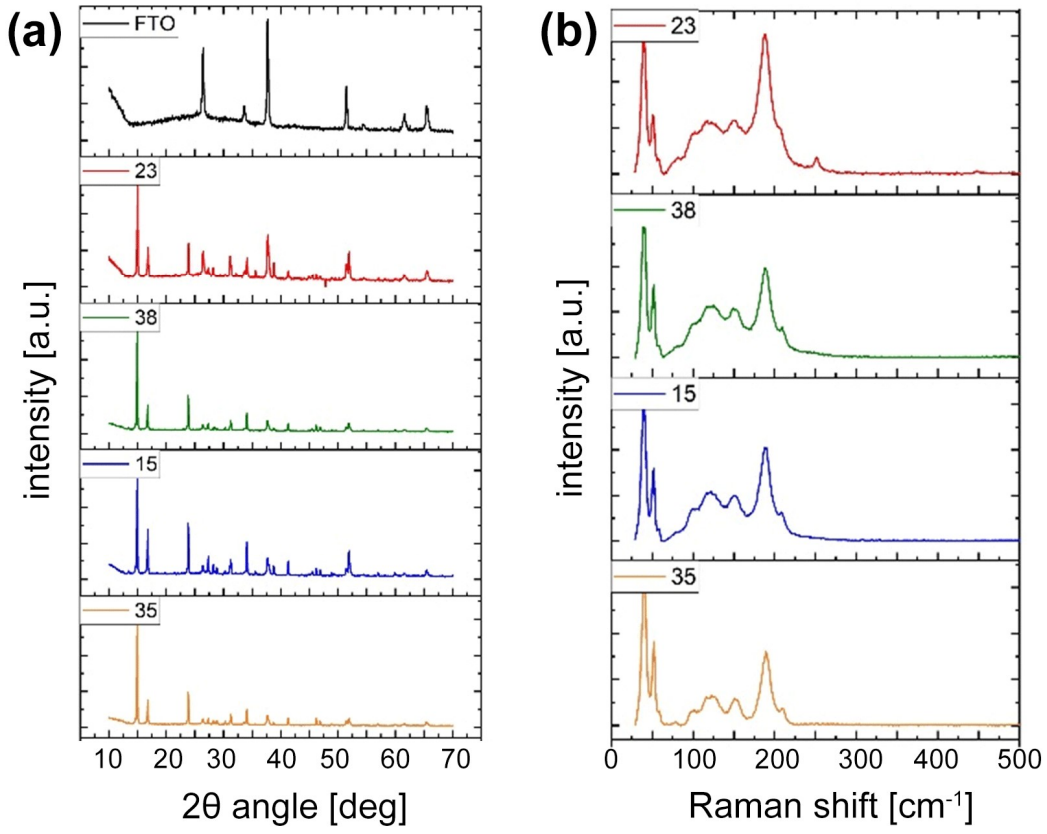

Figure 4.46 – XRD and Raman spectra of prelimiray samples

Further depositions were carried out on the three distinct thickness batches reported in Table 4.8a. The XRD analysis for all the samples revealed minimal variations (Figure 4.47).

Unfortunately the ribbon orientations, once again, is predominant for the l=0 directions, with an average ΣTC(l≠0) value below 20%. The third batch, in particular, showed an even more prominent l=0 preferential orientation and ΣTC(l≠0) values around 10%. These results were also confirmed by SEM images (an example is reported in Figure 4.48), where horizontal Cu-doped Sb_2Se_3 elongated crystals were clearly visible on the film surface

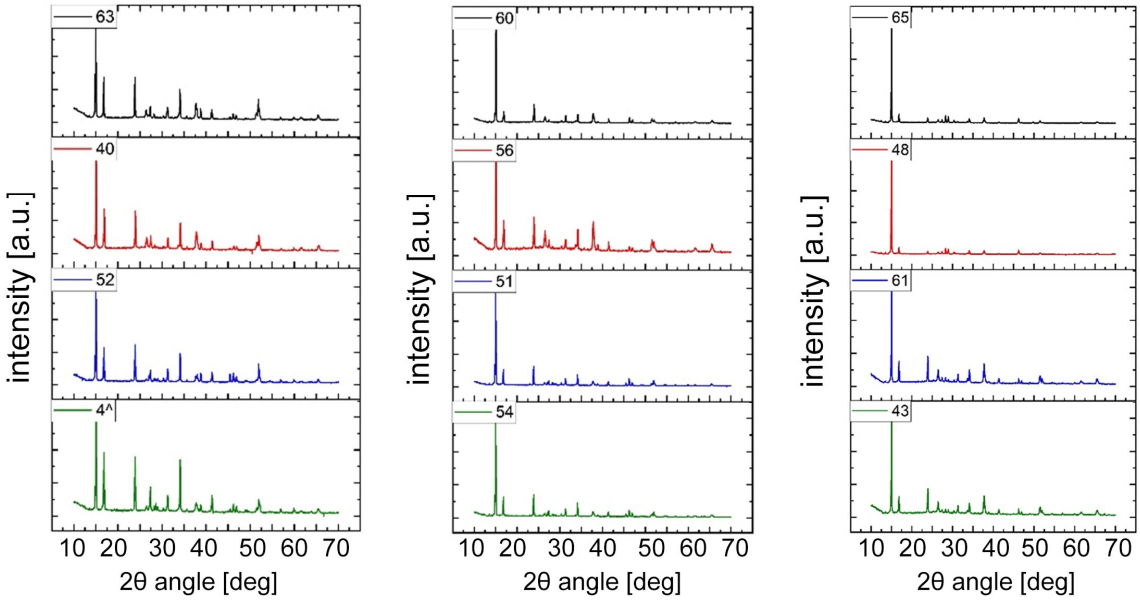

Figure 4.47 – XRD for the ASe films deposited on first and second batch

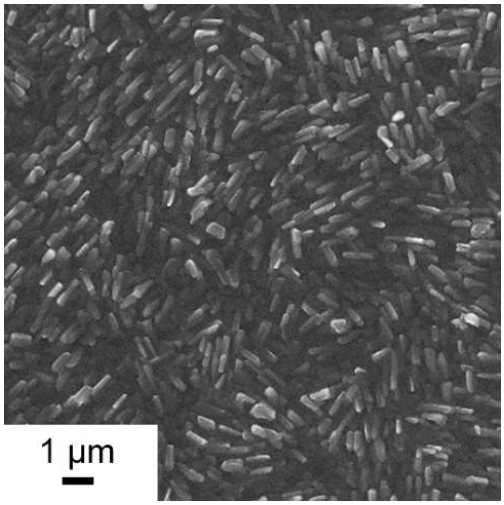

Figure 4.48 – SEM Image of ASe thin film grown on TiO_2 substrate

Regrettably, all the solar cells produced using these absorber layers turned out to be shunted. The cracks in the substrate are currently believed to be the primary cause. Moreover, the ribbons orientation induced by these films was generally bad for the photovoltaic application.

Since some research in literature indicates improved efficiencies when utilizing mesoporous TiO_2, alternative substrate types are currently in preparation for further experiments.

4.7 - Effect of a NaF layer on Sb_2Se_3 thin-films

A second attempt to overcome the problems issued with the FTO back contact, especially regarding the photocarrier extraction at the FTO/Sb_2Se_3 interface, the implementation of a 10 nm **NaF** thin layer deposited by LT-PED onto the FTO/Glass surface was explored.

This strategy was approached due to the well-known beneficial effect of a NaF layer on CIGS solar cells. In this case potential benefit of **Na** is its ability to **passivate grain boundaries**. Various models suggest that Na helps to eliminate donor defects at grain boundaries, thereby reducing recombination sites and elevating carrier concentration. Moreover, the NaF layer has been found to induce targeted local doping at the interface, promoting carrier tunneling via localized defect states, a strategy previously employed for CIGS-based solar cells, especially at the CIGS/AZO junction.

In the case of Sb_2Se_3, the process of Na inducing p-doping in Sb_2Se_3 is likely due to the substitution of Sb by Na. Na acts as an **acceptor**, given the +1 oxidation state of in contrast to the +3 state of Sb. The band diagram of a possible Sb_2Se_3-based solar cells incorporating this NaF interlayer is illustrated in Figure 4.49.

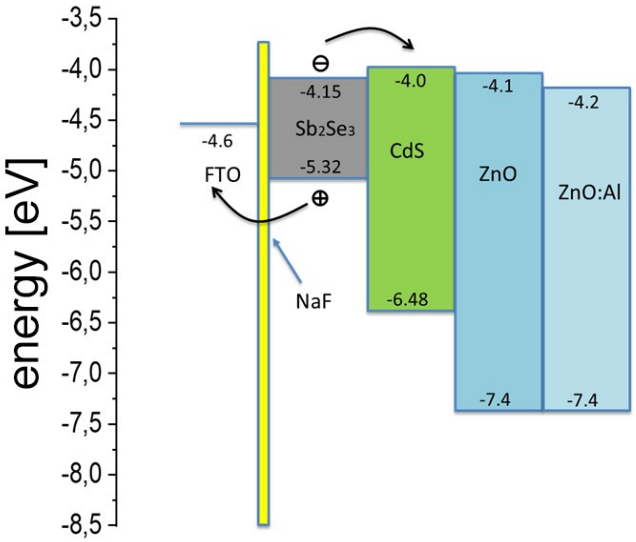

Figure 4.49 - Band diagram of a ZnO:Al/ZnO/CdS/Sb_2Se_3/NaF/FTO/Glass solar cell.

Experiments were conducted by depositing the Sb_2Se_3 absorber both by LT-PED and MS. Since the Cu-doped target was available only for LT-PED, Cu-doped Sb_2Se_3 films were deposited only with this technique.

In the case of the sputtered Sb_2Se_3 layer, a 2:3 stoichiometry with a consistent Sb:Se ratio was obtained, as confirmed by **EDS** microanalysis. The photovoltaic performance of

the solar cells based on these undoped Sb_2Se_3 films is illustrated in the current density-voltage (J-V) plot in Figure 4.50. In this plot it is evident that the addition of the NaF layer into the ZnO:Al/ZnO/CdS/Sb_2Se_3/NaF/FTO/Glass cell led to improved J_{sc} and V_{oc} values, boosting the cell's efficiency from 1.28% to 3.2%.

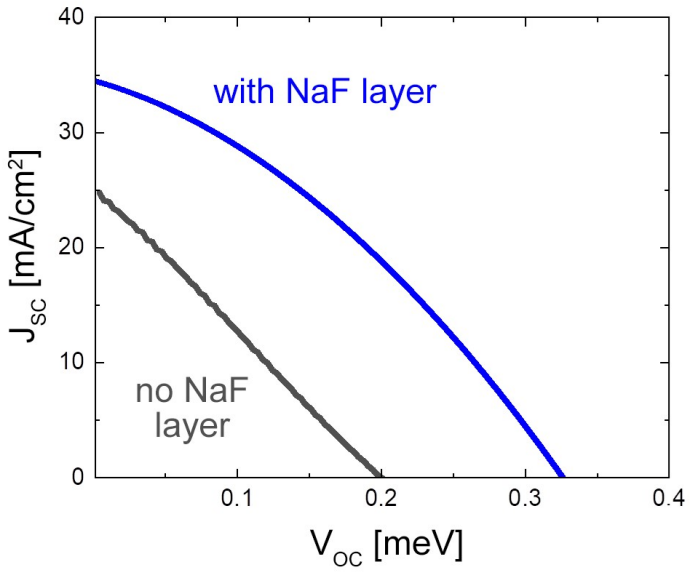

Figure 4.50 - Illuminated current density-voltage (J-V) plots of a solar cell based on Sb_2Se_3 films deposited by MS, with and without NaF interlayer

A 5% Cu concentration was verified with EDS characterization in the in the Cu-doped Sb_2Se_3 films deposited by LT-PED, confirming previous results. The ratio of Sb/Se was determined to be approximately 40/60 at different locations on the films, maintaining the target's original composition.

Solar cells where these LT-PED-grown Cu-doped Sb_2Se_3 films were used as p-type layer and structured as ZnO:Al/ZnO/CdS/Cu:Sb_2Se_3/FTO/Glass, exhibited a higher V_{oc} than that obtained with their undoped LT-PED-grown Sb_2Se_3 counterparts (0.35V-0.51V versus 0.26V). However, they also showed a significantly lower J_{sc}, around 0.3 mA/cm^2. The incorporation of the NaF layer, instead, amplified the J_{sc} by 5-10 times for solar cells with Cu-doped Sb_2Se_3 film, as shown in Figure 4.51.

The potential role of the NaF thin layer at the FTO/Sb_2Se_3 interface, inducing trap-assisted tunneling, was further evidenced by studies examining the effect of annealing treatments. As shown in Figure 4.52, the V_{oc} for the ZnO:Al/ZnO/CdS/ Cu:Sb_2Se_3/NaF/FTO/Glass cell rose after several annealing cycles at 175°C in air.

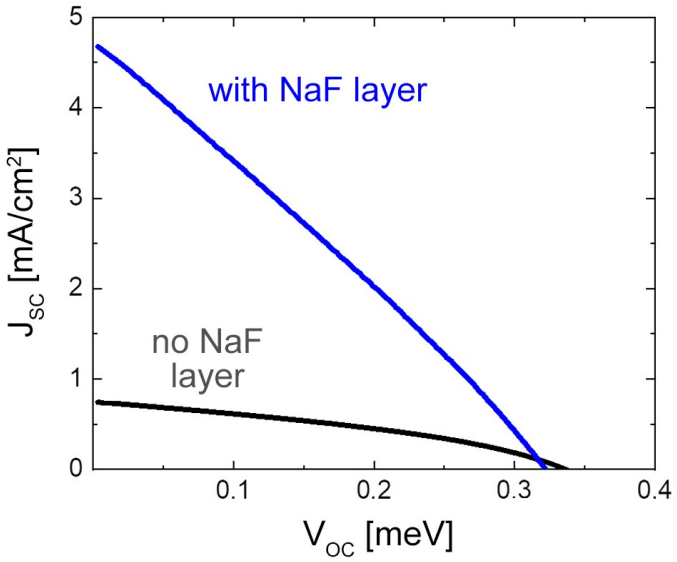

Figure 4.51 - Illuminated current density-voltage (J-V) plots of a solar cell based on Cu-doped Sb_2Se_3 films deposited by LT-PED, with and without NaF interlayer

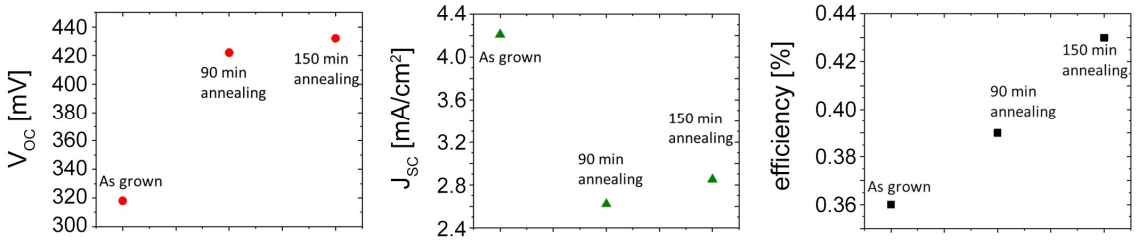

Figure 4.52 - Voc, Jsc and efficiency of solar cells based on Cu-doped Sb_2Se_3 film with NaF layer, without or with annealing treatments.

On the contrary, the J_{sc} decreased. As previously mentioned, during the annealing procedure Na atoms from the NaF layer should diffuse from the interface into the Sb_2Se_3 film, passivating ground boundaries and other defects. Yet, as the defect concentration diminishes at the interface, tunneling via localized states also drops, leading to reduced photocarrier extraction and consequently, a decrease in J_{sc}.

While NaF boosted J_{sc} for solar cells made with films deposited by LT-PED, its value remained substantially lower than that of solar cells with sputtered Sb_2Se_3 films. For this reason, also the PCE of the cell based on Cu-doped Sb_2Se_3 films deposited by LT-PED is as low as 0.36%. Since the Cu doped Sb_2Se_3 have carrier concentrations that are two orders of magnitude higher than their undoped counterparts, there should be a barrier impeding photocarrier extraction, either between the FTO and Cu:Sb_2Se_3 film or at the CdS interface.

One possible reason is that Cu elevates the conduction band's minimum (given that the minimum conduction band of $CuSbSe_2$ is located at -4.07 eV), thereby increasing the band offset with FTO. Another possible reason could be the orientation of the ribbons in these films. It is however worth noting that despite the diminished photocurrent, solar cells with Sb_2Se_3 films deposited by LT-PED generally exhibit higher V_{oc} and FF, suggesting reduced non-radiative recombination and overall material quality.

4.8 - Multilayered Sb_2Se_3 absorber

Since different type of Sb_2Se_3 films showed different properties, the hypothesis of creating a **multilayered Sb_2Se_3 absorber** made with films deposited by different techniques and/or with different doping seemed potentially more promising.

From the previous results it is possible to summarize the following observations:

- **Cu-doped Sb_2Se_3 thin-films** were successfully deposited by **LT-PED**, but while Cu-doping produced a considerable **high V_{OC}** value, the imperfect grain orientation and bulk or **interface defects** resulted in **low J_{SC}** values, even lower than for undoped films.
- **Undoped Sb_2Se_3 thin-films** deposited by **RF-MS** on FTO and CdS were characterized by a very **high J_{SC}** (probably also thanks to the very high $\Sigma TC(l \neq 0)$ values), but only poor **V_{OC}** values
- **NaF layer** induced a decrease in V_{oc} and a substantial increase in J_{SC} when coupled with Cu-doped Sb_2Se_3 thin-films; after an additional annealing at 175°C for 150 minutes overall cell performance were improved since a **good V_{OC}** value was recovered in the face of a decrease **not excellent J_{SC}** value, which is however much higher than the one achieved without NaF (Figure 4.53).

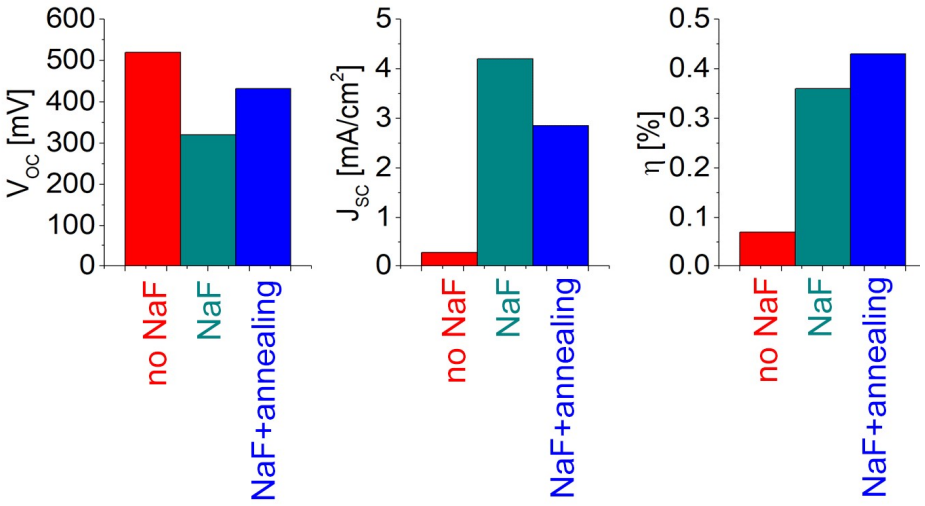

Figure 4.53 – Voc, Jsc and FF for three different cells based on Cu:Sb_2Se_3 films, without or with NaF layer, without or with annealing

To exploit all the "good" results showed by different type of films, a set of different Sb_2Se_3-based solar cells with the architectures illustrated in Figure 4.54 were produced, and with p-region thicknesses detailed in Table 4.9. In particular the cells A2 to A6 employ a

Sb_2Se_3 bilayer sequentially deposited via RF-MS first and then via LT-PED, resulting in a ZnO:Al/ZnO/CdS/Cu:Sb_2Se_3(PED)/Sb_2Se_3(MS)/NaF/ FTO/Glass cell configuration. On the contrary, the B2 to B4 cells were assembled with the reversed sequence (LT-PED first and then MS), creating a ZnO:Al/ZnO/ CdS/Sb_2Se_3(MS)/Cu:Sb_2Se_3(PED)/NaF/FTO/Glass cell configuration.

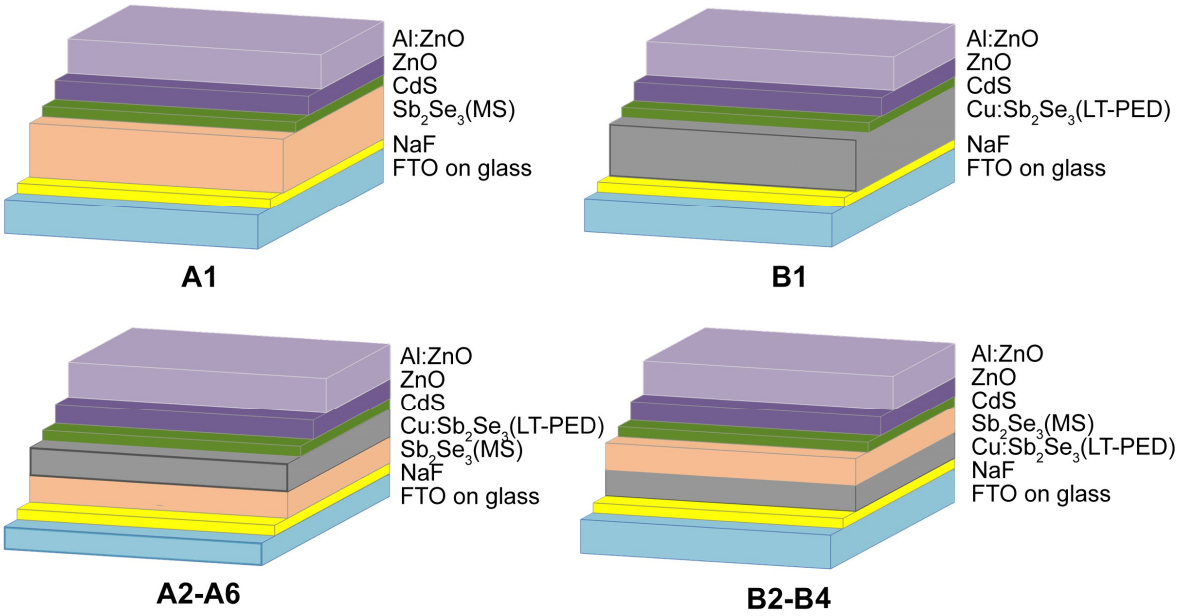

Figure 4.54 – Solar cells architectures with single and double Sb_2Se_3 layer.

Table 4.9 – Thickness of the layers deposited by MS and LT-PED in the different tested cells

Sample	***RF-MS layer [nm]***	***LT-PED layer [nm]***
A1	1200	0
A2	1100	100
A3	950	250
A4	800	400
A5	400	800
A6	200	200
Sample	***LT-PED layer [nm]***	***RF-MS layer [nm]***
B1	1200	0
B2	1000	200
B3	200	1000
B4	100	1100

All the films were characterized by **XRD** and a high crystalline quality was revealed, but with l=0 dominant orientations, especially (020), (120), (130), where the ribbons lay parallel to the substrate. However, for some samples with mixed RF-MS/LT-PED layers like A3, A4, A5, and B3, orientations with $l \neq 0$ values, especially (041), (061), and (141), were as pronounced as or even more than (hk0) peaks. This is generally the case of thicker layer grown by RF-MS, in agreement with previous results obtained with this technique.

SEM was also used to characterize the bilayer solar cells (Figure 4.55). As depicted in Figures 4.55b and 4.55d, the layers formed by the PED/sputtering methods are indistinguishable, suggesting seamless crystalline continuity across the active cell region. The top-view SEM images for a typical sputtering-terminated surface (B4 cell) of a Sb_2Se_3 (MS)/Sb_2Se_3 (PED)/NaF/FTO/Glass structure is shown in Figure 4.55a, while the image for a PED-terminated surface (A5) is shown in Figure 4.55c. The PED-terminated surface exhibits higher roughness and a needle-like texture, whereas the sputtering-terminated surface shows larger, more compact grains.

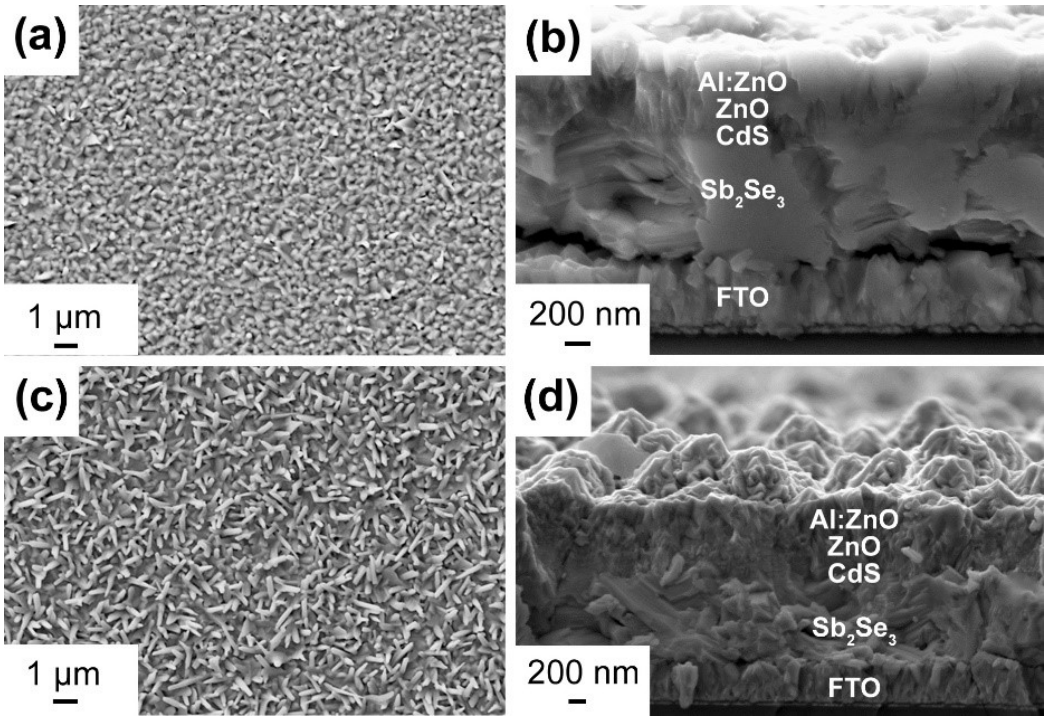

Figure 4.55 - SEM images of: (a) B4 cell MS-terminated surface and (b) B4 cell cross section; (c) A5 cell PED-terminated surface and (b) A5 cell cross section.

Figure 4.56 shows the performance of the A-series photovoltaic devices, together with B1 for comparison, while Figure 4.57 shows the performance of the B-series photovoltaic devices, together with A1 for comparison. A1 and B1, indeed, can be also seen as the two extremes cases, having a completely sputtered (A1) or PED-grown (B1) Sb_2Se_3 p-region.

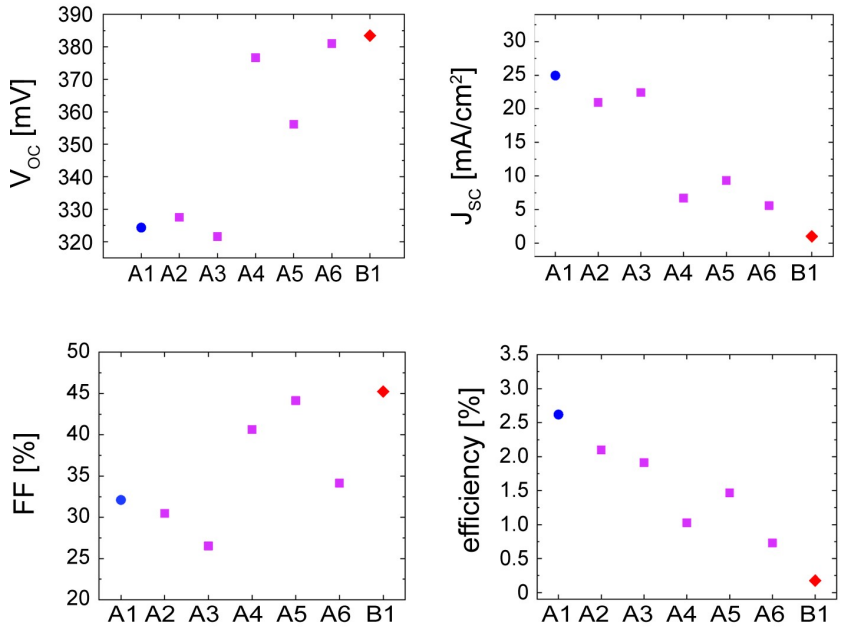

Figure 4.56 - Photovoltaic performances of the different A-series solar cells (violet squares) compared to the completely PED-grown Cu:Sb_2Se_3 solar cell (red rhombus), B1, and the completely sputtered Sb_2Se_3 solar cell (blue circle), A1.

For A-series devices it's evident that as the PED Cu:Sb_2Se_3 layers increase in thickness, both Voc and FF tend to rise. In fact, the Cu: Sb_2Se_3 layer only deposited by PED demonstrates the peak Voc and FF values. However, Jsc drops significantly with thicker PED-layers, leading to reduced overall efficiencies.

For B-series devices, which opposite PED/MS order of depositions, the trends are presented in Figure 4.57. Similarly, as PED layer thickness increases, both Voc and FF rise, but Jsc starts to decline. Notably, the Jsc only starts diminishing for PED Cu:Sb_2Se_3 layers exceeding 100 nm in thickness. Among the cells examined, the B4 solar cell, with a 100 nm PED-grown Cu:Sb_2Se_3 layer followed by a 1 µm sputtered Sb_2Se_3 layer, stands out with the highest efficiency.

Table 4.10 summarizes the average and peak values for all devices.

It's clear that thicker Cu:Sb_2Se_3 PED-grown layers lead to more consistent data, particularly regarding J_{SC} and efficiency, accompanied by higher R_{sh}, lower J_0, and N values closer to 1. Significantly reduced J_0 values in B-series cells, compared to A1 and A2, suggest a diminished carrier recombination with PED-grown Cu:Sb_2Se_3 layers. However, when these PED-grown layers exceed 100 nm, there's a noticeable drop in J_{sc}. This suggests that while the Cu:Sb_2Se_3 layer limits carrier recombination, it also hinders photocarrier extraction.

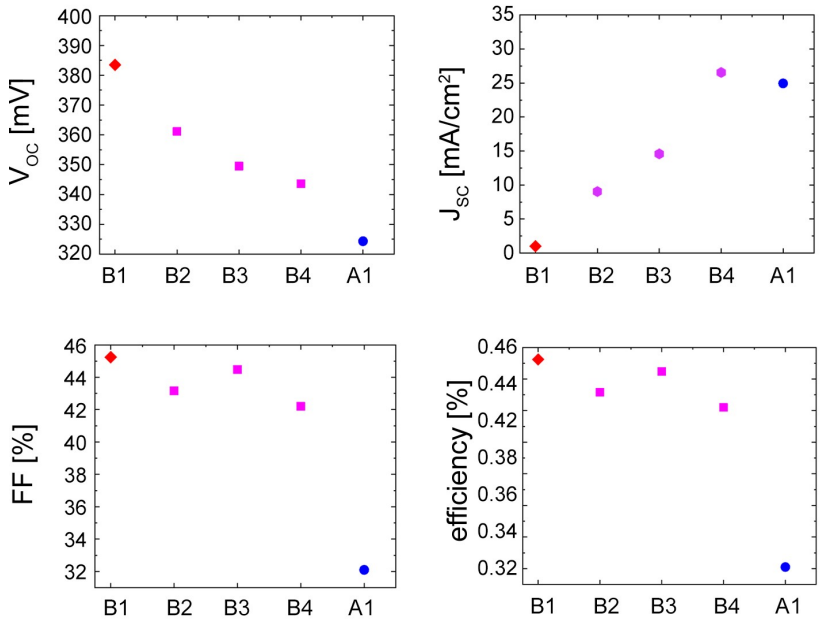

Figure 4.57 - Photovoltaic performances of the different B-series solar cells (violet squares) compared to the completely PED-grown Cu:Sb_2Se_3 solar cell (red rhombus), B1, and the completely sputtered Sb_2Se_3 solar cell (blue circle), A1.

Table 4.10 - Average and record (between parentheses) device performance parameters of the different Sb_2Se_3-based solar cells.

Sample	*V_{oc} [mV]*	*J_{sc} [mA/cm^2]*	*FF [%]*	*PCE [%]*	*Rs [Ωcm²]*	*Rsh [Ωcm²]*	*J_0*	*N*
A1	305±32 (324)	22.5±6.6 (31.2)	29.3±2.2 (32.0)	2.03±0.66 (3.24)	6.86	342.7	$6.7X10^{-3}$	2.7
A2	296±62 (327)	9.15±7.66 (20.95)	37.2±8 (30.4)	0.9±0.6 (2.04)	4.17	149.2	$9.5X10^{-4}$	3.5
A3	343±43 (321)	9.35±7.5 (22.4)	33.9±4.5 (26.5)	0.93±0.52 (1.91)	18.34	4566.6	$6.7X10^{-5}$	2.4
A4	373±9 (377)	5.46±0.95 (6.7)	37.1±1.9 (40.6)	0.76±0.16 (1.02)	9.05	5754.4	$7.4X10^{-5}$	1.3
A5	342±22 (356)	8.08±1.7 (9.32)	41.3±5.4 (44.0)	1.15±0.28 (1.47)	3.6	405.9	$1.7X10^{-3}$	2.5
A6	395±13 (381)	3.67±1.18 (5.58)	35.3±1.1 (34.0)	0.51±0.14 (0.73)	4.45	26833.2	$7.6X10^{-6}$	1.3
B1	385±19 (355)	0.74±0.2 (1.25)	42.6±3.7 (40.6)	0.12±0.02 (0.18)	3.75	21298.0	$4.6X10^{-6}$	1.4
B2	359±3 (361)	9.07±0.47 (9.05)	41.1±1.9 (43.2)	1.35±0.06 (1.41)	2.35	3314.1	$7.2X10^{-5}$	1.3
B3	358±7 (349)	9.89±2.6 (14.58)	45.0±2.5 (44.5)	1.58±0.38 (2.27)	4.59	1633.4	$8.5X10^{-5}$	1.4
B4	347±7 (344)	14.65±3.3 (26.6)	48.8±3.5 (42.2)	2.45±0.39 (3.85)	1.808	460.2	$5.4X10^{-5}$	1.3

Comparisons between PED/MS and MS/PED sequences for similar thicknesses (e.g., A6 vs. B2, A2 vs. B4) reveal that B-series cells, where the PED-grown Cu:Sb_2Se_3 layer is directly grown on NaF/FTO, generally outperform their A-series counterparts. A potential reason is the superior interface quality of the sputtered Sb_2Se_3 with CdS and/or the slightly be V_{OC} values typical of the Cu doped films.

A final optimization of the annealing process time, that allowed Na to diffuse, together with an improvement in the cell contacting, produced a further enhancement of the performance of the cells made with this procedure. In Figure 4.58, the J-V curves of the top-performing cells with A1 and B4 configurations, are compared. The most efficient solar cell, featuring a ZnO:Al/ZnO/CdS/Sb_2Se_3 (MS)/Cu:Sb_2Se_3 (PED)/NaF/FTO/Glass structure with a 100 nm thick Cu:Sb_2Se_3 PED-grown layer and a 1.1 µm sputtered Sb_2Se_3 layer, reached a **PCE of 5.25%**, a **V_{oc} of 343 meV**, a **J_{sc} of 31.4 mA/cm²**, and an **FF of 49%** (shown by the red curve). These values surpass those of the sputtered solar cell (black curve), primarily due to the elevated FF and V_{oc}, credited to the thin Cu: Sb_2Se_3 layer deposited by PED.

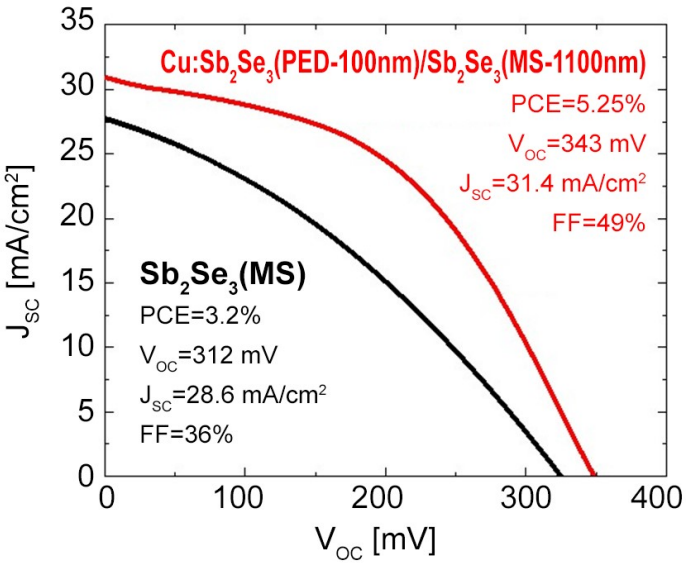

Figure 4.58 - The current density–voltage (J–V curve) of the best Sb_2Se_3 cell obtained entirely by sputtering (black curve) and the best Sb_2Se_3 cell with a Sb_2Se_3 bilayer (red curve).

4.9 -TERS analysis of interfaces

In this study and in general, in the optimization of solar cells performances, interfaces have been proved to play a very important role.

In recent decades, **Tip-Enhanced Raman Spectroscopy** (**TERS**) has emerged as a potential analytical technique for examining a variety of materials including 2D materials, catalysts, polymers, and for studying surface chemical reactions at the nanoscale. As explained in chapter 2, in a TERS experiment a plasmonic metal scanning probe is positioned at the focal spot center of an excitation laser and is scanned across the sample. This leads to the enhancement and confinement of the electromagnetic field (EM) at the tip-apex. This enhancement primarily relies on two phenomena: localized surface plasmon resonance (LSPR) and the lightning rod effect (LRE). The near-field, consequently created at the TERS tip, allows for surpassing the diffraction-limited spatial resolution of a conventional Raman microscope. Leveraging these two effects (enhancement and confinement of the EM) enables the detection of molecules with low Raman cross-section and offers **nanometer-scale resolution**.

In a collaboration with ETH Zurich (*Prof. Renato Zenobi* group), under the supervision of *Dr. Naresh Kumar* and with the co-work of *PhD student Siiri Bienz,* it was proved **for the first time** how TERS can be a powerful tool to study **inorganic solar cells interfaces**, providing important information about what happens in these critical regions with nanometric precision.

4.9.1 - TERS samples preparation

The first step required to face TERS analysis of interfaces, was the preparation of samples for the investigation. The chosen samples for this preliminary test to demonstrate the feasibility of this characterization were:

1. a AZO/ZnO/CdS/Cu:Sb_2Se_3/Mo/Glass cell
2. a AZO/ZnO/CdS/Cu:Sb_2Se_3/FTO/Glass cell

Since no previous work could be used as a reference, two different approaches to get thin cross-section samples of the cell were tried:

- **TEM-like lamella** by Focused Ion Beam (FIB) processing
- Sample cut and thinning by abrasive polishing

In the first case a tiny cross-section slice was cut from the area of the solar cell where all the interfaces are present, with a final lateral dimension of 24x2 μm^2, was prepared. SEM images of some intermediate steps of this procedure on the cell with Mo back-contact are

reported in Figure 4.59. In particular, Figure 4.59b shows the deposition of a tiny protective platinum layer and the following two show the carved volume from the cell around the lamella. The same process was applied for the preparation of a thin lamella sample from the cell with FTO back-contact.

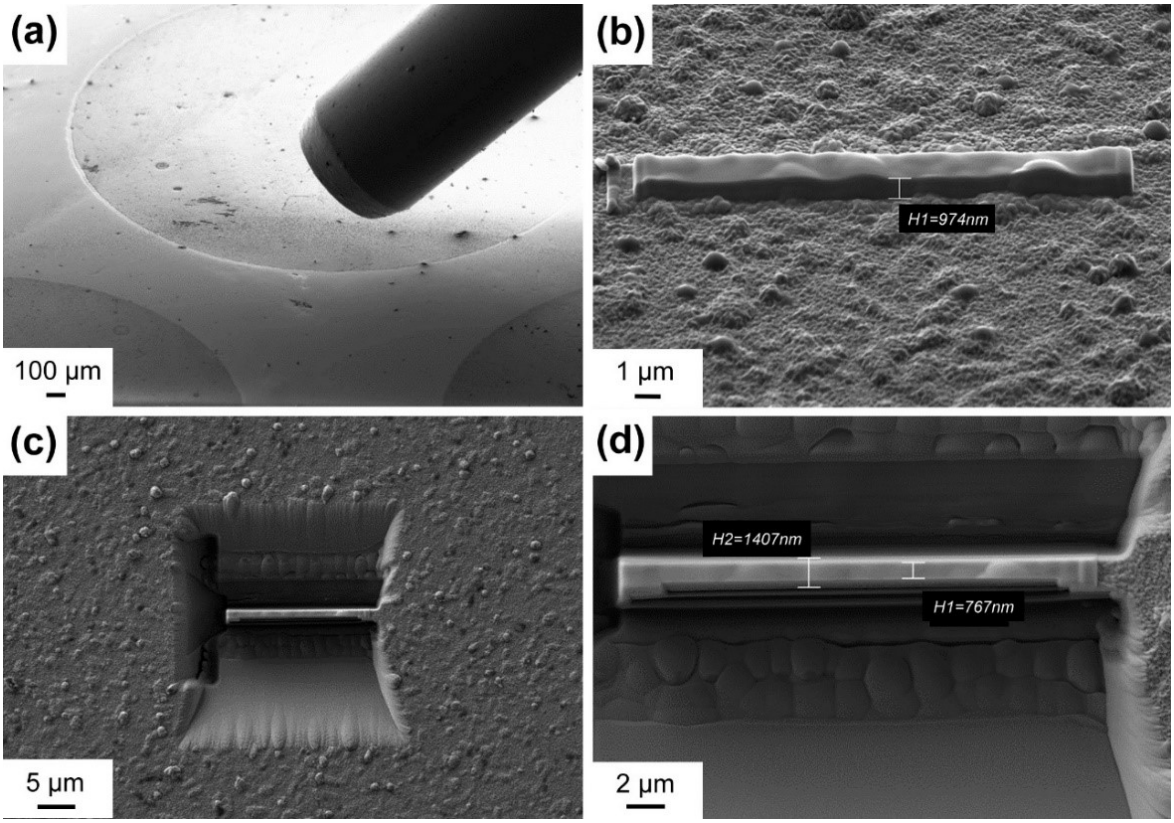

Figure 4.59 – SEM images of the lamella preparation procedure from the cell with Mo back-contact: (a) selected cell; (b) protective platinum layer deposition; (c) top-view of the carved area; (d) higher magnification of the carved area

After the final cut, the result of this process is a thin cross section (Figure 4.60), despite the thickness was higher than the one usually required for TEM because in this case the electronic transparence was not required. The obtained lamellas where fixed on the side of a TEM metal grid and the metal grid was then fixed on a Silicon wafer, to have just Silicon on the background (with a ≈50 microns gap between them).

The second procedure used to thin samples implied the cutting and abrasive polishing of thin slices of the solar cell. In this case both the procedure and final thickness are less refined but on the other hand it is a cheaper and faster sample preparation procedure, that also provides a much longer cross-section area for the characterization.

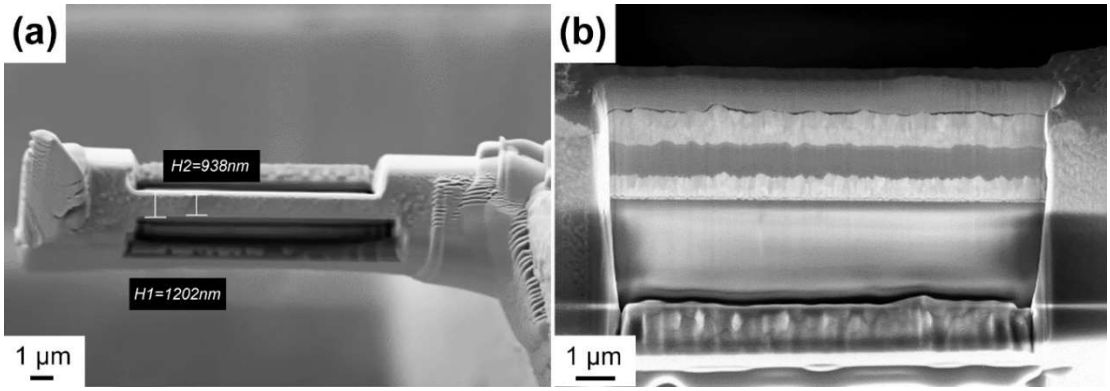

Figure 4.60 – SEM images of the lamella preparation procedure from the cell with FTO back-contact: (a) top view of the cutted lamella; (b) side view of the cutted lamella

The first step was the cut of the sample with a thin diamond coated blade, after the fixing of a second protective glass on the top of the cell with cyanoacrylate adhesive (Figure 4.61).

Slices with a thickness of about 640 µm were obtained. These slices were subsequently fixed on silicon substrates using cyanoacrylate adhesive. This process was essential to ensure the stability of the slices during the subsequent polishing procedure, which was implemented to reduce the thickness of the slices even further.

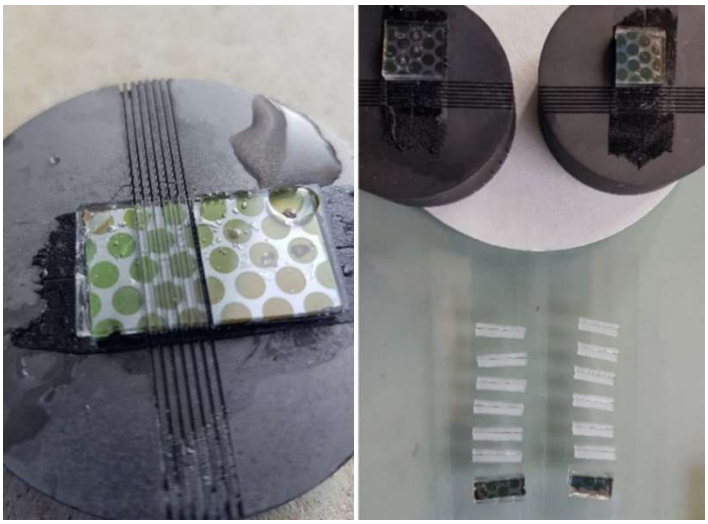

Figure 4.61 – preliminar cut of thin slices from the cells

The thinning by abrasive polishing was made in two different ways: a nearly uniform and flat thinning (F) of slices down to a thickness ranging between 10 and 50 microns, and an intentionally tilted thinning (W), aimed at producing a sample with a wedge shape. The thickness of the latter samples varied, increasing gradually from zero to 600 microns, so that the potential influence of different thickness on the characterization could be explored. (Figure 4.62).

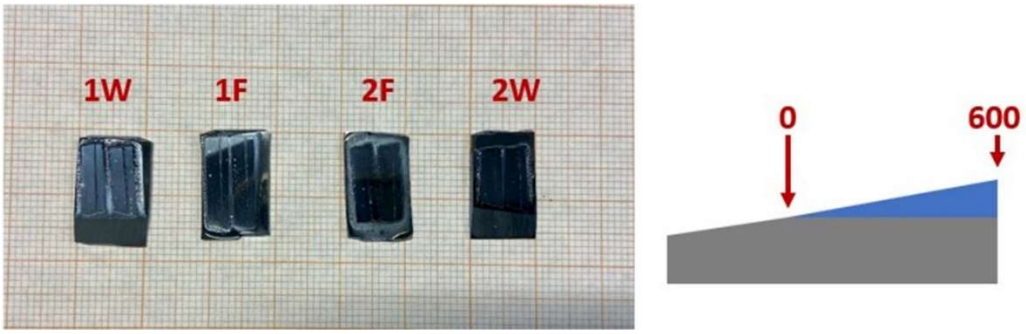

Figure 4.62 – the 4 different samples obtained by abrasive polishing.

After the preparation of the samples, EDS maps were made on them to have an elemental composition counterpart at microscopic level. Unfortunately, the resolution of SEM-EDS was insufficient to accurately assess the real distribution of the elements (Figure 4.63).

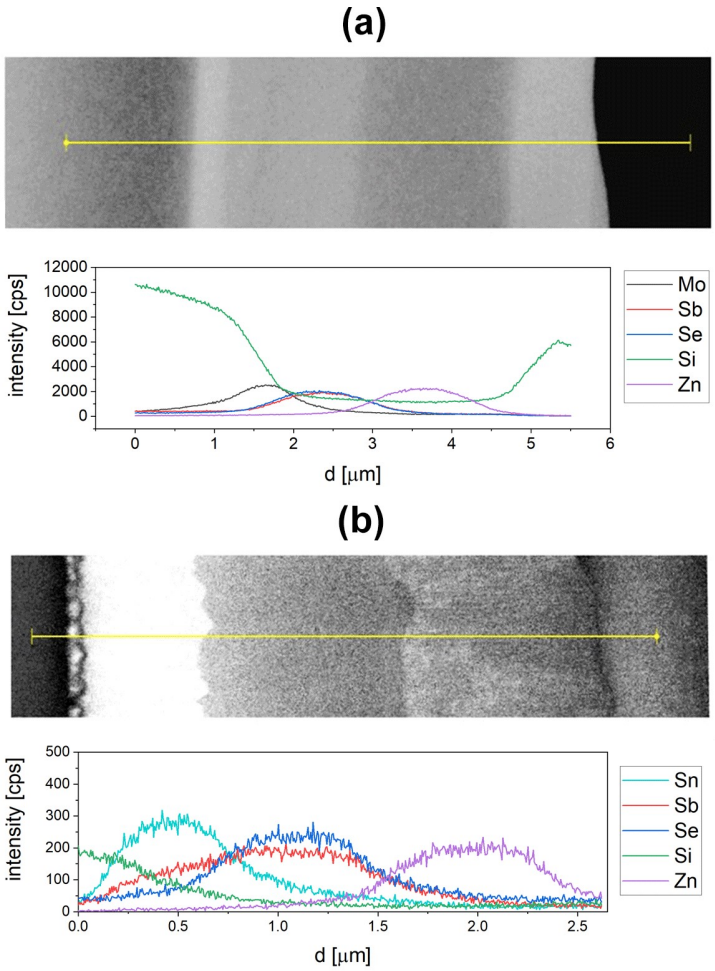

Figure 4.63 – EDS profile along the cross section of: (a) the cell with Mo back-contact; (b) the cell with FTO back-contact.

In this study, our attention was predominantly concentrated on the interface between Sb_2Se_3 and CdS layers. We were interested in this specific interface due to the suspect that it might be contributing to the observed efficiency limitations. By addressing these specifics, we sought to construct a more comprehensive understanding of the underlying mechanisms at play, which could be pivotal in devising strategies for optimization and correction, potentially leading to enhancements in efficiency and functionality of such interfaces in the future.

4.9.2 – Results of TERS analysis

At the moment of this thesis writing, one of the prepared samples, from the cell with FTO back-ground with abrasive polishing thinning, has been successfully analyzed.

The investigation mainly revealed that the Sb_2Se_3 and CdS layers possess an interface region where interdiffusion signals from both layers were observed. For the purpose of this study, the extent of the interface region was determined based on specific criteria: it was defined at points where the signal of the Raman marker band reduced to 2/3 of its peak intensity, or where the I_{Sb2Se3}/I_{CdS} ratio was between 0.6 and 4. To obtain accurate readings, three TERS maps with distinctly identifiable layers were analyzed, as illustrated in Figure 4.64. The computations yielded an average interface region measurement of (270 ± 80) nm.

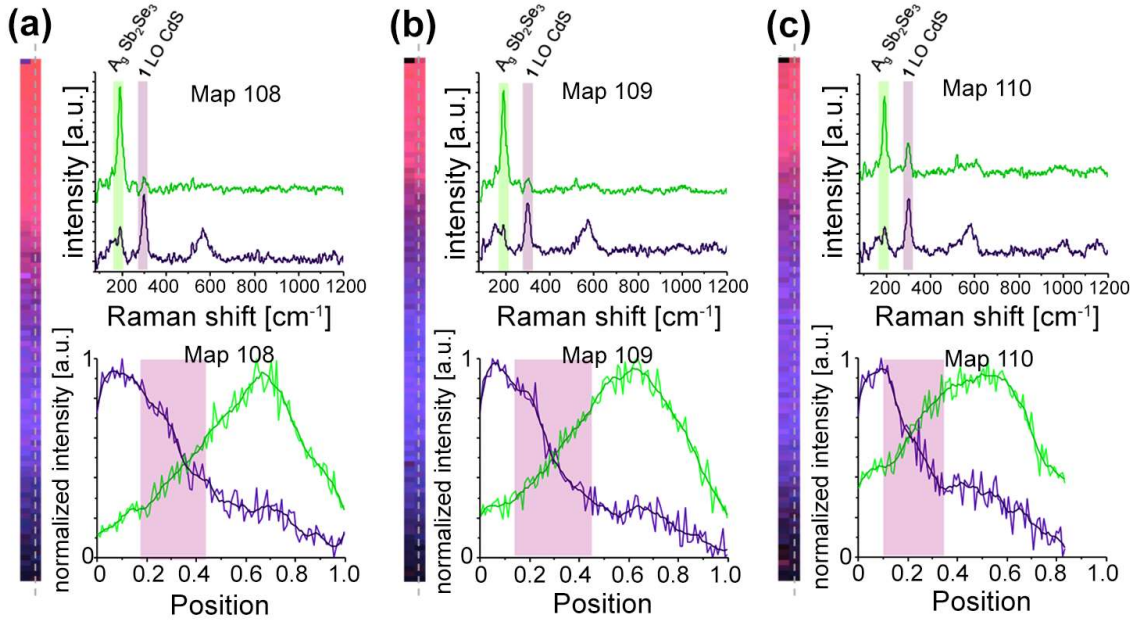

Figure 4.64 – TERS analysis of average interface region, measured in three different maps.

Previous studies have already demonstrated, by means of other techniques, that in analogous thin-film solar cell structures, such as the most common one for $Cu(In,Ga)Se_2$ (CIGS), the interface between the absorber and the CdS buffer layer is more "diffuse" than "sharp" when the buffer layer is deposited by Chemical Bath Deposition (CBD).

A plausible reason for the observed apparent extension of the thickness values of both the interface and CdS layer could be attributed to the irregular surface of the $Cu:Sb_2Se_3$ layer. Figure 4.65 depicts the needle-like structures emerging from the surface of the $Cu:Sb_2Se_3$ before the deposition of CdS layer. If measurements are captured where the CdS layer incorporated these needle structures, a mediated thicker CdS layer could be measured. It's also crucial to acknowledge that the sample preparation method (polishing) could potentially alter the surface structure, thereby impacting the measurements.

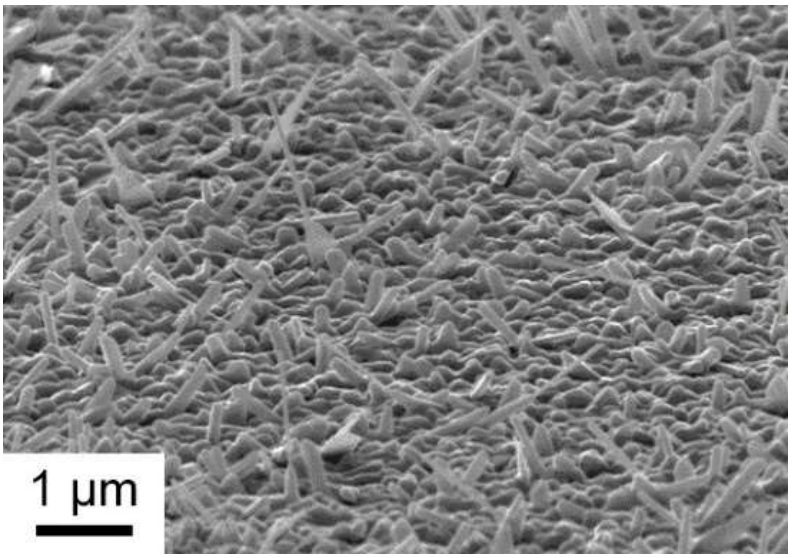

Figure 4.65 - SEM image of the surface of a Sb_2Se_3 film grown on FTO substrate

Aside areas where the CdS and Sb_2Se_3 layers were distinctly separated, we observed portions of the sample exhibiting clear indications of diffusing compounds. A TERS map measuring 500x20 nm, like the one reported in Figure 4.66a illustrates this point, delineating the Raman marker bands for CdS (in violet) and Sb_2Se_3 (in green).

With increments of 10 nm, individual pixels predominantly reveal the Raman marker band of CdS within the Sb_2Se_3 layer (Figure 4.66b). This is a sign of CdS permeating into the Sb_2Se_3 layer.

Along with the Raman bands from Sb_2Se_3 and CdS, a peak around 436 cm^-1 was discerned (Figure 4.66c). Established literature assigns this peak to ZnO. This signal at 436 cm^{-1} is visible only in the pixels where a strong presence of CdS is detected. It is noteworthy that, due to insufficient signal-to-noise ratio, assigning the peak at 436 cm^{-1} was unfeasible

in some spectra from region A. Nevertheless, outcomes seem to indicate that ZnO infiltrated into the CdS layer but not into the Sb_2Se_3 layer.

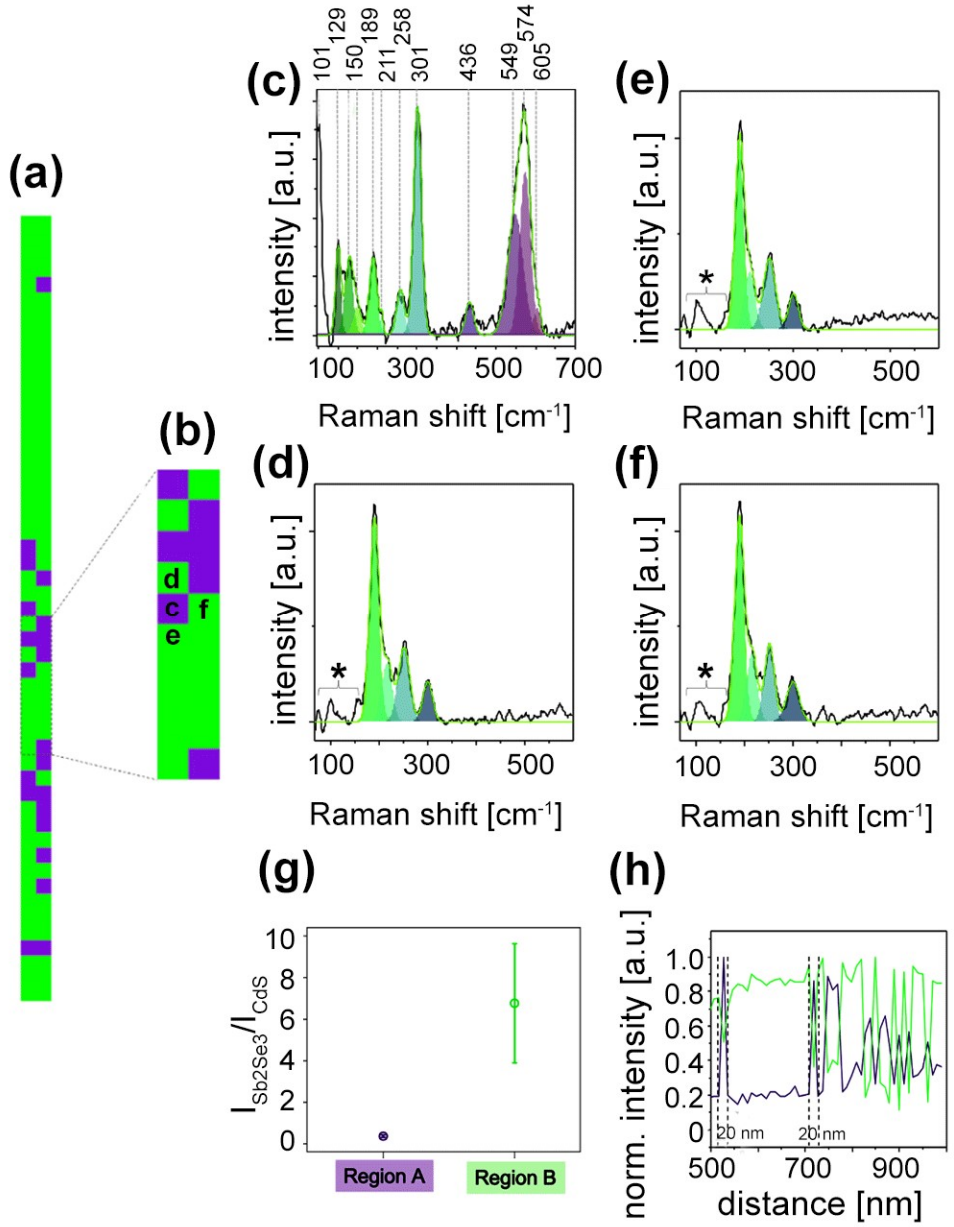

Figure 4.66 - (a) TERS images overlay map, with intensity indicated by Raman marker bands: Sb_2Se_3 at 190 cm^{-1} in green and CdS at 300 cm^{-1} in violet; size: 500x20 nm, with a 10 nm step size. (b) magnification of the region of interest from the TERS map; size: 100x20 nm. (c) a point spectrum at the position marked the map showing distinct signals from CdS and ZnO, with peaks fitted with a Gauss function. (d-f) point spectra from different locations in the map, mainly showcasing Sb_2Se_3 signal at 190 cm^{-1}, with some areas marked with "*" indicating insufficient signal-to-noise ratio for peak fitting. (g) intensity ratio between I_{Sb2Se3} and I_{CdS}, helping to define areas A and B, correlating to the violet and green pixels in the map. (h) normalized TERS intensities of CdS and Sb2Se3 along the axes in the 500x20 nm map, helping to estimate a spatial resolution of about 20 nm. Laser power: 263 µW; acquisition time: 5 sec.

In the 500–600 cm^{-1} spectral range, a pronounced peak is visible, enabling spectrum deconvolution with Gaussian function peaks. At 600 cm^{-1} the secondary phonon mode of CdS is identified and can be fitted with a Gaussian function. However, the high measured intensity between 510 cm^{-1} and 610 cm^{-1} isn't accountable to CdS only. Prior research attributed the Peak at 576 cm^{-1} to the A1 (LO) mode of ZnO, and in cases where oxygen vacancies (Vo) exist, vibrational modes are recognized to occur at 576 cm^{-1}. So this attribution is not trivial. Given that the peak at 540 cm^{-1} can also be related to oxygen vacancies, our assumption leans towards an overlap of the two vibrational modes at 576 cm^{-1}, contributing collectively to the observed peak. This might confirm a penetration of a vacancies-rich ZnO into the absorber layer.

Chapter 5
Ga_2O_3

In this chapter all the characterization research made on Ga_2O_3 thin-films is reported. A meticulously devised protocol was developed specifically for analyzing thin films of this material with micro-Raman, so that limitations of other structural characterizations techniques on this kind of samples, such as XRD, were overcome.
The films here under investigation were deposited using two distinct methods: Metal-Organic Chemical Vapor Deposition (MOCVD) and Low-Temperature Pulsed Electrodeposition (LT-PED).
Raman characterization proved to be a fundamental tool in the study of these samples. In one scenario, it proved instrumental in observing the development of different structural phases, highlighting its utility in distinguishing and identifying varied crystalline structures within the films. In another, it enabled the correlation of Raman spectra with domain size, providing valuable insights into the structural intricacies and alterations due to doping.
Raman structural characterization was an important feed-back in the process of Ga_2O_3 thin-films depositions, allowing the improvement of the functionalities and performance of devices based on this material.
After a brief introduction on the applications and properties of this material, the different experimental scenarios and their results are described in the following paragraphs:

5.1 - Material properties and applications

Gallium oxide (Ga_2O_3) has been gaining more and more interest in the past few years due to its intrinsic characteristics, such as its exceptionally wide bandgap (E_g=4.5 eV) and a high critical breakdown field, approximated at about 8 MV/cm, which surpasses those of other wide bandgap materials like SiC and GaN. These characteristics make gallium oxide a formidable contender for **high-power electronics**, presenting applications that complement those of SiC and GaN, especially today that large accumulation systems, fast charge apparatus and high-power production systems are more and more requested (Figure 5.1).

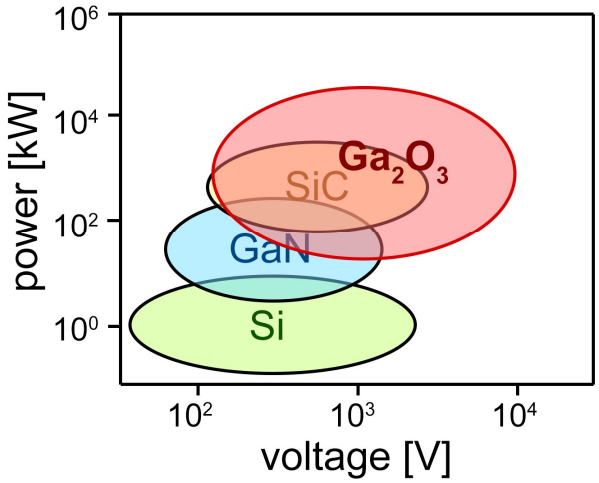

Figure 5.1 – Approximate application range for different materials in high-power electronics.

Moreover, its extra-wide bandgap makes this semiconductor ideal for the creation of **solar-blind detectors** for UV-C radiation (wavelength below 280 nm). At the same time, doping could be the key to have a highly transparent and robust material that can be used in transparent electronics and for **making transparent conducting oxide** (TCO) layers. Heavy doping can be used, as well, to tune the band-gap to specific values of interest.

However, it's essential to clarify that discussing Ga_2O_3 in broad terms can be ambiguous as this material is known to exhibit **five polymorphs**, with only one (**β phase**, monoclinic) being thermodynamically stable, whereas the others are metastable and typically transform to β upon exposure to high-temperature treatments. Studies on the polymorphism of Ga_2O_3 have unveiled various novel polymorphs in addition to the known ones, contributing to a total of six explored polymorphs (although two of them, **ε** and **κ** have been recently attribute to the same crystalline structure), as shown in Figure 5.2.

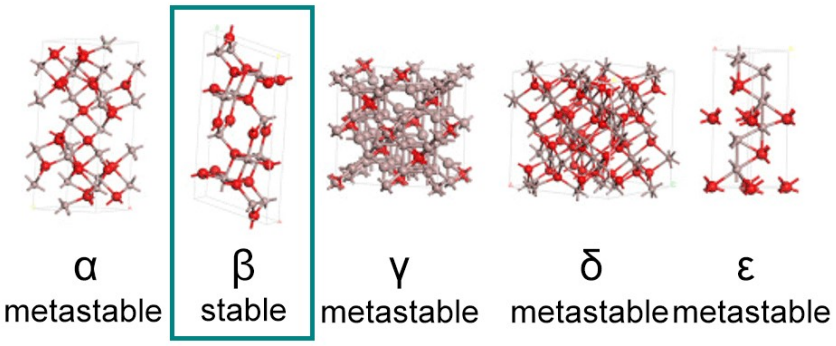

Phase	Symmetry	Space group	Lattice const.
α	rombohedral	$R\bar{3}c$	*a*=4.9825Å *c*=12.433Å
β	monoclinic	C2/m	*a*=12.214Å *b*=3.0371Å *c*=5.7981Å *β*=103.83°
γ	cubic (spinel)	$Fd\bar{3}m$	*a*=8.2376Å
δ	cubic (bixbyite)	$Ia\bar{3}$	*a*=10.00Å
ε	hexagonal	$P6_3mc$	*a*=2.9036Å *c*=9.2554Å
(κ)	orthorombic	$Pna2_1$	*a*=5.0557Å *b*=8.6884Å *c*=9.2759Å

same crystalline structure

Figure 5.2 – Different pholymorps of Ga_2O_3 and their crystallographic cell details

The primary focus of researchers has been mostly on the thermodynamically stable β-Ga2O3 phase, due to its capability to be grown both as a single crystal and as a thin epitaxial layer, facilitating homoepitaxy and a reduction in the density of structural defects. Alloys with Al or In can adjust the β-Ga2O3 band-gap, paving the way for the construction of heterostructures and the generation of a modulation-doped 2D electron gas (2DEG) at the heterojunction, fostering high-performance electronics.

However, β phase also has apparent disadvantages, mainly due to its highly asymmetric monoclinic structure, leading to significant anisotropy of thermal and optical properties and mild anisotropy of electrical properties. Moreover, bulk β-Ga_2O_3 is vulnerable to cleavage, and homoepitaxially-grown epi-layers on certain crystal orientations have shown high density of twin lamellae, which can limit the n-type doping and electron mobility. These challenges can be addressed by selecting different substrate orientations for homoepitaxy or by growing on off-oriented substrates, although these solutions could make homoepitaxy less appealing.

Because of the aforementioned factors, recent research on Ga_2O_3 was extended to include phases that exhibit higher symmetry and more manageable epitaxial conditions than **β**-Ga_2O_3, namely **α** and **κ** (**ε** when the hexagonal cell is used to describe the crystal structure). Properties of these three main phases are reported in Table 5.1.

Table 5.1 - Main known properties of the most common Ga_2O_3 polymorphs

	***β*-Ga_2O_3**	***α*-Ga_2O_3**	***κ*-Ga_2O_3**
Bandgap (E_g) [eV]	4.9	5.2	4.9
Structure	Monoclinic	Rombohedral (corundum)	Orthorombic
Dielectric constant (ε_r)	10	n.r.	10
Electron mobility [$cm^2V^{-1}s^{-1}$] *(theoretical)*	300	n.r.	n.r.

These continuous explorations and developments in the field of Ga_2O_3 are crucial as they aid in enriching our understanding of the material and its potential applications, including its suitability for high-power electronics and its capability to enable advancements in multiple technological fields.

5.2 – Ga_2O_3 thin-films: a difficult characterization context

The required thickness for most of Ga_2O_3 thin-films application is generally low. This low thickness typically results in a low signal for most of the common structural characterization techniques.

In the case of **XRD**, for example, the measurement is mediated over a rather substantial volume/area and the diffraction signal coming from the Ga_2O_3 thin-films is often hidden by the strongest peaks of the crystalline substrates. As a result, even if the main phase can generally be distinguished in an XRD pattern, the presence of secondary phases cannot be addressed.

Also **Raman spectroscopy**, which often proves to be conclusive, unfortunately encounters some challenges in this context. Despite the peaks for each of the main phases have been identified (Table 5.2), the collected signal on these samples is generally quite low.

Table 5.2 – Main Raman peaks for Ga_2O_3 polymorphs. The **highlighted** values are for the most intense peaks; purple values generally overlaps with water vapor peaks; orange values generally overlaps with sapphire peaks

phase	*Raman peaks [cm^{-1}]*
β-Ga_2O_3	111, 115, 145, 170, **200**, 320, 347, 353, 416, 475, 630, 652, 658, 767
α-Ga_2O_3	221, 289, 431, **577**, 692
κ-Ga_2O_3	**82**, 99, 105, 113, 127, 128, 141, **147**, 154, 149, 162, 166, 179, 187, 189, 209, 230, 252, 279, 301, 318, 348

So, the measurement of Ga_2O_3 thin-films Raman spectra requires relatively long measurement times. Moreover, as in the case of XRD, the signal from the crystalline substrate significantly interferes with the signal collection of the material itself. Only some peaks of Ga_2O_3 phases indeed have sufficiently high signals and/or do not overlap with those of the sapphire (the most frequently used substrate in this research), the spectra from the air (or more precisely, from water molecules primarily present in the air in the form of humidity, which may differ in concentration and hence in intensity from day to day), or sometimes other phases of the Ga_2O_3 itself.

For all these reasons, a **specific protocol** for analyzing Ga_2O_3 thin-films with Raman spectroscopy was developed. Before each set of measurements, the signal from the sapphire substrate and the "air" was collected under the same conditions (laser and time) that then was intended to be used for the sample studies. The signal from the air, in particular, proved to be fundamental because, even though the instrument's environment was always maintained at controlled temperature (about 21°C), relative humidity wasn't and could be

subject to huge daily variations. Only once these two spectra were available (Figure 5.3), an accurate subtraction of the background signal could be executed, thus obtaining enhanced spectra for the study of various phases of Ga_2O_3.

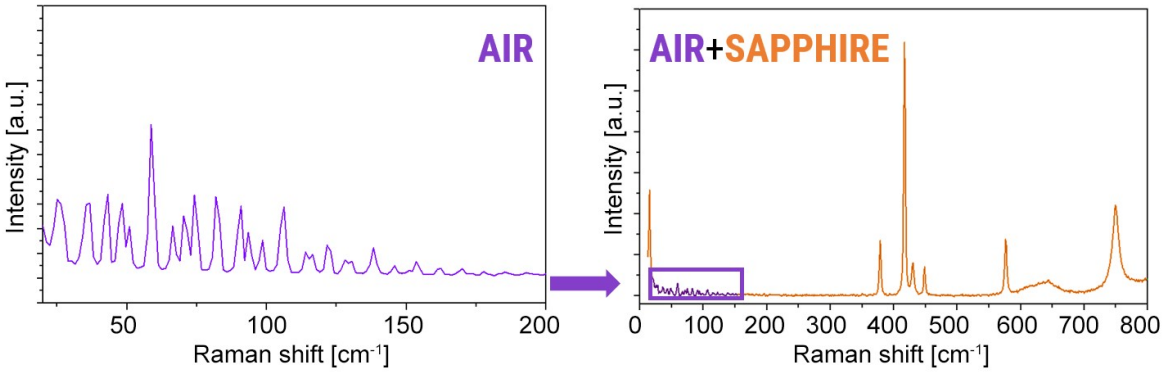

Figure 5.3 – Raman Spectra of Air (water vapor in air) and Sapphire substrate

A fundamental study to validate this protocol was conducted on a particularly challenging Ga_2O_3 sample, grown using Metal Organic Chemical Vapor Deposition (**MOCVD**) on a large sapphire wafer. In this instance, the surface morphology exhibited noticeable variations across three distinct zones of the sample, directly correlated with the flow direction and concentration of the precursors (Figure 5.4).

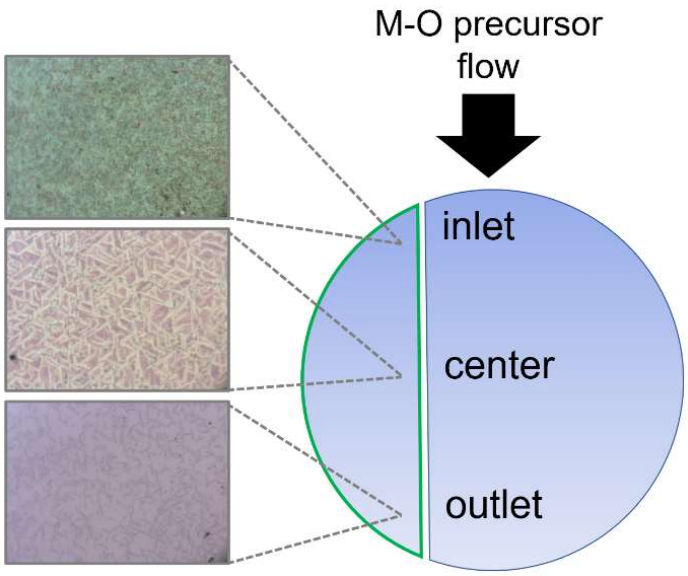

Figure 5.4 – schematic wafer image with morphological images

The use of such a large substrate was intentional, for a preliminary exploration of the effect of different growth parameters, such as metal organic precursors flows,

concentrations and substrate temperatures, all at once by exploiting the gradients generated inside the reactor and the different resulting conditions in different part of the wafer.

On this kind of sample XRD was only able to clearly uncover the main Ga_2O_3 phase, i.e. β, which was present on all the analyzed areas, and secondary phases in a few cases. Instead, Raman spectra of the three different zones shown in Figure 5.4, after the aforementioned meticulous subtraction of "background signal", more clearly revealed the presence of secondary phases (Figure 5.5). In the "inlet" part of the wafer, the clear presence of three distinct phases was highlighted: the stable β and the two metastable phases α and ε/κ. α phase disappeared in the "central" part, while it then reappeared in the "outlet" part of the sample, even if in a different ratio.

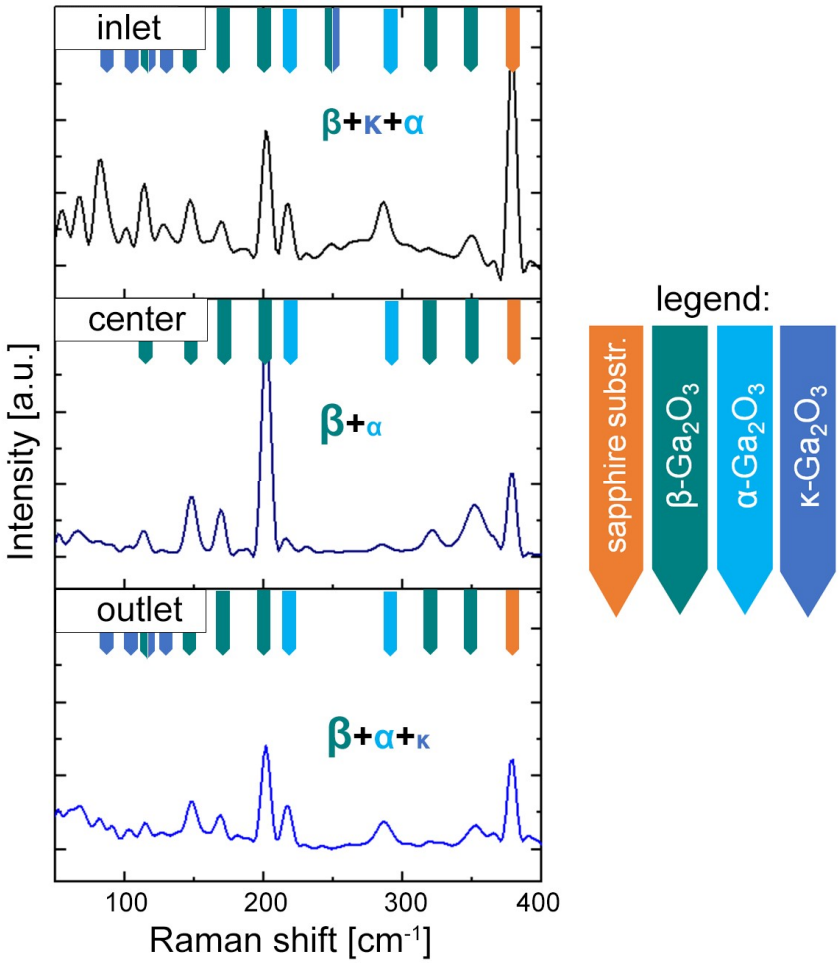

Figure 5.5 – Raman spectra collected in different areas of the wafer. Main peaks are identified accordingly with the color code shown on the right.

This result also proved that Raman spectroscopy can be used to make detailed **maps of the sample composition**.

5.3 – Effect of Si-doping on epitaxial Ga_2O_3 films deposited by MOCVD

As anticipated in the previous paragraphs, κ-Ga_2O_3 (also known as ε-Ga_2O_3 when the hexagonal cell is used to describe the crystal structure) and α-Ga_2O_3 are studied as potential rivals to β-Ga_2O_3 in the domain of high-power electronic applications. These polymorphs exhibit a higher unit cell symmetry compared to the monoclinic one, which makes them more compatible with relatively economical crystalline substrates like sapphire. Additionally, for these metastable polymorphs, a comparatively broad range of synthesis parameters has been determined for various epitaxial deposition techniques of both physical and chemical vapor phases (PVD and CVD, respectively), facilitating their single-phase stabilization.

Remarkably, orthorhombic **κ-Ga_2O_3** displays a unique spontaneous polarization along the (001) direction, estimated to exceed that of GaN (23–26 μCcm^{-2}). This property is predicted to allow the confinement of high mobility 2D electron gases (2DEGs) at κ-Ga_2O_3/$Al_xGa_{2-x}O_3$ heterointerfaces, showcasing higher carrier densities ($n \approx 10^{14}$ cm^{-2}) compared to what is achievable in β-based heterostructures, potentially without the requirement for modulation doping. The exploration of these polymorphs' properties and synthesis parameters can lead to refined understandings and advancements in the technological applications of gallium oxide.

Doping of Ga_2O_3 films can be obtained "ex-situ", like in the case, for example, of thermally-induced diffusion of Sn. But when Ga_2O_3 thin-films are deposited through CVD, and more precisely through metal-organic vapor phase epitaxy (MOCVD), they can be also directly doped during the deposition process. Si-doping, for example, have been successfully obtained by using a flow of silane (SiH_4). Si doping was expected to partly dissolve into κ-Ga_2O_3, predominantly occurring as Si_{Ga} substitutional in the tetrahedral Ga3 lattice sites and consequently creating a shallow donor state.

Epitaxial (001)-oriented κ-Ga_2O_3 thin-films on sapphire substrate are characterized by a peculiar columnar structure, induced by the presence of **120°-rotated domains**. The width of these domains is usually in the range of 5-10 nm. They usually have a detrimental role in the in-plane electronic transport and in the possibility to obtain conductive doped films.

In this part of the work, it is reported that the conventional rotational domain size in **electrically conductive Si-doped κ-Ga_2O_3 layers** deposited on *c*-plane **sapphire** substrates, has the potential to enlarge from approximately 10 to around 300 nm. More in

detail, this phenomenon proved to be deeply connected to the incorporation of silane throughout the MOCDV deposition process. This incorporation can either increase the mobility of the adsorbed species during the growth phase or reduce the initial nuclei density, leading to the formation of larger domains.

Both undoped and doped κ-Ga_2O_3 thin-films were deposited by MOCVD at IMEM-CNR. Increasing Si-doping in the sample was obtained by increasing the **silane flow** (Φ_{SiH4}=5-10-15-17.5 sccm). These samples were then studied by confocal Raman spectroscopy, using back-scattering geometry for both the sample **surface** and **cross-section**. Cross-section measurements were carried out in collaboration with Paul Drude Institute (PDI) in Berlin by *Dr. Markus Wagner* group. Surface back-scattering evaluations were conducted on all samples that were also previously investigated by Transmission Electron Microscopy (TEM) and Atomic Probe Tomography (APT), in order to have a reference. The latter analyses, in particular, brought to light that the domain size in Si-doped samples increased with increasing Φ_{SiH4}.

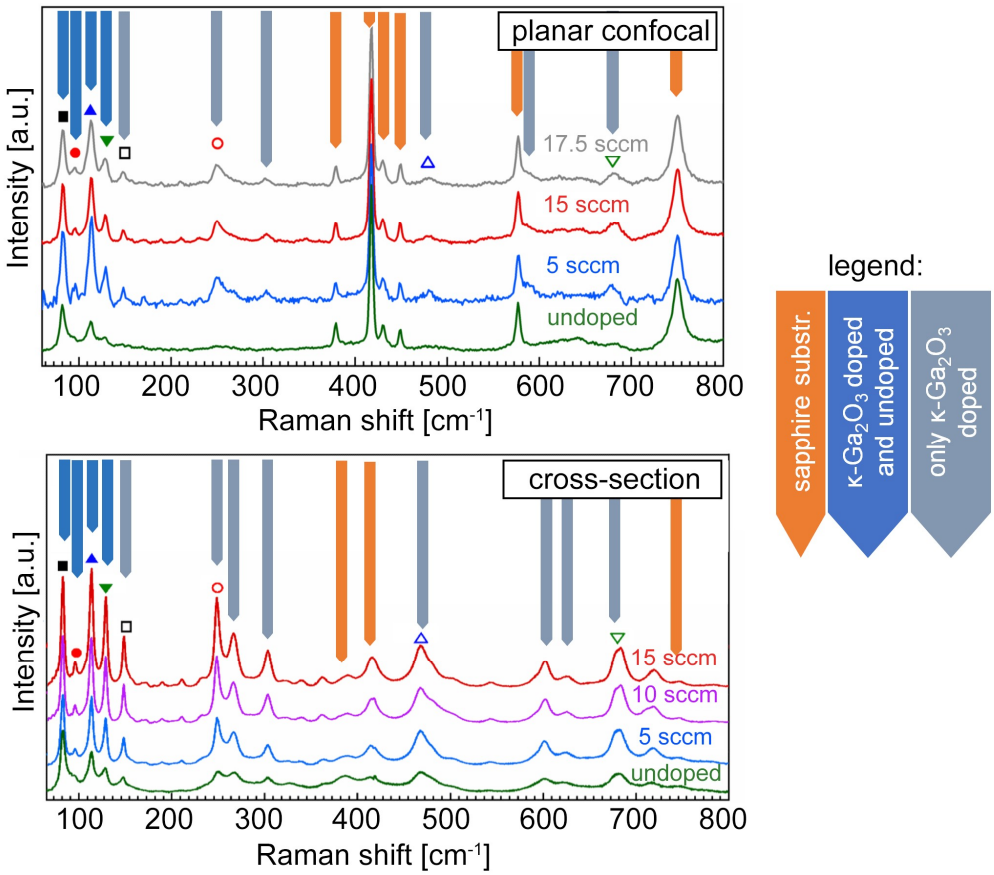

Figure 5.6 – Planar confocal and cross-section Raman measurements of doped and undoped κ-Ga_2O_3 thin films. The Si-doping is expected to be proportional to the silane flow (Φ_{SiH4}) here reported. Symbols on specific peaks are used as a quick reference for plots in Figure 5.7. Main peaks are identified accordingly with the color code shown on the right

The Raman spectra were measured using two distinct laser wavelengths (633 and 532 nm). Both wavelengths produced analogous results. Cross-section measurements were performed on the same samples utilizing a 532 nm laser wavelength parallelly polarized to the *c*-plane. All the collected spectra ranged between 50–800 cm^{-1}. The daily recorded "air" spectrum was subtracted from all the recorded spectra and then they were normalized on the most intense peak from the sapphire substrate (Figure 5.6).

The analysis identified only modes of the orthorhombic κ polymorph of Ga_2O_3, in agreement with the findings from XRD and TEM investigations. Despite varying analysis setups, both surface and cross-section spectra parallelly underscored analogous differences amongst undoped and doped films.

More specifically, the peak-fitting analysis of selected peaks in both setups indicates that the introduction of the Si dopant during deposition influences the **intensity ratio** among several Raman modes (Figure 5.6).

In particular, as the domain size of samples increased with larger SiH_4 flows, a substantial decrease in the Raman peaks' **FWHM** was observed (Figure 5.7). This evidence is more pronounced in cross-sectional spectra, where the substrate contribution is minimized, and κ-Ga_2O_3 peaks are more discernable. Furthermore, the most substantial reduction of the peak width of all phonon modes was observed between the undoped and 5 sccm sample.

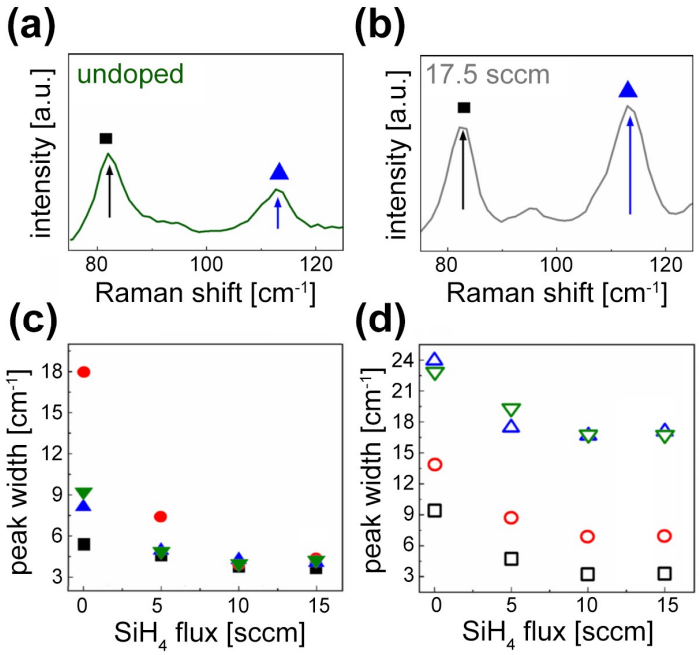

Figure 5.7 – Inversion of intensity for two different peaks at about 82 and 114 cm^{-1}in undoped (a) and doped (b) samples. Decrease of FWHM value for two sets of main Raman peaks, (c) and (d), as a function on Si-doping. Peaks symbols are referred to those reported in Figure 5.6.

This meticulous study in both configurations revealed the complex impact of doping, contributing significantly to the understanding of the structural properties of κ-Ga_2O_3 layers. Moreover, these results provided a few keys to distinguish between the Raman spectra of undoped and doped layers, offering a much **easier** and **nondestructive** way to quantify the increment in average domain size.

The uniform trend in the narrowing of Raman peaks, emphasized in both confocal and cross-sectional configurations, could generally be associated with the alteration in phonon lifetimes due to varying domain sizes of the samples examined. To elaborate, in samples with the smallest domains around 5–20 nm (i.e., no SiH_4), phonons are notably influenced by boundary scattering at the domain wall. This leads to a reduction in both the phonon mean free path and phonon lifetimes, causing substantial broadening of the Raman modes' peak width.

The inclusion of silane, on the contrary, resulted to increase the domain size, which in turn reduces the impact of domain boundary scattering, leading to a noticeable and proportional reduction in the Raman peak width. This effect, however, becomes progressively less significant for the largest domains, over 100 nm (i.e., Φ_{SiH4}>5 sccm), when their size is large enough to have negligible influence phonon lifetimes or wavelength.

Raman also exhibited significant potential for exploring the role of the dopant in this material system, for instance, the alteration in intensity of specific peaks. The unraveling of this result, however, needs dedicated research, for a more detailed understanding of the implications of dopant roles and their interaction with the matrix material.

5.4 - Ga_2O_3 thin-films deposited by LT-PED

Ga_2O_3 thin films have been also deposited, for the **first time**, by **LT-PED** technique. Samples were studied by varying the deposition parameters in order to assess whether the PED technique was suitable for the production of Ga_2O_3 films or not. The characterizations mainly focused on the following aspects: XRD measurements were used to determine which phases were predominant in the sample and to what degree of crystallinity they exist; Raman measurements were used to gain deeper insights into the phase of the sample and the possible presence of secondary phases.

As in the case of depositions of Sb_2Se_3 thin-films described in Chapter 4, the deposition of Ga_2O_3 by LT-PED was studied starting from the variation of deposition parameters, in order to identify the optimal deposition conditions for different substrates.

Four kinds of experiments were designed to answer as many research questions:

1) **Amorphous substrate** – The first inquiry was whether Ga_2O_3 can crystallize effectively even on an amorphous substrate, thanks to the high energy typical of LT-PED. This would require a detailed exploration of the interaction dynamics between the substrate and the depositing material, analyzing how the lack of a crystalline structure in the substrate impacts the crystallization of Ga_2O_3.
2) **Sapphire substrate** - Given the crystalline nature of sapphire and the previous positive results obtained with MOCVD, another significant question was whether Ga_2O_3 can be effectively deposited on it. The affinity between the crystalline structure of sapphire and the Ga_2O_3 could potentially facilitate the effective crystallization and stabilization of specific phases, despite the higher energy of LT-PED may lead to different results.
3) **Polymorphic variations** - The exploration of the deposition parameters also aims to uncover if different polymorphs of Ga_2O_3 can be obtained under different conditions. Understanding if this option is available would be of paramount importance to define which are the possible applications.
4) **Influence of doping** - Doping elements like Sn and Ge can potentially modulate the crystalline structure of the Ga_2O_3, so the study was intended to understand whether the incorporation of these elements can favor the formation of specific polymorphs or not. Identifying how these dopants influence the structural attributes and stability of the different Ga_2O_3 polymorphs can provide crucial insights into the possibility to tune material's properties.

For the aims of the first part of this study, an undoped target was prepared by pressing and sintering 50 g of Ga_2O_3 powder, featuring a purity of 99.999% (5N), at 200 bar and then up to 1000°C. Proper pressure and temperature ramp were used to reduce as much as possible inner stress in the target.

The first substrate investigated for the PED growth was soda-lime glass. This substrate was particularly advantageous due to its significantly low cost. The substrate was 1"x1" in size.

As in the case of other oxide thin-films deposited by LT-PED, an inert working gas generally leads to losses of the extremely volatile oxygen. So, **oxygen** is usually introduced in the LT-PED chamber for the plasma generation.

As a first step, it was essential to determine which oxygen flow was sufficient to support the generation and maintenance of a stable and well-localized plasma plume. The distance between the target and the substrate was fixed at 6 cm, and the distance between the target and the electron gun was set to 2-3 mm. In this condition, it was thereby assessed that 35 sccm of O_2 flow can produce a good plasma plume.

The initial depositions were conducted at room temperature (RT) while the acceleration voltage of the electron gun was varied. Despite after the growth the substrate was still completely transparent, colored interference fringes were clearly visible as a function of the illumination angle, indicating that material was deposited. Unfortunately both Raman spectroscopy and XRD showed that only amorphous films were deposited. Evidences of crystalline Ga_2O_3 began to manifest only when the substrate temperature was increased up to 400°C. The corresponding XRD pattern and Raman spectrum are reported in Figure 5.8.

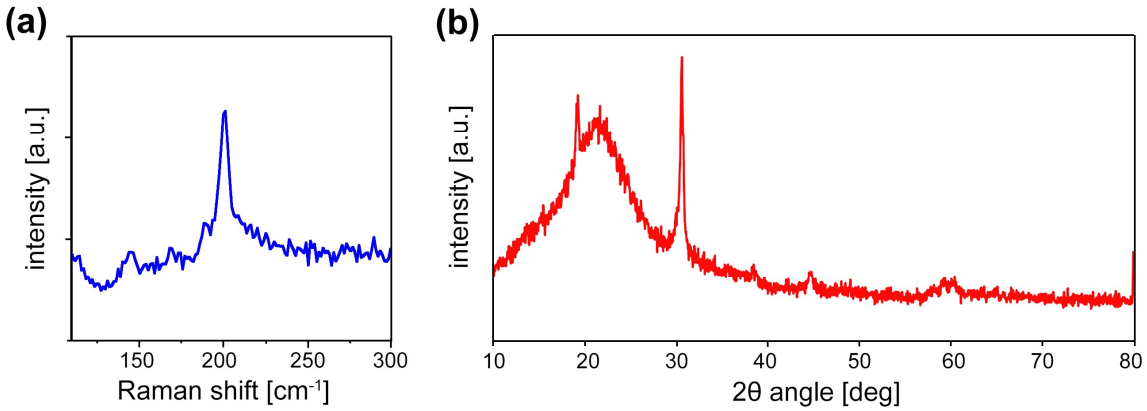

Figure 5.8 – (a) Raman spectrum and (b) XRD patter of the Ga_2O_3 thin-film deposited on glass by LT-PED at 400°C.

Even at this higher substrate temperature, Ga_2O_3 films appeared to exhibit a mixture of amorphous and crystalline phases. The main peaks in Figure 5.8, however, are typical of the **β phase**.

The second series of experiments was made on sapphire substrate: specifically, a *c*-oriented (0001) crystalline sapphire sample, chosen to leverage the lattice compatibility between the substrate and the β-phase of Ga_2O_3.

LT-PED depositions were done at different substrate temperature. At T>530°C, XRD showed three reflection peaks that could be solely attributed to the β-phase of Ga_2O_3 (2θ=18.9°, 38.4°, 59.2°), without indications of the presence of secondary phases. Also Raman spectroscopy confirmed the presence of just the **β-phase**, independently on the substrate temperature, as shown in Figure 5.9a.

Also the impact of different acceleration voltages was studied, yielding the outcomes depicted in Figure 5.9b, where it is clear that a good crystallization of β-Ga_2O_3 was obtained also at 14 KV (even if a low deposition rate is achieved).

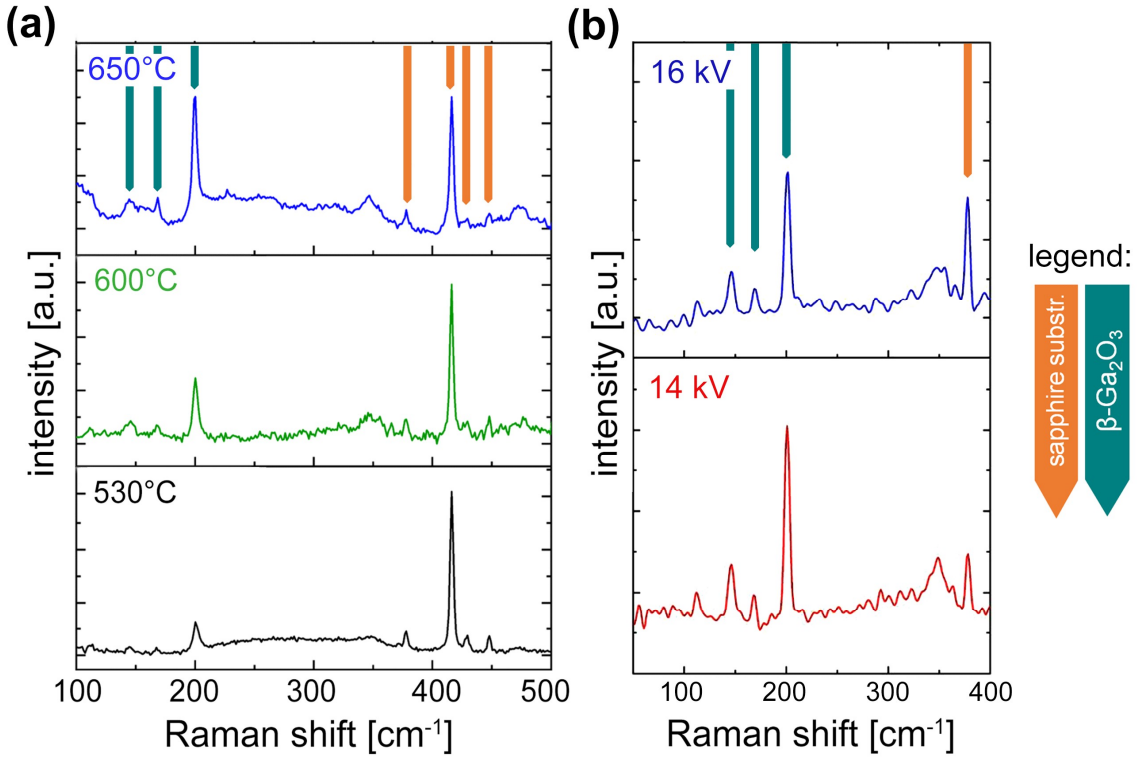

Figure 5.9 – Raman Spectra of Ga_2O_3 thin films grown on sapphire by LT-PED: (a) at different substrate temperatures; (b) with different accelerating voltage. Main peaks are identified accordingly with the color code shown on the right

The incorporation of a dopant within a semiconductor has consistently proven to be a meticulous and sometimes notably challenging procedure. The significance of this process

is paramount for device fabrication since the inclusion of dopants enables the ability to tailor a semiconductor conductivity. Various studies concerning gallium oxide have concluded that p-type doping is generally not possible, while numerous attempts have been successfully made towards n-type doping.

Sn, has emerged as a particularly effective donor element. This element has been utilized to attain conductive Ga_2O_3 films through various techniques such as Pulsed Laser Deposition (PLD), Molecular Beam Epitaxy (MBE), and Chemical Vapor Deposition (CVD), but never with the Pulsed Electron Deposition (PED) technique. Preliminary results obtained in the growth and characterization of Sn-doped Ga_2O_3 films are here shown.

First of all, Ga_2O_3 targets containing 10% atomic Sn, were fabricated. To verify the quality of the prepared targets, several EDX measurements were conducted to determine the dopant distribution within the material. The recorded concentrations clearly indicate that the tin distribution within the target was not as anticipated — 10% atomic — but substantially lower in most of the measured points: 0.5%-1%. On the contrary, stoichiometry was correct only in a limited number of examined points. As revealed by SEM images, the target surface indeed appeared notably heterogeneous and rough (Figure 5.10), characterized by peculiar prismatic structures which are present almost over the entire surface of the target.

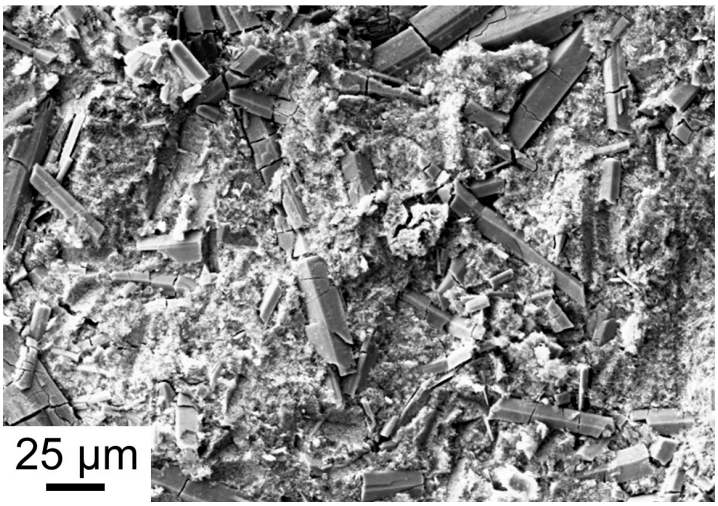

Figure 5.10 – SEM image of the surface of a Sn-doped Ga_2O_3 target

EDX measurements further highlighted that those prismatic crystals are predominantly composed of gallium oxide, around which aggregates tin oxide. Throughout the rest of the target, a varying dopant concentration between 1.2% and 1.8% was be observed. The dopant distribution is markedly non-uniform because of the separation of its two components (Ga_2O_3 and SnO_2).

The deposition of **Sn-doped Ga_2O_3 films** on quartz substrate were carried out with the accelerating voltage set at 16 kV, while the substrate temperature was varied from 480 °C to 615 °C. An EDX map was employed to visually highlight the distribution of various elements within the deposited film. The images reaffirmed that also the Sn distribution within the film is definitely non-uniform, primarily segregating near the Ga_2O_3 larger crystals (Figure 5.11).

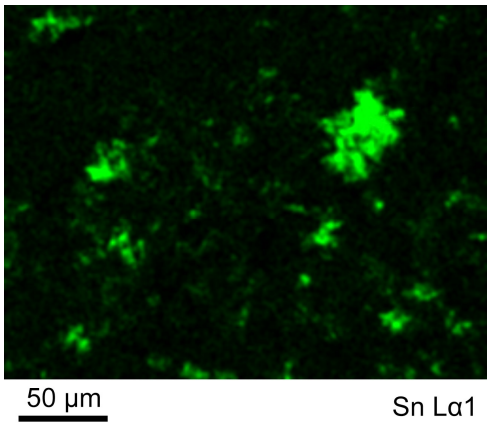

Figure 5.11 –EDX map of Sn distribution in a Sn-doped Ga_2O_3 thin film deposited by LT-PED

Raman spectroscopy was then utilized to better explore the phases present in the doped film and to detect any formation of aggregates containing secondary compounds, such as tin oxides for instance. The Raman measurements in this case were conducted using a 532 nm laser, for 60x10 seconds. The subtraction of the background related to the substrate signal and the "air" enabled the identification of two distinct Ga_2O_3 phases, β and ε. However, traces of other compounds were not detected (Figure 5.12).

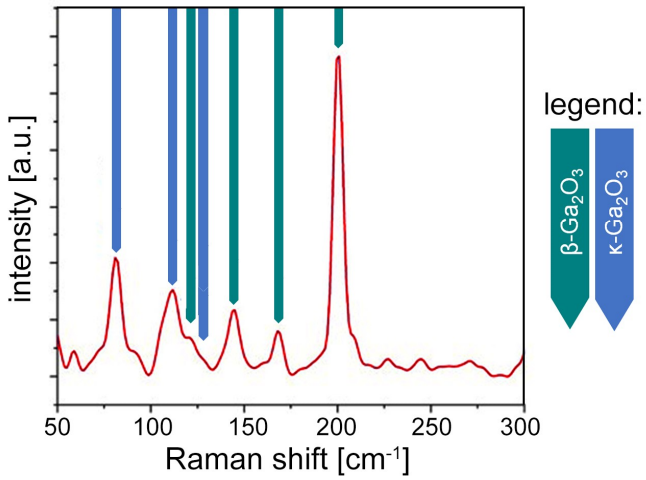

Figure 5.12 – Raman spectrum of a Sn-doped Ga_2O_3 thin film deposited by LT-PED

The fact that mixed Ga_2O_3 phases are often obtained in Sn-doped films, even at high temperature, has been reported in literature and attributed to the surfactant effect of Sn.

Ge doping was then studied, being this element just above Sn in the periodic table and having the same oxidation states but different ionic size. Ga_2O_3 targets with 1% of Ge doping were sintered and preliminary LT-PED deposition carried out.

Raman spectroscopy was employed one again to study polymorphism in these thin films. However, in the case of **Ge-doped Ga_2O_3 thin-films** only **β phase** was detected (Figure 5.13).

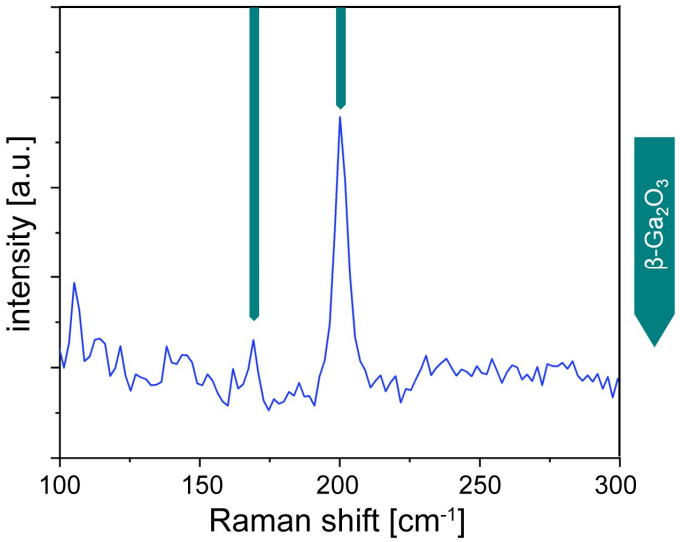

Figure 5.13 - Raman Spectra of Ge-doped Ga2O3 thin film

These preliminary results are opening the way for further experiments on doped Ga_2O_3 thin films with single phase, fundamental characteristic for devices applications.

Chapter 6
$BaFe_2O_4$

In this chapter the characterization research made on $BaFe_2O_4$ powders and thin-films is reported. This material, in its γ phase, demonstrated to be an extremely rare composite showing multiferroic properties at room temperature. The structural characterization here reported, mainly performed by micro-Raman and XRD, significantly contributed to the identification and isolation of the right phase during the synthesis processes and hence to obtain pure samples, in which ordering at room temperature was observed for the first time.

After a brief introduction on the multiferroic materials and the properties of this ferrite, the results of the two main stages of the structural characterization are described in the following paragraphs, highlighting once more the fundamental contribution of Raman spectroscopy in otherwise uncertain research scenarios:

6.1 - Material properties and applications

Multiferroics, materials that exhibit two or more primary ferroic orderings like ferroelectricity and ferri/ferro-magnetism (Figure 6.1), have gained substantial attention, particularly magneto-electric materials, due to their potential to revolutionize logic-memory devices by reducing energy consumption or enhancing information density, leveraging both electric and magnetic domains.

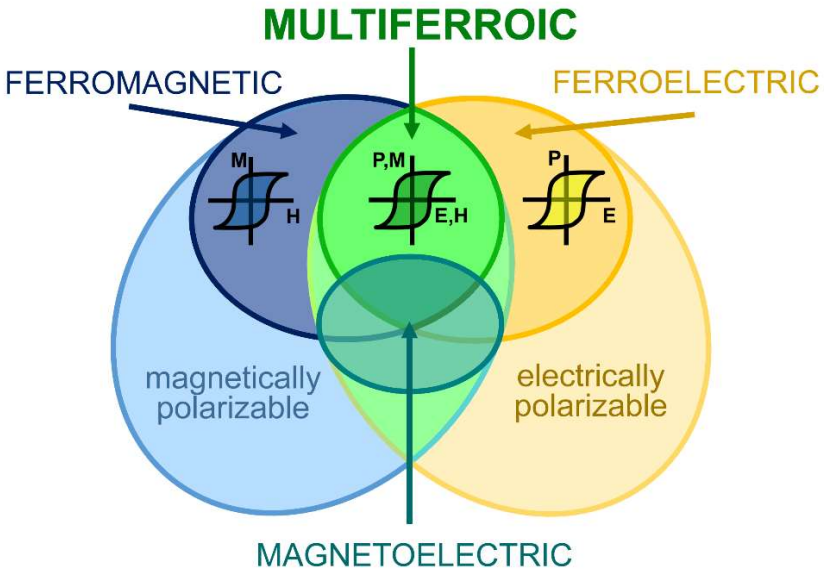

Figure 6.1 - General classification of multiferroic materials

The early 2000s' observation that antiferromagnetic domains in 600-nm-thick $BiFeO_3$ films could be controlled with an electric field, further atttracted interest in this field. Beyond the concurrent control of ferroelectricity and ferromagnetism, the coexistence of various ferroic orders in a single device paves the way for new possible applications, such as electric field-controlled spintronic devices, tunnel magnetoresistance sensors, and spin valves, among others.

Notably, antiferromagnetic ferroelectrics have become particularly enticing in recent years as magnetoelectric coupling can be accomplished through exchange bias in a ferromagnetic/antiferromagnetic magnetoelectric composite. Additionally, antiferromagnets, with their lower switching energy, facilitate power conservation and inherent reduced volatility, making them suitable for developing next-gen magnetoelectric spin field-effect transistors or magnetoelectric random access memories.

Attaining specific goals in magnetoelectric materials necessitates stability in electric and magnetic orderings under ambient conditions, substantial magnetoelectric coupling,

compatibility with current silicon-based architectures, and, as more and more compelling is in most of technological fields, environmental friendliness. Achieving these in a single-phase material is challenging due to issues like sub-room temperature transition temperatures and weak couplings found in most of the candidates. $BiFeO_3$ has been a preferred choice in this arena, meeting various prerequisites and being widely used for magnetoelectric device development. However, the exploration of new magnetoelectric multiferroics, each offering unique features per application, is crucial for the field's evolution.

The room temperature ferroelectric and magnetic attributes of γ-$BaFe_2O_4$ were explored, demonstrating its improper ferroelectricity and room-temperature antiferromagnetism, without involving health-adverse elements like Pb and Bi, and maintaining robustness in both ambient conditions and thin film form. Preliminary results indicate easy deposition of γ-$BaFe_2O_4$ on silicon substrates, positioning it as a promising new multiferroic material candidate. Additionally, during this work also the idea that the stuffed tridymite class of materials, with varied chemical substitutions at the A and B sites, could serve as a yet unexplored reservoir for multiferroic properties at room temperature.

Barium monoferrite comes in 4 different polymorphs (Figure 6.2), showing different crystalline structures and different stability range. γ-$BaFe_2O_4$ is the only one stable at room temperature.

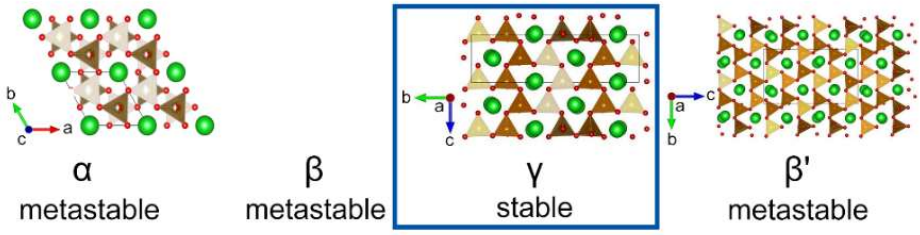

	α metastable	β metastable	γ stable	β' metastable
crystal structure	hexagonal ($P6_322$)	(pseudo) hexagonal	ortorhombic ($Cmc2_1$)	ortorhombic ($Pmc2_1$)
cell parameters [Å]	a=b=5.458 c=9.016	hexagonal a=b=5.463 c=8.710 orthorhombic a=5.463 b=9.461 c=8.710	a=8.4370 b=18.9980 c=5.3840	a=8.568 b=9.394 c=16.268
stability	stable at 1000°C	stable between 800°C and 1000°C	stable at room temperature	metastable at low T (400°C) turns into stable γ-phase

Figure 6.2 – Different $BaFe_2O_4$ polymorphs

The new γ phase has been identified and synthetized for the first time during this research and it has been studied in-depth through various techniques. Firstly, single-crystal diffraction highlighted its structure, assigning the correct cell parameters (Table 6.1) and allowing the Curie Temperature calculation, which resulted in an impressive T_{Curie}>1038K value. Neutron diffraction, on the other hand, was used to study its magnetic structure, assigning the magnetic space group and clarifying the role of Fe^{3+} (Figure 6.3), showing that each Fe^{3+} moment lies along the b-axis and is coupled antiferromagnetically with the nearest neighbor ones.

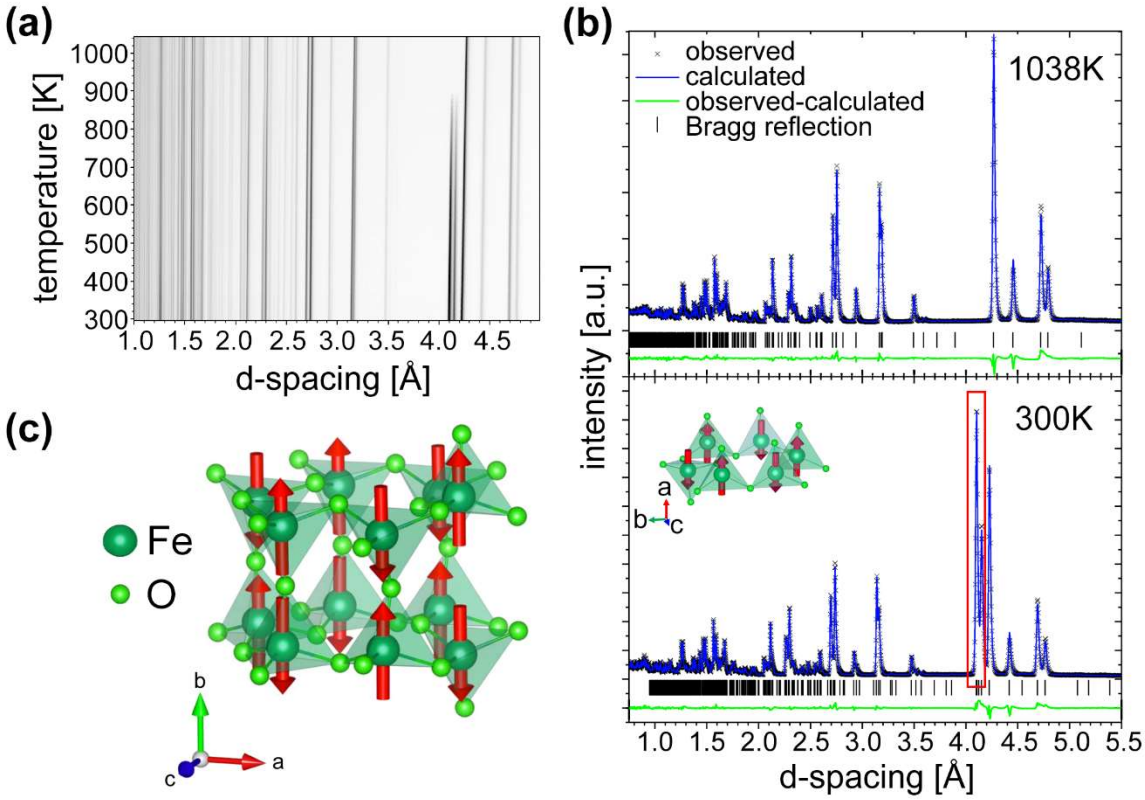

Figure 6.3 – (a) Contour plot of the neutron data collected on WISH on the back scattering detector bank with average 2θ=152.7 degrees. The data shows the development of extra reflection below $T_{Néel}$=890 K. (b) Rietveld plots of the WISH time of fight data collected on the detector banks with average 2θ of 152.7 at 300K and 1038K. (c) Magnetic structure of γ-$BaFe_2O_4$ with the G-type arrangement of the Fe^{3+} moments in the UUUUUD pattern of tetrahedra. This unit is coupled antiferromagnetically with the first neighbor ones.

Electrical measurements such as Positive Negative (PN) electric polarization and Piezo-response Force Microscopy (PFM) showed the hysteresis loop, allowing the calculation of the coercive field and residual polarization (Figure 6.4). Finally, magnetic measurements of SQUID vibrating sample magnetometry enabled the calculation of the Neel temperature

($T_{Néel}$= 890K) and revealed the role of impurities in the magnetic behavior. In this case Fe-containing impurities are responsible for the observed magnetic behavior.

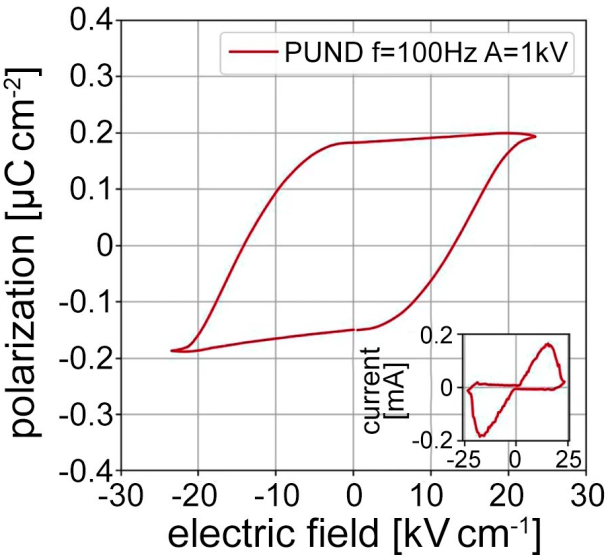

Figure 6.4 - PN electric polarization loop measured at 100 Hz with a triangular pulse of amplitude 1000 V (the inset shows the corresponding integrated current as a function of the applied voltage). γ-BaFe2O4 displays a hard-like hysteresis loop: coercive field E_c=12 kVcm^{-1}, remanent polarization P_r=0.18 μCcm^{-2}.

All of this characterization and the following deposition work were carried out between different facilities: Parma University, ISIS Neutron and Muon Source, CENIDE (Center for Nanointegration Duisburg-Essen), Shanghai University, CNR (IMEM and SPIN institutes).

6.2 - Identification of γ-phase Raman spectrum

In such a complex context, with different possible phases that may be obtained during the synthesis process, the study of the Raman spectrum proved to be fundamental not only for identifying the correct phase, but also to find the growth conditions that allowed to have a pure material, assessing when contaminants or undesired compounds were present.

The first step was to study the spectrum of powders obtained through a solid-state reaction. Powders were obtained by conventional solid-state reaction, by mixing and grinding $BaCO_3$ and Fe_2O_3 in equimolar amounts. The mixture was then heated at 1300 *C for 12 h in air, allowing the following reaction to take place:

$$BaCO_3 + Fe_2O_3 \rightarrow BaFe_2O_4 + CO_2 \qquad (6.1)$$

Thanks to the correlation with XRD analysis (Figure 6.5), Raman measurements of the obtained powders allowed the identify for the first time the characteristic Raman spectra of the new γ phase as shown in Figure 6.6.

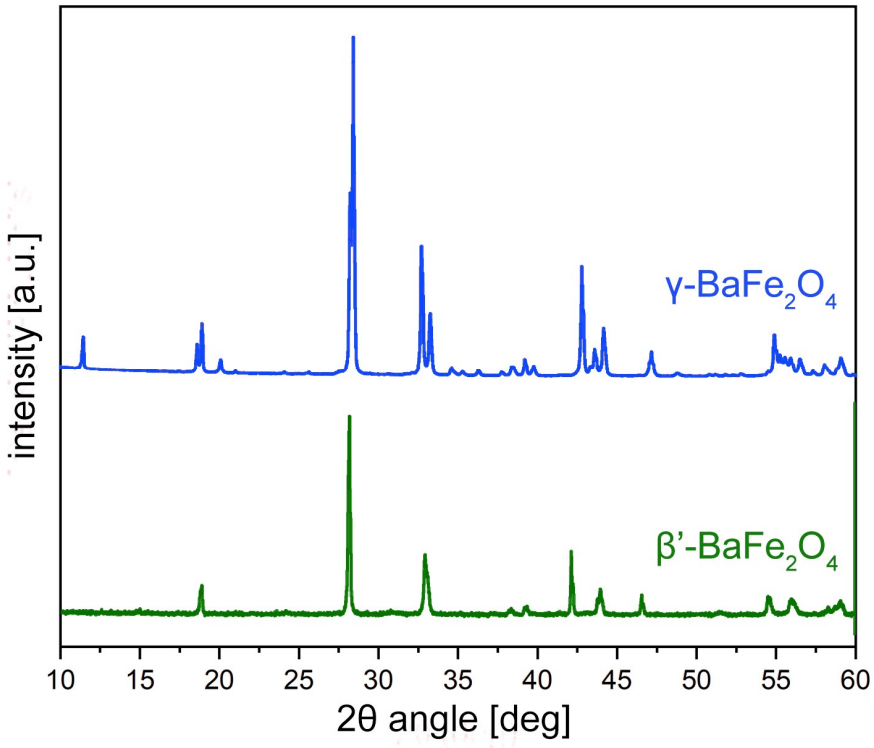

Figure 6.5 - Experimental XRD patterns of γ-$BaFe_2O_4$ and β'-$BaFe_2O_4$ polymorphs.

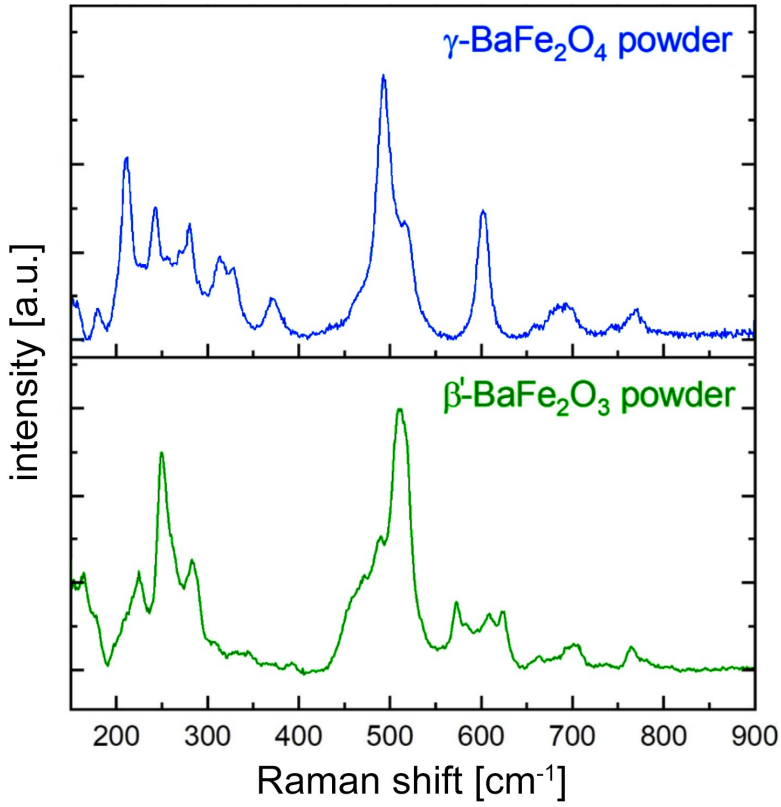

Figure 6.6 – Identified Raman spectra of two different samples, characterized by γ-$BaFe_2O_4$ and β'-$BaFe_2O_4$ polymorphs respectively.

Being this phase completely new, a theoretical study of the Raman spectra is necessary to assign specific vibrational modes to the measured spectra. In order to do so First-principles DFT simulations were performed using the Vienna Ab initio Simulation Package (VASP), but phonon calculations are still in progress. The challenge of these calculations lies in the complexity of the unit cell, which has a substantial number of atoms, hence leading to extended simulation time. A further point of concern is the choice of the structural model: the structure experimentally derived from XRD measurements, indeed, exhibits some differences from the one predicted theoretically. Such variations might not be of great concern when looking at ferroelectric properties, but they become potentially critical when considering phonon behavior.

6.3 - $BaFe_2O_4$ thin-films deposited by LT-PED

As highlighted in previous chapters, the LT-PED deposition technique offers several advantages and is a straightforward method for obtaining high-quality thin films with good stoichiometry. Thin-film samples are the initial step to study and exploit this material in the fabrication and investigation of devices.

The first necessary step was the fabrication of a $BaFe_2O_4$ target, which was crucial for generating the plasma plume. The target was prepared by compressing $BaFe_2O_4$ powders into a pellet with a diameter of 2.5 cm. This pellet was then subjected to a high-temperature sintering process at 1573 K for 6 hours. This sintering process was essential to achieve a dense and robust target that could withstand the intense conditions of the electron beam hits and plasma environment.

The resulting high-density target was then employed for the investigation of the plasma plume's characteristics. During the study, the plasma plume was investigated to identify its constituent elements and their spatial distribution but also to detect the presence of any secondary products, which are byproducts of the plasma plume formation.

In addition, the influence of various operating parameters on the PED process was explored. These parameters include electron-beam energy, pulse duration, and target-to-substrate distance. The optimal conditions for achieving the desired material properties were established by systematically adjusting these parameters.

For this preliminary investigation, the following deposition conditions were tested to obtain γ-$BaFe_2O_4$ in our LT-PED apparatus. Different substrates were tested: quartz, platinum, (100)-Silicon, SiO_2 glass. The accelerating voltage was set between 14 kV and 16 kV. The frequency of the pulses was maintained at 6 Hz, and the working temperature was set at a nominal value in the range 600–800°C. The pressure within the working chamber was kept between $7x10^{-3}$ and $1x10^{-2}$ mbar and target-to-substrate distance was set between 5 cm and 7 cm. The whole deposition process took between $3x10^4$ and $1x10^5$ electron pulses to obtain the desired thickness. The obtained samples then underwent a post-deposition annealing at the operating temperature for 20 minutes, under a pressure of 2 mbar.

The Raman spectra shown in Figure 6.7 shows that the stoichiometric transfer from the target to the thin-film was successful and, in the right conditions, the γ phase is obtained (in this case on a Si substrate).

Raman measurements were also widely employed in the study of the PED plume by evaluating the angular-dependency of the resulting deposition (Figure 6.8).

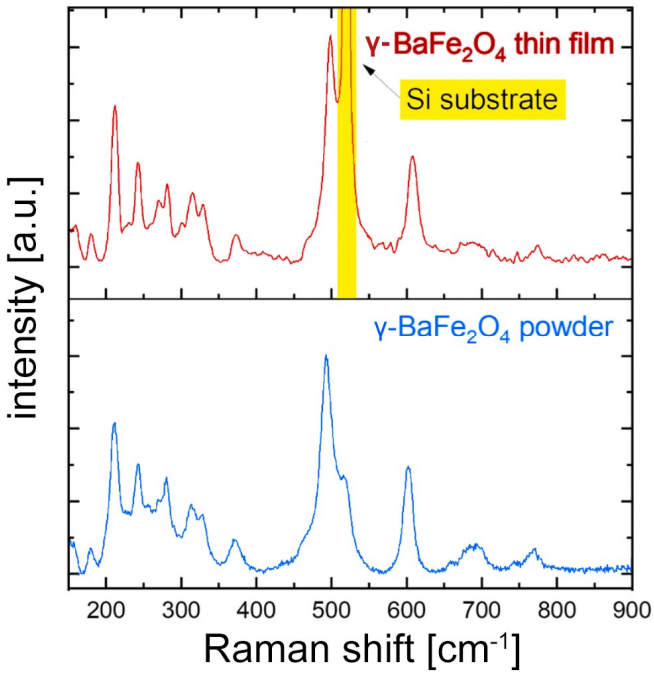

Figure 6.7 – Raman spectra of $BaFe_2O_4$ thin film deposited by LT-PED on (001)-Si substrate and of the powders used to synthetize the target. Both exibits the typical peaks of γ-$BaFe_2O_4$ polymorph.

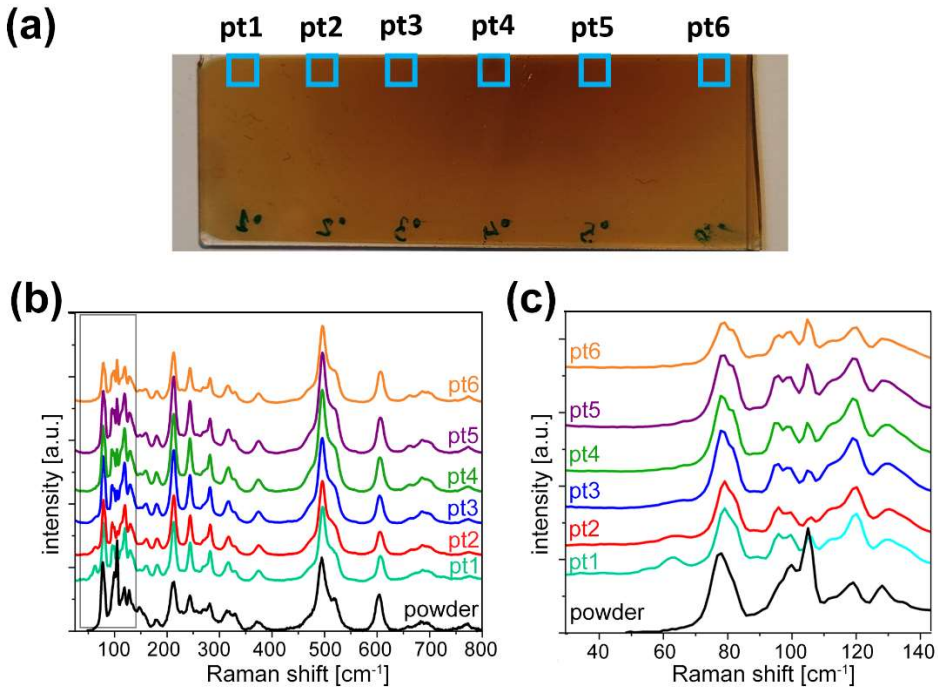

Figure 6.8 – (a) $BaFe_2O_4$ thin film deposites on a wide 3"x1" SiO_2 glass substrate to study the deposition homogeneity; the 6 point marked on the image are the one studied by Raman spectroscopy. (b) Raman spectra measured in the 6 different points compared with the spectrum of γ-$BaFe_2O_4$ powders. (c) Maginifcation of the Raman spectra in the range 30-140 cm^{-1}.

Luckily, the deposited films showed excellent compositional uniformity, especially near the center of the plume deposition. The only exception was related to a peak at about 60 cm^{-1}, present only in the peripheral area of the plume (points 1 and 2 in Figure 6.8), that cannot be attributed to the monoferrite phase and defining the limits of the available deposition area. These results are in complete agreement with the XRD measurements taken at the same points (Figure 6.9), showing also extra peaks for point1 and point2, tentatively ascribed to a Ba-rich $Ba_2Fe_2O_5$ compound.

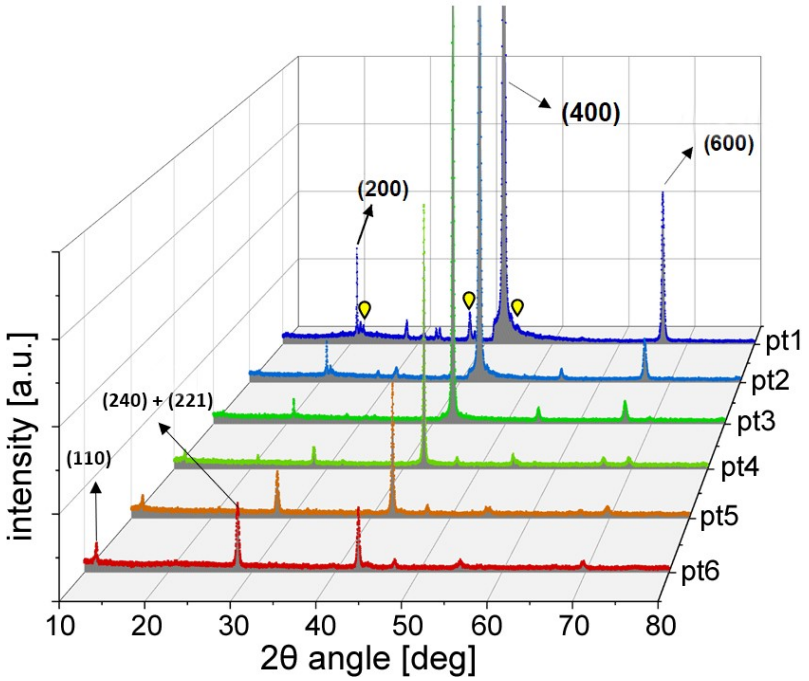

Figure 6.9 – XRD patterns of the 6 different points shown in Figure 6.8a. Indexed peaks are referred to γ-$BaFe_2O_4$. The yellow markers indicate possible peaks from $Ba_2Fe_2O_5$.

The ideal operation conditions for the deposition of γ-$BaFe_2O_4$ thin-films were hence determined: accelerating tension = 16 kV; frequency pulse = 6 Hz, substrate working temperature = 700 °C, working chamber pressure = $1.2x10^{-3}$ mbar, number of pulses = 10^5, target-to-substrate distance = 7 cm.

After optimizing the deposition parameters, a different challenge was addressed: the deposition of a very thin-film to characterize almost 2D properties. Unfortunately, in the case very thin films, XRD signal is extremely low because of the really low amount of material, so XRD was not a resolutive characterization technique for a film thinner than 200 nm.

Despite the measured signal was very low also in Raman spectra Figure 6.10a, a careful measurement and data analysis allowed a significant enhancement of the signal-to-noise

ratio. The use of 532 nm laser line, closing as much as possible the pin hole, and a careful subtraction of the substrate signal, allowed to achieve the best result, shown in Figure 6.10b. In this case was possible to confirm once more that the γ-$BaFe_2O_4$ signal was present.

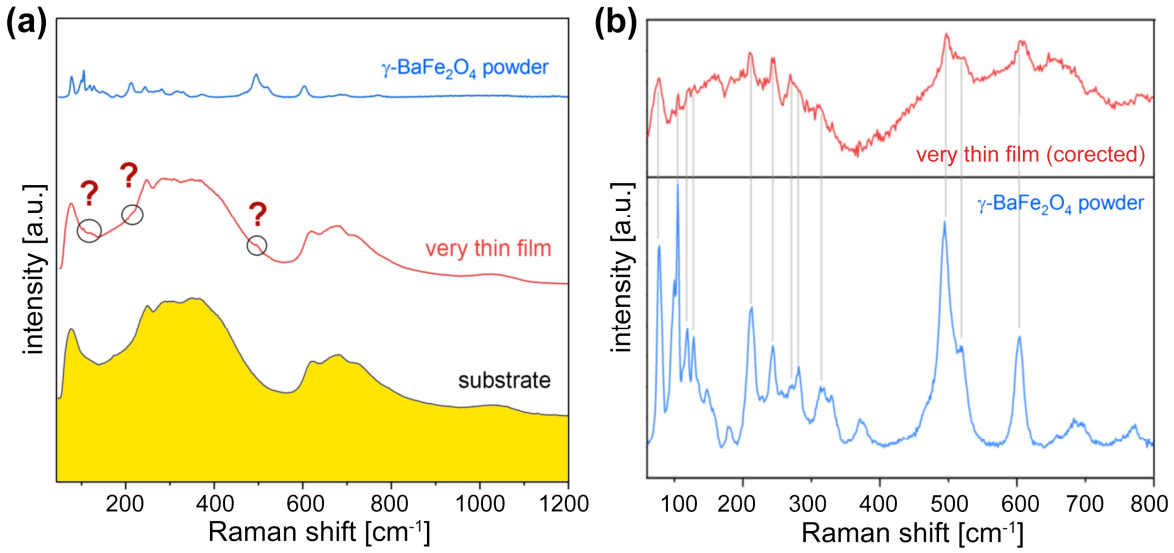

Figure 6.10 – (a) Raman spectrum of a ~180nm thin-film of $BaFe_2O_4$ deposited by LT-PED, compared with the one of the substrate and the one of γ-$BaFe_2O_4$ powders. (b) Raman spectrum of the same thin-film after the correction by background substraction compared with the one of reference γ-$BaFe_2O_4$ powders.

Chapter 7
Conclusions

In this PhD thesis I wanted to highlight the importance of a multidisciplinary approach to applied research, like in the case of the production of thin-films for the realization of different devices. In the study of innovative materials, the optimization of the growth process is always a fundamental step, both for characterizing correctly the material properties and for evaluating the feasibility of a technological transfer of the discovered potential to working devices and their possible industrial production. Cross-linking characterization results are very important to resolve uncertainties due to instrumental limits at the nanoscale and to build up a more complete picture of the materials properties.

The materials I have chosen to present in this thesis are three, even though my research work actually included a larger number of them. Antimony selenide (Sb_2Se_3), gallium oxide (Ga_2O_3) and barium monoferrite ($BaFe_2O_4$) are the three materials that, in form of thin-films, I mainly dealt with. Despite the are quite different materials, they are all promising materials for devices realization, and they were deposited in form of thin-films by similar techniques. The systematic feed-back information from their characterization was fundamental to tune and define the optimal deposition conditions.

Multiple techniques have been used to study the crystalline structure, composition, morphology, optical and electrical properties of deposited thin-films and devices: X-ray diffraction (XRD), Raman spectroscopy, Scanning Electron Microscope (SEM), Energy Dispersive X-Ray Spectroscopy (EDS/EDX), current-voltage measurements in dark and under Solar Simulator illumination, capacitance measurements and admittance spectroscopy.

In all the samples characterization, Raman spectroscopy turned out to be a fundamental complementary tool to finalize the structural characterization provided by XRD measurements and to reach the goal of depositing thin-films with the correct crystallographic phase or properties. Moreover, for the first time a preliminary study is presented on the application of Tip Enhanced Raman Spectroscopy (TERS) in the characterization of interfaces at the nanoscale.

A quick overall view on all the presented results, indeed, clearly shows that as we venture deeper into the microscopic and nanoscopic realms of material exploration, tools like the ones here described can be a guiding beacon, illuminating pathways and helping to settle scientific questions that were previously unresolved.

The main results achieved during my PhD research are here resumed, grouped for each material.

7.1 – Main results for Sb_2Se_3 thin-films

Sb_2Se_3 thin-films suitable for photovoltaic applications can be proficiently fabricated using the **LT-PED** technique, achieving high crystal quality and optimal chemical composition for substrate temperatures just between 200°C–350°C. The structural anisotropy of Sb_2Se_3 leads to variations in physical properties, mainly in electrical conductivity, depending on the orientation of the 1D $(Sb_4Se_6)_n$ ribbons.

The obtained Sb_2Se_3 films had consistent compositional and morphological properties across various substrates but differed in grain orientations. A good alignment for photovoltaic application (*i.e.* with most of the ribbons not laying parallel to the substrates) was obtained on FTO, whereas on Mo the worst alignment was found. Micro-Raman spectra and EDX analysis confirmed the presence of a single chemical phase with a slight excess of Se, while optical characterizations indicate a variable direct optical band-gap based on the used templating substrate.

Solar cells constructed on FTO/glass resulted in a J_{SC} vale of 20.28 mA/cm² and 29.60 mA/cm² upon front and bifacial illumination respectively, corresponding to conversion efficiencies of 2.1% and 3.1%. These low values are due to a rather low V_{OC} value for all the tested cells. In contrast, the solar cells made on a Mo/glass substrate confirmed the poor performances predicted by theoretical simulations, showing a maximum J_{SC} as low as 0.3 mA/cm². This research highlighted the critical role of ribbon alignment in Sb_2Se_3-based solar cells current collection and the impact of the substrate on the crystallographic orientation and transport properties of highly anisotropic films.

Crystalline and stoichiometric Sb_2Se_3 thin-films have been also successfully deposited using the magnetron RF sputtering (**RF-MS**) technique at temperatures below 350°C. In MS both the crystal structure and the $(Sb_4Se_6)_n$ ribbon orientation were significantly influenced by the deposition temperature and the substrate type (glass, Mo, FTO, CdS, and ZnO). The best ribbon alignment was achieved at 300°C on thick Sb_2Se_3 samples grown on CdS and ZnO.

SEM revealed an island grain nucleation mechanism, leading to the formation of three-dimensional Sb_2Se_3 isolated and elongate crystals, with almost vertical orientation above (or within) the film. EDS analysis confirmed the presence of a stoichiometric phase, irrespective of the substrate, eliminating the need for additional selenization steps. However, Micro-Raman spectra showed the high films susceptibility to oxidation, which cause the formation of antimony oxide on their surface after long time exposure to air or because of any sufficient heating (like the one from Raman laser) in air.

Optical characterization displayed a broad direct optical band-gap at lower growth temperatures, becoming 1.22 eV above 300°C. Sb_2Se_3-based solar cells exhibited a common narrow V_{OC}<300 mV, influenced by the low Sb_2Se_3 acceptor level $<10^{14}$ cm^{-3}, with variations in the Jsc of the cells depending on the type of substrate used and the resulting preferential ribbons orientations.

All these results confirmed the effectiveness of the RF-MS technique in producing stoichiometric films with good ribbons alignment at relatively low temperatures, enhancing the transport properties in such a strongly anisotropic material. Nonetheless, both LT-PED and RF-MS resulted in the production of Sb_2Se_3-based solar cells with low efficiency, with the main limitations coming from the cell engineering. Improvements were researched by exploring appropriate extrinsic dopings for Sb_2Se_3, a better engineering of the cell structure, an optimization of inter-layers interfaces and a better sub-cell isolation.

Polycrystalline targets with different Cu content were synthesized and examined for the development of Cu-doped Sb_2Se_3 films, deposited by LT-PED. Due to $CuSbSe_2$ phase segregation over a Cu concentration threshold limit, targets with a maximum of 5% Cu were utilized.

An initial study was conducted utilizing various LT-PED accelerating voltages, with optimal crystallinity, morphology, and composition results emerging at 14 kV and 16 kV. The substrate's role was studied once again, pinpointing FTO substrate as yielding the best ribbons orientation and Mo as yielding the worst ribbons orientation (as in the case of undoped films). Photovoltaic cells were also made with these Cu-doped Sb_2Se_3 thin-films deposited on Mo and FTO to verify the performances of films with very different anisotropy. A comparison with undoped films revealed an increase in V_{OC} from 315 mV to 388 mV with

the Mo substrate and a notable rise from 256 mV to 509 mV with the FTO substrate. J_{SC} experienced a minor increase for the cell with Mo substrate, from 0.3 mA/cm² to 1.5 mA/cm², and it regrettably decreased for the cell with FTO substrate from 25.6 mA/cm² to a very low value of 0.3 mA/cm², despite the enhancement in the FF from 39.2% to 51.9%.

Given that Sb_2Se_3 is inherently a nearly intrinsic semiconductor with extremely low free carrier density, the Cu doping effectively increased the free carrier concentration by approximately two orders of magnitude.

Conversely, the significantly low J_{SC} values measured in the cell developed on FTO revealed the inefficiency of the used layer architecture for Cu-doped Sb_2Se_3. This cell design, adapted from the one of a typical CIGS-based solar cells, is suboptimal for this alternative material, underscoring the requirement for distinct adaptations.

The use of a **TiO_2 layer** as templating substrate and interlayer for improving the FTO/Sb_2Se_3 interface was regrettably ineffective, mainly due to the extremely high $\Sigma TC(l=0)$ observed for the Sb_2Se_3 films deposited on this kind of layer. This critical issue could make meaningless the further optimization of the TiO_2 deposition process to reduce the presence of undesired cracks.

Another attempt to address the aforementioned challenges was made by adding a **thin NaF layer** on FTO prior to the deposition of Sb_2Se_3. Na, migrating from the NaF layer with the proper annealing treatments, was not only capable of passivating grain boundaries but also of introducing a calibrated interface doping, improving the carrier extraction through tunneling mechanisms. This addition was fundamental to increase the J_{SC} value by 5-10 times in solar cells with Cu:Sb_2Se_3 films deposited by LT-PED. Additionally, the incorporation of a NaF layer in a structured configuration, specifically ZnO:Al/ZnO/CdS/Sb_2Se_3/NaF/FTO/Glass, resulted in a clear improvement in efficiency from 1.28% to 3.2%.

A final attempt to combine the best achieved result on different Sb_2Se_3 films was made by depositing a Sb_2Se_3 bilayer absorber over the NaF/FTO/glass substrate. The best result was measured on a cell where a 100 nm thin layer of Cu doped Sb_2Se_3 deposited by LT-PED was followed by a 1100nm film of Sb_2Se_3 deposited by RF-MS. This cell structure exploited the good V_{OC} values obtained with Cu doped Sb_2Se_3 films, the NaF improvements at the Cu:Sb_2Se_3/FTO interface, the better free-charge collection through the bulkier part of the film of Sb_2Se_3 sputtered film, and the smoother face of this latter film for a more homogeneous deposition of CdS layer. This Al:ZnO/ZnO/CdS/**Sb_2Se_3(MS)/Cu:Sb_2Se_3(PED)/NaF**/FTO/glass cell produced the highest measure efficiency: **5.25%**.

Despite this value is still far from the maximum potential efficiency of Sb_2Se_3, it has been proved that the reasoned combination of different solutions to the intrinsic problems of this material leaded to a huge performance improvement. Clearly, further actions will be

required in the future to improve even more the still-not-optimal ribbons orientation in the Sb_2Se_3 film, the low free-carriers density, the complete cell structure layers engineering, and the barriers/defects at the interfaces.

Tip-Enhanced Raman Spectroscopy (TERS) was finally tested for the first time to see if it was capable to provide better insights of the possible problems at the interfaces of solar cells layers. A preliminary experiment was made for the Sb_2Se_3/CdS interface of a cell cross-section. The measurement fully demonstrated its high potentialities, providing Raman spectral analysis with a spatial resolution of just 20 nm, marking a pivotal advancement and potentially positioning TERS as an auxiliary methodology for probing the interfaces of thin-film solar cells. Several TERS maps, in particular, evidenced the partial interpenetration of CdS layer into the Sb_2Se_3 film, a phenomenon possibly resultant from the Chemical Bath Deposition (CBD) process of CdS on the Sb_2Se_3 surface. Other important Raman peaks around 436 cm^{-1} and between 540-570 cm^{-1} also revealed the presence and penetration of highly defective ZnO into CdS, providing first empirical evidence of undesired ZnO at the CdS/Sb_2Se_3 interface.

The findings from this study unequivocally revealed heterogeneity at the interface between the absorber and buffer layers, warranting further examination. Further developments of a Sb_2Se_3 thin-film solar cell will be attempted in the future, experimenting the deposition of Cu doped Sb_2Se_3 films with MS (a customized commercial target is required), the use of different layers for the buffer and window layer of the cells, and a careful study of all the interfaces that are present in the cell.

As a final comment, I'd like to highlight how **a systematic study of the deposition processes and characterization of the obtained samples leaded to unravel their strengths and the weaknesses, to understand which of the measured properties were affected by problems that could undermine the device properties (crystalline orientation, defect, conductivity, interfaces, etc.) and to solve them. The overall result of all the advances in the knowledge of this material and its photovoltaic cell architecture, is testified by the significant increase in the efficiency of Sb_2Se_3-based cells, from a starting 2.1% value up to 5.25%, paving the way for further improvements in a relatively short time.**

7.2 – Main results for Ga_2O_3 thin-films

A specific measurement protocol for analyzing **Ga_2O_3 thin-films** with Raman spectroscopy was defined, marking a significant advancement in the detection of secondary

phases that otherwise are often hidden by a complex and strong background signal.

Of paramount importance in this research was the study of polymorphism in Ga_2O_3 films. Structural characterization has been a fundamental reference during all the optimization of deposition processes. Renowned for its capacity to distinguish and identify different crystalline structures, also on a very small scale, micro-Raman measurements were central to the analytical pursuits of this investigation. In particular, the presence of secondary phases, often hidden in the XRD patterns, was brought to light in some of the studied films only thanks to this characterization.

An in-depth characterization of the deposited films also helped to elucidate the structural transformations induced by dopants or different deposition parameters. A comparison between Transmission Electron Microscopy (TEM) results and other characterization techniques was very important to unveil the intricate relationship between the introduction of **dopants** and the ensuing formation and growth of specific **crystalline domains** within the κ-Ga_2O_3 structure. In particular, the direct association of the variations in the Raman spectra induced by Si-doping allowed the study of these domains in a much easier and nondestructive way (TEM sample need a complex and destructive preparation).

In a pioneering series of experiments, both **doped** and **undoped** Ga_2O_3 thin-films were also successfully deposited for the first time by **LT-PED**. This deposition technique allowed for a finer control over film characteristics, presenting a novel approach to understand their intrinsic properties and potential applications. Thin-films doped with Sn and Ge were preliminary deposited to explore the possibility to dope the obtained films and hence change their properties. Both growth conditions and doping resulted to affect the presence of one or more Ga_2O_3 polymorphs in the obtained samples.

Such insights have not only deepened the understanding of Ga_2O_3's versatile properties but also paved the way for optimizing its functional capabilities for a range of different applications.

In brief, **the rich picture provided by the characterization of these samples concretely helped to tune the deposition process in order to have Ga_2O_3 thin-films with more controlled crystalline phases and properties. The doping of this material is crucial in the development of Ga_2O_3-based devices, from solar-blind UV sensors to high-power electronics applications, and the studies here presented are contributing to the huge research in this field.**

7.3 – Main results for $BaFe_2O_4$ thin-films

Samples of **γ-$BaFe_2O_4$** in form of **powder** and then in form of **thin-films** have been obtained for the first time. This phase, that is the only stable one at room temperature within different polymorphs, was characterized both from a crystallographic and magnetic point of view and growth processes were optimized to isolate samples such pure and single structure.

Powder samples have been obtained with a solid-state reaction. The same powders obtained in this way were then pressed and sintered into pellets to obtain a solid target for the deposition of $BaFe_2O_4$ thin-films. These films were deposited exploiting once more the peculiarities of LT-PED technique, such as the easy stoichiometric transfer from the target material to the substrate. Different deposition conditions and substrates have been tested in order to find out the optimal ones. The γ phase was successfully identified in the obtained thin-films.

Thanks to the correlation of different characterization techniques, also the Raman spectrum of the compound **γ-$BaFe_2O_4$** has been successfully measured and identified for the first time, adding a significant milestone in the study of this material. The use of Raman spectroscopy, indeed, also in this case has emerged as a pivotal tool in the accurate identification of phases present in the samples, each characterized by different fingerprints on the measured spectra. Moreover, the high sensitivity and precision of this technique, together with an accurate data analysis procedure, made it possible to detect and differentiate phases even in extremely thin films, with a thickness lower than 200 nm, for which XRD was unable to collect a sufficient and resolutive signal.

Accordingly, **the structural characterization performed on the powder and thin-film samples was very important to determine the optimal growth and deposition conditions to obtain and isolate this material in samples with a single and specific crystalline phase: γ-$BaFe_2O_4$. The availability of these pure sample was crucial to demonstrate the multiferroic behavior of this material at room temperature and to proof the feasibility of a possible thin-film-based device production.**

References

Sb_2Se_3

Abou-Ras, D.; Kostorz, G.; Romeo, A.; Rudmann, D.; Tiwari, A. N., Structural and chemical investigations of CBD- and PVD-CdS buffer layers and interfaces in Cu(In,Ga)Se2-based thin film solar cells. Thin Solid Films 2005, 480-481, 118-123.

Akari, S., Chantana, J., Nakatsuka, S., Nose, Y., Minemoto, T., 2018. ZnSnP2 solar cell with (Cd, Zn)S buffer layer: Analysis of recombination rates. Sol. Energy Mater. Sol. Cells 174, 412–417.

Al-Douri, Y., Khasawneh, Q., Kiwan, S., Hashim, U., Hamid, S.A., Reshak, A., Bouhemadou, A., Ameri, M., Khenata, R., 2014. Structural and optical insights to enhance solar cell performance of CdS nanostructures. Energy Convers. Manage. 82, 238–243.

Al-Douri, Y., Waheb, J.H., Ameri, M., Khenata, R., Bouhemadou, A., Reshak, A., 2013. Morphology, analysis and properties studies of CdS nanostructures under thiourea concentration effect for photovoltaic applications. Int. J. Electrochem. Sci 8, 10688–10696.

Alamri, S., 2003. The growth of CdTe thin film by close space sublimation system. Physica Status Solidi (A) 200 (2), 352–360.

Alemi, A., Hanifehpour, Y., Joo, S.W., Min, B.-K., 2011a. Structural studies and physical properties of novel Sm3+-doped Sb2Se3 nanorods. Physica B 406 (20), 3831–3835.

Alemi, A., Hanifehpour, Y., Joo, S.W., Min, B.-K., 2011b. Synthesis of novel LnxSb2−xSe3 (Ln: Lu3+, Ho3+, Nd3+) nanomaterials via co-reduction method and investigation of their physical properties. Colloids Surf., A 390 (1–3), 142–148.

Alemi, A., Hanifehpour, Y., Joo, S.W., Min, B.-K., Oh, T.H., 2012. Structural studies and optical and electrical properties of novel Gd3+-doped Sb2Se3 nanorods. J. Nanomater. 2012, 70.

Alharbi, F.H., Kais, S., 2015. Theoretical limits of photovoltaics efficiency and possible improvements by intuitive approaches learned from photosynthesis and quantum coherence. Renew. Sustain. Energy Rev. 43, 1073–1089.

Altamura, G., Wang, M., Choy, K.-L., 2016. Influence of alkali metals (Na, Li, Rb) on the performance of electrostatic spray-assisted vapor deposited Cu2ZnSn(S, Se)4 solar cells. Sci. Rep. 6, 22109.

Amin, A.; Duan, X.; Wall, J.; Khawaja, K.A.; Xiang, W.; Li, L.; Yan, F. Heterostructured CdS Buffer Layer for Sb2Se3 Thin Film Solar Cell. Sol. RRL 2023, 7, 2300417

Asaduzzaman, M., Hasan, M., Bahar, A.N., 2016. An investigation into the effects of band gap and doping concentration on Cu(In, Ga)Se2 solar cell efficiency. SpringerPlus 5 (1), 578.

Ashfold, M.N.R.; Claeyssens, F.; Fuge, G.M.; Henley, S.J. Pulsed Laser Ablation and Deposition of Thin Films. Chem. Soc. Rev. 2004, 33, 23.

Asghari-Khiavi, M.; Wood, B. R.; Hojati-Talemi, P.; Downes, A.; McNaughton, D.; Mechler, A., Exploring the origin of tip-enhanced Raman scattering; preparation of efficient TERS probes with high yield. J. Raman Spectrosc. 2012, 43 (2), 173-180.

Baghbanzadeh-Dezfuli, B.; Jamali-Sheini, F.; Cheraghizade, M. Electrochemical Synthesis of S-Doped Sb2Se3 Nanostructures and Photo-Switching Behaviour. Opt. Quantum Electron. 2023, 55, 4

Banu, S., Ahn, S.J., Ahn, S.K., Yoon, K., Cho, A., 2016. Fabrication and characterization of cost-efficient CuSbS2 thin film solar cells using hybrid inks. Sol. Energy Mater. Sol. Cells 151, 14–23.

Banu, S., Cho, Y., Kim, K., Ahn, S.K., Cho, J.S., Gwak, J., Cho, A., 2019. Effect of Cu content in CuSbS2 thin films using hybrid inks: Their photovoltaic properties and defect characteristics. Sol. Energy Mater. Sol. Cells 189, 214–223.

Baranowski, L.L., McLaughlin, K., Zawadzki, P., Lany, S., Norman, A., Hempel, H., Eichberger, R., Unold, T., Toberer, E.S., Zakutayev, A., 2015. Effects of disorder on carrier transport in Cu2SnS3. Phys. Rev. Appl 4 (4), 044017.

Bartolomeo, G. L.; Zhang, Y.; Kumar, N.; Zenobi, R., Molecular Perturbation Effects in AFM-Based Tip-Enhanced Raman Spectroscopy: Contact versus Tapping Mode. Anal. Chem. 2021, 93 (46), 15358-15364.

Belas, E., Grill, R., Franc, J., Turjanska, L., Turkevych, I., Moravec, P., Höschl, P., 2003. Electrical properties of CdTe near the melting point. J. Electron. Mater. 32 (7), 752–755.

Bhattacharya, R., Pramanik, P., 1982. A photoelectrochemical cell based on chemically deposited Sb2Se3 thin film electrode and dependence of deposition on various parameters. Solar Energy Materials 6 (3), 317–322.

Bibin, J., Kunjomana, A., 2019. Facile synthesis of novel antimony selenide nanocrystals with hierarchical architecture by physical vapor deposition technique. J. Appl. Crystallogr. 52 (2).

Bienz, S.; van Vreeswijk, S. H.; Pandey, Y.; Bartolomeo, G. L.; Weckhuysen, B. M.; Zenobi, R.; Kumar, N., Probing coke formation during the methanol-to-hydrocarbon reaction on zeolite ZSM-5 catalyst at the nanoscale using tip-enhanced fluorescence microscopy. Catal. Sci. Technol. 2022, 12 (19), 5795-5801.

Black, E., 1957. Bismuth sulfide (Bi2Se3) optical properties, dielectric constants. J. Phys. Chem. Solids 2, 240.

Bosio, A., Rosa, G., Menossi, D., Romeo, N., 2016. How the chlorine treatment and the stoichiometry influences the grain boundary passivation in polycrystalline CdTe thin films. Energies 9 (4), 254.

Bosio, A., Rosa, G., Romeo, N., 2018. Past, present and future of the thin film CdTe/CdS solar cells. Sol. Energy.

Bouich, A.; Guaita, J.M.; Soucase, B.M.; Palacios, P. Manufacture of High-Efficiency and Stable Lead-Free Solar Cells through Antisolvent Quenching Engineering. Nanomaterials 2022, 12, 2901.

Busacca, A. C., Rocca, V., Curcio, L., Parisi, A., Cino, A. C., Pernice, R., Andò, A., Adamo, G., Tomasino, A., Palmisano, G., Stivala, S., Caruso, M., Cipriani, G., La Cascia, D., Di Dio, V., Ricco Galluzzo, G., Miceli, R., 2014. Parametrical study of multilayer structures for CIGS solar cells, IEEE Proceedings of International Conference on Renewable Energy Research and Applications (ICRERA), 2014.

Burst, J.M., Duenow, J.N., Albin, D.S., Colegrove, E., Reese, M.O., Aguiar, J.A., Jiang, C.-S., Patel, M., Al- Jassim, M.M., Kuciauskas, D., 2016. CdTe solar cells with open-circuit voltage breaking the 1 V barrier. Nat. Energy 1 (3), 16015.

Butt, F.K., Li, C., Haq, B.U., Tariq, Z., Aleem, F., 2018. First-principles calculations of nitrogen-doped antimony triselenide: A prospective material for solar cells and infrared optoelectronic devices. Front., Phys. 13 (3), 137805.

Cai, Z. F.; Merino, J. P.; Fang, W.; Kumar, N.; Richardson, J. O.; De Feyter, S.; Zenobi, R., Molecular-Level Insights on Reactive Arrangement in On-Surface Photocatalytic Coupling Reactions Using Tip-Enhanced Raman Spectroscopy. J. Am. Chem. Soc. 2022, 144 (1), 538-546.

Caño, I.; Vidal-Fuentes, P.; Calvo-Barrio, L.; Alcobé, X.; Asensi, J.M.; Giraldo, S.; Sánchez, Y.; Jehl, Z.; Placidi, M.; Puigdollers, J.; et al. Does Sb2Se3 Admit Nonstoichiometric Conditions? How Modifying the Overall Se Content Affects the Structural, Optical, and Optoelectronic Properties of Sb2Se3 Thin Films. ACS Appl. Mater. Interfaces 2022, 14, 11222–11234.

Cao, Y., Stavrinadis, A., Lasanta, T., So, D., Konstantatos, G., 2016. The role of surface passivation for efficient and photostable PbS quantum dot solar cells. Nat. Energy 1 (4), 16035.

Cao, Y., Zhu, X., Jiang, J., Liu, C., Zhou, J., Ni, J., Zhang, J., Pang, J., 2020. Rotational design of charge carrier transport layers for optimal antimony trisulfide solar cells and its integration in tandem devices, Solar Energy Materials and Solar Cells.

Caracas, R., Gonze, X., 2005. First-principles study of the electronic properties of A2B3 minerals, with A=Bi, Sb and B= S, Se. Phys. Chem. Minerals 32 (4), 295–300.

Cavallari, N., Pattini, F., Rampino, S., Annoni, F., Barozzi, M., Bronzoni, M., Gilioli, E., Gombia, E., Maragliano, C., Mazzer, M., Pepponi, G., Spaggiari, G., Fornari, R., 2017. Low temperature deposition of bifacial CIGS solar cells on Al-doped Zinc Oxide back contacts. Applied Surface Science 412, 52-57.

Cebriano, T., MÚndez, B., Piqueras, J., 2012. Micro-and nanostructures of Sb2O3 grown by evaporation–deposition: Self assembly phenomena, fractal and dendritic growth. Mater. Chem. Phys. 135 (2–3), 1096–1103.

Chandrasekharan, K., Kunjomana, A., 2009. Growth and microindentation analysis of pure and doped Sb2Se3 crystals. Turkish J. Phys. 33 (4), 209–217.

Chantana, J., Kato, T., Sugimoto, H., Minemoto, T., 2017a. Aluminum-doped Zn1–xMgxO as transparent conductive oxide of Cu(In, Ga)(S, Se)2-based solar cell for minimizing surface carrier recombination. Prog. Photovoltaics Res. Appl. 25 (12), 996–1004.

Chantana, J., Kato, T., Sugimoto, H., Minemoto, T., 2017b. Thin-film Cu(In, Ga)(Se, S)2-based solar cell with (Cd, Zn)S buffer layer and Zn1–xMgxO window layer. Prog. Photovoltaics Res. Appl. 25 (6), 431–440.

Chantana, J., Kato, T., Sugimoto, H., Minemoto, T., 2018a. 20% Efficient Zn0. 9Mg0.1O: Al/Zn0.8Mg0.2O/Cu(In, Ga)(S, Se)2 Solar Cell Prepared by All-Dry Process through a Combination of Heat-Light-Soaking and Light-Soaking Processes. ACS Appl. Mater. Interfaces 10 (13), 11361–11368.

Chantana, J., Kato, T., Sugimoto, H., Minemoto, T., 2018b. Heterointerface recombination of Cu(In, Ga)(S, Se)2-based solar cells with different buffer layers. Prog. Photovoltaics Res. Appl. 26 (2), 127–134.

Chantana, J., Kawano, Y., Nishimura, T., Kato, T., Sugimoto, H., Minemoto, T., 2019a. Characteristics of Zn1–xMgxO: B and its application as transparent conductive oxide layer in Cu(In, Ga)(S, Se)2 solar cells with and without CdS buffer layer. Sol. Energy 184, 553–560.

Chantana, J., Kawano, Y., Nishimura, T., Kimoto, Y., Kato, T., Sugimoto, H., Minemoto, T., 2019b. 22%-efficient Cd-free Cu(In, Ga)(S, Se)2 solar cell by all-dry process using Zn0. 8Mg0.2O and Zn0. 9Mg0.1O: B as buffer and transparent conductive oxide layers. Progress Photovolt.: Res. Appl.

Chantana, J., Suzuki, K., Minemoto, T., 2017c. Introduction of Na into Cu2SnS3 thin film for improvement of its photovoltaic performances. Sol. Energy Mater. Sol. Cells 168, 207–213.

Chantana, J., Uegaki, H., Minemoto, T., 2017d. Influence of Na in Cu2SnS3 film on its physical properties and photovoltaic performances. Thin Solid Films 636, 431–437.

Chen, C., Bobela, D.C., Yang, Y., Lu, S., Zeng, K., Ge, C., Yang, B., Gao, L., Zhao, Y., Beard, M.C., 2017a. Characterization of basic physical properties of Sb2Se3 and its relevance for photovoltaics. Front. Optoelectron. 10 (1), 18–30.

Chen, C.; Li, K.H.; Tang, J. Ten Years of Sb2Se3 Thin Film Solar Cells. Solar RRL 2022, 6, 2200094.

Chen, C., Li, K., Chen, S., Wang, L., Lu, S., Liu, Y., Li, D., Song, H., Tang, J., 2018a. Efficiency Improvement of Sb2Se3 Solar Cells via Grain Boundary Inversion. ACS Energy Lett. 3 (10), 2335–2341.

Chen, C., Li, W., Zhou, Y., Chen, C., Luo, M., Liu, X., Zeng, K., Yang, B., Zhang, C., Han, J., 2015. Optical properties of amorphous and polycrystalline Sb2Se3 thin films prepared by thermal evaporation. Appl. Phys. Lett. 107 (4), 043905.

Chen, C., Wang, L., Gao, L., Nam, D., Li, D., Li, K., Zhao, Y., Ge, C., Cheong, H., Liu, H., 2017b. 6.5% Certified efficiency Sb2Se3 solar cells using PbS colloidal quantum dot film as hole-transporting layer. ACS Energy Lett. 2 (9), 2125–2132.

Chen, C., Zhao, Y., Lu, S., Li, K., Li, Y., Yang, B., Chen, W., Wang, L., Li, D., Deng, H., 2017c. Accelerated optimization of TiO2/Sb2Se3 thin film solar cells by high through put combinatorial approach. Adv. Energy Mater. 7 (20), 1700866.

Chen, G.; Li, X.; Abbas, M.; Fu, C.; Su, Z.; Tang, R.; Chen, S.; Fan, P.; Liang, G. Tellurium Doping Inducing Defect Passivation for Highly Effective Antimony Selenide Thin Film Solar Cell. Nanomaterials 2023, 13, 1240

Chen, S., Qiao, X., Zheng, Z., Cathelinaud, M., Ma, H., Fan, X., Zhang, X., 2018. Enhanced electrical conductivity and photoconductive properties of Sn-doped Sb2Se3 crystals. J. Mater. Chem. C. 6.

Chen, S.; Luo, P.; Ren, D.-L.; Duan, C.-Y.; Ma, X.-F.; Su, Z.-H.; Zheng, Z.-H.; Fan, P.; Liang, G.-X.; Tang, R. An Effective Engineering with Simultaneous Carrier Density Enhancement and Interface Optimization Enables Efficient Sb2Se3 Solar Cells. Appl. Surf. Sci. 2023, 619, 156783

Chen, Z., Guo, X., Guo, H., Ma, C., Qiu, J., Yuan, N., Ding, J., 2019. Fabrication of a semitransparent thinfilm Sb2Se3 solar cell. Mater. Lett. 236, 503–505.

Cheng, J.; Zhang, Z.; Zhao, M.; Guan, Y.; Chen, X.; Meng, X.; Tang, H.; Li, L.; Wang, S. High-Efficiency Sb2Se3 Thin-Film Solar Cells Based on Cd(S,O) Buffer Layers Prepared via Spin-Coating. Mater. Chem. Phys. 2023, 303, 127794.

Choi, Y.C., Lee, D.U., Noh, J.H., Kim, E.K., Seok, S.I., 2014a. Highly improved Sb2S3 sensitized-inorganic–organic heterojunction solar cells and quantification of traps by deep-level transient spectroscopy. Adv. Funct. Mater. 24 (23), 3587–3592.

Choi, Y.C., Lee, Y.H., Im, S.H., Noh, J.H., Mandal, T.N., Yang, W.S., Seok, S.I., 2014b. Efficient Inorganic-Organic Heterojunction Solar Cells Employing Sb2(Sx/Se1-x)3 Graded-Composition Sensitizers. Adv. Energy Mater. 4 (7), 1301680.

Choi, Y.C., Mandal, T.N., Yang, W.S., Lee, Y.H., Im, S.H., Noh, J.H., Seok, S.I., 2014c. Sb2Se3-sensitized inorganic–organic heterojunction solar cells fabricated using a single-source precursor. Angew. Chem. 126 (5), 1353–1357.

Costa, M.B., de Souza Lucas, F.W., Mascaro, L.H., 2017. Thermal treatment effects on electrodeposited Sb2Se3 photovoltaic thin films. ChemElectroChem 4 (10), 2507–2514.

Costa, M.B., de Souza Lucas, F.W., Mascaro, L.H., 2018. Electrodeposition of Fe-doped Sb2Se3 thin films for photoelectrochemical applications and study of the doping effects on their properties. J. Solid State Electrochem. 22 (5), 1557–1562.

Cwil, M.; Igalson, M.; Zabierowski, P.; Siebentritt, S. Charge and doping distributions by capacitance profiling in Cu(In,Ga)Se2Cu(In,Ga)Se2 solar cells. J. App. Phys. 2008, 103, 06370.

Dalapati, G.K., Kushwaha, A.K., Sharma, M., Suresh, V., Shannigrahi, S., Zhuk, S., Masudy-Panah, S., 2018. Transparent heat regulating (THR) materials and coatings for energy saving window applications: Impact of materials design, micro-structural, and interface quality on the THR performance. Prog. Mater Sci. 95, 42–131.

Deringer, V.L., Stoffel, R.P., Wuttig, M., Dronskowski, R., 2015. Vibrational properties and bonding nature of Sb2Se3 and their implications for chalcogenide materials. Chem. Sci. 6 (9), 5255–5262.

Dharsana, M. and S. Sindhu (2016). "Antimony selenide nanoparticles as panchromatic sensitizer: Fast synthesis and study of their photovoltaic behavior." Materials Letters 183: 448-450.

Dittrich, H., Bieniok, A., Brendel, U., Grodzicki, M., Topa, D., 2007. Sulfosalts—a new class of compound semiconductors for photovoltaic applications. Thin Solid Films 515 (15), 5745–5750.

Dong, J.; Liu, Y.; Wang, Z.; Zhang, Y. Boosting VOC of Antimony Chalcogenide Solar Cells: A Review on Interfaces and Defects. Nano Sel. 2021, 2, 1818–1848.

Dong, S.; Sun, L.; Yue, F. Influence of Selenium Growth Condition on the Photovoltaic Conversion Efficiency of Sb2Se3 as the Solar Cell Absorption Layer. J. Mater. Sci Mater. Electron. 2022, 33, 10335–10342.

Dong, Y.; Huang, L.; Wang, H.; Peng, X.; Wang, Y.; Tang, R.; Zhu, C.; Chen, T. Zinc Chloride-Treated Indium Sulfide as Buffer Layer for Cd-Free Antimony Selenide Solar Cells. Sol. RRL 2023, 7, 2300440.

Dönges, E., 1950. Über Chalkogenohalogenide des dreiwertigen Antimons und Wismuts. II. Über Selenohalogenide des dreiwertigen Antimons und Wismuts und über Antimon (III)-selenid Mit 2 Abbildungen. Zeitschrift für anorganische und allgemeine. Chemie 263 (5–6), 280–291.

Duan, Z.; Liang, X.; Feng, Y.; Ma, H.; Liang, B.; Wang, Y.; Luo, S.; Wang, S.; Schropp, R.E.I.; Mai, Y.; et al. Sb2Se3 Thin-Film Solar Cells Exceeding 10% Power Conversion Efficiency Enabled by Injection Vapor Deposition Technology. Adv. Mater. 2022, 34, 2202969.

El-Salam, F.A., Afifi, M., El-Wahabb, E.A., 1993. Electrical resistivity of crystalline Sb2Se3. Vacuum 44 (2), 111–116.

El-Sayad, E., Moustafa, A., Marzouk, S., 2009. Effect of heat treatment on the structural and optical properties of amorphous Sb2Se3 and Sb2Se2S thin films. Physica B 404 (8–11), 1119–1127.

Ellmer, K., 2000. Magnetron sputtering of transparent conductive zinc oxide: relation between the sputtering parameters and the electronic properties. J. Phys. D Appl. Phys. 33 (4), R17.

Faheem, M.B., Khan, B., Feng, C., Farooq, M.U., Raziq, F., Xiao, Y., Li, Y., 2019. Allinorganic perovskite solar cells: energetics, key challenges and strategies towards commercialization. ACS Energy Lett.

Fan, P.; Chen, G.J.; Chen, S.; Zheng, Z.H.; Azam, M.; Ahmad, N.; Su, Z.H.; Liang, G.X.; Zhang, X.H.; Chen, Z.G. Quasi-Vertically Oriented Sb2Se3 Thin-Film Solar Cells with Open-Circuit Voltage Exceeding 500 mV Prepared via Close-Space Sublimation and Selenization. ACS Appl. Mater. Int. 2021, 13, 46671–46680.

Fernandez, A., Merino, M., 2000. Preparation and characterization of Sb2Se3 thin films prepared by electrodeposition for photovoltaic applications. Thin Solid Films 366 (1–2), 202–206.

Fleck, N., Hobson, T. D. C., Savory, C. N., Buckeridge, J., Veal, T. D., Correia, M. R., Scanlon, D. O., Durose, K., Jäckel, F., 2020. Identifying Raman modes of Sb2Se3 and their symmetries using angle-resolved polarised Raman spectra. J. Mater. Chem. A 8, 8337.

Fouad, S., Ammar, A., Abo-Ghazala, M., 1997. The relationship between optical gap and chemical composition in SbxSe1−x system. Physica B 229 (3–4), 249–255.

Fritsche, J.; Klein, A.; Jaegermann, W., Thin Film Solar Cells: Materials Science at Interfaces. Adv. Eng. Mater. 2005, 7 (10), 914-920.

Furlong, M., Froment, M., Bernard, M., Cortes, R., Tiwari, A., Krejci, M., Zogg, H., Lincot, D., 1998. Aqueous solution epitaxy of CdS layers on CuInSe2. J. Cryst. Growth 193 (1–2), 114–122.

Ganose, A.M., Savory, C.N., Scanlon, D.O., 2017. Beyond methylammonium lead iodide: prospects for the emergent field of ns 2 containing solar absorbers. Chem. Commun. 53 (1), 20–44.

Gautam, S.; Thakur, A.; Tripathi, S.K.; Goyal, N. Effect of Silver Doping on the Electrical Properties of A- Sb2Se3. J. Non-Cryst. Solids 2007, 353, 1315–1321.

Gilbert, L., Van Pelt, B., Wood, C., 1974. The thermal activation energy of crystalline Sb2Se3. J. Phys. Chem. Solids 35 (12), 1629–1632.

Giraldo, S.; Jehl, Z.; Placidi, M.; Izquierdo-Roca, V.; Perez-Rodriguez, A.; Saucedo, E. Progress and Perspectives of Thin Film Kesterite Photovoltaic Technology: A Critical Review. Adv. Mater. 2019, 31, 1806692.

Green, M.A., 2019. How did solar cells get so cheap? Joule 3, 631–640.

Green, M.A.; Dunlop, E.D.; Hohl-Ebinger, J.; Yoshita, M.; Kopidakis, N.; Bothe, K.; Hinken, D.; Rauer, M.; Hao, X. Solar Cell Efficiency Tables (Version 60). Prog. Photovolt. 2022, 30, 687–701.Grundmann, M., 2015. The Physics of Semiconductors: AN Introduction Including Nanophysics and Applications. Springer.

Guo, L.; Zhang, B.; Qin, Y.; Li, D.; Li, L.; Qian, X.; Yan, F. Tunable Quasi-One-Dimensional Ribbon Enhanced Light Absorption in Sb2Se3 Thin-Film Solar Cells Grown by Close-Space Sublimation. Sol. RRL 2018, 2, 1800128

Guo, L.; Zhang, B.; Ranjit, S.; Wall, J.; Saurav, S.; Hauser, A.J.; Xing, G.; Li, L.; Qian, X.; Yan, F. Interface Engineering via Sputtered Oxygenated CdS:O Window Layer for Highly Efficient Sb2Se3 Thin-Film Solar Cells with Efficiency Above 7%. Sol. RRL 2019, 3, 1900225.

Guo, H., Z. Chen, X. Wang, Q. Cang, X. Jia, C. Ma, N. Yuan and J. Ding (2019). "Enhancement in the Efficiency of Sb2Se3 Thin-Film Solar Cells by Increasing Carrier Concertation and Inducing Columnar Growth of the Grains." Solar RRL 3(3): 1800224.

Guo, H.; Zhao, C.; Xing, Y.; Tian, H.; Yan, D.; Zhang, S.; Jia, X.; Qiu, J.; Yuan, N.; Ding, J. High-Efficiency Sb2Se3 Solar Cells Modified by Potassium Hydroxide. J. Phys. Chem. Lett. 2021, 12, 12352–12359.

Guo, X., H. Guo, Z. Ma, C. Ma, J. Ding and N. Yuan (2018). "Low-temperature deposited SnO2 used as the buffer layer of Sb2Se3 solar cell." Materials Letters 222: 142-145

Hamri, Y., Bourezig, Y., Medles, M., Ameri, M., Toumi, K., Ameri, I., Al-Douri, Y., Voon, C.H., 2019. Improved efficiency of Cu (In, Ga) Se2 thinfilm solar cells using a buffer layer alternative to CdS. Sol. Energy 178,150–156.

Han, G.Z.S., Boix, P.P., Wong, L.H., Sun, L., Lien, S.Y., 2017. Towards high efficiency thin film solar cells. Prog. Mater Sci. 87, 246–291.

Hanifehpour, Y., Joo, S.W., Min, B.-K., 2013. Lu3+/Yb3+ and Lu3+/Er3+ co-doped antimony selenide nanomaterials: synthesis, characterization, and electrical, thermoelectrical, and optical properties. Nanoscale Res. Lett. 8 (1), 141.

Haque, F., Elumalai, N.K., Wright, M., Mahmud, M.A., Wang, D., Upama, M.B., Xu, C., Uddin, A., 2018. Annealing induced microstructure engineering of antimony tri-selenide thin films. Mater. Res. Bull. 99, 232–238.

Hartnauer, S., Körbel, S., Marques, M.A., Botti, S., Pistor, P., Scheer, R., 2016. Research update: stable single-phase Zn-rich Cu2ZnSnSe4 through In doping. APL Mater. 4 (7), 070701.

Hironiwa, D., Matsuo, N., Chantana, J., Sakai, N., Kato, T., Sugimoto, H., Minemoto, T., 2015. Annealing effect on Cu2ZnSn(S, Se)4 solar cell with Zn1−xMgxO buffer layer. Phys. Status Solidi (A) 212 (12), 2766–2771.

Hegedus, S.S.; Shafarman, W.N. Thin-film solar cells: Device measurements and analysis. Prog. Photovolt. Res. Appl. 2004, 12, 155–176.

Heske, C.; Eich, D.; Fink, R.; Umbach, E.; van Buuren, T.; Bostedt, C.; Terminello, L. J.; Kakar, S.; Grush, M. M.; Callcott, T. A.; Himpsel, F. J.; Ederer, D. L.; Perera, R. C. C.; Riedl, W.; Karg, F., Observation of

intermixing at the buried CdS/Cu(In,Ga)Se2 thin film solar cell heterojunction. Appl. Phys. Lett. 1999, 74 (10), 1451-1453.

Hobson, T.D.C.; Phillips, L.J.; Hutter, O.S.; Shiel, H.; Swallow, J.E.N.; Savory, C.N.; Nayak, P.K.; Mariotti, S.; Das, B.; Bowen, L.; et al. Isotype Heterojunction Solar Cells Using N-Type Sb2Se3 Thin Films. Chem. Mater. 2020, 32, 2621−2630.

Hobson, T.D.C.; Shiel, H.; Savory, C.N.; Swallow, J.E.N.; Jones, L.A.H.; Featherstone, T.J.; Smiles, M.J.; Thakur, P.K.; Lee, T.-L.; Das, B.; et al. P-Type Conductivity in Sn-Doped Sb2Se3. J. Phys. Energy 2022, 4, 045006.

Hofmann, W., 1933. Die struktur der minerale der antimonitgruppe. Zeitschrift für Kristallographie-Crystalline. Materials 86 (1–6), 225–245.

Honma, T., Sato, R., Benino, Y., Komatsu, T., Dimitrov, V., 2000. Electronic polarizability, optical basicity and XPS spectra of Sb2O3–B2O3 glasses. J. Non-Cryst. Solids 272 (1), 1–13.

Hossain, E.S., Chelvanathan, P., Shahahmadi, S.A., Sopian, K., Bais, B., Amin, N., 2018. Performance assessment of Cu2SnS3 (CTS) based thin film solar cells by AMPS-1D. Curr. Appl Phys. 18 (1), 79–89.

Hu, X., Tao, J., Weng, G., Jiang, J., Chen, S., Zhu Z., Chu, J., 2018. Investigation of electrically-active defects in Sb2Se3 thin-film solar cells with up to 5.91% efficiency via admittance spectroscopy. Solar Energy Materials and Solar Cells 186: 324-329

Hu, L., Zhang, Z., Patterson, R.J., Hu, Y., Chen, W., Chen, C., Li, D., Hu, C., Ge, C., Chen, Z., 2018a. Achieving high-performance PbS quantum dot solar cells by improving hole extraction through Ag doping. Nano Energy 46, 212–219.

Hu, X., Tao, J., Chen, S., Xue, J., Weng, G., Hu, Z., Jiang, J., Chen, S., Zhu, Z., Chu, J., 2018b. Improving the efficiency of Sb2Se3 thin-film solar cells by post annealing treatment in vacuum condition. Sol. Energy Mater. Sol. Cells 187, 170–175.

Huang, M., Xu, P., Han, D., Tang, J., Chen, S., 2019. Complicated and Unconventional Defect Properties of the Quasi-One-Dimensional Photovoltaic Semiconductor Sb2Se3. ACS Appl. Mater. Interfaces.

Huang, W., Li, Q., Chen, Y., Xia, Y., Huang, H., Dun, C., Li, Y., Carroll, D.L., 2014. Surface modification enabled carrier mobility adjustment in CZTS nanoparticle thin films. Sol. Energy Mater. Sol. Cells 127, 188–192.

Huang, M.L.; Lu, S.C.; Li, K.H.; Lu, Y.; Chen, C.; Tang, J.; Chen, S.Y. p-Type Antimony Selenide via Lead Doping. Sol. RRL 2021, 6,2100730.

Hübler, A.W., Osuagwu, O., 2010. Digital quantum batteries: Energy and information storage in nanovacuum tube arrays. Complexity 15 (5), 48–55.

Hurych, Z., Davis, D., Buczek, D., Wood, C., Lapeyre, G., Baer, A., 1974. Photoemission studies of crystalline and amorphous Sb2Se3. Physical Review B 9 (10), 4392.

Hutter, O.S., Phillips, L.J., Durose, K., Major, J.D., 2018a. 6.6% efficient antimony selenide solar cells using grain structure control and an organic contact layer. Sol. Energy Mater. Sol. Cells 188, 177–181.

Hutter, O.S., Phillips, L.J., Yates, P., Major, J.D., Durose, K., 2018b. CSS Antimony Selenide Film Morphology and High Efficiency PV Devices, WCPEC-7 Conference Paper.

Hutter, O.S.; Phillips, L.J.; Durose, K.; Major, J.D. 6.6% Efficient Antimony Selenide Solar Cells Using Grain Structure Control and an Organic Contact Layer. Sol. Energy Mater. Sol. Cells 2018, 188, 177–181.

Hutter, O.S., Phillips, L.J., Yates, P.J., Major, J.D., Durose, K., 2018c. CSS Antimony selenide film morphology and high efficiency PV devices. In: 2018 IEEE 7th World Conference on Photovoltaic Energy Conversion (WCPEC) (A Joint Conference of 45th IEEE PVSC, 28th PVSEC & 34th EU PVSEC). IEEE, pp. 0027–0031.

Ibraheam, A., Al-Douri, Y., Azman, A., 2016. Characterization and analysis of wheat-like CdS nanostructures under temperature effect for solar cells applications. Optik 127 (20), 8907–8915.

Iovu, M., Colomeico, E., Vasiliev, I., 2007. Photoconductivity of amorphous Sb2Se3 and Sb2Se3: Sn thin films. Chalcogenide Lett 4, 109–113. IRENA, 2019. Renewable Power Generation Costs in 2018, International Renewable Energy Agency, Abu Dhabi.

Ishaq, M., Deng, H., Yuan, S., Zhang, H., Khan, J., Farooq, U., Song, H., Tang, J., 2018. Efficient Double Buffer Layer Sb2(SexS1−x)3 Thin Film Solar Cell Via Single Source Evaporation. Solar RRL, 1800144.

Ishizuka, S., Sakurai, K., Yamada, A., Matsubara, K., Fons, P., Iwata, K., Nakamura, S., Kimura, Y., Baba, T., Nakanishi, H., 2005. Fabrication of wide-gap Cu(In1−xGax)Se2 thin film solar cells: a study on the correlation of cell performance with highly resistive i-ZnO layer thickness. Sol. Energy Mater. Sol. Cells 87 (1–4), 541–548.

Jackson, P., Wuerz, R., Hariskos, D., Lotter, E., Witte, W., Powalla, M., 2016. Effects of heavy alkali elements in Cu(In, Ga)Se2 solar cells with efficiencies up to 22.6%. Phys. Status Solidi (RRL)–Rapid Res. Lett. 10 (8), 583–586.

Jakomin, R., Rampino, S., Spaggiari, G., Pattini, F. Advances on Sb2Se3 solar cells fabricated by Physical Vapor Deposition techniques», Solar 2023, 3(4), 566-595

Jelken, J.; Aviles, M. O.; Lagugne-Labarthet, F., The Hidden Flower in WS2 Flakes: A Combined Nanomechanical and Tip-Enhanced Raman Exploration. ACS Nano 2022, 16, 12352–12363.

Jena, A.K.; Kulkarni, A.; Miyasaka, T. Halide Perovskite Photovoltaics: Background, Status, and Future Prospects. Chem. Rev.2019, 119, 3036–3103.

Kamaruddin, N., Yusoff, Y., Hossain, T., Amin, N., Akhtaruzzaman, M., 2017. Surface morphological properties of CdxZn(1-x)S thin films deposited by low-cost atmospheric pressure metal organic chemical vapour deposition technique (AP-MOCVD). In: IOP Conference Series: Materials Science and Engineering. IOP Publishing, p. 012063.

Kamruzzaman, M., Liu, C., Islam, A.F.U., Zapien, J., 2017. A comparative study on the electronic and optical properties of Sb2Se3 thin film. Semiconductors 51 (12), 1615–1624.

Katagiri, H.; Sasaguchi, N.; Hando, S.; Hoshino, S.; Ohashi, J.; Yokota, T. Preparation and evaluation of Cu2ZnSnS4 thin films by sulfurization of E B evaporated precursors. Sol. Energy Mater. Sol. Cells 1997, 49, 407

Kato, T., Kitani, K., Tai, K.F., Kamada, R., Hiroi, H., Sugimoto, H., 2016. Characterization of the back contact of CIGS solar cell as the origin of rollover effect. In: 32nd European Photovoltaic Solar Energy Conference and Exhibition. pp. 1085–1088.

Kaur, K., Kumar, N., Kumar, M., 2017. Strategic review of interface carrier recombination in earth abundant Cu–Zn–Sn–S–Se solar cells: current challenges and future prospects. J. Mater. Chem. A 5 (7), 3069–3090.

Kazmerski, L., Hallerdt, M., Ireland, P., Mickelsen, R., Chen, W., 1983. Optical properties and grain boundary effects in CuInSe2. J. Vacuum Sci. Technol. A: Vacuum, Surf., Films 1 (2), 395–398.

Kazmerski, L.L.; White, F.R.; Ayyagari, M.S.; Juang, Y.J.; Patterson, R.P. Growth and characterization of thin-film compound semiconductor photovoltaic heterojunctions. J. Vac. Sci. Technol. 1977, 14, 65

Kim, J., Yang, W., Oh, Y., Lee, H., Lee, S., Shin, H., Kim, J., Moon, J., 2017. Self-oriented Sb2Se3 nanoneedle photocathodes for water splitting obtained by a simple spincoating method. J. Mater. Chem. A 5 (5), 2180–2187.

Koc, H., Mamedov, A.M., Deligoz, E., Ozisik, H., 2012. First principles prediction of the elastic, electronic, and optical properties of Sb2S3 and Sb2Se3 compounds. Solid State Sci. 14 (8), 1211–1220.Kondrotas, R., Chen, C., Tang, J., 2018. Progress and Prospects of Sb2S3-Based Thin Film and Tandem Solar Cells. Joule.

Kosek, F., Tulka, J., Štourač, L., 1978. Optical, photoelectric and electric properties of single-crystalline Sb2Se3. Czechoslovak J. Phys. B 28 (3), 325–330.

Krautmann, R.; Spalatu, N.; Gunder, R.; Abou-Ras, D.; Unold, T.; Schorr, S.; Krunks, M.; Oja Acik, I. Analysis of Grain Orientation and Defects in Sb2Se3 Solar Cells Fabricated by Close-Spaced Sublimation. Sol. Energy 2021, 225, 494–500.

Kulkarni, A.N., Arote, S.A., Pathan, H.M., Patil, R.S., 2015. Sb2Se3 sensitized heterojunction solar cells. Mater. Renewable Sustainable Energy 4 (3), 15.

Kumar, N.; Kalirai, S.; Wain, A. J.; Weckhuysen, B. M., Nanoscale Chemical Imaging of a Single Catalyst Particle with Tip-Enhanced Fluorescence Microscopy. ChemCatChem 2019, 11 (1), 417-423.

Kumar, N.; Zoladek-Lemanczyk, A.; Guilbert, A. A.; Su, W.; Tuladhar, S. M.; Kirchartz, T.; Schroeder, B. C.; McCulloch, I.; Nelson, J.; Roy, D.; Castro, F. A., Simultaneous topographical, electrical and optical microscopy of optoelectronic devices at the nanoscale. Nanoscale 2017, 9 (8), 2723-2731.

Kumar, N.; Mignuzzi, S.; Su, W.; Roy, D., Tip-enhanced Raman spectroscopy: principles and applications. EPJ tech. instrum. 2015, 2 (1), 1-23.

Kumar, N.; Su, W.; Vesely, M.; Weckhuysen, B. M.; Pollard, A. J.; Wain, A. J., Nanoscale chemical imaging of solid-liquid interfaces using tip-enhanced Raman spectroscopy. Nanoscale 2018, 10 (4), 1815-1824.

Kumar, V., Kr Sharma, S., Sharma, T. P., Singh, V., 1999. Bandgap determination in thick films from reflectance measurements Opt. Mater. 12, 115–119.

Kumar, V., Artegiani, E., Kumar, A., Mariotto, G., Piccinelli, F., Romeo, A., 2019. Effects of post-deposition annealing and copper inclusion in superstrate Sb2Se3 based solar cells by thermal evaporation. Sol. Energy 193, 452–457.

Kwon, Y.H., Kim, Y.B., Jeong, M., Do, H.W., Cho, H.K., Lee, J.Y., 2017. Crystal growth direction-controlled antimony selenide thin film absorbers produced using an electrochemical approach and intermediate thermal treatment. Sol. Energy Mater. Sol. Cells 172, 11–17.

Kyono, A., Kimata, M., Matsuhisa, M., Miyashita, Y., Okamoto, K., 2002. Low-temperature crystal structures of stibnite implying orbital overlap of Sb 5s2 inert pair electrons. Phys. Chem. Miner. 29 (4), 254–260.

Lahmar, H., Azizi, A., Schmerber, G., Dinia, A., 2016. Effect of the thickness of the ZnO buffer layer on the properties of electrodeposited p-Cu2O/n-ZnO/n-AZO heterojunctions. RSC Adv. 6 (73), 68663–68674.

Lai, Y., Chen, Z., Han, C., Jiang, L., Liu, F., Li, J., Liu, Y., 2012a. Preparation and characterization of Sb2Se3 thin films by electrodeposition and annealing treatment. Appl. Surf. Sci. 261, 510–514.

Lai, Y., Han, C., Lv, X., Yang, J., Liu, F., Li, J., Liu, Y., 2012b. Electrodeposition of antimony selenide thin films from aqueous acid solutions. J. Electroanal. Chem. 671, 73–79.

Lakhdar, M.H., Ouni, B., Amlouk, M., 2014. Thickness effect on the structural and optical constants of stibnite thin films prepared by sulfidation annealing of antimony films. Optik-Int. J. Light Electron Opt. 125 (10), 2295–2301.

Lawal, A., Shaari, A., Ahmed, R., Taura, L., 2018. Investigation of excitonic states effects on optoelectronic properties of Sb2Se3 crystal for broadband photo-detector by highly accurate first-principles approach. Curr. Appl Phys. 18 (5), 567–575.

Lee, D., Cho, J. Y., Heo, J., 2018. "Improved efficiency of Sb2Se3/CdS thin-film solar cells: The effect of low-temperature pre-annealing of the absorbers." Solar Energy 173: 1073-1079.

Lei, H., Chen, J., Tan, Z., Fang, G., 2019. Review of Recent Progress in Antimony Chalcogenide-Based Solar Cells: Materials and Devices. Solar RRL, 1900026.

Leng, M., Luo, M., Chen, C., Qin, S., Chen, J., Zhong, J., Tang, J., 2014. Selenization of Sb2Se3 absorber layer: An efficient step to improve device performance of CdS/Sb2Se3 solar cells. Appl. Phys. Lett. 105 (8), 083905.

Li, D.-B., Yin, X., Grice, C.R., Guan, L., Song, Z., Wang, C., Chen, C., Li, K., Cimaroli, A.J., Awni, R.A., Zhao, D., Song, H., Tang, W., Yan, Y., Tang, J., 2018a. Stable and efficient CdS/Sb2Se3 solar cells prepared by scalable close space sublimation. Nano Energy 49, 346–353.

Li, D.-F., Luo, M., Li, B.-L., Wu, C.-B., Deng, B., Dong, H.-N., 2013. Low-resistivity p-type doping in wurtzite ZnS using codoping method. Advances in Condensed Matter Physics 2013.

Li, G., Li, Z., Chen, J., Chen, X., Qiao, S., Wang, S., Xu, Y., Mai, Y., 2018b. Self-powered, high-speed Sb2Se3/Si heterojunction photodetector with close spaced sublimation processed Sb2Se3 layer. J. Alloy. Compd. 737, 67–73.

Li, G., Zhu, R., Yang, Y., 2012. Polymer solar cells. Nat. Photonics 6 (3), 153.

Li, J., Wang, B., Liu, F., Yang, J., Li, J., Liu, J., Jia, M., Lai, Y., Liu, Y., 2011. Preparation and characterization of Bi-doped antimony selenide thin films by electrodeposition. Electrochim. Acta 56 (24), 8597–8602.

Li, J.V., Grover, S., Contreras, M.A., Ramanathan, K., Kuciauskas, D., Noufi, R., 2014. A recombination analysis of Cu(In, Ga)Se2 solar cells with low and high Ga compositions. Sol. Energy Mater. Sol. Cells 124, 143–149.

Li, K., Kondrotas, R., Chen, C., Lu, S., Wen, X., Li, D., Luo, J., Zhao, Y., Tang, J., 2018. Improved efficiency by insertion of Zn1−xMgxO through sol-gel method in ZnO/Sb2Se3 solar cell. Sol. Energy 167, 10–17.

Li, W., Chen, J., Yan, C., Hao, X., 2015. The effect of ZnS segregation on Zn-rich CZTS thin film solar cells. J.Alloy. Compd. 632, 178–184.

Li, W.H.; Li, M.; Hu, Y.J.; Cheng, C.H.; Kan, Z.M.; Yu, D.Q.; Leng, J.; Jin, S.Y.; Cong, S.L. Enhanced performance of antimony selenide thin film solar cell using PbI2 as a dopant. Appl. Phys. Lett. 2021, 118, 093903.

Li, Y., Zhou, Y., Luo, J., Chen, W., Yang, B., Wen, X., Lu, S., Chen, C., Zeng, K., Song, H., 2016a. The effect of sodium on antimony selenide thin film solar cells. RSC Adv. 6 (90), 87288–87293.

Li, Y., Zhou, Y., Zhu, Y., Chen, C., Luo, J., Ma, J., Yang, B., Wang, X., Xia, Z., Tang, J., 2016b. Characterization of Mg and Fe doped Sb2Se3 thin films for photovoltaic application. Appl. Phys. Lett. 109 (23), 232104.

Li, J.; Wang, B.; Liu, F.Y.; Yang, J.; Li, J.Y.; Liu, J.; Jia, M.; Lai, Y.Q.; Liu, Y.X. Preparation and characterization of Bi-doped antimony selenide thin films by electrodeposition. Electrochim. Acta 2011, 56, 8597–8602.

Li, Z., Chen, X., Zhu, H., Chen, J., Guo, Y., Zhang, C., Zhang, W., Niu, X., Mai, Y., 2017. Sb2Se3 thin film solar cells in substrate configuration and the back contact selenization. Sol. Energy Mater. Sol. Cells 161, 190–196.

Li, Z., Liang, X., Li, G., Liu, H., Zhang, H., Guo, J., Chen, J., Shen, K., San, X., Yu, W., 2019. 9.2%-efficient core-shell structured antimony selenide nanorod array solar cells. Nature Commun. 10 (1) 125–125.

Liang, X.; Feng, Y.; Dang, W.; Huang, H.; Wang, X.; Guo, Y.; Shen, K.; Schropp, R.E.I.; Li, Z.; Mai, Y. High-Efficiency Flexible Sb2Se3 Solar Cells by Back Interface and Absorber Bulk Deep-Level Trap Engineering. ACS Energy Lett. 2023, 8, 213–221.

Li, Z., Zhu, H., Guo, Y., Niu, X., Chen, X., Zhang, C., Zhang, W., Liang, X., Zhou, D., Chen, J., 2016c. Efficiency enhancement of Sb2Se3 thin-film solar cells by the co-evaporation of Se and Sb2Se3. Appl. Phys Express 9 (5), 052302.

Liang, G.X.; Chen, M.D.; Ishaq, M.; Li, X.R.; Tang, R.; Zheng, Z.H.; Su, Z.H.; Fan, P.; Zhang, X.H.; Chen, S. Crystal Growth Promotion and Defects Healing Enable Minimum Open-Circuit Voltage Deficit in Antimony Selenide Solar Cells. Adv. Sci. 2022,9, 2105142.

Liang, G.X.; Chen, X.Y.; Ren, D.L.; Jiang, X.X.; Tang, R.; Zheng, Z.H.; Su, Z.H.; Fan, P.; Zhang, X.H.; Zhang, Y.; et al. Ion doping simultaneously increased the carrier density and modified the conduction type of Sb2Se3 thin films towards quasi-homojunction solar cell. J. Mater. 2021, 7, 1324–1334.

Liang, G.-X., Zhang, X.-H., Ma, H.-L., Hu, J.-G., Fan, B., Luo, Z.-K., Zheng, Z.-H., Luo, J.-T., Fan, P., 2017. Facile preparation and enhanced photoelectrical performance of Sb2Se3 nano-rods by magnetron sputtering deposition. Sol. Energy Mater. Sol. Cells 160, 257–262.

Liang, G.-X., Zheng, Z.-H., Fan, P., Luo, J.-T., Hu, J.-G., Zhang, X.-H., Ma, H.-L., Fan, B., Luo, Z.-K., Zhang, D.-P., 2018. Thermally induced structural evolution and performance of Sb2Se3 films and nanorods prepared by an easy sputtering method. Sol. Energy Mater. Sol. Cells 174, 263–270.

Liang, G.-X., Luo, Y. D., Chen, S., Tang, R., Zheng, Z. H., Li, X. J., Liu, X. S., Liu, Y. K., Chen, X. Y., Su, Z. H., Zhang, Z. H., Ma, H. L., Fan, P., 2020. Sputtered and selenized Sb2Se3 thin-film solar cells with open circuit voltage exceeding 500 mV. Nano Energy 73, 104806.

Lin, J.; Chen, G.; Ahmad, N.; Ishaq, M.; Chen, S.; Su, Z.; Fan, P.; Zhang, X.; Zhang, Y.; Liang, G. Back Contact Interfacial Modification Mechanism in Highly-Efficient Antimony Selenide Thin-Film Solar Cells. J. Energy Chem. 2023, 80, 256–264.

Lindahl, J., Wätjen, J.T., Hultqvist, A., Ericson, T., Edoff, M., Törndahl, T., 2013. The effect of Zn1−xSnxOy buffer layer thickness in 18.0% efficient Cd-free Cu(In, Ga)Se2 solar cells. Prog. Photovoltaics Res. Appl. 21 (8), 1588–1597.

Liao, D.; Rockett, A., Cd doping at the CuInSe2/CdS heterojunction. J. Appl. Phys. 2003, 93 (11), 9380-9382.

Liu, T., Chen, K., Hu, Q., Zhu, R., Gong, Q., 2016. Inverted perovskite solar cells: progresses and perspectives. Adv. Energy Mater. 6 (17), 1600457.

Liu, X., Chen, C., Wang, L., Zhong, J., Luo, M., Chen, J., Xue, D.J., Li, D., Zhou, Y., Tang, J., 2015. Improving the performance of Sb2Se3 thin film solar cells over 4% by controlled addition of oxygen during film deposition. Prog. Photovoltaics Res. Appl. 23 (12), 1828–1836.

Liu, X., Chen, J., Luo, M., Leng, M., Xia, Z., Zhou, Y., Qin, S., Xue, D.-J., Lv, L., Huang, H., 2014a. Thermal evaporation and characterization of Sb2Se3 thin film for substrate Sb2Se3/CdS solar cells. ACS Appl. Mater. Interfaces 6 (13), 10687–10695.

Liu, X., Xiao, X., Yang, Y., Xue, D.J., Li, D.B., Chen, C., Lu, S., Gao, L., He, Y., Beard, M.C., 2017. Enhanced Sb2Se3 solar cell performance through theory-guided defect control. Prog. Photovoltaics Res. Appl. 25 (10), 861–870.

Liu, Y.-Q., Zhang, M., Wang, F.-X., Pan, G.-B., 2014b. Facile microwave-assisted synthesis of uniform Sb2Se3 nanowires for high performance photodetectors. J. Mater. Chem. C 2 (2), 240–244.

Liu, Y., Gibbs, M., Puthussery, J., Gaik, S., Ihly, R., Hillhouse, H.W., Law, M., 2010. Dependence of carrier mobility on nanocrystal size and ligand length in PbSe nanocrystal solids. Nano Lett. 10 (5), 1960–1969.

Lomas-Zapata, R.A., Prior, A.W., Mendis, B.G., 2023. A simulation study of the role of anisotropic charge transport and grain boundary recombination in thin-film Sb2Se3 photovoltaics. Solar Energy 264, 112054

López-Marino, S., Sánchez, Y., Espindola-Rodriguez, M., Alcobé, X., Xie, H., Neuschitzer, M., Becerril, I., Giraldo, S., Dimitrievska, M., Placidi, M., 2016. Alkali doping strategies for flexible and light-weight Cu2ZnSnSe4 solar cells. J. Mater. Chem. A 4 (5), 1895–1907.

Lu, S., Zhao, Y., Chen, C., Zhou, Y., Li, D., Li, K., Chen, W., Wen, X., Wang, C., Kondrotas, R., 2018. Sb2Se3 thin-film photovoltaics using aqueous solution sprayed SnO2 as the buffer layer. Adv. Electron. Mater. 4 (1), 1700329.

Lundin, D., Minea, T., Gudmundsson, J. T., 2020. High Power Impulse Magnetron Sputtering: Fundamentals, Technologies, Challenges and Applications. Elsevier.

Luo, L., Luan, W., Yuan, B., Zhang, C., Jin, L., 2015. High efficient and stable solid solar cell: based on FeS2 nanocrystals and P3HT: PCBM. Energy Procedia 75, 2181–2186.

Luo, M., Leng, M., Liu, X., Chen, J., Chen, C., Qin, S., Tang, J., 2014. Thermal evaporation and characterization of superstrate CdS/Sb2Se3 solar cells. Appl. Phys. Lett. 104 (17), 173904.

Luo, X.; Ren, D.L.; Zhang, R.;Wang, Y.P.; Chen, S.; Cathelinaud, M.; Xu, Y.; Qiao, X.S.; Zhang, X.H.; Fan, X.P. Homogroup Bi/Sb Lattice Substitution to Enhance the Photoelectric Properties of Sb2Se3 Crystals. J. Phys. Chem C 2022, 126, 8913–8921.

Ma, Y.Y.; Tang, B.B.; Lian, W.T.; Wu, C.Y.; Wang, X.M.; Ju, H.X.; Zhu, C.F.; Fan, F.J.; Chen, T. Efficient defect passivation of Sb2Se3 film by tellurium doping for high performance solar cells. J. Mater. Chem. A 2020, 8, 6510–6516.

Ma, J., Wang, Y., Wang, Y., Peng, P., Lian, J., Duan, X., Liu, Z., Liu, X., Chen, Q., Kim, T., 2011. One dimensional Sb2Se3 nanostructures: solvothermal synthesis, growth mechanism, optical and electrochemical properties. CrystEngComm 13 (7), 2369–2374.

Mao, X.; Wang, C.; Bian, M.; Wan, L.; Yang, X.; Zhou, R. The Design of SnO2 - Dominated Electron Transport Layer for High Efficiency Sb2 (S,Se)3 Solar Cells. Phys. Status Solidi A 2022, 219, 2200576.

Madelung, O., 2012. Semiconductors: Data Handbook. Springer Science & Business Media.

Mahuli, N., Halder, D., Paul, A., Sarkar, S.K., 2019. Atomic Layer Deposition of an Sb2Se3 Photoabsorber Layer Using Selenium Dimethyldithiocarbamate as a New Se Precursor. Chem. Mater. 31 (18), 7434–7442.

Mallick, A., Basak, D., 2018. Revisiting the electrical and optical transmission properties of co-doped ZnO thin films as n-type TCOs. Prog. Mater Sci. 96, 86–110.

Matsuo, N., Hironiwa, D., Chantana, J., Sakai, N., Kato, T., Sugimoto, H., Minemoto, T., 2015. Evaluation of sputtering damage in Cu2ZnSn(S, Se)4 solar cells with CdS and (Cd, Zn)S buffer layers by photoluminescence measurement. Jpn. J. Appl. Phys. 54 (4), 042302.

Mavlonov, A., Razykov, T., Raziq, F., Gan, J., Chantana, J., Kawano, Y., Nishimura, T., Wei, H., Zaktayev, A., Minemoto, T., Zu, X., Li, S., Qiao, L., 2020. A review of Sb2Se3 photovoltaic absorber materials and thin-film solar cells. Solar Energy 201, 227–246.

Mazzer, M., Rampino, S., Spaggiari, G., Annoni, F., Bersani, D., Bissoli, F., Bronzoni, M., Calicchio, M., Gombia, E., Kingma, A., Pattini, F., Gilioli, E., 2017. Bifacial CIGS solar cells grown by low temperature pulsed electron deposition, Solar Energy Materials and Solar Cells 166, 247-253.

Mazzer, M.; Rampino, S.; Gombia, E.; Bronzoni, M.; Bissoli, F.; Pattini, F.; Calicchio, M.; Kingma, A.; Annoni, F.; Calestani, D.; et al. Progress on Low-Temperature Pulsed Electron Deposition of CuInGaSe2 Solar Cells. Energies 2016, 9, 297.

Mavlonov, A.; Razykov, T.; Raziq, F.; Gan, J.T.; Chantana, J.; Nishimura, T.; Wei, H.M.; Zakutayev, A.; Minemoto, T.; Zu, X.T.; et al. A review of Sb2Se3 photovoltaic absorber materials and thin-film solar cells. Sol. Energy 2020, 201, 227–246.

McMeekin, D.P., Sadoughi, G., Rehman, W., Eperon, G.E., Saliba, M., Hörantner, M.T., Haghighirad, A., Sakai, N., Korte, L., Rech, B., 2016. A mixed-cation lead mixedhalide perovskite absorber for tandem solar cells. Science 351 (6269), 151–155.

Mehta, R.J., Karthik, C., Jiang, W., Singh, B., Shi, Y., Siegel, R.W., Borca-Tasciuc, T., Ramanath, G., 2010. High electrical conductivity antimony selenide nanocrystals and assemblies. Nano Lett. 10 (11), 4417– 4422.

Messina, S., Nair, M., Nair, P., 2009. Antimony selenide absorber thin films in all-chemically deposited solar cells. J. Electrochem. Soc. 156 (5), H327–H332.

Minemoto, T., Hashimoto, Y., Satoh, T., Negami, T., Takakura, H., Hamakawa, Y., 2001a. Cu(In, Ga)Se2 solar cells with controlled conduction band offset of window/Cu(In, Ga)Se2 layers. J. Appl. Phys. 89 (12), 8327–8330.

Minemoto, T., Hashimoto, Y., Shams-Kolahi, W., Satoh, T., Negami, T., Takakura, H., Hamakawa, Y., 2003. Control of conduction band offset in wide-gap Cu(In, Ga)Se2 solar cells. Sol. Energy Mater. Sol. Cells 75 (1–2), 121–126.

Minemoto, T., Matsui, T., Takakura, H., Hamakawa, Y., Negami, T., Hashimoto, Y., Uenoyama, T., Kitagawa, M., 2001b. Theoretical analysis of the effect of conduction band offset of window/CIS layers on performance of CIS solar cells using device simulation. Sol. Energy Mater. Sol. Cells 67 (1–4), 83–88.

Minemoto, T., Murata, M., 2015. Theoretical analysis on effect of band offsets in perovskite solar cells. Sol. Energy Mater. Sol. Cells 133, 8–14.

Minemoto, T., Okamoto, A., Takakura, H., 2011. Sputtered ZnO-based buffer layer for band offset control in Cu(In, Ga)Se2 solar cells. Thin Solid Films 519 (21), 7568–7571.

Mohamed, A.E.R., Rohani, S., 2011. Modified TiO2 nanotube arrays (TNTAs): progressive strategies towards visible light responsive photoanode, a review. Energy Environ. Sci. 4 (4), 1065–1086.

Möller, H.J., 1991. Semiconductors for solar cell applications. Prog. Mater Sci. 35 (3-4), 205–418. Mueller, R., Wood, C., 1972. The preparation of amorphous thin films. J. Non-Cryst. Solids 7 (4), 301–308.

Mrdenovic, D.; Abbott, D.; Mougel, V.; Su, W.; Kumar, N.; Zenobi, R., Visualizing Surface Phase Separation in PS-PMMA Polymer Blends at the Nanoscale. ACS Appl. Mater. Interfaces 2022, 14 (21), 24938-24945.

Mrdenovic, D.; Cai, Z. F.; Pandey, Y.; Bartolomeo, G. L.; Zenobi, R.; Kumar, N., Nanoscale chemical analysis of 2D molecular materials using tip-enhanced Raman spectroscopy. Nanoscale 2023, 15 (3), 963-974.

Murata, M., Chantana, J., Ashida, N., Hironiwa, D., Minemoto, T., 2015. Influence of conduction band minimum difference between transparent conductive oxide and absorber on photovoltaic performance of thin-film solar cell. Jpn. J. Appl. Phys. 54 (3), 032301.

Mustafa, F.I., Gupta, S., Goyal, N., Tripathi, S., 2009. Effect of temperature on the optical parameter of amorphous Sb-Se thin films. J. Optoelectron. Adv. Mater. 11 (12), 2019.

Mustafa, F.I., Gupta, S., Goyal, N., Tripathi, S., 2011. Non-Ideal p-n junction Diode of SbxSe1−x (x= 0.4, 0.5,0.6, 0.7) Thin Films. In: AIP Conference Proceedings. AIP, pp. 75–76.

Nakada, T.; Kunioka, A., Direct evidence of Cd diffusion into Cu(In,Ga)Se2 thin films during chemical-bath deposition process of CdS films. Appl. Phys. Lett. 1999, 74 (17), 2444-2446.

Ngo, T.T., Chavhan, S., Kosta, I., Miguel, O., Grande, H.-J., Tena-Zaera, R.N., 2014. Electrodeposition of antimony selenide thin films and application in semiconductor sensitized solar cells. ACS Appl. Mater. Interfaces 6 (4), 2836–2841.

Nishimura, T., Kim, S., Chantana, J., Kawano, Y., Ishizuka, S., Minemoto, T., 2019. Application of Al-Doped (Zn, Mg)O on pure-sulfide Cu(In, Ga)S2 solar cells for enhancement of open-circuit voltage. Sol. Energy Mater. Sol. Cells 202, 110157.

NREL, 2020. Cells and Modules Efficiency Charts. https://www.nrel.gov.

Ojo, A., Dharmadasa, I., 2016. 15.3% efficient graded bandgap solar cells fabricated using electroplated CdS and CdTe thin films. Sol. Energy 136, 10–14.

Ou, X., Yang, C., Xiong, X., Zheng, F., Pan, Q., Jin, C., Liu, M., Huang, K., 2017. A new rGO-overcoated Sb2Se3 nanorods anode for Na+ battery: in Situ X-ray diffraction study on a live sodiation/desodiation process.dv. Funct. Mater. 27 (13), 1606242.

Ou, C., Shen, K., Li, Z., Zhu, H., Huang, T., Mai, Y., 2019. Bandgap tunable CdS: O as efficient electron buffer layer for high-performance Sb2Se3 thin film solar cells. Solar Energy Materials and Solar Cells 194: 47-53.

Pandey, Y.; Abbott, D. F.; Mougel, V.; Kumar, N.; Zenobi, R., Probing the Role of Environmental and Sample Characteristics in Gap Mode Tip-Enhanced Raman Spectroscopy. Anal. Chem. 2023, 95 (23), 8869-8878.

Park, J., Yang, W., Oh, Y., Tan, J., Lee, H., Boppella, R., Moon, J., 2019. Efficient Solar to Hydrogen Conversion from Neutral Electrolytes using Morphology-Controlled Sb2Se3 Light Absorber. ACS Energy Lett.

Palmer, J., 2020. Solar Reaches for Grid Parity. Engineering 6 (2020) 105–106.

Pasini, S.; Spoltore, D.; Parisini, A.; Foti, G.; Marchionna, S.; Vantaggio, S.; Fornari, R.; Bosio, A. Sb2Se3 Polycrystalline Thin Films Grown on Different Window Layers. Coatings 2023, 13, 338.

Pathan, H., Lokhande, C., 2004. Deposition of metal chalcogenide thin films by successive ionic layer adsorption and reaction (SILAR) method. Bull. Mater. Sci. 27 (2), 85–111.

Patrick, C.E., Giustino, F., 2011. Structural and electronic properties of semiconductor sensitized solar-cell interfaces. Adv. Funct. Mater. 21 (24), 4663–4667.

Pattini, F.; Bronzoni, M.; Mezzadri, F.; Bissoli, F.; Gilioli, E.; Rampino, S. Dynamics of evaporation from CuGaSe2 targets in pulsed electron deposition technique. J. Phys. D Appl. Phys. 2013, 46, 245101.

Pattini F., Rampino, S., Mezzadri, F., Calestani, D., Spaggiari, G., Sidoli, M., Delmonte, D., Sala, A., Gilioli, E., Mazzer, M., 2020. Role of the substrates in the ribbon orientation of Sb2Se3 films grown by Low-Temperature Pulsed Electron Deposition. Solar Energy Materials and Solar Cells 218, 110724.

Paudel, N.R., Young, M., Roland, P.J., Ellingson, R.J., Yan, Y., Compaan, A.D., 2014. Postdeposition processing options for high-efficiency sputtered CdS/CdTe solar cells. J. Appl. Phys. 115 (6), 064502.

Phillips, L., Yates, P., Hutter, O.S., Baines, T., Bowen, L., Durose, K., Major, J.D., 2017. Close-spaced sublimation for Sb2Se3 solar cells, In: 2017 IEEE 44rd Photovoltaic Specialists Conference (PVSC).

Phillips, L. J., Savory, C. N., Hutter, O. S., Yates, P. J., Shiel, H., Mariotti, S., Bowen, L., Birkett, M., Durose, K., Scanlon, D. O., 2019. Current Enhancement via a TiO2 Window Layer for CSS Sb 2 Se 3 Solar Cells: Performance Limits and High V oc. IEEE Journal of Photovoltaics 9(2): 544-551.

Pianezzi, F., Reinhard, P., Chirilă, A., Bissig, B., Nishiwaki, S., Buecheler, S., Tiwari, A.N., 2014. Unveiling the effects of post-deposition treatment with different alkaline elements on the electronic properties of CIGS thin film solar cells. PCCP 16 (19), 8843–8851.

Polman, A., Knight, M., Garnett, E.C., Ehrler, B., Sinke, W.C., 2016. Photovoltaic materials: Present efficiencies and future challenges. Science 352 (6283), aad4424. Poplavskyy, D., Nelson, J., 2003. Nondispersive hole transport in amorphous films of methoxy-spirofluorene-arylamine organic compound. J. Appl. Phys. 93 (1), 341–346.

Punathil, P.; Artegiani, E.; Zanetti, S.; Lozzi, L.; Kumar, V.; Romeo, A. A simple method for Ge incorporation to enhance performance of low temperature and non-vacuum based CZTSSe solar cells. Sol. Energy 2022, 236, 599–607.

Rajpure, K., Bhosale, C., 2000. Effect of Se source on properties of spray deposited Sb2Se3 thin films. Mater. Chem. Phys. 62 (2), 169–174.

Rajpure, K., Bhosale, C., 2002. Preparation and characterization of spray deposited photoactive Sb2S3 and Sb2Se3 thin films using aqueous and non-aqueous media. Mater. Chem. Phys. 73 (1), 6–12.

Rajpure, K., Lokhande, C., Bhosale, C., 1997. Effect of the substrate temperature on the properties of spray deposited Sb–Se thin films from non-aqueous medium. Thin Solid Films 311 (1–2), 114–118.

Ramanujam, J., Singh, U.P., 2017. Copper indium gallium selenide based solar cells–a review. Energy Environ. Sci. 10 (6), 1306–1319.

Ramanujam, J., Verma, A., González-Díaz, B., Guerrero-Lemus, R., del Canizo, C., Garcia-Tabares, E., Rey-Stolle, I., Granek, F., Korte, L., Tucci, M., 2016. Inorganic photovoltaics–planar and nanostructured devices. Prog. Mater Sci. 82, 294–404.

Rampino, S., Pattini, F., Bronzoni, M., Mazzer, M., Sidoli, M., Spaggiari, G., Gilioli, E., 2018. CuSbSe2 thin film solar cells with~ 4% conversion efficiency grown by low-temperature pulsed electron deposition. Solar Energy Materials and Solar Cells 185, 86-96.

Rampino, S., Bissoli, F., Gilioli, E., Pattini, F.Growth of Cu(In,Ga)Se2 thin films by a novel single-stage route based on pulsed electron deposition. Prog. Photovolt. 21, 588–594 (2013).

Raziq, F., Humayun, M., Ali, A., Wang, T., Khan, A., Fu, Q., Luo, W., Zeng, H., Zheng, Z., Khan, B., 2018. Synthesis of S-Doped porous g-C3N4 by using ionic liquids and subsequently coupled with Au-TiO2 for exceptional cocatalyst-free visible-light catalytic activities. Appl. Catal. B 237, 1082–1090.

Razykov, T., Boltaev, G., Bosio, A., Ergashev, B., Kouchkarov, K., Mamarasulov, N., Mavlonov, A., Romeo, A., Romeo, N., Tursunkulov, O., 2018a. Characterisation of SnSe thin films fabricated by chemical molecular beam deposition for use in thin film solar cells. Sol. Energy 159, 834–840.

Razykov, T., Shukurov, A., Atabayev, O., Kuchkarov, K., Ergashev, B., Mavlonov, A., 2018b. Growth and characterization of Sb2Se3 thin films for solar cells. Sol. Energy 173, 225–228.

Rehman, S.; Butt, F.K.; Li, C.B.; Ul Haq, B.; Tariq, Z.; Aleem, F. First-principles calculations of nitrogen-doped antimony triselenide: A prospective material for solar cells and infrared optoelectronic devices. Front. Phys. 2018, 13, 137805.

Ren, D.L.; Chen, S.; Cathelinaud, M.; Liang, G.X.; Ma, H.L.; Zhang, X.H. Fundamental Physical Characterization of Sb2Se3-Based Quasi-Homojunction Thin Film Solar Cells. ACS Appl. Mater. Int. 2020, 12, 30572–30583.

Rimmaudo, I., Salavei, A., Artegiani, E., Menossi, D., Giarola, M., Mariotto, G., Gasparotto, A., Romeo, A., 2017. Improved stability of CdTe solar cells by absorber surface etching. Sol. Energy Mater. Sol. Cells 162, 127–133.

Rijal, S.; Li, D.-B.; Awni, R.A.; Bista, S.S.; Song, Z.; Yan, Y. Influence of Post-Selenization Temperature on the Performance of Substrate-Type Sb2Se3 Solar Cells. ACS Appl. Energy Mater. 2021, 4, 4313–4318.

Rodriguez-Lazcano, Y., Peña, Y., Nair, M., Nair, P., 2005. Polycrystalline thin films of antimony selenide via chemical bath deposition and post deposition treatments. Thin Solid Films 493 (1–2), 77–82.

Romeo, A., Artegiani, E., Menossi, D., 2018. Low substrate temperature CdTe solar cells: A review. Sol. Energy.

Rovira, D.; Ros, E.; Tom, T.; Jiménez, M.; Miguel Asensi, J.; Voz, C.; López-Vidrier, J.; Puigdollers, J.; Bertomeu, J.; Saucedo, E. Polymeric Interlayer in CdS-Free ElectronSelective Contact for Sb2Se3 Thin-Film Solar Cells. Int. J. Mol. Sci. 2023, 24, 3088

Rühle, S., 2016. Tabulated values of the Shockley-Queisser limit for single junction solar cells. Sol. Energy 130, 139–147.

Saleem, M. F.; Zhang, H.; Deng, Y.; Wang, D., Resonant Raman scattering in nanocrystalline thin CdS film. J. Raman Spectrosc. 2017, 48 (2), 224-229.

Sann, J.; Stehr, J.; Hofstaetter, A.; Hofmann, D. M.; Neumann, A.; Lerch, M.; Haboeck, U.; Hoffmann, A.; Thomsen, C., Zn interstitial related donors in ammonia-treated ZnO powders. Phys. Rev. B Condens. Matter 2007, 76 (19), 1-6.

Sajid-ur-Rehman, Butt, F.K., Li, C., Haq, B.U., Tariq, Z., Aleem, F., 2018. First-principles calculations of nitrogen-doped antimony triselenide: A prospective material for solar cells and infrared optoelectronic devices. Front. Phys. 13 (3), 137805.

Salem, M.S.; Shaker, A.; Abouelatta, M.; Alanazi, A.; Al-Dhlan, K.A.; Almurayziq, T.S. Numerical Analysis of Hole Transport Layer-Free Antimony Selenide Solar Cells: Possible Routes for Efficiency Promotion. Opt. Mater. 2022, 129, 112473.

Saliba, M., Matsui, T., Domanski, K., Seo, J.-Y., Ummadisingu, A., Zakeeruddin, S.M., Correa-Baena, J.-P., Tress, W.R., Abate, A., Hagfeldt, A., 2016. Incorporation of rubidium cations into perovskite solar cells improves photovoltaic performance. Science 354 (6309), 206–209.

Sankapal, B., Pathan, H., Lokhande, C., 2001. Growth of multilayer Bi2Se3-Sb2Se3 thin films by SILAR technique. Indian Journal of Engineering and Materials Sciences 8, 223–227.

Savory, C.N., Scanlon, D.O., 2019. The complex defect chemistry of antimony selenide. J. Mater. Chem. A.

Schmidt, J., Merkle, A., Brendel, R., Hoex, B., de Sanden, M.V., Kessels, W., 2008. Surface passivation of high-efficiency silicon solar cells by atomic-layer-deposited Al2O3. Prog. Photovoltaics Res. Appl. 16 (6), 461–466.

Schmid, T.; Opilik, L.; Blum, C.; Zenobi, R., Nanoscale chemical imaging using tip-enhanced Raman spectroscopy: a critical review. Angew. Chem. Int. Ed. 2013, 52 (23), 5940-54.

Shaaban, E., Abdel-Rahman, M., Dessouky, M., 2007. Compositional dependence of the optical properties of amorphous antimony selenide thin films using transmission measurements. Thin Solid Films 515 (7–8), 3810–3815.

Shaffer, J., Van Pelt, B., Wood, C., Freeouf, J., Murase, K., Osmun, J., 1972. Electronic structure of single crystal and amorphous Sb2Se3. Phys. Status Solidi (B) 54 (2), 511–518.

Shen, K., Ou, C., Huang, T., Zhu, H., Li, J., Li, Z., Mai, Y., 2018. Mechanisms and modification of nonlinear shunt leakage in Sb2Se3 thin film solar cells. Sol. Energy Mater. Sol. Cells 186, 58–65.

Shimakawa, K., 1981. On the compositional dependence of the optical gap in amorphous semiconducting alloys. J. Non-Cryst. Solids 43 (2), 229–244.

Shockley, W., Queisser, H.J., 1961. Detailed balance limit of efficiency of p-n junction solar cells. J. Appl. Phys. 32 (3), 510–519.

Shongalova, A., Correia, M., Teixeira, J., Leitão, J., González, J., Ranjbar, S., Garud, S., Vermang, B., Cunha, J., Salomé, P., 2018a. Growth of Sb2Se3 thin films by selenization of RF sputtered binary precursors. Sol. Energy Mater. Sol. Cells 187, 219–226.

Shongalova, A., Correia, M., Vermang, B., Cunha, J., Salomé, P., Fernandes, P., 2018b. On the identification of Sb2Se3 using Raman scattering. MRS Commun. 8 (3), 865–870.

Shongalova, A., Muratov, D., Rakhmetov, B., Aimaganbetov, K., Zhantuarov, S., 2019. On thermal stability of antimony thin films for solar cells applications. Recent Contributions to. Physics (Rec. Contr. Phys.) 68 (1), 47–51.

Singh, Y.; Maurya, K.K.; Singh, V.N. A review on properties, applications, and deposition techniques of antimony selenide. Sol. Energy Mater. Sol. Cells 2021, 230, 111223.

Song, Y.; Zhang, S.; Zhang, C.; Yang, Y.; Lv, K., Raman Spectra and Microstructure of Zinc Oxide irradiated with Swift Heavy Ion. Crystals 2019, 9 (8), 1-8.

Spaggiari, G.; Pattini, F.; Bersani, D.; Calestani, D.; De Iacovo, A.; Gilioli, E.; Mezzadri, F.; Sala, A.; Trevisi, G.; Rampino, S. Growth and structural characterization of Sb2Se3 solar cells with vertical Sb4Se6 ribbon alignment by RF magnetron sputtering. J. Phys. D Appl. Phys. 2021, 54, 385502.

Spaggiari G., Bersani D., Calestani D., Gilioli E., Gombia E., Mezzadri F., Casappa M., Pattini F., Trevisi G., Rampino S.., Exploring Cu-Doping for Performance Improvement in Sb2Se3 Photovoltaic Solar Cells. Int. J. Mol. Sci. 2022, 23 (24), 15529.

Spalatu, N.; Krautmann, R.; Katerski, A.; Karber, E.; Josepson, R.; Hiie, J.; Acik, I.O.; Krunks, M. Screening and Optimization of Processing Temperature for Sb2Se3 Thin Film Growth Protocol: Interrelation between Grain Structure, Interface Intermixing and Solar Cell Performance. Sol. Energy Mater. Sol. Cells 2021, 225, 111045. Steinmann, V., Brandt, R.E., Buonassisi, T., 2015. Photovoltaics: Non-cubic solar cell materials. Nat. Photonics 9 (6), 355.

Stoliaroff, A.; Lecomte, A.; Rubel, O.; Jobic, S.; Zhang, X.H.; Latouche, C.; Rocquefelte, X. Deciphering the Role of Key Defects in Sb2Se3, a Promising Candidate for Chalcogenide-Based Solar Cells. ACS Appl. Energy Mater. 2020, 3, 2496–2509.

Sun, L., He, J., Kong, H., Yue, F., Yang, P., Chu, J., 2011. Structure, composition and optical properties of Cu2ZnSnS4 thin films deposited by Pulsed Laser Deposition method. Sol. Energy Mater. Sol. Cells 95 (10), 2907–2913.

Sunny, A.; Ahmed, S.R.A. Numerical Simulation and Performance Evaluation of Highly Efficient Sb2Se3 Solar Cell with Tin Sulfide as Hole Transport Layer. Phys. Status Solidi B 2021, 258, 2000630.

Tan, L., Tang, A., Zou, Y., Long, M., Zhang, Y., Ouyang, J., Chen, J., 2017. Sb2Se3 assembling Sb2O3@attapulgite as an emerging composites for catalytic hydrogenation of p-nitrophenol. Sci. Rep. 7 (1), 3281.

Tang, R., Chen, X.-Y., Liang, G.-X., Su, Z.-H., Luo, J.-T., Fan, P., 2019a. Magnetron sputtering deposition and selenization of Sb2Se3 thin film for substrate Sb2Se3/CdS solar cells. Surf. Coat. Technol. 360, 68–72.

Tang, R.; Chen, S.; Zheng, Z.H.; Su, Z.H.; Luo, J.T.; Fan, P.; Zhang, X.H.; Tang, J.; Liang, G.X. Heterojunction Annealing Enabling Record Open-Circuit Voltage in Antimony Triselenide Solar Cells. Adv. Mater. 2022, 34, 2109078.

Tang, R., Zheng, Z.-H., Su, Z.-H., Li, X.-J., Wei, Y.-D., Zhang, X.-H., Fu, Y.-Q., Luo, J.-T., Fan, P., Liang, G.- X., 2019b. Highly efficient and stable planar heterojunction solar cell based on sputtered and postselenized Sb2Se3 thin film. Nano Energy 64, 103929.

Tao, J., Hu, X., Guo, Y., Hong, J., Li, K., Jiang, J., Chen, S., Jing, C., Yue, F., Yang, P., 2019. Solutionprocessed SnO2 interfacial layer for highly efficient Sb2Se3 thin film solar cells. Nano Energy.

Tao, J., Hu, X., Xue, J., Wang, Y., Weng, G., Chen, S., Zhu, Z., Chu, J., 2019. Investigation of electronic transport mechanisms in Sb2Se3 thin-film solar cells. Solar Energy Materials and Solar Cells 197: 1-6.

Tao, R.; Tan, T.; Zhang, H.; Meng, Q.; Zha, G. Sb2Se3 Solar Cells Fabricated via Close-Space Sublimation. J. Vac. Sci. Technol. B 2021, 39, 052203.

Terheggen, M., Heinrich, H., Kostorz, G., Baetzner, D., Romeo, A., Tiwari, A., 2004. Analysis of bulk and interface phenomena in CdTe/CdS thin-film solar cells. Interface Sci. 12 (2–3), 259–266.

Tian, Y., Li, G., Zhang, Y., Luo, D., Wang, X., Zhao, Y., Liu, H., Ji, P., Du, X., Li, J., 2019. Low-Bandgap Se-Deficient Antimony Selenide as a Multifunctional Polysulfide Barrier toward High-Performance Lithium-Sulfur Batteries. Adv. Mater.

Tideswell, N., Kruse, F., McCullough, J., 1957. The crystal structure of antimony selenide, Sb2Se3. Acta Crystallogr. A 10 (2), 99–102.

Torane, A., Rajpure, K., Bhosale, C., 1999. Preparation and characterization of electrodeposited Sb2Se3 thin films. Mater. Chem. Phys. 61 (3), 219–222.

Uphoff, H., Healy, J., 1963. Thermoelectric Properties of Diphasal Systems Combining As2Te3 and Tl2Se with Sb2Te3, Bi2Te3, or Sb2Se3. J. Appl. Phys. 34 (2), 390–395.

Vadapoo, R., Krishnan, S., Yilmaz, H., Marin, C., 2011. Electronic structure of antimony selenide (Sb2Se3) from GW calculations. Phys. Status Solidi (B) 248 (3), 700–705.

Versluys, J., Clauws, P., Nollet, P., Degrave, S., Burgelman, M., 2004. Characterization of deep defects in CdS/CdTe thin film solar cells using deep level transient spectroscopy. Thin Solid Films 451, 434–438.

Vidal-Fuentes, P., Guc, M., Alcobe, X., Jawhari, T., Placidi, M., Pérez-Rodríguez, A., Saucedo, E., Izquierdo Roca, V., 2019. Multiwavelength excitation Raman scattering study of Sb2Se3 compound: fundamental vibrational properties and secondary phases detection. 2D Materials 6, 045054.

Voutsas, G., Papazoglou, A., Rentzeperis, P., Siapkas, D., 1985. The crystal structure of antimony selenide, Sb2Se3. Zeitschrift für Kristallographie-Crystalline. Materials 171 (1–4), 261–268.

Wang, L., Li, D.-B., Li, K., Chen, C., Deng, H.-X., Gao, L., Zhao, Y., Jiang, F., Li, L., Huang, F., 2017. Stable 6%-efficient Sb2Se3 solar cells with a ZnO buffer layer. Nat. Energy 2 (4), 17046.

Wang, L., Luo, M., Qin, S., Liu, X., Chen, J., Yang, B., Leng, M., Xue, D.-J., Zhou, Y., Gao, L., Song, H., Tang, J., 2015. Ambient CdCl2 treatment on CdS buffer layer for improved performance of Sb2Se3 thin film photovoltaics. Appl. Phys. Lett. 107 (14), 143902.

Wang, Y.Z.; Ji, S.; Shin, B. Interface engineering of antimony selenide solar cells: A review on the optimization of energy band alignments. J. Phys. Energy 2022, 4, 044002.

Wang, W., Wang, X., Chen, G., Chen, B., Cai, H., Chen, T., Chen, S., Huang, Z., Zhu, C., Zhang, Y., 2018a. Promising Sb2(S, Se)3 solar cells with high open voltage by application of a TiO2/CdS double buffer layer. Solar RRL 1800208.

Wang, W.; Yao, L.; Dong, J.; Wu, L.; Cao, Z.; Hui, L.; Chen, G.; Luo, J.; Zhang, Y. Interface Modification Uncovers the Potential Application of SnO2/TiO2 Double Electron Transport Layer in Efficient Cadmium-Free Sb2Se3 Devices. Adv. Mater. Interfaces 2022, 9, 2102464.

Wang, Y.; Ji, S.; Shin, B. Interface Engineering of Antimony Selenide Solar Cells: A Review on the Optimization of Energy Band Alignments. J. Phys. Energy 2022, 4, 044002.

Wang, Y.; Tang, R.; Huang, L.; Qian, C.; Lian, W.; Zhu, C.; Chen, T. Post-Treatment of TiO2 Film Enables High-Quality Sb2Se3 Film Deposition for Solar Cell Applications. ACS Appl. Mater. Interfaces 2022, 14, 33181–33190.

Wang, X., Tang, R., Wu, C., Zhu, C., Chen, T., 2018b. Development of antimony sulfide– selenide Sb2(S, Se)3-based solar cells. J. Energy Chem. 27 (3), 713–721.

Wang, X., Tang, R., Yin, Y., Ju, H., Zhu, C., Chen, T., 2019. Interfacial engineering for high efficiency solution processed Sb2Se3 solar cells. Sol. Energy Mater. Sol. Cells 189, 5–10.

Wasa, K., Kitabatake, M., Adachi, H., 2004. THIN FILM MATERIALS TECHNOLOGY: Sputtering of Compound Materials. Springer.

Welch, A.W., Baranowski, L.L., Peng, H., Hempel, H., Eichberger, R., Unold, T., Lany, S., Wolden, C., Zakutayev, A., 2017. Trade-offs in thin film solar cells with layered chalcostibite photovoltaic absorbers. Adv. Energy Mater. 7 (11), 1601935.

Welch, A.W., Baranowski, L.L., Zawadzki, P., Lany, S., Wolden, C.A., Zakutayev, A., 2015. CuSbSe2 photovoltaic devices with 3% efficiency. Appl. Phys Express 8 (8), 082301.

Wen, X., Chen, C., Lu, S., Li, K., Kondrotas, R., Zhao, Y., Chen, W., Gao, L., Wang, C., Zhang, J., 2018. Vapor transport deposition of antimony selenide thin film solar cells with 7.6% efficiency. Nature Commun. 9 (1), 2179.

Wen, X., He, Y., Chen, C., Liu, X., Yang, B., Leng, M., Song, H., Zeng, K., Li, D., Li, K., 2017. Magnetron sputtered ZnO buffer layer for Sb2Se3 thin film solar cells. Sol. Energy Mater. Sol. Cells 172, 74–81.

Wen, X.; Lu, Z.; Yang, X.; Chen, C.; Washington, M.A.; Wang, G.-C.; Tang, J.; Zhao, Q.; Lu, T.-M. Vertically Aligned OneDimensional Crystal-Structured Sb2Se3 for High-Efficiency Flexible Solar Cells via Regulating Selenization Kinetics. ACS Appl. Mater. Interfaces 2023, 15, 22251–22262.

Wood, C., Mueller, R., Gilbert, L., 1973. The amorphous Sb-Se system. J. Non-Cryst. Solids 12 (3), 295–313.

Wood, C., Shaffer, J., Proctor, W., 1972. Electron Energy States in Sb2Se3. Phys. Rev. Lett. 29 (8), 485.

Wu, H.-J., Lee, P.-C., Chiu, F.-Y., Chen, S.-W., Chen, Y.-Y., 2015. Self-assisted nucleation and growth of [010]-oriented Sb2Se3 whiskers: the crystal structure and thermoelectric properties. J. Mater. Chem. C 3 (40), 10488–10493.

Wu, W.Y., Xu, Y., Ong, X., Bhatnagar, S., Chan, Y., 2019. Thermochromism from Ultrathin Colloidal Sb2Se3 Nanowires Undergoing Reversible Growth and Dissolution in an Amine-Thiol Mixture. Adv. Mater. 31 (4), 1806164.

Xia, Z., Zhong, J., Leng, M., Hu, L., Xue, D.-J., Yang, B., Zhou, Y., Liu, X., Qin, S., Cheng, Y.-B., 2015. Generalized water-processed metal chalcogenide complexes: synthesis and applications. Chem. Mater. 27 (23), 8048–8057.

Xue, D.J., Yang, B., Yuan, Z.K., Wang, G., Liu, X., Zhou, Y., Hu, L., Pan, D., Chen, S., Tang, J., 2015. CuSbSe2 as a potential photovoltaic absorber material: studies from theory to experiment. Adv. Energy Mater. 5 (23), 1501203.

Yan, H.; Xiao, R.; Pei, Y.; Yang, K.; Li, B. Structural, electrical and optical characteristics of CuSbSe2 films prepared by pulsed laser deposition and magnetron sputtering processes. J. Mater. Sci. Mater. Electron. 2020, 31, 644–651.

Yang, C., Wang, Y., Li, S., Wan, D., Huang, F., 2012. CuSbSe2-assisted sintering of CuInSe2 at low temperature. J. Mater. Sci. 47 (20), 7085–7089.

Yang, K.; Li, B.; Zeng, G. Sb2Se3 thin film solar cells prepared by pulsed laser deposition. J. Alloys Compd. 2020, 821, 153505.

Yang, R.B., Bachmann, J., Pippel, E., Berger, A., Woltersdorf, J., Gösele, U., Nielsch, K., 2009. Pulsed vapor liquid-solid growth of antimony selenide and antimony sulfide nanowires. Adv. Mater. 21 (31), 3170–3174.

Yang, Y.; Guo, T.; Wang, D.; Xiong, X.; Li, B. Preparation and Characterization of Pulsed Laser Deposited CdSe Window Layer for Sb2Se3 Thin Film Solar Cell. J. Mater. Sci Mater. Electron. 2020, 31, 13947–13956.

Yao, L., He, J., 2014. Recent progress in antireflection and self-cleaning technology–From surface engineering to functional surfaces. Prog. Mater Sci. 61, 94–143.

Yeo, B. S.; Amstad, E.; Schmid, T.; Stadler, J.; Zenobi, R., Nanoscale probing of a polymer-blend thin film with tip-enhanced Raman spectroscopy. Small 2009, 5 (8), 952-960.

Yin, W.J., Shi, T., Yan, Y., 2014. Unique properties of halide perovskites as possible origins of the superior solar cell performance. Adv. Mater. 26 (27), 4653–4658.

Yu, L., Chen, J., Fu, Z.-W., 2010. Pulsed laser deposited heterogeneous mixture of Li2Se–Sb2Se3 nanocomposite as a new storage lithium material. Electrochim. Acta 55 (3), 1258–1264.

Yu, L., Kokenyesi, R.S., Keszler, D.A., Zunger, A., 2013. Inverse design of high absorption thin-film photovoltaic materials. Adv. Energy Mater. 3 (1), 43–48.

Yuan, C., Jin, X., Jiang, G., Liu, W., Zhu, C., 2016a. Sb2Se3 solar cells prepared with selenized dc-sputtered metallic precursors. J. Mater. Sci.: Mater. Electron. 27 (9), 8906–8910.

Yuan, C., Zhang, L., Liu, W., Zhu, C., 2016b. Rapid thermal process to fabricate Sb2Se3 thin film for solar cell application. Sol. Energy 137, 256–260.

Zakutayev, A., 2017. Brief review of emerging photovoltaic absorbers. Curr. Opin. Green Sustainable Chem. 4, 8–15.

Zardetto, V., Williams, B., Perrotta, A., Di Giacomo, F., Verheijen, M., Andriessen, R., Kessels, W., Creatore, M., 2017. Atomic layer deposition for perovskite solar cells: research status, opportunities and challenges. Sustainable Energy Fuels 1 (1), 30–55.

Zayed, H., Abo-Elsoud, A., Ibrahim, A., Kenawy, M., 1995. Transport properties of SbxSe1-x thin films. J. Phys. D Appl. Phys. 28 (4), 770.

Zeng, K., Xue, D.-J., Tang, J., 2016. Antimony selenide thin-film solar cells. Semicond. Sci. Technol. 31 (6), 063001.

Zhang, J., Kondrotas, R., Lu, S., Wang, C., Chen, C., Tang, J., 2019. Alternative back contacts for Sb2Se3 solar cells. Sol. Energy 182, 96–101.

Zhang, J.; Guo, H.; Jia, X.; Ning, H.; Ma, C.; Wang, X.; Qiu, J.; Yuan, N.; Ding, J. Improving the Performance of Sb2Se3 Thin-Film Solar Cells Using n-Type MoO3 as the Back Contact Layer. Sol. Energy 2021, 214, 231–238.

Zhao, B., Wan, Z., Luo, J., Han, F., Malik, H.A., Jia, C., Liu, X., Wang, R., 2018a. Efficient Sb2Se3 sensitized solar cells prepared through a facile SILAR process and improved performance by interface modification. Appl. Surf. Sci. 450, 228–235.

Zhao, B., Wan, Z., Luo, J., Jia, C., Liu, X., Wang, R., 2018b. Improving the performance of Sb2Se3 sensitized solar cells with a versatile CdSe layer modification. Appl. Mater. Today 12, 191–197.

Zhao, Y.; Wang, S.; Li, C.; Che, B.; Chen, X.; Chen, H.; Tang, R.; Wang, X.; Chen, G.; Wang, T.; et al. Regulating Deposition Kinetics via a Novel Additive-Assisted Chemical Bath Deposition Technology Enables Fabrication of 10.57%-Efficiency Sb2Se3 Solar Cells. Energy Environ. Sci. 2022, 15, 5118–5128.

Zhou, J.; Meng, D.; Yang, T.; Zhang, X.; Tang, Z.; Cao, Y.; Ni, J.; Zhang, J.; Hu, Z.; Pang, J. Enhanced Charge Carrier Transport via Efficient Grain Conduction Mode for Sb2Se3 Solar Cell Applications. Appl. Surf. Sci. 2022, 591, 153169.

Zhou, J.; Zhang, X.; Chen, H.; Tang, Z.; Meng, D.; Chi, K.; Cai, Y.; Song, G.; Cao, Y.; Hu, Z. Dual-Function of CdCl2 Treated SnO2 in Sb2Se3 Solar Cells. Appl. Surf. Sci. 2020, 534, 147632.

Zhou, Y., Leng, M., Xia, Z., Zhong, J., Song, H., Liu, X., Yang, B., Zhang, J., Chen, J., Zhou, K., 2014. Solution processed antimony selenide heterojunction solar cells. Adv. Energy Mater. 4 (8), 1301846.

Zhou, Y., Li, Y., Luo, J., Li, D., Liu, X., Chen, C., Song, H., Ma, J., Xue, D.-J., Yang, B., 2017. Buried homojunction in CdS/Sb2Se3 thin film photovoltaics generated by interfacial diffusion. Appl. Phys. Lett. 111 (1), 013901.

Zhou, Y., Wang, L., Chen, S., Qin, S., Liu, X., Chen, J., Xue, D.-J., Luo, M., Cao, Y., Cheng, Y., 2015. Thin film Sb2Se3 photovoltaics with oriented one-dimensional ribbons and benign grain boundaries. Nat. Photonics 9 (6), 409.

Zi, W.; Mu, F.; Lu, X.; Liu, Z.; Pang, X.; Yu, Z.; Li, Y.; Zhao, Z.; Lei, B.; Cheng, N.; et al. Sputtering Al2O3 as an Effective Interface Layer to Improve Open-Circuit Voltage and Device Performance of Sb2Se3 Thin-Film Solar Cells. Mater. Sci. Semicond. Process. 2023, 153, 107185.

Ga_2O_3

Ahmadi E., O. S. Koksaldi, X. Zheng, T. Mates, Y. Oshima, U. K. Mishra, J. S. Speck, Appl. Phys. Express 2017, 10, 071101.

Baldini M., Z. Galazka, G. Wagner, Wide Band Gap Semicond. Technol. Gener. Energy Effic. Power Electron. 2018, 78, 132.

Bartasyte A., S. Margueron, T. Baron, S. Oliveri, P. Boulet, Adv. Mater. Interfaces 2017, 4, 1600998.

Bierwagen O., Z. Galazka, Appl. Phys. Lett. 2018, 112, 092105.

Bosi M., P. Mazzolini, L. Seravalli, R. Fornari, J. Mater. Chem. C 2020, 8, 10975.

Bosi M., L. Seravalli, P. Mazzolini, F. Mezzadri, R. Fornari, Cryst. Growth Des. 2021, 21, 6393.

Bosio A., C. Borelli, A. Parisini, M. Pavesi, S. Vantaggio, R. Fornari, ECS J. Solid State Sci. Technol. 2020, 9, 055002.

Budde M., D. Splith, P. Mazzolini, A. Tahraoui, J. Feldl, M. Ramsteiner, H. von Wenckstern, M. Grundmann, O. Bierwagen, Appl. Phys. Lett. 2020, 117, 252106.

Caplins B. W., P. T. Blanchard, A. N. Chiaramonti, D. R. Diercks, L. Miaja-Avila, N. A. Sanford, Ultramicroscopy 2020, 213, 112995.

Chen Z., Z. Luo, Y. Qi, P. Yang, S. Wu, C. Huang, T. Wu, J. Wang, C. Gao, T. Sritharan, L. Chen, Appl. Phys. Lett. 2010, 97, 242903.

Cho S. B., R. Mishra, Appl. Phys. Lett. 2018, 112, 162101.

Cora I., F. Mezzadri, F. Boschi, M. Bosi, M. Čaplovičová, G. Calestani, I. Dódony, B. Pécz, R. Fornari, Cryst. Eng. Comm. 2017, 19, 1509.

Diercks D. R., B. P. Gorman, Ultramicroscopy 2018, 195, 32.

Fiedler A., R. Schewski, M. Baldini, Z. Galazka, G. Wagner, M. Albrecht, K. Irmscher, J. Appl. Phys. 2017, 122, 165701.

Fujita S., K. Kaneko, Proc. 17th Int. Conf. Cryst. Growth Epitaxy ICCGE-17 2014, 401, 588.

Green J., J. Speck, G. Xing, P. Moens, F. Allerstam, K. Gumaelius, T. Neyer, A. Arias-Purdue, V. Mehrotra, A. Kuramata, K. Sasaki, S. Watanabe, K. Koshi, J. Blevins, O. Bierwagen, S. Krishnamoorthy, K. Leedy, A. R. Arehart, A. T. Neal, S. Mou, S. A. Ringel, A. Kumar, A. Sharma, K. Ghosh, U. Singisetti, W. Li, K. Chabak, K. Liddy, A. Islam, S. Rajan, et al, APL Mater. 2022, 10, 029201.

Grundmann M., T. Böntgen, M. Lorenz, Phys. Rev. Lett. 2010, 105,146102. Z. Guo, A. Verma, X. Wu, F. Sun, A. Hickman, T. Masui, A. Kuramata, M. Higashiwaki, D. Jena, T. Luo, Appl. Phys. Lett. 2015, 106, 111909.

Golz C., Z. Galazka, J. Lähnemann, V. Hortelano, F. Hatami, W. T. Masselink, O. Bierwagen, Phys. Rev. Mater. 2019, 3, 124604.

Gorman B. P., D. Diercks, N. Salmon, E. Stach, G. Amador, C. Hartfield, Microsc. Today 2008, 16, 42.

Guo S.-D., H.-M. Du, Eur. Phys. J. B 2020, 93, 7.

Higashiwaki M., K. Sasaki, A. Kuramata, T. Masui, S. Yamakoshi, Appl. Phys. Lett. 2012, 100, 013504.

Janzen B. M., P. Mazzolini, R. Gillen, V. F. S. Peltason, L. P. Grote, J. Maultzsch, R. Fornari, O. Bierwagen, M. R. Wagner, J. Mater. Chem. C 2021, 9, 14175.

Kaufmann S., R. Niemann, T. Thersleff, U. K. Rößler, O. Heczko, J. Buschbeck, B. Holzapfel, L. Schultz, S. Fähler, New J Phys 2011, 13, 053029.

Kneiß M., A. Hassa, D. Splith, C. Sturm, H. von Wenckstern, T. Schultz, N. Koch, M. Lorenz, M. Grundmann, APL Mater. 2018, 7, 022516.

Kneiß M., P. Storm, A. Hassa, D. Splith, H. von Wenckstern, M. Lorenz, M. Grundmann, APL Mater. 2020, 8, 051112.

Kneiß M., A. Hassa, D. Splith, C. Sturm, H. von Wenckstern, M. Lorenz, M. Grundmann, APL Mater. 2019, 7, 101102.

Kneiß M., D. Splith, P. Schlupp, A. Hassa, H. von Wenckstern, M. Lorenz, M. Grundmann, J. Appl. Phys. 2021, 130, 084502.

Lany S., APL Mater. 2018, 6, 046103.

Larson D. J., Local electrode atom probe tomography: a user's guide, Springer, New York 2013.

Leone S., R. Fornari, M. Bosi, V. Montedoro, L. Kirste, P. Doering, F. Benkhelifa, M. Prescher, C. Manz, V. Polyakov, O. Ambacher, J. Cryst. Growth 2020, 534, 125511.

Li J. Z., Z. Z. Chen, S. F. Li, Q. Q. Jiao, Y. L. Feng, S. X. Jiang, Y. F. Chen, T. J. Yu, B. Shen, G. Y. Zhang, Superlattices Microstruct. 2016, 96, 234.

Liu Q., Z. Chen, X. Zhou, ACS Omega 2022, 7, 11643.

Mazzolini P., O. Bierwagen, J. Phys. D: Appl. Phys. 2020, 53, 354003.

Mazzolini P., A. Falkenstein, Z. Galazka, M. Martin, O. Bierwagen, Appl. Phys. Lett. 2020, 117, 222105.

Mazzolini P., Z. Fogarassy, A. Parisini, F. Mezzadri, D. Diercks, M. Bosi, L. Seravalli, A. Sacchi, G. Spaggiari, D. Bersani, O. Bierwagen, B. Janzen.2, M. Marggraf, M. Wagner, I. Cora, B. Pécz, A. Tahraoui, A. Bosio, C. Borelli, S. Leone, R. Fornari Advanced Functional Materials, 33 (2023) 2207821. DOI:10.1002/adfm02207821

Mazzolini P., P. Vogt, R. Schewski, C. Wouters, M. Albrecht, O. Bierwagen, APL Mater. 2018, 7, 022511.

Mazzolini P., A. Falkenstein, C. Wouters, R. Schewski, T. Markurt, Z. Galazka, M. Martin, M. Albrecht, O. Bierwagen, APL Mater. 2020, 8, 011107.

Mezzadri F., G. Calestani, F. Boschi, D. Delmonte, M. Bosi, R. Fornari, Inorg. Chem. 2016, 55, 12079.

Miller W., D. Meiling, R. Schewski, A. Popp, S. B. Anooz, M. Albrecht, Phys. Rev. Res. 2020, 2, 033170.

Mott N. F., E. A. Davis, Electronic processes in non-crystalline materials, 2nd ed., Clarendon Press, Oxford 2012.

Mott N. F., Metal-insulator transitions, 2nd ed., Taylor & Francis, London; New York 1990.

Nikolaev V. I., S. I. Stepanov, A. I. Pechnikov, S. V. Shapenkov, M. P. Scheglov, A. V. Chikiryaka, O. F. Vyvenko, ECS J. Solid State Sci. Technol. 2020, 9, 045014.

Nishinaka H., H. Komai, D. Tahara, Y. Arata, M. Yoshimoto, Jpn. J. Appl. Phys. 2018, 57, 115601.

Nishinaka H., O. Ueda, D. Tahara, Y. Ito, N. Ikenaga, N. Hasuike, M. Yoshimoto, ACS Omega 2020, 5, 29585.

Orita M., H. Ohta, M. Hirano, H. Hosono, Appl. Phys. Lett. 2000, 77, 4166.

Oshima Y., E. G. Víllora, Y. Matsushita, S. Yamamoto, K. Shimamura, J. Appl. Phys. 2015, 118, 085301.

Parisini A., A. Bosio, V. Montedoro, A. Gorreri, A. Lamperti, M. Bosi, G. Garulli, S. Vantaggio, R. Fornari, APL Mater. 2019, 7, 031114.

Parisini A., A. Bosio, H. J. von Bardeleben, J. Jimenez, S. Dadgostar, M. Pavesi, A. Baraldi, S. Vantaggio, R. Fornari, Mater. Sci. Semicond. Process. 2022, 138, 106307.

Parisini A., P. Mazzolini, O. Bierwagen, C. Borelli, K. Egbo, A. Sacchi, M. Bosi, L. Seravalli, A. Tahraoui, R. Fornari, J Vac Sci Technol A 2022, 40, 042701.

Pearton S. J., J. Yang, P. H. Cary, F. Ren, J. Kim, M. J. Tadjer, M. A. Mastro, Appl. Phys. Rev. 2018, 5, 011301.

Rafique S., L. Han, A. T. Neal, S. Mou, J. Boeckl, H. Zhao, Phys. Status Solidi A 2018, 215, 1700467.

Ranga P., S. B. Cho, R. Mishra, S. Krishnamoorthy, Appl. Phys. Express 2020, 13, 061009.

Roy R., V. G. Hill, E. F. Osborn, J. Am. Chem. Soc. 1952, 74, 719.

Sasaki K., A. Kuramata, T. Masui, E. G. Víllora, K. Shimamura, S. Yamakoshi, Appl. Phys. Express 2012, 5, 035502.

Schewski R., K. Lion, A. Fiedler, C. Wouters, A. Popp, S. V. Levchenko, T. Schulz, M. Schmidbauer, S. Bin Anooz, R. Grüneberg, Z. Galazka, G. Wagner, K. Irmscher, M. Scheffler, C. Draxl, M. Albrecht, APL Mater. 2018, 7, 022515.

Shklovskii B. I., A. L. Ėfros, Electronic properties of doped semiconductors, 1st ed. Springer, Berlin Heidelberg 2013.

Swallow J. E. N., C. Vorwerk, P. Mazzolini, P. Vogt, O. Bierwagen, A. Karg, M. Eickhoff, J. Schörmann, M. R. Wagner, J. W. Roberts,P. R. Chalker, M. J. Smiles, P. Murgatroyd, S. A. Razek, Z. W. Lebens-Higgins, L. F. J. Piper, L. A. H. Jones, P. K. Thakur, T.-L. Lee,J. B. Varley, J. Furthmüller, C. Draxl, T. D. Veal, A. Regoutz, Chem. Mater. 2020, 32, 8460.

Tremblay F., M. Pepper, D. Ritchie, D. C. Peacock, J. E. F. Frost, G. A. C. Jones, Phys. Rev. B 1989, 39, 8059.

Villora E. G., K. Shimamura, K. Kitamura, K. Aoki, Appl. Phys. Lett. 2006, 88, 031105.

Vogt P., O. Brandt, H. Riechert, J. Lähnemann, O. Bierwagen, Phys. Rev. Lett. 2017, 119, 196001.

Von Bardeleben H. J., J. L. Cantin, A. Parisini, A. Bosio, R. Fornari, Phys. Rev. Mater. 2019, 3, 084601.

Wang W., L. Li, J. Liu, B. Chen, Y. Ji, J. Wang, G. Cheng, Y. Lu, G. Rijnders, G. Koster, W. Wu, Z. Liao, npj Quantum Mater. 2020, 5, 73.

Xia X., Y. Chen, Q. Feng, H. Liang, P. Tao, M. Xu, G. Du, Appl. Phys.Lett. 2016, 108, 202103.

Zhang Y., Y. Gong, X. Chen, Y. Kuang, J. Hao, F.-F. Ren, S. Gu, R. Zhang, J. Ye, ACS Appl. Electron. Mater. 2022, 4, 461.

Zhang Z.-C., Y. Wu, S. Ahmed, Mater. Res. Express 2019, 6,125904.

$BaFe_2O_4$

Arlt, G. Twinning in ferroelectric and ferroelastic ceramics: stress relief. J. Mater. Sci. 25, 2655 (1990).

Benedek, N. A. & Fennie, C. J. Hybrid improper ferroelectricity: a mechanism for controllable polarization-magnetization coupling. Phys. Rev. Lett. 106, 107204 (2011). 9.

Bibes, M. & Barthélémy, A.Multiferroics: towards a magnetoelectric memory. Nat. Mater. 7, 425–426 (2008).

Blöchl, P. E. Projector augmented-wave method. Phys. Rev. B 50, 17953 (1994).

Bousquet, E. et al. Improper ferroelectricity in perovskite oxide artificial superlattices. Nature 452, 732–736 (2008).

Bousquet, E. & Spaldin, N. J dependence in the LSDA+U treatment of noncollinear magnets. Phys. Rev. B 82, 220402(R) (2010).

Bruker, APEX2, SAINT, TWINABS. Bruker AXS Inc., Madison (2014).

Burns, S. R., Paull, O., Juraszek, J., Nagarajan, V. & Sando, D. The experimentalist's guide to the cycloid, or non collinear antiferro magnetism in epitaxial BiFeO3. Adv. Mater. 32, 2003711 (2020).

Campbell, B. J., Stokes, H. T., Tanner, D. E. & Hatch, D. M. ISODISPLACE: a web-based tool for exploring structural distortions. J. Appl. Crystallogr. 39, 607–614 (2006).

Chapon, L. C. et al. Wish: the new powder and single crystal magnetic diffractometer on the second target station. Neutron N. 22, 22–25 (2011).

Chen, X., Hochstrat, A., Borisov, P. & Kleemann,W. Magnetoelectric exchange bias systems in spintronics. Appl. Phys. Lett. 89, 202508 (2006).

Chun, S. H. et al. Electric field control of nonvolatile four-state magnetization at room temperature. Phys. Rev. Lett. 108,177201 (2012).

Dashwood, C. D. et al. Spontaneous cycloidal order mediating a spin-reorientation transition in a polar metal. Phys. Rev. B 102, 180410(R) (2020).

Delmonte, D. et al. Poling-written ferroelectricity in bulk multiferroic double-perovskite BiFe0.5Mn0.5O3. Inorg. Chem. 55, 6308–6314 (2016).

Dmitriev, V. P., Rochal, S. B., Gufan, Yu. M. & Tolédano, P. Reconstructive transitions between ordered phases: the martensitic fcchcp and the graphite-diamond transitions. Phys. Rev. Lett. 62, 2495 (1989).

Dowben, P. A., Nikonov, D. E., Marshall, A. & Binek, C. H. Magnetoelectric antiferromagnetic spin–orbit logic devices. Appl. Phys. Lett. 116, 080502 (2020).

Ederer, C. & Spaldin, N. A. Weak ferromagnetism and magnetoelectric coupling in bismuth ferrite. Phys. Rev. B 71,060401–060404 (2005).

Ferreira, T. et al. -C BaFe4O7 and K0.22Ba0.89Fe4O7: canted antiferromagnetic diferrites with exceptionally high magnetic ordering temperatures. Chem. Mater. 29, 2689–2693 (2017).

Fukuda, K. & Fukushima, K. Crystal structure of hexagonal SrAl2O4 at 1073 K. J. Solid State Chem. 178, 2709–2714 (2005).

Gnewuch, S. & Rodriguez, E. E. The fourth ferroic order: current status on ferrotoroidic materials. J. Solid State Chem. 271, 175–190 (2019).

Graziosi, P. et al. Conditions for the growth of smooth La0.7Sr0.3MnO3 thin films by pulsed electron ablation. Thin Solid Films 534, 83–89 (2013).

He, X. et al. Robust isothermal electric control of exchange bias at room temperature. Nat. Mater. 9, 579–585 (2010).

Hill, N. A. Why are there so few magnetic ferroelectrics? J. Phys.Chem. B 104, 6694–6709 (2000).

Hoerkner, W. & Mueller-Buschbaum, H. Zur kristallstruktur von CaAl2O4. J. Inorg. Nucl. Chem. 38, 983–984 (1976).

Jang, H. M., Han, H. & Lee, J.-H. Spin-coupling-induced improper polarizations and latent magnetization in multiferroic BiFeO3. Sci. Rep. 8, 405 (2018).

Kadomtseva, A. M., Zvezdin, A. K., Popov, Y. F., Pyatakov, A. P. & Vorob'ev, G. P. Space-time parity violation and magnetoelectric interactions in antiferromagnets. Jetp Lett. 79, 571–581 (2004).

Kahlenberg, V. & Fischer, R. X. Structural characterization of strontium monoferrite SrFe2O4, a new stuffed framework compound. Solid State Sci. 3, 433–439 (2001).

Kahlenberg, V., Fischer, R. X. & Shaw, C. S. J. Polymorphism of strontium monogallate: the framework structures of β - SrGa2O4 and ABW - type γ - SrGa2O4. J. Solid State Chem. 153, 294–300 (2000).

Kahlenberg, V. & Weidenthaler, C. High temperature single crystal diffraction study onmonobarium gallate—the crystal structure of β- BaGa2O4. Solid State Sci. 4, 963–968 (2002).

Keeney, L. et al. Magnetic field-induced ferroelectric switching in multiferroic aurivillius phase thin films at room temperature. J. Am.Ceram. Soc. 96, 2339–2357 (2013).

Khalyavin, D. D. et al. Emergent helical texture of electric dipoles. Science 369, 680–684 (2020).

Kingsmith, R. D. & Vanderbilt, D. Theory of polarization of crystalline solids. Phys. Rev. B 47, 1651 (1993).

Kitagawa, Y. et al. Low-field magnetoelectric effect at room temperature. Nat. Mater. 9, 797–802 (2010).

Kosub, T. et al. Purely antiferromagnetic magnetoelectric random access memory. Nat. Commun. 8, 13985 (2017).

Kresse, G. & Furthmüller, J. Efficient iterative schemes for ab initio total-energy calculations using a plane-wave basis set. Phys. Rev. B 54, 11169 (1996).

Kresse, G. & Furthmüller, J. Efficiency of ab-initio total energy calculations for metals and semiconductors using a plane-wave basis set. Comput. Mater. Sci. 6, 15 (1996).

Kresse, G. & Joubert, D. From ultrasoft pseudopotentials to the projector augmented-wave method. Phys. Rev. B. 59, 1758 (1999).

Kubel, F. & Schmid, H. Structure of a ferroelectric and ferroelastic monodomain crystal of the perovskite BiFeO3. Acta Cryst. B 46, 698–702 (1990).

Lebeugle, D., Colson, D., Forget, A. & Viret, M. Very large spontaneous electric polarization in BiFeO3 single crystals at room temperature and its evolution under cycling fields. Appl. Phys., Lett. 91, 022907–3 (2007).

Li, M. R. et al.Magnetostriction-polarization coupling in multiferroic Mn2MnWO6. Nat. Commun. 8, 2037 (2017).

Liechtenstein, A. I., Anisimov, V. I. & Zaanen, J. Density-functional theory and strong interactions: orbital ordering in Mott-Hubbard insulators. Phys. Rev. B 52, R5467 (1995).

Marsh, R. E. & Bernal, I. More space-group changes. Acta Crystallogr. B 51, 300–307 (1995).

Meriani, S. Polymorphism of barium monoferrite, BaFe2O4. Acta Cryst. B 28, 1241–1243 (1972).

Mitsuda, H., Mori, S. & Okazaki, C. The crystal structure of barium monoferrite, BaFe2O4. Acta Cryst. B 27, 1263–1269 (1971).

Orlandi, F. et al. L. Extended “orbital molecules” and magnetic phase separation in Bi0.68Ca0.32MnO3. Phys. Rev. B 103, 104105 (2021).

F. Orlandi, D. Delmonte, G. Calestani, E. Cavalli, E. Gilioli, V. V. Shvartsman, P. Graziosi, S. Rampino, G. Spaggiari, C. Liu, W. Ren, S. Picozzi, M. Solzi, M. Casappa, F. Mezzadri, γ-BaFe2O4: a fresh playground for room temperature multiferroicity, Nature Communications, 13 (2022) 7968.

Petricek, V., Dusek, M. & Palatinus, L. Crystallographic computing system JANA2006: general features. Z. Kristallogr. - Cryst. Mater. 229, 345–352 (2014).

Perez-Mato, J. M., Orobengoa, D. & Aroyo, M. I. Acta Cryst. A66, 558–590 (2010).

Perdew, J. P., Burke, K. & Ernzerhof, M. Generalized gradient approximation made simple. Phys. Rev. Lett. 77, 3865 (1996).

Resta, R. Theory of the electric polarization in crystals. Ferroelectrics 136, 51 (1992).

Sanchez, D. A. et al. Room-temperature single phase multiferroic magnetoelectrics: Pb(Fe, M)x(Zr,Ti)(1–x)O3 [M = Ta, Nb]. J. Appl. Phys.113, 074105 (2013).

Sanchez, D. A., Kumar, A.,Ortega, N., Katiyar, R. S. & Scott, J. F. Near-room temperature relaxor multiferroic. Appl. Phys. Lett. 97, 202910 (2010).

Shevlin, S. Multiferroics and the path to the market. Nat. Mat. 18, 191–192 (2019).

Schmid, H. Multi-ferroic magnetoelectrics. Ferroelectrics 162, 317–338 (1994).

Sheldrick, G. M. Crystal structure refinement with SHELXL. Acta Cryst. A 71, 3–8 (2015).

Sheldrick, G. M. A short history of SHELX. Acta Cryst. A 64, 112–122 (2008).

Shvartsman, V. V., Kleemann, W., Haumont, R. & Kreisel, J. Large bulk polarization and regular domain structure in ceramic BiFeO3. Appl. Phys. Lett. 90, 172115 (2007).

Shvartsman, V. V. & Kholkin A. L. Nanoscale investigation of polycrystalline ferroelectric materials via piezoresponse force microscopy. Multifunctional Polycrystalline Ferroelectric Materials: Processing and Properties, (eds Pardo, L. & Ricote, J.) (Springer,Dordrecht, 2011).

Sosnowskaa, I. & Zvezdin, K. Origin of the long period magnetic ordering in BiFeO3. J. Magn. Magn. Mater. 140, 167 (1995).

Stokes,H. T.Hatch,D.M.&Campbell, B. J. ISODISTORT, ISOTROPY Software Suite, iso.byu.edu.

Sui-Yang, H. Von, Der Mühll, R., Ravez, J. & Couzi, M. Phase transition and symmetry in BaAl2O4. Ferroelectrics 159, 127–132 (1994).

Tan, G. & Chen, X. Structure and multiferroic properties of barium hexaferrite ceramics. J. Magn. Magn. Mat. 327, 87–90 (2013).

Toby, B. H. & Von Dreele, R. B. GSAS-II: the genesis of a modern open-source all purpose crystallography software package. J. Appl. Cryst. 46, 544–549 (2013).

Trassin, M. Low energy consumption spintronics using multiferroic heterostructures. J. Phys. Condens. Matter 28, 033001 (2016).

Trukhanov, S. V. et al. Coexistence of spontaneous polarization and magnetization in substituted M-type hexaferrites BaFe12–x Alx O19 (x⩽ 1.2) at room temperature. JETP Lett. 103, 100–105 (2016).

Turchenko, V. et al. Structural features, magnetic and ferroelectric properties of SrFe10.8In1.2O19 compound. Mater. Res. Bull. 138, 111236 (2021).

Wang, L., Maxisch, T. & Ceder, G. Oxidation energies of transition metal oxides within the GGA+U framework. Phys. Rev. B 73, 195107 (2006).

Wang, J. et al. Epitaxial BiFeO3 multiferroic thin film heterostructures. Science 299, 1719–1722 (2003).

Xue, L. & Guo-Long, T. Multiferroic and magnetoelectronic polarizations in BaFe12O19 system. J. Alloy. Compd. 858, 157722 (2021).

Zhang,G. et al. Visible-light photovoltaic effect in high-temperature ferroelectric BaFe4O7. J. Mater. Chem. C. 8, 16234–16240 (2020).

Zhao, T. et al. Electrical control of antiferromagnetic domains in multiferroic BiFeO3 films at room temperature. Nat. Mater. 5, 823–829 (2006).

Acknowledgments

And here we are at the part that perhaps is the most difficult to write. In these three years of this doctorate, many things have happened, both professionally and personally. None of the results presented in this thesis would have been achieved if there hadn't been other people around me. People who already know how much I have appreciated their closeness and support, but whom I still want to thank formally.

The first person I have to, but above all, want to thank is my supervisor, Prof. Danilo Bersani. I don't think I could have found a better supervisor. I know that in the world of doctoral studies, one can sometimes feel undervalued. This has never happened to me. Thank you, Danilo, for always listening and supporting the ideas I proposed, for always finding time to discuss, and for allowing me to have a lot of stimulating experiences.

Thank you also because I know that, regardless of what my professional future will be, I will always find an open door. Thank you from the bottom of my heart.

Along with Danilo, I also want to thank Laura and Lorenzo, who are a fundamental part of the group and who are not only two excellent scientists but also two fantastic individuals. Thank you very much, Lore, for the companionship in Perugia, especially during the way to the train station, and thank you, Laura, for all the coffees! If it weren't for you always being on top of things, the Friday morning "stretching" would be caffeine-free.

On the other hand, since part of my work was carried out at IMEM, I feel compelled to thank first and foremost Dr. Stefano Rampino, who has been my unofficial supervisor for these years. Thank you for always answering all my questions and for indulging even

some quirky ideas, like our foray into the world of influencers (which we quickly realized just wasn't our thing).

Thank you, of course, to all my colleagues at IMEM: Francesco, Edi, Roberto, Massimo, Giovanna, Villo, Patrizia, Michele, Matteo, and Davide, not to forget Chiara and Elena, who are also my official suppliers of crackers and hugs in difficult times. A special thank you to Enos, who dedicated a lot of time and energy to teach me the secrets of photolithography and deep levels. Thank you very much for your patience!

Staying within the professional context, there are truly many people to thank. All my colleagues and friends at Unipr, including Francesco, Michele, Giacomo, Anna, Piero, Daniele, Rino, just to name a few. It has been a pleasure to collaborate with Roberto, Antonella, Maura, Matteo, and many others. Each of these individuals has enriched my experience with their expertise and the opportunity for discussion. I will never stop emphasizing that no result is achieved alone, and after these three years, I believe in teamwork more than ever. I'm sure I've forgotten someone, as age catches up, but in case it's an unintentional omission, I'll definitely make it up with a toast at the earliest opportunity.

I also want to extend my thanks to the group that hosted me during my visits to ETH in Zurich. I thank Dr. Kumar for the opportunity, and I want to express my gratitude to my colleague Siiri Bienz, who is not only a very smart woman but also a wonderful person. Working with her is a real pleasure, and I hope our collaboration will continue in the future. Thank you, Siiri, for everything! Your laugh always manages to lift my spirits!

However, in life, it's not just about work; in fact, thanking all the people in my life would perhaps be an even more challenging task than writing this thesis. I believe I am truly fortunate to have so many people who have always been there for me in one way or another. My lifelong friends (especially Chiara, Arianna, Laura and Agnese) for the endless chats that often take on the shape of psychotherapy sessions. Michele and Mikako for our online dinners, filled with science and laughter. To all my friends overseas... thanks to technology, we can finally chat (even if often with some delay) and pretend that all those miles don't separate us.

There are many things that make life easier. I would like to take this moment to remember some that have made and continue to make my life more peaceful. Beers on summer evenings and whiskey on winter ones. Sundays in the countryside, walking with Aida, because the best view is always between a horse's ears. My cats curled up on the couch 90% of the time, except during Teams calls. The book club with my favorite librarian and the scent of paper that these evenings bring with them. Those random acts of kindness

that sometimes happen among strangers and give hope for a better world. Activists, because I can't stand those who don't get involved and don't take a stand. Travel, both the big and important trips and those small getaways that allow the mind and soul to regenerate.

A lunch on a bench in a park on the first days of spring. My dogs who can read people's souls. A spontaneous phone call just to say, "how are you." People who respect all forms of life. The figs and blackberries that grow even on my balcony and taste of care. The exhaustion after a hike rewarded by incredible views. AVIS breakfasts.

Friday's nights at "Bonfa". Gina and Fabio's warm hospitality and huge heart.

The folks at Intercultura, especially Clelia, who may not be a young girl in terms of age but possesses the spirited fight of a twenty-year-old.

Concerts (especially those of Green Day, where I feel like a teenager again for a few hours) and good music (the loud one you need when cleaning the house).

Festivaletteratura, the sharp intelligence of Chiara Valerio, and Michela Murgia's "Morgana" podcast. The hours spent on trains daydreaming while looking out the window and the car rides with Cristina. The hot water bottle on cold winter days. Those moments when a small thing reminds you of how beautiful it is to be alive.

And this has been the greatest lesson that these three years have taught me: how beautiful life is, how the most ordinary moments can turn into the most significant memories.

To my family, my siblings, my cousins, and my aunts and uncles. To my mom, who remains my anchor in this often-stormy sea. To Davide, who has become my safe harbor and without whose support none of this would have been possible. And to my dad, who is in every hour, minute, and page of this thesis and every day. I miss you.